FORMULATION OF AN UNCERTAINTY BASED METHODOLOGY FOR ADVANCED TECHNOLOGY PERFORMANCE PREDICTION

A Thesis
Presented to
The Academic Faculty

by

Henry D. Schwartz

In Partial Fulfillment
of the Requirements for the Degree
Doctor of Philosophy in the
School of Aerospace Engineering

Georgia Institute of Technology
May 2017

FORMULATION OF AN UNCERTAINTY BASED METHODOLOGY FOR ADVANCED TECHNOLOGY PERFORMANCE PREDICTION

Approved by:

Professor Dimitri N. Mavris, Advisor
School of Aerospace Engineering
Georgia Institute of Technology

Professor Daniel Schrage
School of Aerospace Engineering
Georgia Institute of Technology

Professor Lakshmi Sankar
School of Aerospace Engineering
Georgia Institute of Technology

Dr. Jimmy Tai
School of Aerospace Engineering
Georgia Institute of Technology

Dr. Jeff Schutte
General Electric

Date Approved: 6 April 2017

To my wonderful family, friends, and especially my wonderful wife. If it were not for your endless love and support, this journey may have never ended.

ACKNOWLEDGEMENTS

I would like to express my gratitude to the numerous people who have helped me achieve this great milestone. First and foremost I would like to thank my advisor, professor Dimitri Mavris. I had no idea what I was getting myself into when I moved to Atlanta seven years ago for grad school, but he was there to guide me through every step of the PhD process. Doc, you have taught me far more in the past seven years at ASDL than I could have ever imagined, and I hope there will be many more. Thanks to your patience, guidance, inspiration, and many lessons I feel extremely prepared for my future.

I am grateful to my committee professor Mavris, professor Sankar, professor Schrage, Dr. Tai, and Dr. Schutte for their guidance and feedback throughout this process. I owe a special thank you to Dr. Tai and Dr. Schutte who generously spent hundreds of hours reviewing my research along the way.

I would like to thank the NASA GSRP program for funding this research. Specifically Dr. Ruben Del Rosario and Mr. Bill Haller from NASA's Glenn Research Center. I would also like to thank Dr. Eric Hendricks who served as my mentor during the three summers I spent up at NASA in Cleveland. I am grateful for your friendship, wisdom, and encouragement.

I would also like to express my thanks to all of my fellow students and colleagues at Georgia Tech, specifically the ERA ITD research team and the fall 2012 quals group, for their input, feedback, and encouragement. While it may not have always felt like constructive criticism, I could not have finished without their support. I would specifically like to thanks Christian Perron who took time out of his busy schedule to set up CFD simulations for me.

To my family and friends, thank you for your love and support. To my mom and dad, none of these opportunities would have been possible without everything you have done for me. To my brother, thank you for always being the big brother there when I needed you.

Lastly, I would like to thank my wife Katie. You have been an instrumental part of my life since the day we met. You were always there to keep me motivated when it felt like I would never make it to the end. I am grateful for you endless love and support.

TABLE OF CONTENTS

LIST OF TABLES

LIST OF FIGURES

SUMMARY

The aviation industry is a significant part of the global economy. To address the environmental concerns due to the rapid growth in aviation, government and industry partners from around the world are striving to meet aggressive goals to reduce fuel burn, noise, and emissions of commercial aircraft. Existing technologies are capable of reaching these goals individually, but reaching these goals simultaneously creates additional challenges. These challenges stem from interdependencies between the fuel burn, emissions, and noise metrics that require engineers to make trade-offs between them. Thus, to meet these future goals, advanced technologies such as the open rotor engine or the blended wing body must be developed.

When faced with multi-objective problems like this one, engineers and decision makers need the ability to rapidly understand how making changes to one variable affects all of these objectives simultaneously. A key enabler is the development of a credible performance estimation tool that can be used to parametrically explore large areas of the design space. To ensure the credibility of the tool, it must include a traceable and transparent prediction of the uncertainty throughout the design space. This will enable engineers and decision makers to parametrically explore the design space while giving them an understanding of the confidence level of the prediction. Additionally, by including the level of uncertainty throughout the design space, decision makers can apply additional resources for experimentation more efficiently by applying them where there is a high level of uncertainty.

The creation of a modeling environment for an advanced technology, such as the open rotor engine, is challenging because large amounts of data is needed. Unfortunately, it is difficult to obtain this data for a number of reasons. High order

computational models or physical experiments are used sparingly in the early phases of design because they are too expensive and too slow. In contrast, while lower order methods are fast, they lack credibility due to the number of assumptions made, and empirical methods resulting from historical data are only appropriate for traditional concepts. One way of decreasing the computational effort and time associated with high fidelity simulations is to utilize information from multiple sources of data at multiple fidelity levels. These methods are commonly referred to as multifidelity methods in the literature. They capitalize on the fact that inaccuracies in low fidelity methods does make them completely ineffective. Instead, low fidelity methods can be run throughout large areas of the design space and then be augmented with sparse high fidelity data to create a more accurate model. Therefore, the research objective for this thesis is as follows:

Given the resulting uncertainty distributions of disparate sources of multifidelity data simulations, develop a method to rapidly characterize the uncertainty throughout the design space based on relative location of the desired design to the higher fidelity design(s) for sparse data situations.

It is important to clarify that this research focuses on the synthesis of the resulting uncertainty distributions from multiple simulations at different fidelity levels of the same technology. This is in contrast to propagating the uncertainty distributions on the design variables through some sort of modeling and simulation environment to create the resulting uncertainty distribution. The research described in this dissertation assumes that the resulting uncertainty distributions from probabilistic simulations are given.

The research discussed in this document shows that the Multifidelity Uncertainty using Statistical Inference Characterization (MUSIC) methodology will provide a more accurate uncertainty characterization of a technology's performance throughout the entire design space compared to Bayesian model averaging with sparse data. The

first step in the methodology is to gather or generate the different data sets and their corresponding uncertainty distributions. Next, the low fidelity uncertainty distributions are biased based on the relative proximity to higher fidelity data points. After the biasing process, all of the data points and the biased distributions are combined into one data set. The distributions are then propagated throughout the entire design space. From literature review, the best method for propagating uncertainty is through a Monte Carlo simulation. Thus, the distributions are sampled and fit with a surrogate model to propagate the distributions throughout the entire design space. This process is carried out numerous times to ensure an accurate representation of the distributions. The final synthesized performance prediction is found by calculating the mean of all the surrogates at every point in the design space. The overall bounds of all the surrogates are used to represent the final uncertainty characterization. It is important for the reader to understand that no sources of uncertainty are identified or reduced by this method. The uncertainty characterization in this method is an inference based on knowledge from known points nearby.

A canonical example is generated from known mathematical functions to test the initial feasibility of the method as well as to address two of the research questions. The first research question asks what type of proximity function should be used to bias the data, and should this function be allowed to change for each dimension? A common uncertainty modeling algorithm called Kriging led the author to the squared exponential function. The squared exponential function is a versatile smooth function that is scaled by one parameter. Kriging uses a genetic algorithm to determine an optimal set of scaling parameters that results in the best fit to a set of training data. The squared exponential function with a unique set of scaling parameters set by the Kriging algorithm is compared against the squared exponential function with fixed scaling parameters as well as a linear function. The hypothesis is that using the Kriging algorithm to select unique parameters for the squared exponential function

in each dimension will give the best results. The truth model for this experiment is represented by a quadratic function in one dimension and cubic function in the other. A small number of points are selected from this function to represent the high fidelity data set. Another function similar to the truth, but with some imperfections, is created to give the appearance of a lower fidelity simulation that is missing some physics. A Gaussian distribution is used to represent the uncertainty of the high fidelity data. The largest amount of error between the high and low fidelity functions is used to define the uncertainty for the low fidelity data throughout the entire design space. From past experiences working with industry, the author chose to represent the low fidelity uncertainty distributions with triangular distributions. The model representation error as well as the average reduction of uncertainty were used to determine which proximity function is best. The results support the hypothesis that using the Kriging algorithm to determine the scaling parameters provides the best uncertainty characterization. The other functions tend to move the bounds of the distributions such that they no longer encompass the truth model.

As stated above, the first experiment uses a triangular distribution to represent the low fidelity uncertainty distributions; however other distributions could be used. Therefore, the second experiment looks into whether or not the type of uncertainty distribution used for the low fidelity data matters. Comparisons are made between the triangular and Weibull distributions using the same mathematical functions from the first experiment. The same metrics are used to evaluate the results. The results support the hypothesis that the type of distribution used to represent the low fidelity uncertainty does not make a significant difference as long as it has a unique mode and can be bounded.

Another question that arose pertains to the situation where there are more than two levels of fidelity. If additional data sets that include supplementary knowledge are obtained, then the methodology must be able to account for them. Do changes need

to be made to the biasing calculations? Does a fidelity level weight factor need to be developed? The analysis of a two-dimensional section of an infinite wing span made up of NACA 16-series airfoils is used for this experiment. The NACA 16-series airfoils were chosen as the test case for this experiment because there is a large amount of wind tunnel data available. They are also the airfoils used on the outer sections of the Hamilton Standard propeller that will be discussed later. The results show that the addition of a mid fidelity level data set improves the final prediction as expected. However, the results are not sensitive to a fidelity level weight factor which came as a surprise. Some additional testing was done on drag instead of lift to determine if the unexpected results were problem dependent, yet there was no change in the results.

The final experiment substantiates the overall thesis statement that this method provides a better result compared to Bayesian model averaging. Bayesian model averaging (also referred to as Bayesian model combination) is commonly used to synthesize data sets. However, it requires a significant amount of data. The NACA 16-series airfoils are again used for this experiment because of the large amount of wind tunnel data available for validation. The experimental results support the hypothesis that the method presented in this thesis provides a more accurate uncertainty characterization of the performance throughout the design space when compared against Bayesian model averaging with sparse data. The most significant being that this method reduced the level of inferred uncertainty by approximately 20% more compared to Bayesian model averaging. In addition, Bayesian model averaging requires significantly more data since two separate surrogates are necessary for this research.

After all the research questions are answered, the MUSIC method is applied to a Hamilton Standard propeller data set for the demonstration and validation of the method on a representative problem. This case study was selected due to the availability of a large data set associated with this propeller. Advanced propeller concepts

like the prop fan and open rotor do not have enough data for validation, but demonstrating the method on the Hamilton Standard data is sufficient. The results for this final application show that the MUSIC method provides a useful uncertainty characterization of the performance of a representative engine technology throughout the entire design space.

CHAPTER I

INTRODUCTION AND MOTIVATION

The aviation industry has become, and will continue to be a significant part of the global economy. In a report published in 2016, the FAA predicts the available seat miles (common measure of an airline's passenger carrying capacity) will increase by approximately 3.5% annually through 2033[34]. Boeing and Airbus project the need for approximately 33,000 new aircraft over the next 20 years to replace aging aircraft and to increase the global fleet[14, 5]. Both companies are predicting the world wide fleet to double in the next thirty years. While the increase in air traffic bodes well for the global economy, the environmental impact of this increase, namely noise and air pollution, is becoming a major source of concern for local and global communities. Coupled with these rapidly emerging environmental issues is the ever-rising cost of fuel[90].

To address these economic and environmental concerns, industry and governments from around the world are striving to meet aggressive goals to reduce the fuel burn, noise, and emissions of commercial aircraft. There are technologies capable of meeting the goals individually, but what makes this area of research challenging is that these goals must be met simultaneously. Interdependencies between the three goals make this difficult, and trade-offs among the goals must be considered and analyzed.

Many existing technologies have the ability to target one of the specific goals; however, to meet these goals simultaneously, manufacturers will need to move away from traditional technologies to new advanced technologies, such as the open rotor engine or the hybrid wing body airframe. Unfortunately, additional obstacles arise

when researching advanced technologies because there is a general lack of understanding of the concepts' behavior. Thus, the primary goal of this research will focus on increasing the amount of engineering knowledge available early in the design process.

One of the primary methods engineers explore the capabilities of new technologies is through parametric design space exploration. A key enabler for this type of exploration is a modeling environment that can rapidly predict the performance of the concept under investigation throughout large areas of the design space. The result of this is to provide engineers with a way to parametrically explore the design space which is particularly important during the conceptual design phase. However, advanced technologies with limited experimental data readily available create the additional challenge of finding an appropriate performance model. This research aims to provide a way to utilize available data in a way that maximizes the amount of knowledge that is able to be gained about the performance of an advanced concept.

In addition to requiring an accurate representation of a high fidelity design space, a decision maker needs to understand the amount of uncertainty surrounding the prediction. This will enable the decision maker to make more informed decisions about how to efficiently allocate resources. A poor understanding of the uncertainty during the conceptual design phase leads to increased performance risk at the technology level which ultimately leads to consequences at the system level.

The following section will provide a brief introduction to uncertainty modeling. Next, the open rotor engine technology will be introduced, and an explanation for its choice in this study will be given. Both sections provide some motivating questions that were instrumental in scoping this research. Lastly, the final section in this chapter will harmonize the motivating observations into a formal research objective for this thesis.

1.1 Uncertainty Modeling

The following section provides a brief introduction to uncertainty modeling. A detailed discussion about uncertainty quantification is provided in Section 2.4. Various surrogate modeling techniques are commonly used to model uncertainty. One specific method called Kriging, expresses an observers uncertainty about a response that has not yet been observed, based on a sample. Note that Kriging can be thought of as a specific type of Gaussian process if the reader is familiar with Gaussian processes.

Kriging is a type of surrogate model that is fit to a set of observations, and then yields a predictive probability distribution on the response at new locations in the design space[65]. This predictive distribution is sometimes used to represent the amount of uncertainty throughout a design space. Decision makers can subsequently use the predictive uncertainty distribution to determine where additional resources should be applied. A detailed explanation of Kriging is provided in Section 2.6.

The only problem is that the predictive uncertainty distribution is relative. Meaning that it only provides a prediction of the amount of uncertainty in one area of the design space relative to another. It does not represent the true uncertainty. Another way to think of it is that it provides the change in uncertainty. However, what if the uncertainty at specific points in the space is known? Can the change in uncertainty modeled by the Kriging algorithm be combined in some way with the known uncertainty at specific points in the design space be used to provide a more accurate representation of the uncertainty throughout the entire design space? This motivating question is the primary motivation for the biasing process described in Section 3.3.

1.2 Advanced Technologies: Open Rotor Engines

This section provides a brief introduction to the open rotor engine technology, which is the motivating technology for the methodology developed within this thesis. The

Figure 1: GE Unducted Fan mounted on an MD-80[27].

goal of this research is to formulate, substantiate, and demonstrate the resulting methodology. The methodology is not applied to an advanced technology, like the open rotor, within this thesis because of the limited access to data required for proper validation. Despite this limitation, it is believed that this approach will enable the reader to understand the proposed approach and will allow for the implementation to a real world technology, like the open rotor, when necessary data becomes available in the future.

One of the primary goals of engine technologies is to reduce the fuel consumption. Even though the price of a barrel of crude oil is difficult to project, the US Energy Information Administration (EIA) and the Organization of the Petroleum Exporting Countries (OPEC) both predict the price to steadily rise over the next 30 years[2, 90]. As a result of the rising cost along with the volatility, the airlines are demanding more efficient aircraft. They must become more robust to changes in fuel price. Therefore, aircraft engine manufacturers are once again researching advanced propeller driven

engines because of their efficiency advantage over typical turbofan engines seen on today's aircraft. These propeller driven engines - commonly referred to as prop-fans, unducted fans, or open rotors - are an attempt to combine the efficiency benefit of a propeller with the speed and altitude capabilities of a typical turbofan.

Engineers have known about the efficiency advantages of propeller driven engines since the beginning of the jet age. In fact, research on the open rotor engine architecture began more than 30 years ago during the spike in oil prices in the 1970s due to the Middle East oil embargo [16, 42]. Engine manufacturers successfully tested and flew full scale engines, such as the GE UDF pictured in Figure 1. This engine, which features two unducted counter-rotating blade sets, was mounted on an MD-80 and flew across the Atlantic in 1988 to the Farnborough airshow. Removing the nacelle all together allows for larger diameters and lower fan pressure ratios without the additional weight and drag penalty of a larger nacelle. Incorporating two blade rows allows engineers to achieve a given amount of thrust with a smaller diameter propeller while avoiding losses due to high tip speeds. The counter-rotation of the blade rows removes the losses due to the swirl of the air behind the propeller [42].

Unfortunately, airlines were still hesitant to return to propeller engines after these successful demonstrations because of concerns relating to noise, maintenance, and the perception of the general public that propellers are a step back in technology. Furthermore, the 1980s brought a drop in the oil prices and it no longer made financial sense for airlines to invest in these engines. Therefore, manufacturers were forced to shelve the concept due to the decrease in economic viability.

In order for this concept to become economically viable again, manufacturers must address fuel burn reduction while maintaining speeds that are comparable to current commercial aircraft. Some estimates put the fuel burn savings of this architecture upward of 30%[42, 117]. For air breathing engines, thrust is produced by ingesting

air at the free stream velocity and ejecting it at a higher velocity. Thrust is a function of the velocity difference multiplied by the mass flow of air through the engine. Essentially, it is equal to the change of momentum of the air flow moving through the engine, while the power required is equal to the rate of change of kinetic energy. Propeller driven engines are more efficient because of their large mass flow, which allows them to achieve a desired amount of thrust with a smaller change in velocity, or kinetic energy. The propulsive efficiency of the engine is defined as the ratio of the aircraft power (thrust times velocity) to the power out of the engine [76]. This means that the larger the change in the air velocity within the engine, the lower the propulsive efficiency.

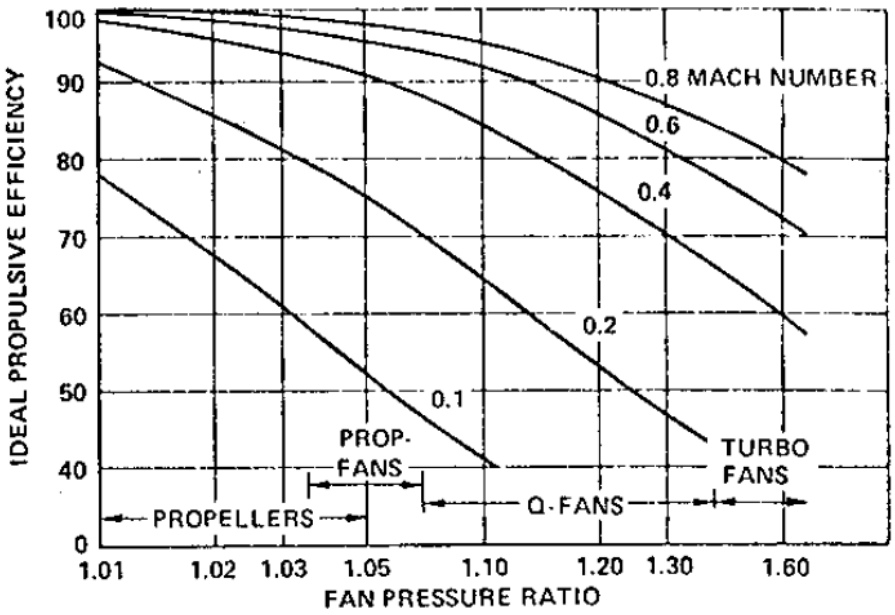

Figure 2: Ideal propulsive efficiency as a function of Mach number and fan pressure ratio[98]

Figure 2 depicts the relationship between the fan pressure ratio and ideal propulsive efficiency for typical aircraft engines provided by a simple calculation utilizing momentum theory. The initial prop-fans studied in the 1970s had fan pressure ratios near 1.05 resulting in an ideal propulsive efficiency of approximately 97%. This is approximately 17% higher than a typical turbofan which has a fan pressure ratio around

1.6[98]. However, to accurately predict the fuel burn savings of counter-rotating propellers, a high fidelity and physics-based engine model must be developed.

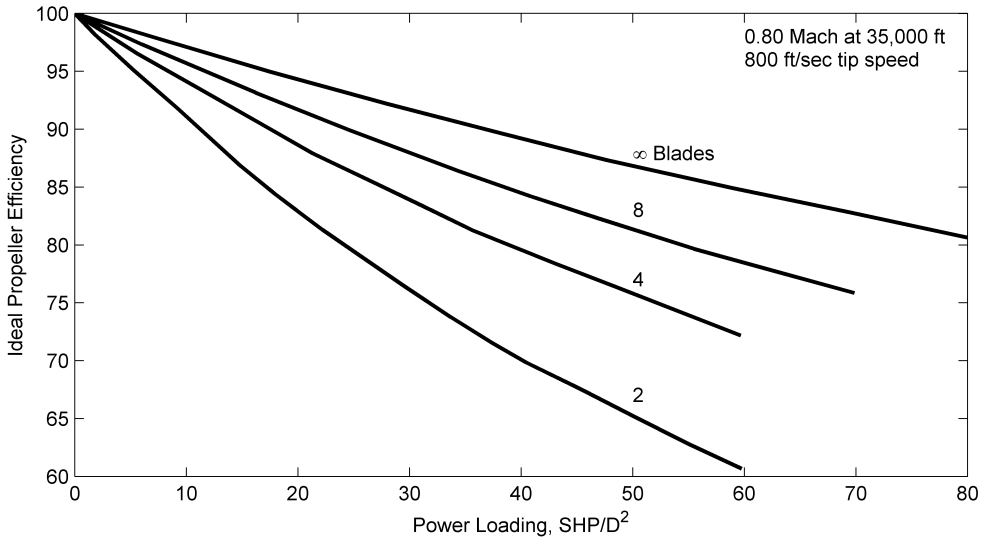

Figure 3: Ideal propulsive efficiency as a function of power loading and number of blades[98]

Large commercial aircraft require a lot of thrust and as the thrust increases either the propeller diameter must increase to capture more air or the power loading must increase. The relationship between power loading and ideal efficiency for a given number of blades is shown in Figure 3. Increasing the diameter is not ideal because it causes installation issues and increases the effective Mach number at the blade tips. As the effective Mach number approaches one, local shocks begin to form, drag increases, and the overall propeller efficiency decreases. This is the same phenomena that occurs on a wing; however, on a propeller the effective Mach is due to both the forward speed and the rotational speed. Therefore, the propeller will reach its drag divergence Mach number in flight regimes below Mach one. To mitigate the losses caused by drag divergence, the blades must feature unique geometries that allow for efficient operation in the transonic speed regime.

Despite the current favorable economic environment for the introduction of open rotor engines, some major hurdles still remain with regard to the noise and installation

issues. Even though experimental tests have proven the open rotor concept to be technically feasible, the concept still may not be economically viable due to these hurdles. A first step in overcoming these obstacles is the development of a credible performance estimation tool that can be used to explore large areas of the design space. This will enable engineers to determine if a concept is economically viable by providing a more accurate estimate of fuel burn reduction. To make an accurate performance estimation, engineers need a better understanding of how blade design affects the complex aerodynamic interactions between the blade rows.

1.3 Research Objective

The creation of a modeling environment for an advanced technology, such as the open rotor, is challenging. Commercial aircraft operate in the transonic speed regime, which poses a challenge to lower fidelity models typically used during the conceptual design phase because they are based on the potential flow equations. These equations are not considered to be applicable in the high speed viscous areas of the design space, yet only low order models meet the execution speed requirements for performing trade studies. These observations have led to a series of high level questions regarding low order models that will be addressed by this research:

- If their uncertainty is to be quantified will they be more useful?
- Can the level of uncertainty be improved by combining them with sparse high fidelity data?
- If there are multiple data sets at different fidelity levels, can information be used from all of them?

Investigating the answers to these questions will give decision makers a better idea of the capabilities of low order models. It is believed that existing low order models

may not be applicable in some areas of the design space, but they may be appropriate in other areas. Therefore, they should not be completely discarded.

In contrast to low fidelity data, it is difficult to obtain high fidelity data. High order computational models or physical experiments are not likely to be used in the early phases of design because they are too expensive and too slow to facilitate trade studies. Furthermore, they can be cumbersome and time consuming to run.

Finally, empirical methods resulting from historical data are only appropriate for traditional concepts. Engineers currently make performance estimations by fitting models to a limited amount of experimental data along with expert engineering judgment, or by scaling the performance of an existing system. However, these approaches do not allow for the exploration of large areas of the design space.

Further complicating the design space exploration problem is the necessity to meet multiple goals simultaneously. Therefore, engineers need the ability to parametrically move throughout the design space to perform trade studies among the different goals. For example, an acoustics engineer working on the open rotor may want to clip the aft blade row by 5% so the aft blades do not slice through the tip vortices of the front blades. This has a significant noise benefit, but it also adversely impacts the propulsive performance. Propulsion engineers need the ability to quickly create a performance map that can be used by an engine cycle analysis team to assess the system level performance of these quieter blade designs. This trade-off study would be more effective if a rapid parametric performance map prediction tool was available.

It has been established that the open rotor technology can provide significant efficiency benefits, which motivates its use for this research. Moreover, the open rotor is an attractive research area because experimental tests have been conducted on this concept in the past resulting in publicly available data from wind tunnel experiments. Furthermore, it is once again being researched as a possible concept for reducing fuel burn[112].

On the other hand, the current methods do not allow engineers to explore large areas of the design space because the existing wind tunnel data is not sufficient, and low order methods that do not require as many resources are not trusted. One way of decreasing the computational effort and time associated with high fidelity simulations is to utilize information from multiple sources of data. These methods are commonly referred to as multifidelity methods in the literature. They capitalize on the fact that, just because low order methods may not be as accurate as others, they are not useless. The low order methods can be run throughout large areas of the design space and can then be augmented with the sparse high order data to create a more accurate model.

The notion of accuracy or uncertainty continues to come up, yet there is no quantitative measurement of uncertainty for any of the physics based modeling methods. Bayesian inference methods such as Bayesian model averaging (also referred to as Bayesian model combination) are only effective when there is a sufficient amount of data. Therefore, there is a need for a methodology that synthesizes all available data sources, along with their corresponding uncertainties, into one data source under a sparse data situation. Having this ability will enable engineers to conduct trade studies that allow them to understand how changes to the geometry impact the noise, fuel burn, and emissions simultaneously. A methodology called the Multifidelity Uncertainty using Statistical Inference Characterization (MUSIC) methodology has been developed to address these requirements. The primary research objective and hypothesis of this research are as follows:

Research Objective: Given the resulting uncertainty distributions of disparate sources of multifidelity data simulations, develop a method to rapidly characterize the uncertainty throughout the design space based on relative location of the desired design to the higher fidelity design(s) for

sparse data situations.

Overarching Hypothesis: The Multifidelity Uncertainty using Statistical Inference Characterization (MUSIC) methodology will provide a more accurate uncertainty characterization of the performance throughout the entire design space compared to Bayesian model averaging with sparse data.

Meeting this research objective will enable rapid parametric design space exploration as well as efficient resource allocation. This will require extensive knowledge in the area of propeller aerodynamics and testing. Advanced propeller systems are being targeted by this research because they have already gone through the beginning stages of development and have proven to be worth investigating, yet the extent of their potential benefit is still unknown. A method like the one described in this thesis will help engineers efficiently obtain a better understanding of advanced propeller systems.

It is important to clarify that this research focuses on the synthesis of the resulting uncertainty distributions from multiple simulations at different fidelity levels of the same concept. This is in contrast to propagating the uncertainty distributions on the design variables through some sort of modeling and simulation environment to create the resulting uncertainty distribution. The research described in this dissertation assumes that the resulting uncertainty distributions from probabilistic simulations are given.

Additionally, it is important for the reader to understand that no sources of uncertainty are identified or reduced by this method. The uncertainty characterization in this method is an inference based on knowledge from known points at nearby locations.

In summary, this first chapter has shown that a methodology is needed to enable design space exploration for advanced technologies, and that the methodology must meet the following requirements:

- Characterize the uncertainty throughout the design space
- Be Capable of handling sparse data sets
- Use knowledge from multiple data sets at multiple fidelity levels

The remainder of this document will go through the details of the development and validation of the MUSIC methodology to meet the requirements. Chapter 2 will provide relevant background information on the aforementioned areas of interest with respect to the primary research objective, such as engine performance estimation, model definition and validation, and multifidelity modeling methods.

Chapter 3 will go through the details of the problem formulation for this research. A set of formal research questions and their corresponding hypotheses are discussed as they come up in the problem formulation. This chapter concludes with a canonical example to help the reader understand the details of the problem formulation.

Chapter 4 provides an experimental plan and discusses the details of each experiment pertaining to the research questions and hypotheses. The first two experiments are conducted on a mathematical test problem. Experiments 3 and 4 are conducted on NACA 16-series airfoils. The results for all four experiments are discussed in Chapter 5. The final experiment is to demonstrate the methodology on the Hamilton Standard propeller data. These results are presented in Chapter 6.

Chapter 7 provides concluding remarks and a discussion about future work in this area of research.

CHAPTER II

BACKGROUND

Relevant background information will be discussed in this chapter starting with performance estimation and propeller maps. The next portion of the chapter discusses models and how they are made. This is followed by a discussion of validation which leads into uncertainty representation and multifidelity methods.

2.1 Engine Performance Estimation and Propeller Maps

A quick high-level introduction to engine cycle design is included in this section. So what are performance maps and why is it so important to have one? Performance maps provide engine cycle designers with important knowledge about how each component performs when integrated into a larger system such as an engine[24]. Efficiency and power requirements at various operating conditions are examples of some important performance characteristics. Examples of some performance maps for propellers are given in Appendix A

During engine cycle design, each component of the engine is sized through a two-step sizing process[76]. The first is the on-design performance analysis which sizes the engine components so that they meet the specified design requirements. However, engine components will never exactly meet their design specifications, and they will not always operate at their design condition. Thus, the engine is analyzed away from its design requirements to make sure that the engine can safely function in all operating conditions. This is called the off-design analysis. This sizing process cannot be done without accurate performance maps for each component. These individual component maps are created through various types of models.

An example of a propeller map is shown in Figure 4. It depicts the coefficient of

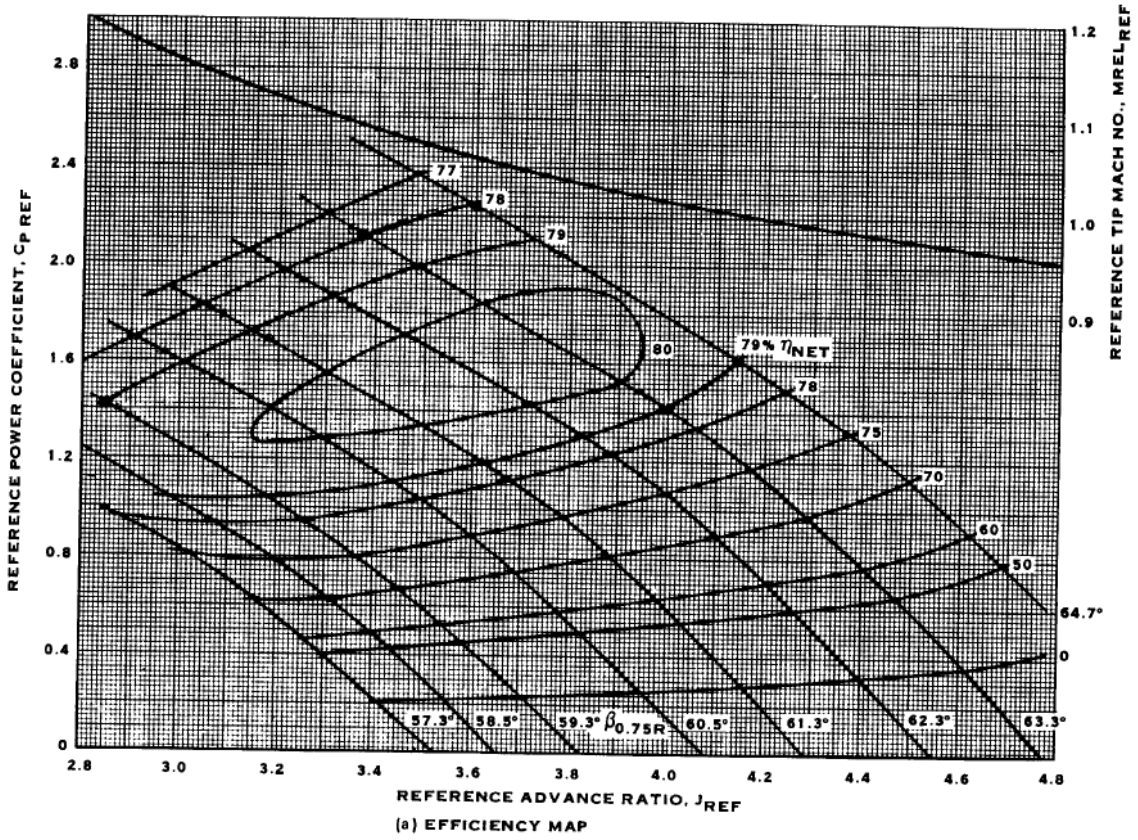

Figure 4: SR3 propeller performance map[99]

power as a function of the advance ratio for different blade angles. The advance ratio is a non-dimensional measurement of distance traveled per revolution. It is explained in more detail in Appendix C.3.3. The map also displays islands of efficiency.

2.2 What Is A Model?

Before discussing the various types of propeller modeling methods, we first need to understand how models are made. Balci describes models in a broad sense as an "abstraction of reality"[9]. More specifically, Neelamkavil states that they are "a representation of a physical system or process intended to enhance our ability to understand, predict, or control its behavior"[85]. Oberkampf and Roy define two categories of mathematical models[88]. The first is called empirical or phenomenological. These models are based on how a system responds to different input conditions. The

system is treated as a black box meaning that the model is only concerned with the global relationship between the inputs and outputs. This type of representation does not attempt to describe the detailed processes within the system. The process of creating this type of model is also referred to as system identification. See Billings for a more detailed description of system identification methods[10].

The other model category is referred to as a physical law or explanatory model. The developer of the model must have in-depth knowledge of the actual processes occurring within the system. Previous observations are used to determine the physical processes and laws that should be considered and what can be ignored. Many of these physical law models were derived hundreds of years ago and form the foundations for modern analysis of physical systems.

The process of creating a good model starts with the proper definition of the problem and an understanding of how the real or designed system is expected to function[19]. It is important for the reader to understand that models are designed for a specific purpose and thus are not universally valid. Problems typically arise when researchers use a model outside of its region of applicability. Unfortunately these researchers tend to criticize the model and its creator as opposed to their own ignorance. Roache gives a common example of this pitfall by describing how some people believe Einstein proved Newton's law of gravity to be wrong, rather than that Einstein defined the limits of applicability for Newton's Law[97].

Error due to solving the wrong problem or using the wrong model is what statisticians call type III error[9]. Law and Kelton stated it best when they said "A great model for the wrong problem will never be used"[63]. It should also be emphasized that a model will not solve a problem by itself, but it will provide valuable tools for identifying areas that need further investigation and testing. For this reason there is increased awareness that code development and experimentation go hand in hand[4, 17, 79, 88].

Properly defining the problem is also important when it comes to model complexity. Unfortunately researchers tend to jump to a complicated solution process due to a poorly defined problem. A model should only include elements and processes that are important to achieve the goals of the computational analysis. The predictive power of a model depends on its ability to identify the dominant factors and their influences on the overall system, not on its completeness[88]. Or, as Einstein would say, "make the model as simple as possible, but no simpler." Unfortunately, many researchers in the engineering and science fields have ignored Einstein's advice due to the lure of rapidly increasing computational power. The majority of this computational power is mostly consumed by increased model complexity which often only leads to a limited improvement in risk-informed decision-making[88]. Researchers should start with a simple model and build up the complexity as needed.

2.3 Verification and Validation

Another important aspect of creating a model is to ensure that the model is trusted by the user. Before diving into the discussion about model validation, the reader should understand that there is also no such thing as a completely valid model [88, 97, 63, 114]. Or as Box and Draper put it "all models are wrong, some are more useful"[88]. Many assumptions must inherently be made, and these assumptions must be properly understood by the model user.

Several terms are sometimes incorrectly used interchangeably when discussing model validation. Therefore, it is important to provide the definitions that will be utilized for these terms within this research. The definitions for verification, validation, and credibility are as follows:

- **Verification** - The first formal definition appears to be given by Fishman and Kiviat as "whether the mathematical structure of a model behaves as the creator intended"[37]. A more concise definition is given by Boehm as "solving the

governing equations right"[13]. Verification can be thought of as pertaining to the proper mathematical definition of the model.

- **Validation** - Fishman and Kiviat were also first to define validation as "whether a simulation model properly approximates the real system"[37]. Again, Boehm concisely states validation as "solving the right governing equations"[13]. Validation can be thought of as the proper understanding of the science/engineering of the problem. The American Institute of Aeronautics and Astronautics (AIAA) and the American Society of Mechanical Engineering (ASME) define validation as the process of determining the degree to which a model is an accurate representation of the real world from the perspective of the intended uses of the model[89].

- **Credibility** - Carson was the first to define a credible model as "one which is accepted by the client as being valid, and is used as an aid in making decisions"[19]. The client in this context could be a manager, customer, or any sort of stakeholder. The important point being that the model is considered credible because the client trusts it enough to use it for decision making.

- **Model Validation** - Assessment of model accuracy as determined by comparison of model outputs with experimental measurements[89, 88].

In general, a model should be used in a manner similar to how experimental data would be used, and it should be validated relative to the same measures of performance that the actual system is measured against[4]. All assumptions should be well documented, and the validation process should be done in parallel with the creation of the model[63]. More specifically, verification and validation are not steps that can be tacked on to the end of a program. The process of validating a code should be jointly designed by experimentalists and code writers. They should be developed in cooperation, yet completed independently. Only after results have been

obtained should any comparisons take place. This is a good way to begin the process of establishing credibility.

A model should have high face validity which can be done by talking to experts in the field[84]. Begin by starting with existing theory or models and rely on comparison to experimental observation. Aeschliman and Oberkampf believe that the model creator should have in depth knowledge of the actual experimental tests that are being used for validation[4]. They strongly feel that simply using journal articles which describe the experiments are not sufficient because critical details about the experimental set up may be left out. It should be noted that Aeschliman and Oberkampf are referring specifically to the validation of CFD codes. This likely becomes less important as the fidelity level of the model being created decreases. Unfortunately it is not always possible to obtain in-depth knowledge of the experimental tests.

A validation process is measured using a validation metric to provide a quantitative measure of agreement between a model's output and experimental observations[68]. Oberkampf and Roy define seven key characteristics that a validation metric should have[88].

- The metric should be an objective and quantitative measure of agreement between a model and physical observations.
- The criteria used by the analyst or designer should be separate from the validation metric.
- Uncertainties from the mathematical models and the physical observations should be included.
- The metric should provide a statistical confidence level associated with the amount of physical data available.
- The metric should differentiate between models containing greater and lessor amounts of uncertainty.

- The metric should be able to assess the local and global predictability.

The main emphasis being that a validation metric should blindly measure a computational model's predictive capability. It is attempting to answer the question *how good is the model?*, instead of optimizing the agreement between the model and experimental observations[86]. The later is referred to as model calibration which is not a part of this research.

There are four major validation methods. The first method is referred to as hypothesis testing where the user constructs an unbiased test statistic with the underlying hypothesis that the physical observations come from the prediction populations. One can decide whether there is enough evidence to reject or not reject a null hypothesis. It is possible to commit type I and type II errors[68].

The second method is called Bayesian updating or the Bayes factor approach. In this approach, statistical parameters (mean, standard deviation, etc.) of the prediction distribution are treated as random variables and they can be updated via the observed physical data. The metric is based on the ratio of posterior distributions of the null and alternative hypotheses to infer whether the experimental data comes from one of the statistical populations derived from the predictive model[68]. Oberkampf and Roy object to this method because they believe that the uncertainty should not be based on an analyst's prior belief. Instead, it should be based on objectively measuring the confidence of data with predictions[88].

The third method developed by Oberkampf et. al is called frequentist's metric[86, 87]. This method measures the distance between the mean of the prediction and the estimated mean of the physical observation. The uncertainty of the distance is quantified by a confidence bound, and the decision criterion of accepting or rejecting a model is separate from the metric itself. One of the benefits of this technique is that it is deterministic and therefore computationally cheap.

The final metric, called the area metric, aims to measure the agreement of the

entire set of distributions of the predictions with the observations. The area metric was first proposed by Ferson et al.[35, 36]. The measurement between the two distributions is found quantitatively with the following equation:

$$d(F^e_{x_i}, F^m_{x_i}) = \int_{-\infty}^{\infty} \left| F^e_{x_i}(x) - F^m_{x_i}(x) \right| dx \tag{1}$$

where $F^e_{x_i}(\cdot)$ is the observed distribution and $F^m_{x_i}(\cdot)$ is the predicted distribution. The technique can be used when only a few data points from predictions or experiments are available[68]. A similar method developed by Oberkampf uses P-boxes[88].

One important point when considering the frequentist's metric and the area metric is that they both only quantify the difference between predictions and observations. There is no criterion for accepting or rejecting a model. The decision to accept or reject a model is up to the decision maker and their requirements at the time.

2.4 Uncertainty Quantification

Technology research and development programs have three primary goals: improvement in relative performance parameters, risk reduction, and technology maturation[73]. Technologies can mature in different ways, with some improving in performance, and other reducing risk[74]. Risk is a function of uncertainty and consequence[50]. Since technology research and development is a function of risk, it is also a function of uncertainty. Thus, the overall goal of research and development programs is to significantly reduce the uncertainty. A program manager must understand the existing uncertainty and what is causing it. A poor understanding of uncertainty leads to increased performance risk at the technology level which could lead to performance degradation at the system level.

Although the goal is to minimize uncertainty, it should be noted that there will always be some degree of uncertainty[50, 53]. The quantification of uncertainty for the data and models is very important to this research. When models do not account for the uncertainty of their parameters properly, any resulting analysis conducted

with these models is misleading. A common assumption is to use a nominal value for uncertain parameters which can lead to a design that degrades rapidly when perturbed from a design point[53]. This is especially true with highly optimized designs. Ironically, a highly optimized design that does not take into account uncertainty is potentially a high risk solution. Therefore, engineers must be able to properly identify the existing uncertainty, understand the uncertainty sources, represent it in a way that makes sense, and quantify its impact on the objectives at hand.

When dealing with developing technologies where a large amount of uncertainty still exists, it is ideal to follow well-defined procedures that are mathematically based. The uncertainty quantification process includes five main steps: identify, characterize, propagate, analyze, and reduce. There are several philosophies for uncertainty classification and strategies for uncertainty characterization and propagation to choose from when conducting uncertainty assessments. The Details on these philosophies will follow to provide some background into why the methods used in the MUSIC methodology were selected.

Many sources of uncertainty exist when developing a new technology or advanced concept. In these situations there is a desire to have a sound taxonomy that categorizes the uncertainty sources. Several taxonomies exist in the literature, but one that is prevalent in the risk assessment community has two main categories: aleatory uncertainty and epistemic uncertainty. Aleatory is commonly referred to as irreducible, but it is also called stochastic or type A. Epistemic uncertainty is due to lack of knowledge and is also called reducible or type B[91, 44, 100, 87]. When utilizing this taxonomy, uncertainty sources are categorized as either aleatory or epistemic, which informs the type of assessment that should be conducted. Since aleatory uncertainties cannot be reduced, the goal of any uncertainty assessment is to quantify and control their impact. In contrast, epistemic uncertainty sources can be reduced. Therefore, the objective is to quantify their impact and determine how to properly eliminate

them over time.

For this research different types of data will be utilized, and it will be assumed that each set of data has a varying amount of uncertainty surrounding it. Within the context of this research, most of the uncertainty that is being discussed can be assumed to be due to lack of knowledge surrounding the performance of the entity being designed and investigated. Therefore, it is assumed that it is epistemic uncertainty. This is important to know when attempting to characterize the uncertainty. Furthermore, the data sets utilized in this research will be from a variety of different experiments and modeling environments of varying fidelity levels.

When these differences in data types exist, the challenge lies in determining the appropriate way to characterize the uncertainty surrounding each of the data sets. After the identification of uncertainty sources, they must be mathematically characterized and represented to enable quantitative assessments. Helton et. al. provide an overview of the many ways that uncertainty is represented[43], including probability theory, possibility theory, evidence theory, and interval analysis. Probability theory assigns probabilities to the variables which represent the amount of likelihood. Evidence theory is less restrictive as it involves two specifications of likelihood: belief and plausibility. Possibility theory is more closely related to fuzzy set theory than probability theory. In this case the likelihood is specified in terms of necessity and possibility. Interval analysis is the least restrictive because it does not attempt to apply any sort of uncertainty structure. Interval analysis attempts to propagate an interval of possible input values and create an interval of possible output function values.

As previously stated, there are two main categories of data within this research: data from physical experiments and data from computational experiments. It is important to separate these two categories because different methods are used for representing their uncertainties. The literature shows that there is widespread agreement

throughout the uncertainty quantification community for the representation of uncertainty surrounding experimental data. The agreement is that a Gaussian distribution is sufficient to represent the uncertainty that surrounds experimental data[88]. Furthermore, I personally have found this to hold true when working with experimental data on probabilistic performance assessments.

In contrast, this same sentiment does not hold true when it comes to computational data. In the literature, there are differing opinions on how the uncertainty should be defined. Kennedy and O'Hagan believe that uncertainty surrounding data from computer simulations should also be represented with probability theory. Specifically, they believe that it can be calculated utilizing Bayesian approaches and be represented with a Gaussian distribution[54]. However, Oberkampf and Roy believe that this type of uncertainty should be represented by an interval[88]. There are pros and cons presented in the literature for both of these approaches, and engineers need to ultimately select the one that is most appropriate for their problem. For this thesis, and for technology development in general, the objective is to utilize technology performance information to gain a better understanding of the performance at the system level. This can, at times, require synthesizing information from multiple uncertain sources into a single source. With this in mind, probability theory was selected to represent the uncertainty surrounding all data sets considered within this research.

Once the uncertainty for individual sources (data points and data sets) are defined, they can be either combined or propagated. Uncertainty propagation is the process of mathematically mapping sources of uncertainty, from wherever they originate, to the uncertainties in simulation results[88]. In this research uncertainty propagation is used to map uncertain inputs to output functions as well as combine several input data sets into a single, synthesized data set. There exist many options for performing uncertainty propagation in the literature, including a common category of methods

called sampling methods. Sampling methods can begin with a set of probability distributions that are sampled a number (usually a large number) of times. The results that come out of the sampled distributions can then be run through a numerical simulation to create a large number of results. The results of the simulations are then used to calculate output probability distributions.

There are many sampling techniques that exist in the literature. The selection of a specific technique depends on the complexity of your problem, the amount of time it takes to execute your simulation, the amount of detail known about your inputs, etc. A sampling technique that is commonly used in probabilistic aircraft design is Monte Carlo simulation. Monte Carlo Simulation (MCS) can be used to characterize the probability distribution, in either PDF or CDF form, of an objective function. MCS is considered a sampling-based uncertainty propagation approach where the inputs are sampled based upon previously defined probability distributions. The resulting samples create a set of input vectors which are used to perform simulations of the analysis code and form the output distribution in question. This process is illustrated in Figure 5.

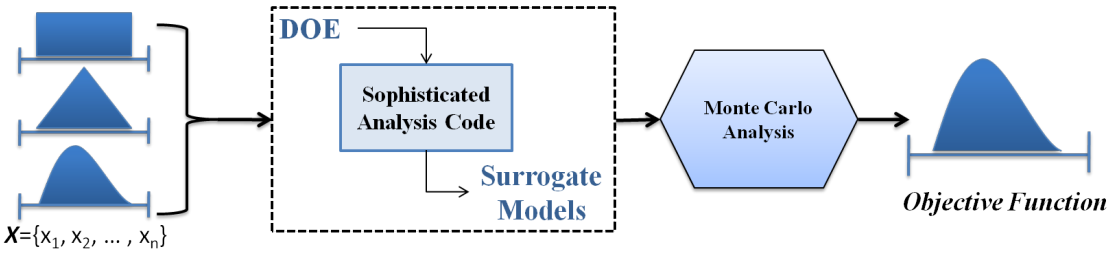

Figure 5: Monte Carlo uncertainty propagation method.

As the number of probabilistic inputs increase, additional samples are required to form the output distribution. This has the potential to lead to issues with computational effort. Therefore, simplifications may need to be made. One such simplification suggested by Delaurentis is the creation of surrogate models, or approximation models, for the analysis code to reduce the complexity and computational effort

required[26].

Surrogate models, or metamodels, are approximations of a complex analysis model. Hence, they can be described as a model of a model[113]. Surrogate models are based upon the original models; therefore, the physics-based relationships between the inputs and outputs is retained. The benefit of using surrogate models is that they are less complex than the original analysis model, but they maintain a certain degree of accuracy. The reduced complexity can lead to faster simulation times and less computational expense.

2.5 Multifidelity Methods

High fidelity models are desirable because of the amount of accuracy, or the low amount of uncertainty, they provide in their results. However, the use of only high fidelity models may not be practical for a variety of reasons. First, the cost associated with performing a high fidelity analysis may be too high to cover the desired design space. Second, the model may not be valid for the entire design space. Lastly, the model may have too high of a run time to be practically utilized. In these situations, engineers can fall back on low fidelity models. However, low fidelity models provide their own unique problems, mostly related to the amount of uncertainty they introduce into the analysis. Therefore, there is a desire to leverage the benefits of both types of models, low and high fidelity. These observations are the motivation for the development of a unique set of methods called multifidelity methods[52, 75].

Multifidelity methods offer a way to further reduce the computational burden while maintaining a high degree of fidelity. These methods use a limited number of high fidelity simulations to augment the results from a low fidelity simulation. Peherstorfer et al. have compiled a survey of all multifidelity methods in the literature and provide a good outline of the advances in this field[93]. One common method that is highlighted by Peherstorfer et al. and is prevalent throughout many scientific

fields is Bayesian Model Averaging (BMA)[46, 72, 115]. Sometimes it is referred to as Bayesian model combination which is a slight variation on BMA[83]. BMA started becoming well known in the field of statistics in the 1990s, and is now utilized widely in the scientific community.

Suppose an engineer has a model M^* that fits a set of data well. They may then use that model to make predictions at unknown location in the design space. However, suppose a different model exists, M^{**}, that also fits the data well, but provides significantly different predictions compared to M^*. Situations like this are more common than people think[96, 29, 71, 51, 95]. It can be risky to make an inference on m^* or M^{**} alone[64, 28, 45]. BMA provides a way to combine the models such that one inference can be made. There are several methods for implementing BMA depending on the number of models and the model parameters. See Hoeting et al. for a detailed description of BMA methods[46].

However, Minka believes that BMA should not be used for model combination[82]. This is because BMA places too much emphasis on the most likely model. BMA is theoretically the optimal method determining which model is correct, but not the best method for determining how to combine the models[83]. This is especially true when the models that are to be combined are not at the same level of fidelity. BMA uses a likelihood test to determine how to weight each model throughout the space. The problem is that it will heavily bias highest fidelity model, rendering the low fidelity model almost useless.

To ensure that the algorithm does not unfairly bias a single model, a correction surrogate is generated. This is done by fitting a surrogate to the difference between the "truth model" and the lower fidelity predictions. The correction surrogate can be made using whatever surrogate modeling technique the user feels is most appropriate. Once the surrogate is made, the predicted difference is added to the lower fidelity data set to form the corrected data set for all n points in the data set.

$$f_C^i = f^i + \hat{y}^i \quad i = 1, ..., n \tag{2}$$

where f_C is the corrected data, f is the initial data set, and $\hat{y}$ is the correction surrogate. The models can now combined using a likelihood ratio test without fear that too much emphasis is being put on the high fidelity model. This requires a second set of "truth model" points and high fidelity data points to determine a variable weighting factor β for the lower fidelity data sets. It is important to note that these secondary data sets are not the same set used to create the correction surrogates. The likelihood, lik_i, is computed for each low fidelity point at a corresponding high fidelity point for all j points. The weighting factor for each point is determined by calculating the normalized likelihood for each data set as shown in the equation below.

$$\beta_i = \frac{lik_i}{\sum_{i=1}^{j} lik_i} \tag{3}$$

A final surrogate, $\hat{z}$, is fit to the normalized likelihood for each data set. The final prediction is formulated by multiplying the normalized likelihood surrogates for each data set by the mean of every point in the data set and then summing them up.

$$\bar{\mathbf{f}}_{total} = \sum_{i=1}^{n} \sum_{l=1}^{k} \hat{z}_l^i M_l^i \tag{4}$$

The final variance prediction is found using the same method.

BMA and other similar multifidelity methods in the literature address the need for a method that combines data from multiple sources with varying fidelity levels to create one synthesized picture. BMA also provides a way to utilize the uncertainty information from each data set. However, it does have some shortcomings and areas that need improvement. One such shortcoming is the amount of data that is required to produce adequate results from the BMA algorithms. As previously stated, there is a very limited amount of high fidelity data available to engineers during the early

development and design of advanced technologies. These sparse data situations make it very difficult for methods like BMA to be useful. Therefore, there is a need for a multifidelity method that is compatible with sparse data situations.

2.6 Kriging

Kriging models express an observer's uncertainty about a response that has not yet been observed, based on a sample. Apley, Liu, and Chen call the uncertainty due to lack of data "interpolation uncertainty" while Kennedy and O'Hagan refer to it as "code uncertainty"[8, 55]. Kriging is given a Bayesian interpretation, or as Lee and Mavris describe it, as a type of surrogate model that is fit to an observed sample and yields a predictive probability distribution on the response at new input points[65]. The predictive distribution from a Bayesian model can be used to select the next sample point in light of the current sample to pursue some goal, such as decreasing the output value or decreasing overall predictive uncertainty. Kriging has been used as a predictive uncertainty model in previous research [101, 25]. In recent years, Kriging has also been studied extensively as a surrogate model for engineering design [38, 39, 52, 62, 104].

Kriging predicts the value of a random field at a new input point from responses at nearby design points[23]. The following is a brief description based on the detailed explanations in Forrester et al. and Jones[38, 49].

Kriging begins with a set of sample data and their observed responses.

$$\mathbf{X} = \{\mathbf{x_1}, \mathbf{x_2}, ..., \mathbf{x_n}\}^T \tag{5}$$

$$\mathbf{y} = \{y(\mathbf{x_1}), y(\mathbf{x_2}), ..., y(\mathbf{x_n})\}^T \tag{6}$$

The responses are assumed to be random vectors with a mean of $\mathbf{1}\mu$, where $\mathbf{1}$ is an $n \times 1$ column vector of ones. Subsequently, the Kriging basis function is used to correlate the random variables:

$$\mathbf{R} = Corr[Y(x_i), Y(x_j)] = \exp\left(-\sum_{l=1}^{k} \theta_l |x_{il} - x_{jl}|^2\right) \tag{7}$$

where subscript l is used to denote the different model variables whereas subscripts i and j represent the known points. If the function is assumed to be continuous, the correlation function intuitively makes sense. The values at $y(\mathbf{x_i})$ and $y(\mathbf{x_j})$ will tend to be close if $\|\mathbf{x_i} - \mathbf{x_j}\|$ is small. If $x_i = x_j$ then the correlation will be 1, and if $\|\mathbf{x_i} - \mathbf{x_j}\| \to \infty$, the correlation tends to zero. The θ_l hyperparameter represents the speed with which the correlation decays as one moves in the l^{th} variable direction. Large values of θ_l mean the function changes rapidly in the l^{th} variable direction. The correlations are then used to form a co-variance matrix.

$$Cov(\mathbf{Y}) = \sigma^2 \mathbf{R}. \tag{8}$$

The distribution of $\mathbf{Y}$ describes how the function is expected to change as each variable is changed, and it depends on μ, σ^2, and θ_l parameters. Maximum likelihood estimation is used to obtain approximate parameters $(\hat{\mu}, \hat{\sigma}^2)$. The likelihood function expressed in terms of the data is

$$L = \frac{1}{(2\pi)^{n/2}(\sigma^2)^{n/2}|\mathbf{R}|^{1/2}} \exp\left[\frac{-(\mathbf{y}) - \mathbf{1}\mu)^T \mathbf{R}^{-1}(\mathbf{y}) - \mathbf{1}\mu)}{2\sigma^2}\right]. \tag{9}$$

Maximum likelihood estimation requires taking the derivative of the likelihood function and then setting it equal to zero. In this case it is easier to take the derivative of the log of the likelihood function. The log of the likelihood function is shown below without the constant terms.

$$\ln(L) = -\frac{n}{2}\ln(\sigma^2) - \frac{1}{2}\ln(|\mathbf{R}|) - \frac{(\mathbf{y}) - \mathbf{1}\mu)^T \mathbf{R}^{-1}(\mathbf{y}) - \mathbf{1}\mu)}{2\sigma^2} \tag{10}$$

By taking the derivatives of Equation 10 with respect to σ^2 and μ and setting them equal to zero, we can solve for the estimates of σ^2 and μ.

$$\hat{\mu} = \frac{\mathbf{1}^T \mathbf{R}^{-1} \mathbf{y}}{\mathbf{1}^T \mathbf{R}^{-1} \mathbf{1}} \tag{11}$$

$$\hat{\sigma}^2 = \frac{(\mathbf{y}) - \mathbf{1}\hat{\mu})^T \mathbf{R}^{-1} (\mathbf{y}) - \mathbf{1}\hat{\mu})}{n} \tag{12}$$

These approximate parameters can now be substituted back into Equation 10 to give what is known as the concentrated log-likelihood function.

$$\ln(L) \approx -\frac{n}{2} \ln(\hat{\sigma}^2) - \frac{1}{2} \ln(\mathbf{R}) \tag{13}$$

Unfortunately maximum likelihood estimation cannot be used to find θ_l because the concentrated log likelihood function cannot be differentiated easily. However, the concentrated log-likelihood function is quick to evaluate, so a global optimization method is used to find approximate parameters $\hat{\theta}_l$ that maximize $\ln(L)$ in Equation 13. A genetic algorithm is used in this research, but other global optimization methods such as simulated annealing would work as well. Essentially, the parameters $\hat{\mu}, \hat{\sigma}^2$, and $\hat{\theta}_l$ are chosen such that the model represents the observed data as best as possible. See Forrester et al. and Jones for a more detailed explanation of the Kriging algorithm[38, 49].

To make predictions at some new point $\mathbf{x}'$, a value of y' is initially guessed. This new point $(\mathbf{x}', y')$ is added to the system as the $(n+1)$ observation and a new likelihood function, referred to as the augmented likelihood function, is computed based on the parameters found from the maximum likelihood estimation. The augmented likelihood function is only a function of y', since the parameters $\hat{\mu}, \hat{\sigma}^2$, and $\hat{\theta}_l$ are fixed. Therefore, the best predictor of y' is a value that maximizes the augmented likelihood function. Hence this value of y' becomes the Kriging predictor. Let $\mathbf{r}$ be

the vector of correlations between $y(\mathbf{x}')$ and $y(\mathbf{x_i})$, for $i = 1, .., n$.

$$\mathbf{r} = \begin{pmatrix} Corr[y(\mathbf{x}'), y(\mathbf{x_1})] \\ \vdots \\ Corr[y(\mathbf{x}'), y(\mathbf{x_n})] \end{pmatrix} \tag{14}$$

The correlation matrix for the augmented data set is:

$$\tilde{\mathbf{R}} = \begin{pmatrix} \mathbf{R} & \mathbf{r} \\ \mathbf{r}' & 1 \end{pmatrix} \tag{15}$$

The augmented correlation matrix is then used to create the augmented likelihood function. To find the value of y' that maximizes the augmented likelihood function, take the derivative of the augmented likelihood function and set it equal to zero. Solving this function for y' results in the following formula for the Kriging predictor.

$$\hat{y}(\mathbf{x}') = \hat{\mu} + \mathbf{r^T R^{-1}}(\mathbf{y} - \mathbf{1}\hat{\mu}) \tag{16}$$

Kriging also yields a predictive uncertainty. The derivation is outside the scope of the present text, but the predictive uncertainty can be expressed as a mean squared error (MSE) of a Gaussian process:

$$\hat{s}^2(\mathbf{x}) = \sigma^2 \left[1 - \mathbf{r^T R^{-1} r} + \frac{1 - \mathbf{1^T R^{-1} r}}{\mathbf{1^T R^{-1} 1}} \right] \tag{17}$$

The maximum of Equation 17 with respect to $\mathbf{x}$ can be used as an adaptive sampling criterion. The point of highest predictive uncertainty on the response can be found with an optimizer such as a genetic algorithm. This point becomes the next sample location, and is evaluated with the underlying function. The Kriging model is updated with the larger sample, and the process is repeated. Note, the sampling criterion becomes 0 at known points.

It is important to clarify that the predictive uncertainty from Equation 17 is relative. It does not provide the true amount of uncertainty. Rather it provides the amount of uncertainty in one location of the design space relative to another.

However Equation 17 can be used to provide the change in uncertainty as one moves away from a known location.

There are other techniques that use maximum MSE or predictive uncertainty as an adaptive sampling criterion for optimization[38, 39, 70]. However, MSE is not always the most effective criterion. In Equation 14, the terms in the correlation matrix are dependent on the distance between observed points, but not on the observed responses. This means information from the observed responses has limited influence on the predictive uncertainty/MSE. Using only the MSE as an infill criteria would be equivalent to filling in the gaps in the data which could also be achieved by simply selecting an offline, uniform sample with a high density[38]. However, a uniformly distributed sample does not necessarily provide the most accurate representation of the underlying function, especially if there are localized regions of complicated, non-linear behavior. This is often the case in multifidelity modeling, where Kriging can be used to model the discrepancy between low and high order codes. For example, if Kriging is used to model the discrepancy between CFD and potential flow over a range of Mach numbers, the discrepancy can become more complicated in the transonic regime.

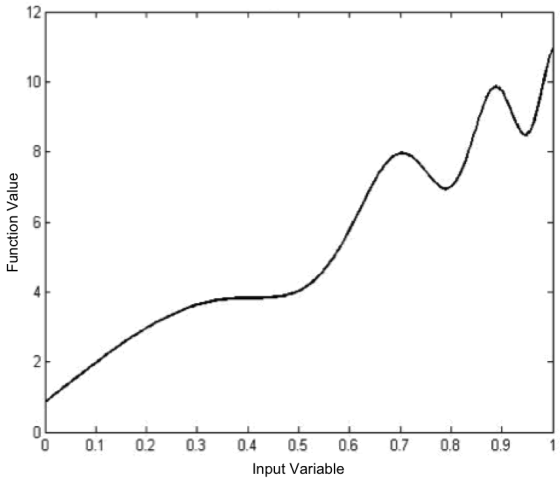

Figure 6: Notional test function used to represent the difference between two levels of fidelity

Figure 6 shows a notional function that represents the difference of between the high and low fidelity codes. The function is given by the following equation.

$$f(x) = 10x + \sin(e^{3x}) \tag{18}$$

Qualitatively, an engineer may prefer to use more of the high fidelity runs in regions where there is a high degree of non-linearity. The function begins to oscillate toward the upper end of the domain which also indicates a high degree of curvature. Schwartz et al. incorporated the curvature into the sampling criterion to improve a simple Kriging-based multifidelity adaptive sampling method[102]. They used a second order (central) finite difference approximation as follows:

$$\frac{\delta^2 f}{\delta x_l^2} \approx \frac{f(x_l + h) - 2f(x_l) + f(x_l - h)}{h^2}, \quad l = 1, 2, ...k \tag{19}$$

where h is a user defined step size and k is the number of the input variables. The second order augmented sampling criterion is the product of the MSE and the sum of the finite differences.

$$q = \hat{s}^2 \sum_{l=1}^{k} \left| \frac{f(x_l + h) - 2f(x_l) + f(x_l - h)}{h^2} \right| \tag{20}$$

CHAPTER III

PROBLEM FORMULATION AND APPROACH

The previous chapter provided relevant background information on several topics that are key to solving the research objective. Recall below the main research objective and hypothesis for this thesis.

Research Objective: Given the resulting uncertainty distributions of multiple sources of multifidelity data simulations, develop a method to characterize the uncertainty throughout the design space based on relative location of the desired design to the higher fidelity design(s) for sparse data situations.

Overarching Hypothesis: The methodology described in this thesis will provide a better uncertainty characterization of the performance throughout the entire design space compared to Bayesian model averaging when applied to advanced concepts with sparse data.

The information provided through the background research discussion led to the following key observations:

- Engineers rely on models, such as propeller maps for the problem at hand, to efficiently explore the design space when designing an advanced concept.
- Models are never completely accurate and will always have some amount of uncertainty surrounding the results they produce.

- Representing a high fidelity design space with a transparent and traceable prediction of uncertainty is necessary so that decision makers have a clear understanding of the information.
- Different data sources introduce different amounts of uncertainty, and the way that uncertainty is represented can differ from source to source.
- Multifidelity methods provide a way to reduce the computational burden by combining data sets to generate an overall improved prediction model.
- Current methods such as Bayesian model averaging are inadequate when used with sparse data sets.

The author also makes two key assumptions with regard to the type of problems that this methodology can be applied to:

- There is a limited amount of experimental data available from prior feasibility tests.
- The data is smooth, meaning that the responses from two different inputs in close proximity to each other are similar.

These observations and assumptions led to the creation of a methodology that aims to reach the overarching research objective. Given the resulting uncertainty distributions of multiple sources of multifidelity data simulations, the method characterizes the uncertainty throughout the design space based on the relative location of the desired design with respect to all of the available data, or knowledge. The overall result of this methodology is a process for creating a parametric performance map with sparse uncertain data. The belief is that this method will result in better performance predictions when compared to Bayesian model averaging. More specifically, this method will result in a decreased amount of inferred uncertainty and will be more useful because of the transparent and traceable uncertainty representation.

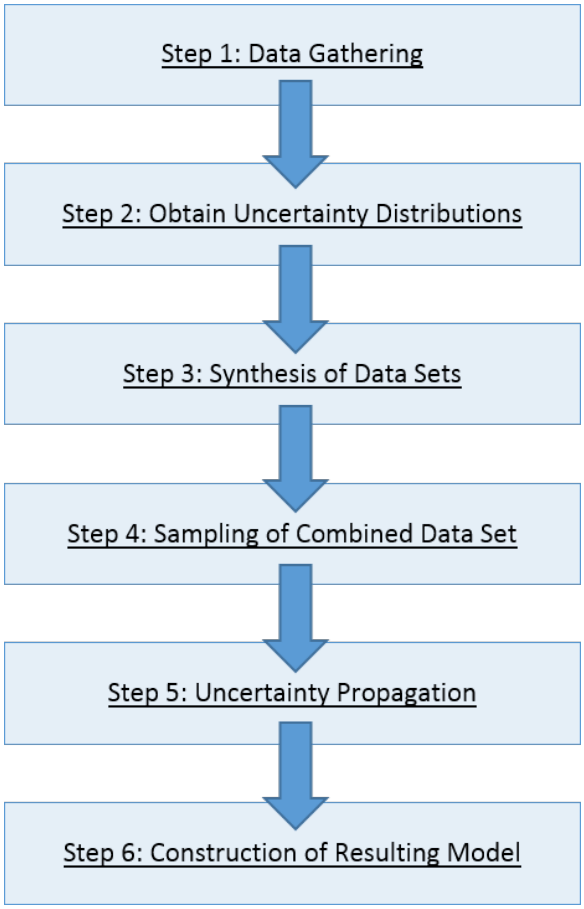

Figure 7: Basic Methodology Flowchart

The primary steps of the process are shown in figure 7. The methodology has six main steps, and they are as follows:

- Step 1: Data Gathering
- Step 2: Obtain Uncertainty Distributions
- Step 3: Synthesis of Data Sets
- Step 4: Sampling of Combined Data Set
- Step 5: Uncertainty Propagation
- Step 6: Construction of Resulting Model

The remainder of this chapter discusses each of the outlined steps of the methodology in more detail. As this method was being developed, specific research questions arose. The corresponding hypotheses for each research question were also defined. A walk through of a canonical example is presented in the final section of the chapter to facilitate the understanding of the methodology. Formal experiments were planned to test each hypotheses, and the details on each are provided in chapter 4.

Note, the research questions and hypothesis are presented in this chapter in the order that they naturally come up during the development of the MUSIC methodology. However, they are numbered to match the order of the experiments. The order of the experiments is determined by what questions need to be answered to develop the MUSIC methodology.

3.1 Step 1: Data Gathering

The first step in the process is to obtain the necessary data. The goal of this methodology is to maximize the amount of knowledge gained from all relevant data that is available. This includes data from all fidelity levels, computational models, physical experiments, etc. As previously mentioned, there are rarely enough resources during the conceptual design phase to generate high fidelity data. However, it is common in the aerospace industry for projects to start and stop, so it is advantageous for researchers to investigate if there may be some data available from previous experiments. For example extensive testing was conducted on the open rotor propulsion concept during the 1980s[42] and more recently as part of NASA's environmentally responsible aviation project[112]. Tests were conducted on both single and counter rotating configurations. Therefore, the researcher should do an exhaustive search for existing data before spending valuable resources generating more data.

For clarity, it is important for the reader to understand that any conclusions about the most appropriate method for obtaining data is not within the scope of

this research. Therefore, this methodology truly begins with data as the input. It is included as a step to remind the user that their search should be exhaustive because the usefulness of the results ultimately depends on the type of data and quality of data that is used as an input. Once all the available data has been obtained and organized, engineers must focus on representing the uncertainty of each data set. The resulting distributions for each data set (or data point) is treated as if it was obtained from some sort of a probabilistic simulation.

3.2 Step 2: Obtain Uncertainty Distributions

Once all of the data sets are readily available, the next step in the process is to obtain the uncertainty distributions for every point in each data set. Data sets can be generated from physical experiments and computational simulations, and the way their uncertainty is depicted is not necessarily the same. Within the background discussion in Chapter 2 it was observed that the uncertainty quantification community agrees that experimental data is typically represented by a normal (Gaussian) distribution[88]. However, there are differing opinions on how computational uncertainty should be represented. Some researchers favor probability theory, and even believe that Gaussian distributions can be utilized for computational uncertainty in a similar manner to experimental data[54]. Others, however maintain that alternative interpretations should be used, such as intervals[88].

It was previously stated that determining the most appropriate method for defining the uncertainty of each type of data is not within the scope of this research. Therefore, within this research, probability theory will be utilized to represent computational uncertainty to provide a straightforward demonstration of the methodology. However, within probability theory one must still determine the appropriate type of distribution for the computational data sets. Despite the fact that finding the proper method for defining the uncertainty is not part of this research, the question arises

about how much the type of uncertainty distribution utilized for the low fidelity data impacts the results? There are two minor limitations to the type of distributions that can be used by the MUSIC methodology:

- The distribution must have a unique mode. A uniform or multimodal distribution can not be used.
- The distribution must be able to be bounded. To clarify, any probability density function that goes to infinity can be used as long as the user is able to truncate the distribution at a specific value.

These limitations are put on the type of distribution because the bias process explained in the next step operates on the mode and the bounds of the given distributions. This thought experiment leads to the first research question defined below.

Research Question 2: Does the type of distribution used to define the uncertainty of the low fidelity data sets affect the results given that it is bounded and it has a unique mode?

The mode and the bounds of the distributions will not change depending on the type of distribution. The synthesis step explained in the next section. The distributions are also not likely to have excessive skew with a large tail, so the difference between the different distributions may not be substantial. The following hypothesis has been developed.

Hypothesis 2: The type of distribution used to represent the uncertainty of the low fidelity data does not significantly impact the results of the methodology as long as it has a unique mode and is bounded.

3.3 Step 3: Synthesis of Data Sets

After Step 2 is completed, the user will have unique uncertainty representations for each data set available to them. The next step is to combine the data sets, which occurs during Step 3 and Step 4. The data combination process is the quintessential step of the MUSIC methodology. Section 2.5 discussed the various methods for combining data, and it was observed that many of the current methods, such as Bayesian model averaging, fit the individual data sets prior to combining them. However, this methodology is different because the data will be combined prior to any sort of fitting. Furthermore, any regression or interpolation method will not be able to distinguish the difference between high and low fidelity points after they are combined. Therefore, there needs to be a biasing process to ensure the data fitting technique is biased toward the higher fidelity points.

Figure 8 shows a notional example of a design space with one low fidelity point in green, L_o, and two high fidelity points shown in black, H_1 and H_2. The given uncertainty distributions associated with each point are shown next to the points. The primary objective of step 3 is to bias the low fidelity distribution based on the proximity to the two high fidelity points. A notional result of the biasing process is shown in Figure 9. The green triangular distribution represents the biased low fidelity distribution due to the proximity of the high fidelity points. Notice how the mode of the low fidelity distribution has shifted up and the bounds of the distribution have been reduced compared to the initial low fidelit distribution shown in red. A detailed example of the biasing process is given later in Section 3.3.1. These figures are only meant to help illustrate the need for a quantitative biasing process.

After some background research and investigation, it was decided that the research presented in this thesis will utilize distance as a way for the higher fidelity points to influence the lower fidelity points. This means lower fidelity points that are closer to a high fidelity point will be biased more than points that are farther away from

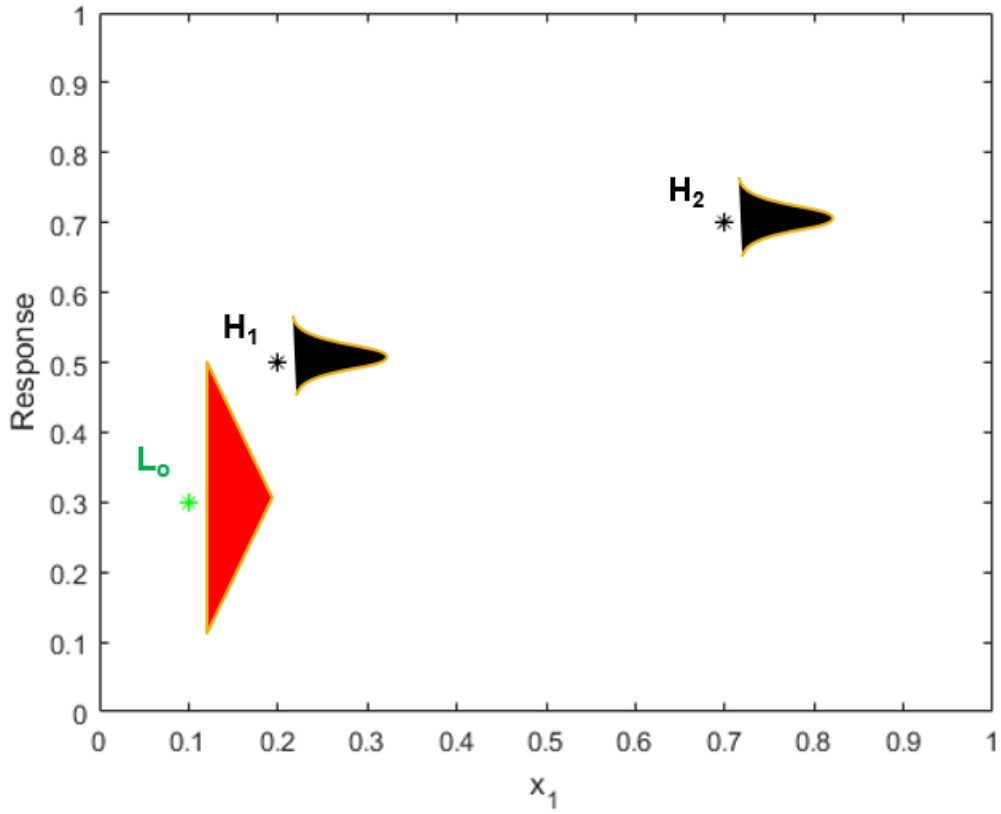

Figure 8: Notional example of a design space with low and high fidelity points and their respective distributions.

a high fidelity point. The area surrounding a high fidelity point can be thought of as a trust region. As one moves further away from the high fidelity point, the trust degrades. The definition of this distance assumption lead to a series of questions:

- What is the appropriate form of this proximity function?
- Is a simple linear function sufficient or is a more complicated, non-linear function required?
- Should there be a different function for each input dimension?

The third question listed arose from the thought that if the space is very uniform in one dimension, then that dimension should be weighted more so that a higher

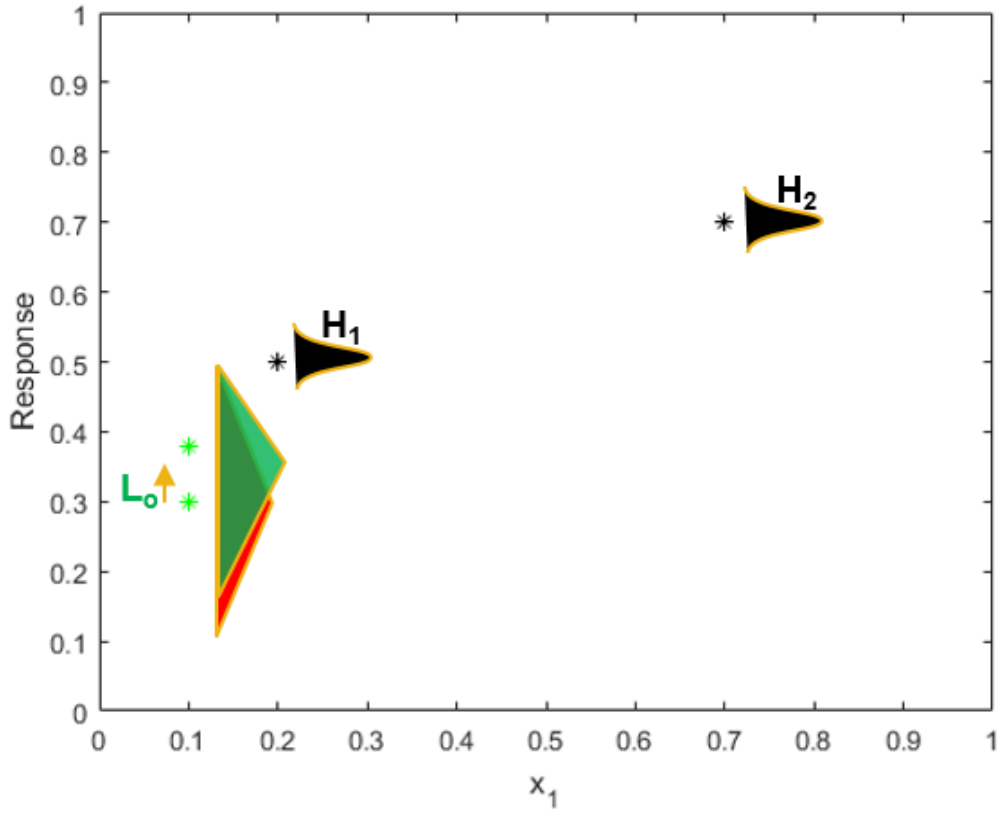

Figure 9: Notional example of a biased low fidelity distribution due to the biasing process.

fidelity point in that dimension has more influence i.e. a larger trust region. These observations have lead to the development of the following formal research question:

Research Question 1: How will the low fidelity uncertainty distributions be biased in the input space?

There are an infinite number of functions that could be used as a proximity function for biasing the low fidelity distributions. The more complex the function is, the more details the function can capture. However, a more complex function may take vital resources away from an already starved experimental budget during the conceptual design phase. A literature review lead to Kriging, which is discussed in Section 2.6. If the reader is familiar with Gaussian processes, Kriging can be thought of as

a specific type of Gaussian process. Kriging is used in the uncertainty community to represent the relative amount of uncertainty in one area of the design space to another. The algorithm can provide the change in uncertainty, but not the true uncertainty. This prompted the motivating question can the change in uncertainty from Kriging be combined with the given uncertainty distributions at specific locations in the design space to predict the true level of uncertainty throughout the design space?

Kriging uses a form of the squared exponential function (Equation 7) along with training data to determine how the uncertainty changes as one moves away from a known location in the design space. A simplified version of the squared exponential function used for this research is shown below

$$f(x_o - x_i) = e^{-\theta(x_o - x_i)^2} \tag{21}$$

where $(x_o - x_i)$ is the distance between a low fidelity point and the i^{th} high fidelity point, and θ is a scaling parameter. Recall that Kriging uses a genetic algorithm to determine the scaling parameters θ_l that maximize the concentrated log likelihood function (Equation 13) in order to provide the best representation of the training data. The scaling parameters, θ_l, can be thought of as a width parameter that affects how far a sample point's influence extends throughout the design space. Examples of the squared exponential function with different scaling parameter values are shown in Figure 10. A low value for the scaling parameter means points will have a high degree of correlation, or that a high fidelity point's influence will extend across a large amount of the design space.

Another aspect of Kriging that motivated the use of the squared exponential function is that it will determine a unique scaling parameter, θ, for each dimension. If a low θ indicates that there is a high degree of correlation or similarity between points in that dimension, then a low value for theta implies that the specific dimension is relatively linear. The scaling parameter is an indication of how active a function is in a specific dimension. Having a unique proximity function for each dimension

is a valuable capability if the user believes the design space has different degrees of linearity among the different dimensions. The user would want a high fidelity point to influence large portions of the design space. This is in contrast to a dimension that is highly non-linear, where the user would not want the high fidelity points to have influence across large portions of the design space. The scaling parameter, θ, found using the Kriging algorithm for all k dimensions can be used to create a unique proximity function (Equation 21) for each dimension for MUSIC.

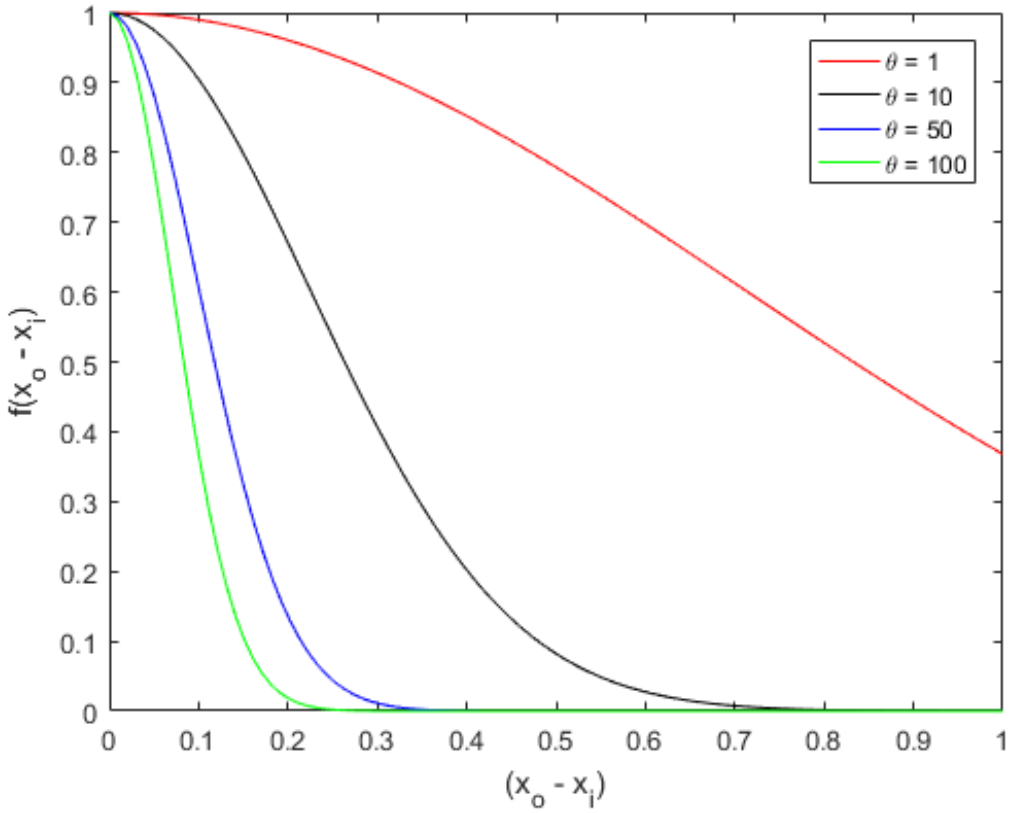

Figure 10: Examples of the squared exponential function with different values for the scaling parameter θ.

Notice that the shape of this function looks similar to half of a Gaussian distribution. This is because the squared exponential function is what gives the Gaussian distribution its bell shape. In fact the squared exponential function is sometimes referred to as the Gaussian kernel in the kernel method community[11]. When used

as a proximity function, the response, $f(x_o - x_i)$ becomes the proximity impact of the i^{th} high fidelity point on the low fidelity point L_o. This means that as the distance between points approaches 0, the proximity impact approaches 1, and as the distance between points approaches 1, the proximity impact approaches 0. Another reason why the squared exponential function will be investigated is because it is smooth. Recall from earlier in this chapter that the MUSIC method assumes a smooth design space.

Based on the observations made about the squared exponential function and the Kriging algorithm, the following hypothesis has been developed for this question:

Hypothesis 1: A proximity function that uses the Kriging algorithm to determine a unique scaling parameter, θ, for each dimension will more effectively bias the low fidelity uncertainty distributions.

The proximity function described above is compared against more basic proximity functions. Their details as well as the specific metrics used to determine which function is most effective is discussed in Section 4.1.

Another important question that needs to be addressed is what to do if there are more than two fidelity levels? For example Figure 11 is the same as Figure 8 except that a mid fidleity data point shown in blue has been added to the design space. Does the addition of a mid fidelity level data set improve final prediction? Do changes need to be made to the biasing calculations? The mid fidelity level data set should not have the same impact on the low fidelity data as the high fidelity data. Does some sort of hierarchy of weightings based on fidelity level need to be developed. The following research questions have been developed.

Research Question 3.1: Will the addition of a mid fidelity level data set further improve the final uncertainty characterization?

Research Question 3.2: By introducing the mid fidelity level data set, do changes need to be made to the existing biasing process?

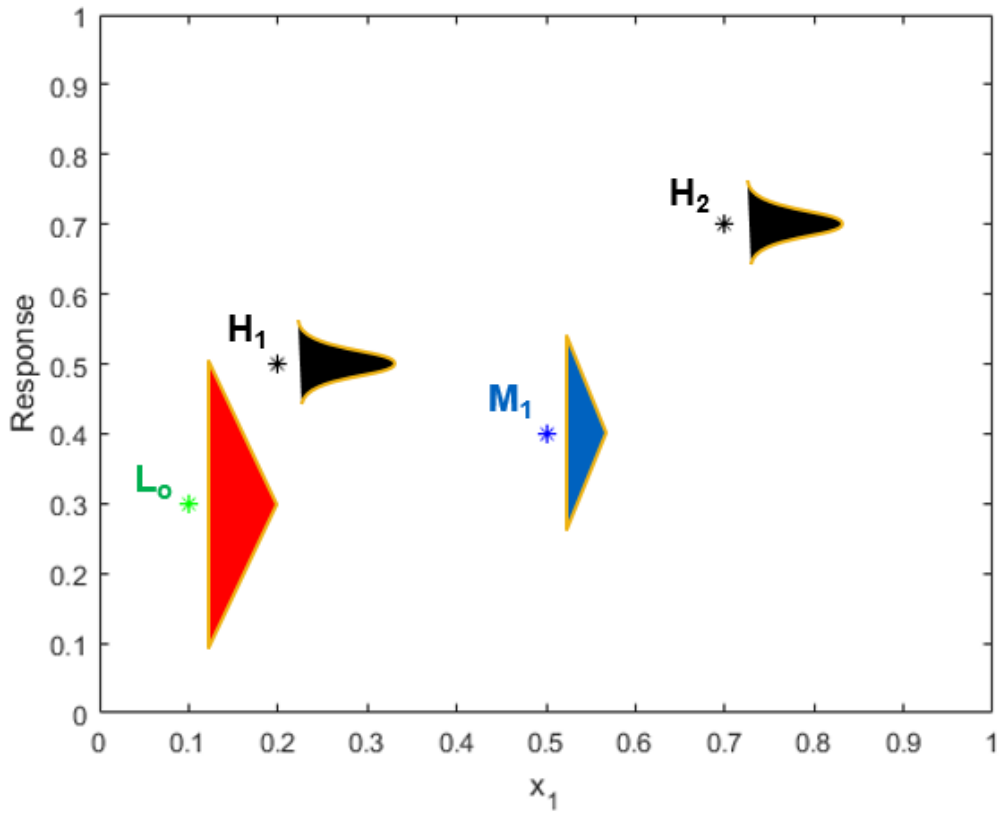

Figure 11: Notional example of a design space with a mid fidelity point.

The purpose of biasing the lower fidelity data sets is to favor higher fidelity simulations and experiments because they include more knowledge of the physics that determines the technology's performance. Introducing a mid fidelity level data set will add more knowledge about the physics within the design space, but not to the same extent as a high fidelity data set. Thus, the following hypotheses have been developed.

Hypothesis 3.1: Including a mid fidelity level data set will improve the final inferred uncertainty prediction.

Hypothesis 3.2: If the final results are sensitive to a weight factor, then a fidelity level weight function needs to be developed.

After the data sets have been biased, they are combined and treated as one data set. This means that the combined data set will have a larger population than the low or high fidelity data sets. The only exception is when the high and low fidelity data points are located at the same point in the design space. In this case those specific low fidelity points are removed from the combined data set. A low fidelity point located at the same point in the design space as a high fidelity point will not add any knowledge about the design space.

Describing the overall vision for this combination process is better represented through an example problem. Therefore, the subsection that follows will provide a walk-through of the proposed data biasing process.

3.3.1 Bias Calculation Example

A quick walk-through of the biasing calculation process is provided in this section using the squared exponential function. Figure 12 shows the squared exponential function with three different options for the scale parameter θ. The squared exponential function is a smooth bell shaped function. The reader may be thinking that this function looks like half of a Gaussian distribution and this intuition is correct. The Gaussian distribution gets its nice smooth bell shape from the squared exponential function.

The input space for the biasing example is shown in Figure 13 where the green point is a low fidelity point that will be biased by the two high fidelity black points. The proximity impact functions for each dimension are shown in the embedded figure in the top right hand corner, where the function for the X_1 dimension is shown in red and the function for the X_2 dimension is shown in blue along with their respective values for θ.

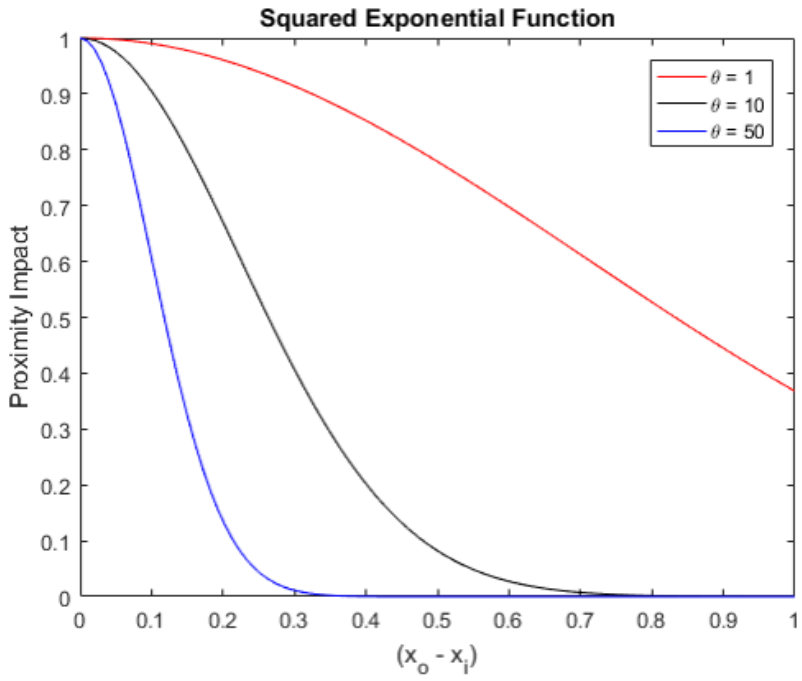

Figure 12: Squared exponential function with scale parameter values

The first step is to calculate the proximity impact of each dimension for every point by imputing the distance into the proximity impact function. The point H_1 is 0.1 away from the low fidelity point in the X_1 dimension. Plugging this into the proximity impact function gives the following result:

$$P_{x_1} = e^{\theta_1(0.1^2)} = 0.90 \tag{22}$$

In the X_2 dimension, the point H_1 is also 0.1 away from the low fidelity point. The proximity impact in this dimension is as follows.

$$P_{X_2} = e^{\theta_2(0.1^2)} = 0.99 \tag{23}$$

The proximity impact is higher because θ_2 is lower which creates a shallower curve. The total proximity impact for H_1 is found by multiplying the impacts from each dimension together.

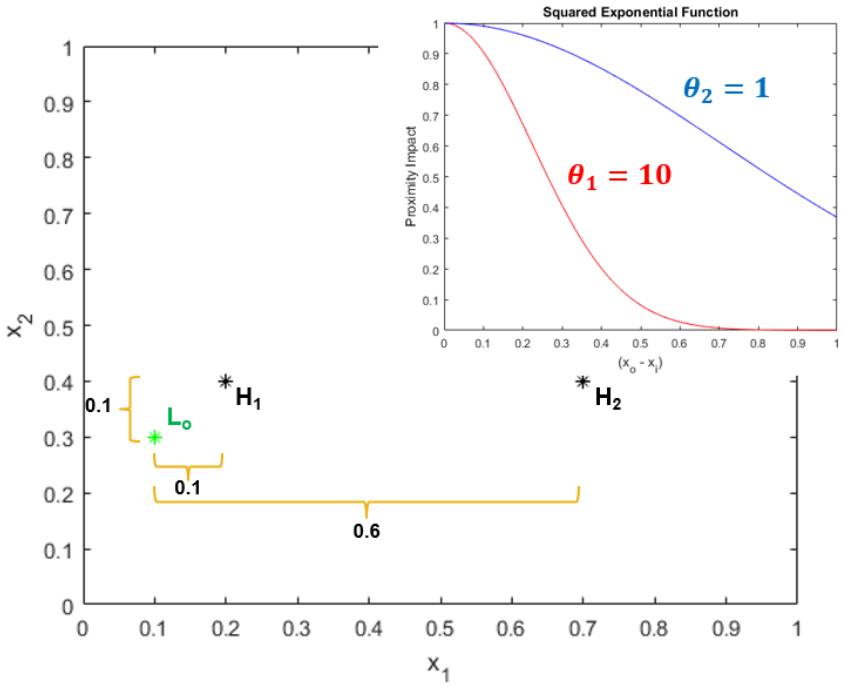

Figure 13: Input space and proximity functions for the biasing demo.

$$P_{H_1} = \frac{P_{X_1} + P_{X_2}}{2} = 0.95 \tag{24}$$

Similarly, the calculations for the impact of H_2 on the low fidelity point are as follows:

$$P_{X_1} = e^{\theta_1(0.6^2)} = 0.03 \tag{25}$$

$$P_{X_2} = e^{\theta_2(0.1^2)} = 0.99 \tag{26}$$

$$P_{H_2} = \frac{P_{X_1} + P_{X_2}}{2} = 0.51 \tag{27}$$

The impact of H_2 on the low fidelity point is much less than H_1 because of how far away H_2 is in the X_1 dimension and the proximity function for the X_1 dimension is much steeper.

Figure 14 show the three points with the X_1 dimension on the horizontal axis and the response on the vertical axis. For clarity, the embedded figure in the top right

shows the two input dimensions as well as the response dimension. The proximity in the response space is simply the difference between the points.

$$R_{H_1} = 0.2 \tag{28}$$

$$R_{H_2} = 0.4 \tag{29}$$

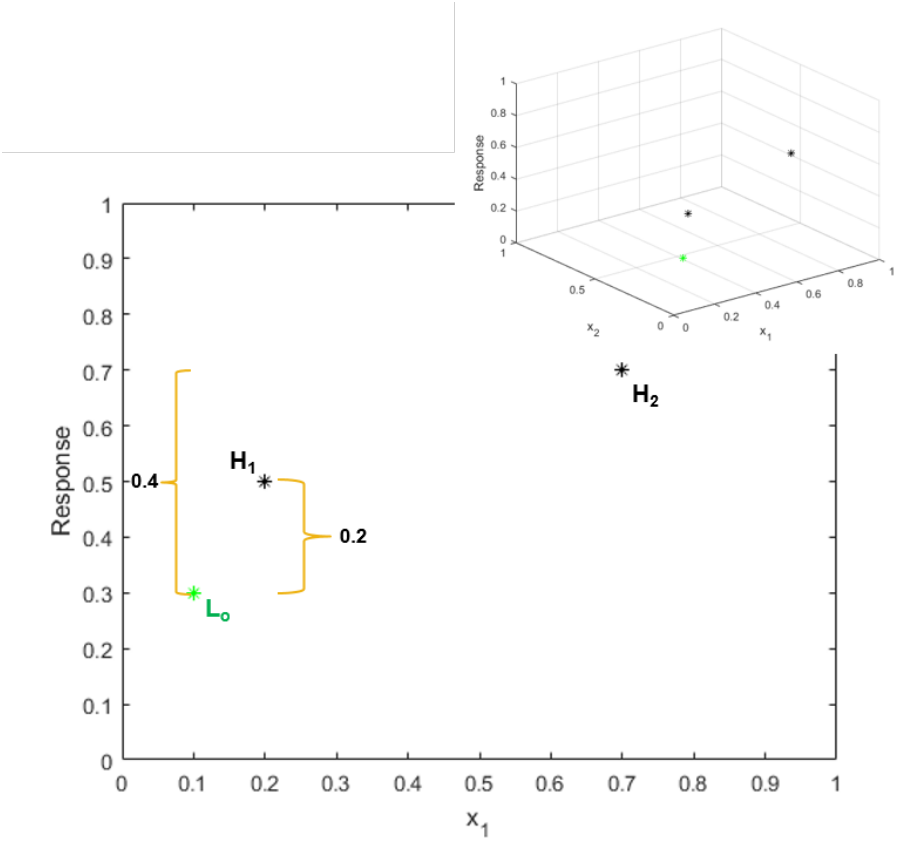

Figure 14: 2D and 3D response space for the biasing demo.

The combined impact for each point is the product of the proximity impact in the response space and the proximity impact in the input space. Therefore the total impact for each high fidelity point is

$$I_{H_1} = P_{H_1} * R_{H_1} = 0.95 * 0.2 = 0.19 \tag{30}$$

$$I_{H_2} = P_{H_2} * R_{H_2} = 0.51 * 0.4 = 0.20 \tag{31}$$

The impact of H_2 is similar to H_1 even though it is farther away. This is because H_2 has double the impact in the response space compared to H_1. The final amount of bias of the low fidelity point due to both of the high fidelity points is the sum of the bias due to each point multiplied by the uncertainty. Assume the uncertainty for the low fidelity point was previously defined to be 0.2.

$$B_{L_o} = U_{L_o} \sum_{i=1}^{n} I_{H_i} = 0.2 * (0.9 + 0.20) = 0.08 \tag{32}$$

This means that the low fidelity point will be biased from 0.30 to 0.38 due to its proximity to H_1 and H_2. The same biasing process is carried out for the uncertainty bounds as well. The biasing result is illustrated in Figure 15 where the low fidelity distribution is shown in red and the biased distribution is shown in green.

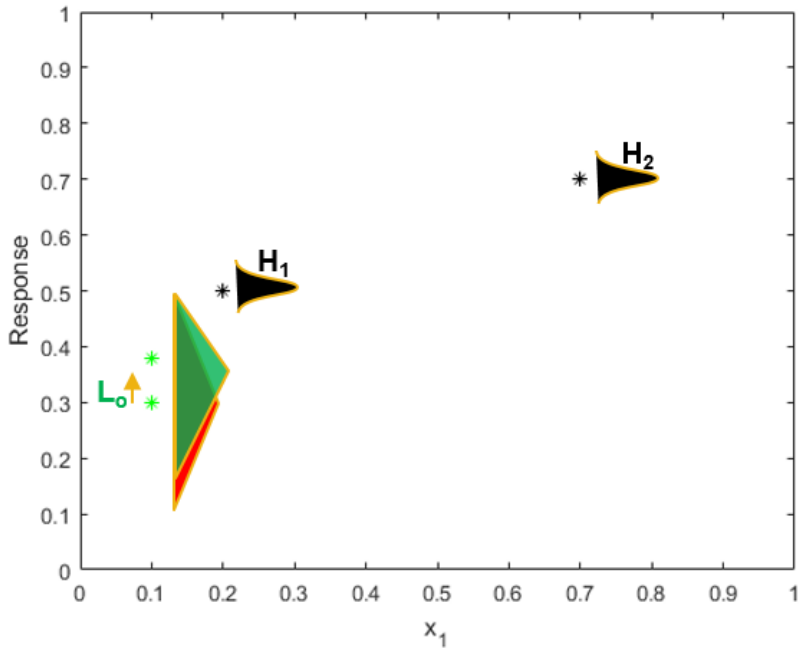

Figure 15: Illustration of the biasing process. The initial low fidelity distribution is shown in red and the final biased distribution is shown in green

3.4 Step 4: Sampling of Combined Data Set

At this point in the methodology the user has a combined data set where each point has an uncertainty distribution associated with it. The distributions on the lower fidelity data points are biased due to their proximity to the higher fidelity data points. Now that distributions have been defined throughout the design space, they need to be propagated throughout the entire design space.

It was observed in the background research in Chapter 2 that the most effective way to combine or propagate uncertainty distributions is through sampling. Therefore, in this methodology uncertainty propagation will be handled through Monte Carlo analysis. The Monte Carlo sampling method will be used to generate a series of samples from the biased response distributions. The sampling is conducted many times to sufficiently represent the distributions throughout the design space. For one iteration of the Monte Carlo sample method, each distribution is sampled once. This results is a set of samples that is the same size as the initial combined data set with the same set of input values. However, there are different values for the responses because they are randomly drawn from the distribution instead of the nominal values. This first sample set is then fit with a surrogate model to create a representation throughout the entire design space. The next iteration in the Monte Carlo sampling method, and each additional one that follows, is carried out in exactly the same manner. This process is carried out many times so that the distributions are accurately represented.

3.5 Step 5: Uncertainty Propagation

After the Monte Carlo samples are formed, the next step is to fit the sample sets with surrogate models. Many types of surrogate models exist in the literature. Kriging and Gaussian process models have both been discussed in depth throughout the background and problem formulation of this research. However, other methods have

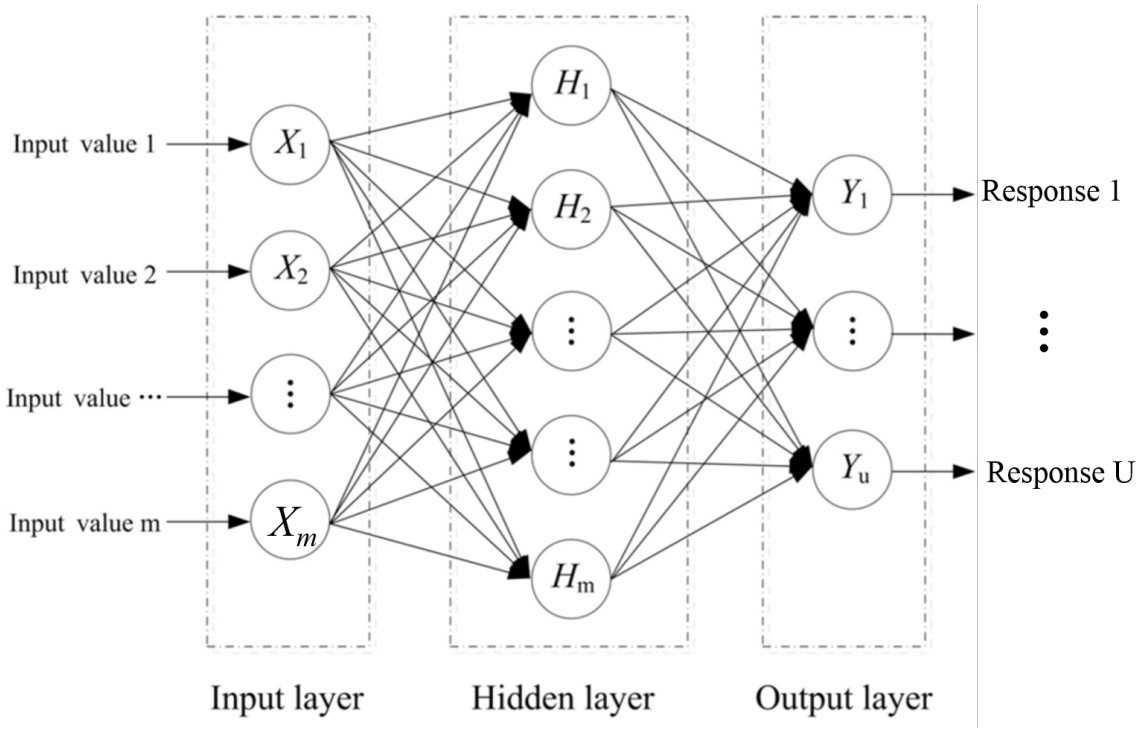

Figure 16: Generic structure of Artificial Neural Network[21].

also been investigated to determine their appropriateness for this research, including Response Surface Equations (RSEs) and Artificial Neural Networks. RSEs represent the outputs of a function through polynomial regressions of the model inputs[80]. As the order of the model increases, the ability of an RSE to capture interactions and more complex phenomena increases. For example, a second order RSE has the ability to capture linear effects, quadratic effects, and two-variable interactions.

Another type of surrogate model commonly used in the uncertainty quantification community is the Artificial Neural Network (ANN)[105]. ANNs are utilized heavily in the machine learning community and inspired by the philosophy and function of the nervous system. When using ANNs, inputs are mapped to outputs through a network of hidden nodes, or neurons, which mimic a biological neural network, as shown in Figure 16. An ANN can have many layers of hidden nodes, and the number of layers depends on the complexity of the problem being modeled. The nodes and their weightings are determined through a set of training data.

However, fitting multidimensional sparse data is not trivial. Regression methods like RSEs do not work well because they smooth out the data. This is a problem with sparse data because every point is important and should included in the fit. Thus, some sort of interpolation method should be used. Kriging, Gaussian processes, and ANNs will not miss any of the data points, but the large spaces between the data points give these types of methods too much freedom to randomly depart from the trend. These methods can also be computationally expensive depending on the number of dimensions and the amount of data. Here are a few key observations with regard to fitting multidimensional sparse data sets:

- Computational time is important to keep in mind because the fitting process will be carried out numerous times.
- Regression methods may smooth out the data too much and miss important data points.
- Nonlinear interpolation methods might have too many degrees of freedom and give highly erratic results.
- Data sets are scattered as opposed to gridded.

A common method that satisfies all of these requirements is linear interpolation. Therefore, all of the surrogate models utilized for this research were created with a scattered linear interpolation algorithm. The next step in the process will utilize the surrogate models from the Monte Carlo fitting process to create a prediction for the overall mean and uncertainty bounds.

3.6 Step 6: Construction of Resulting Model

The final step in the process is to determine the overall mean and uncertainty for the final prediction model. For this research, the mean will be calculated by determining

the mean of all the sample regressions at every point of interest in the design space. The overall bounds of the surrogates at the points of interest are used to represent the final uncertainty bounds for the prediction.

3.7 Validating the Methodology

The sixth step is the final step in the proposed methodology. The previous subsections have provided details on the steps within the methodology. Figure 17 provides a more descriptive methodology flowchart that includes many of details that have been discussed. It is now defined that Step 1 of the methodology involves gathering all of the necessary data, of all fidelity levels, that are available and relevant to the problem at hand. The next step, Step 2, involves defining the uncertainty for each of the selected data sets. It was discussed in Section 3.2 that probability theory will be used to represent all types of data, so this step requires the probability distributions to be set for each data set. Step 3 involves creating the combined, biased data set. It was established that a distance based biasing approach will be utilized, and different weightings will be explored. After the combined data set is created, the resulting data set is sampled in Step 4 and the results are used to form a final combined model in Step 5. Finally, the statistics (mean and variance) and the inferred uncertainty characterization of the final model can be calculated throughout the design space.

After the details for each step are finalized, the methodology as a whole must be assessed. The previous research questions were about specific steps within the methodology, but now the methodology needs to be validated for a realistic engineering problem. Furthermore, it must be questioned if the resulting methodology architected through this problem formulation results in an improvement in the state of the art and successfully fulfills the research objective. Therefore, the final formal research question and hypothesis for this thesis is as follows:

Overarching Research Question: Does the MUSIC method provide

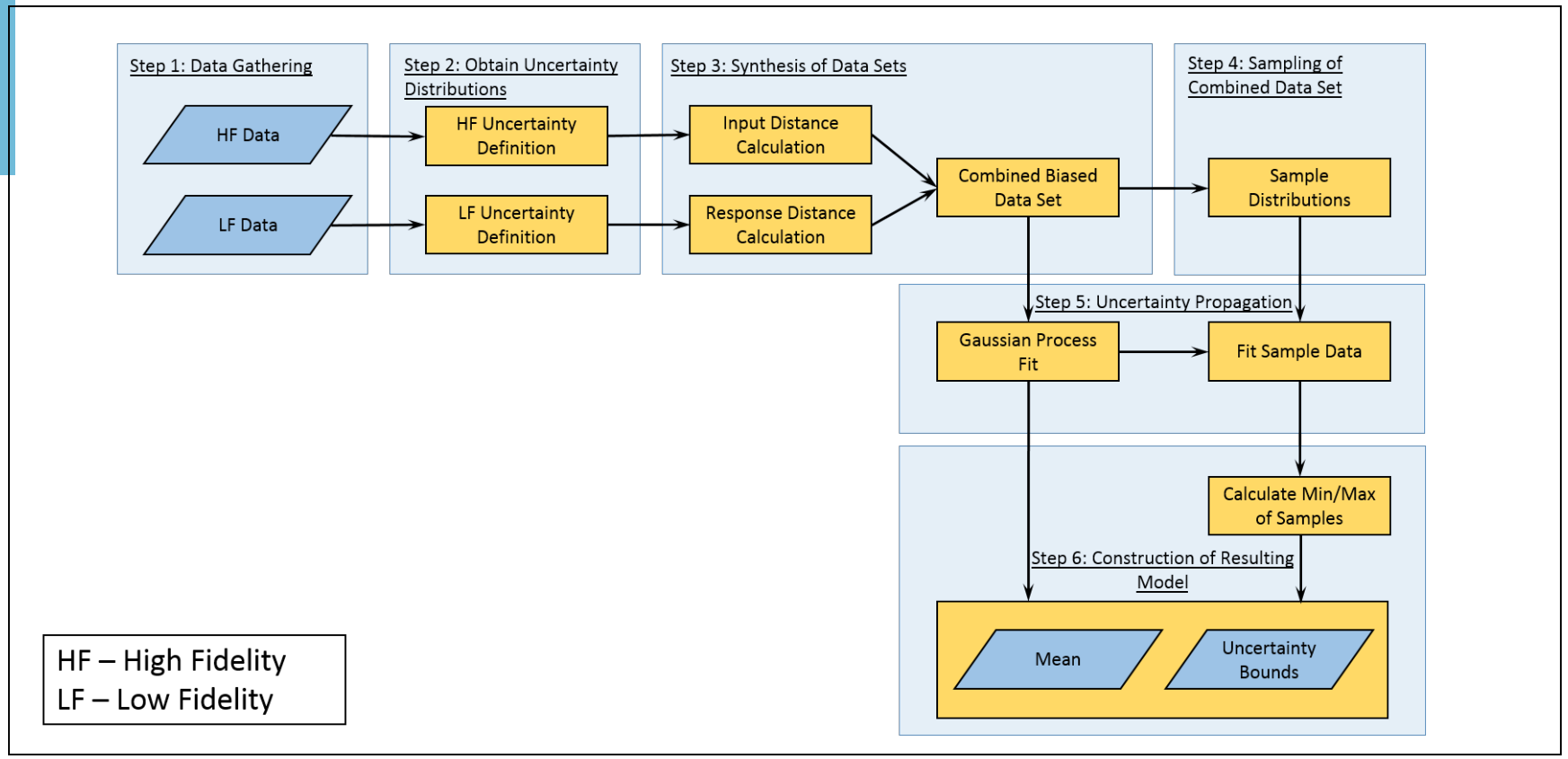

Figure 17: Final Proposed Methodology

a more accurate representation of the inferred uncertainty compared to current methods like Bayesian model averaging?

Overarching Hypothesis: The MUSIC methodology will provide a more accurate uncertainty characterization of the performance throughout the entire design space compared to Bayesian model averaging when applied to advanced technologies with sparse data.

The last step in the process is to validate the method on a representative technology. Recall from earlier discussions that there is not enough data available on advanced propeller concepts to validate the method. Therefore, data from Hamilton Standard general aviation propellers will be used to validate the model. This results for the final validation step are shown in Chapter 6

3.8 Summary of Problem Formulation

The problem formulation has outlined four formal research questions that, once answered, will define the methodology that will meet the overarching research objective of this thesis. The background research presented in Chapter 2, other supporting information, and critical thinking lead to the development of formal hypotheses for each of the research questions. The first four research questions help define the details of steps within the methodology, and the final research question validates the methodology as a whole. Figure 18 depicts the mapping of each research question to the methodology architecture. Furthermore, a summary of the research questions and hypotheses are provided below for reference.

Research Question 1: How will the low fidelity uncertainty distributions be biased in the input space?

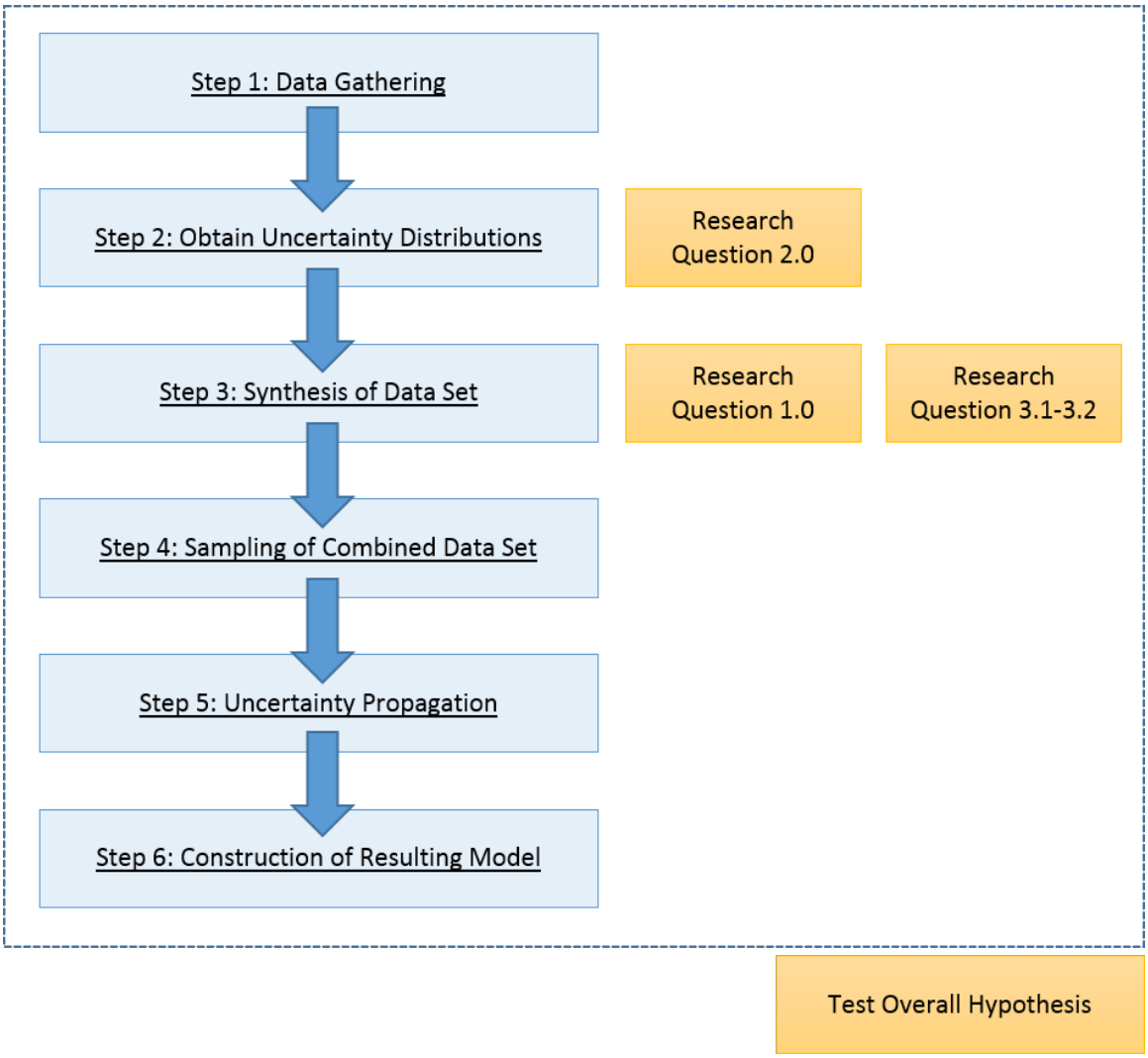

Figure 18: Mapping of the formal research questions to the MUSIC methodology architecture.

Hypothesis 1: A proximity function that uses the Kriging algorithm to determine a unique scaling parameter, θ, for each dimension will more effectively bias the low fidelity uncertainty distributions.

Research Question 2: Does the type of distribution used to define the uncertainty of the low fidelity data sets affect the results given that it is bounded and it has a unique mode?

Hypothesis 2: The type of distribution used to represent the uncertainty of the low fidelity data does not significantly impact the results of the methodology as long as it has a unique mode and is bounded.

Research Question 3.1: Including a mid fidelity level data set will improve the final inferred uncertainty prediction.

Hypothesis 3.1: Including a mid fidelity level data set will improve the final inferred uncertainty prediction.

Research Question 3.2: By introducing the mid fidelity level data set, do changes need to be made to the existing biasing process?

Hypothesis 3.2: If the final results are sensitive to a weight factor, then a fidelity level weight function needs to be developed.

Overarching Research Question: Does the MUSIC method provide a more accurate representation of the inferred uncertainty compared to current methods like Bayesian model averaging?

Overarching Hypothesis: The MUSIC methodology will provide a more accurate uncertainty characterization of the performance throughout the entire design space compared to Bayesian model averaging when applied to advanced technologies with sparse data.

The following chapters will provide the experimental plan that was developed to test these hypotheses and validate the methodology, the results of those experiments, and a final methodology demonstration. First, however, the proposed methodology was utilized on a canonical example to provide the reader with a better understanding of what is proposed and why it is needed in the engineering community. The results of this canonical example are provided in the following section.

3.9 Canonical Example

The equations for predicting the lift curve slope of a wing at different aspect ratios will be used as a demonstration to help the reader understand the methodology. See Anderson Jr. for a more detailed explanation of the equations used in the following example problem[7].

Prandtl developed an equation for high-aspect ratio straight wings from lifting-line theory. The equation is show below,

$$a = \frac{a_o}{1 + \frac{a_o}{\pi AR}} \tag{33}$$

where AR is the aspect ratio and a_o is the lift curve slope for an equivalent infinite wing. Thin airfoil theory says that $a_0 = 2\pi$. This is a useful equation for back of the envelope calculations during the conceptual design process. However, this equation makes numerous assumptions and as a result, it does not work well for low aspect ratio wings. This equation will be used to create the low fidelity data set for this example.

In 1942 Helmbold modified Prandtl's equation to make it more applicable for low-aspect ratio straight wings.

$$a = \frac{a_o}{\sqrt{1 + \left(\frac{a_o}{\pi AR}\right)^2} + \frac{a_o}{\pi AR}} \tag{34}$$

Helmbold's equation gives good results for straight wings below aspect ratio of 4. This equation will be used to generate the high fidelity data set for this example. Figure 19 shows the plots for these equations.

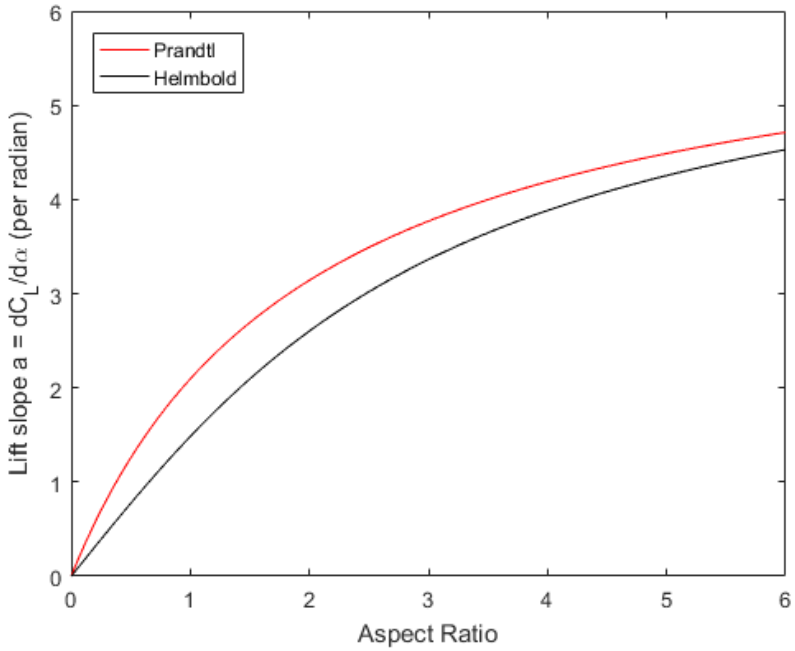

Figure 19: Lift slope predictions from Prandtl's and Helmbold's equations.

For this example, imagine that an engineer is trying to find the lift slope for wings with aspect ratios below 6. Additionally, imagine that the results from Helmbold's equation are expensive to generate and can only be done twice with the given amount of resources, say for aspect ratios of 1.5 and 5.25. Prandtl's equation is not as expensive and results are obtained for aspect ratios of 1, 2, 3, 4, and 6.

In this demonstration the maximum amount of error between the two equations is 0.62, so the author has assumed that they were given triangular distributions for the low fidelity data points with the peak located at the nominal point and the bounds located ± 0.62 from nominal. Assume the two high fidelity data points came from a wind tunnel test with an error of ± 0.1. Their uncertainty distributions are represented by a normal distribution with the mean located at the nominal point and a standard

Table 1: Input data for the canonical example

	x_1	Uncertainty	Distribution
L_1	1	0.62	Triangular
L_2	2	0.62	Triangular
L_3	3	0.62	Triangular
L_4	4	0.62	Triangular
L_5	6	0.62	Triangular
H_1	1.5	0.1	Normal
H_2	5.25	0.1	Normal

deviation of 0.05 so that there is a 95% probability that a random sampling will fall within ± 0.1 from nominal. The actual distribution in the code is truncated at the bounds so that no random sampling occurs outside of the bounds in future steps. Table 1 shows all of the data obtained in the first two steps of the methodology. The data points for each data set are also shown in Figure 20. The circles represent the nominal data points and the triangles represent the upper and lower bounds of the uncertainty distributions.

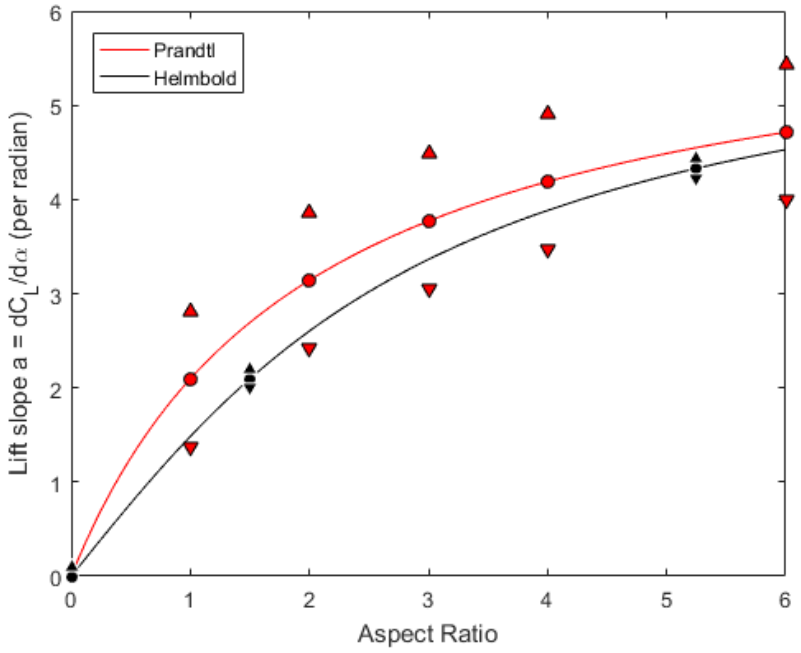

Figure 20: Lift slope predictions from Prandtl's and Helmbold's equations. The circles represent the nominal data points and the triangles represent the uncertainty bounds.

3.9.0.1 *Data Combination*

Now that all of the distributions have been obtained, the low fidelity data needs to be biased. The Kriging algorithm is used to determine the parameter θ for the squared exponential function. This results in the squared exponential proximity function. This proximity function is used to bias the distributions of the 5 low fidelity points. Figure 21 shows the equations for the lift curve slope again; however, notice that the low fidelity points and their bounds (now shown in yellow) have been biased. The original and biased distributions are shown in Figure 21. All of the data points are now considered to be part of one data set.

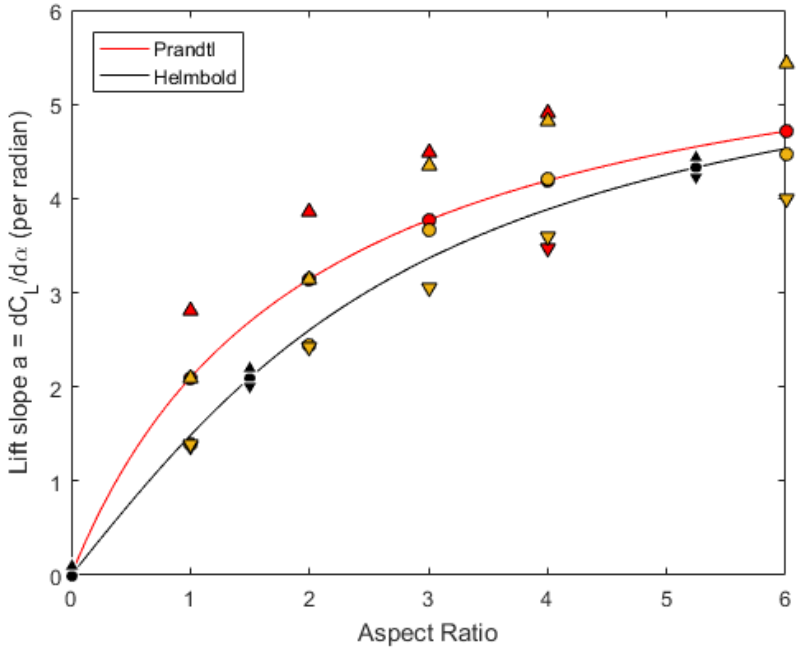

Figure 21: Lift slope predictions from Prandtl's and Helmbold's equations. The biased uncertainty distributions are shown in yellow. The original distributions are shown in red.

3.9.0.2 *Monte Carlo Sampling*

Now that a combined set of biased data has been found, the next step is to sample the distributions to find the overall mean and uncertainty bounds. Every distribution

is randomly sampled one time and then fit with a surrogate. In this example a spline fit is used to generate the surrogate. Figure 22 shows the first sample set represented with an asterisk at each sample location. The spline fit is shown is yellow. The black line represents the truth model (Helmbold's equation) for reference. The distributions and the associated random sample is also shown in Figure 22 for reference.

	X1	Y_B	Sample
L_1	1		S_1
L_2	2		S_1
L_3	3		S_1
L_4	4		S_1
L_5	6		S_1
H_1	1.5		S_1
H_2	5.25		S_1

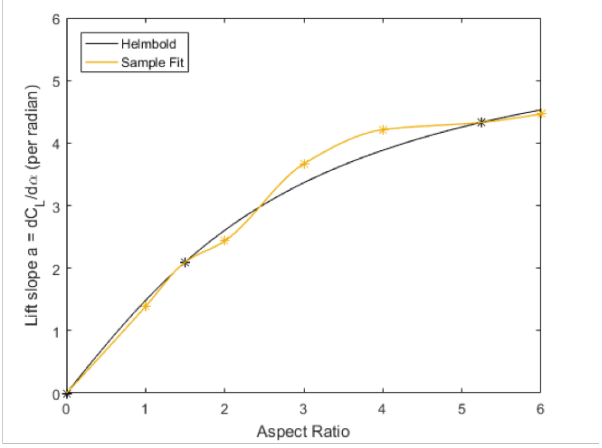

Figure 22: The yellow curve is a spline fit of the first Monte Carlo sample of each distribution. Helmbold's correction for low-aspect ratio wings is shown in black for reference.

Another random sample is taken from each distribution and again fit with a spline curve to create another surrogate. The results of this second random sampling are shown in Figure 23. The results from a third random sample are shown if Figure 24.

This process is repeated 1000 times to achieve an accurate representation of the uncertainty throughout the entire design space. Figure 25 shows the results for all 1000 surrogates.

3.9.0.3 Determination of the Overall Mean and Uncertainty

An average of all the surrogates is found at every point within the design space. This average is what represents the overall mean of the final prediction. The overall bounds of the surrogates at every point in the design space become the final uncertainty prediction. Figure 26 is a depiction of the final prediction model throughout the

	X1	Y_B	Sample
L_1	1		S_2
L_2	2		S_2
L_3	3		S_2
L_4	4		S_2
L_5	6		S_2
H_1	1.5		S_2
H_2	5.25		S_2

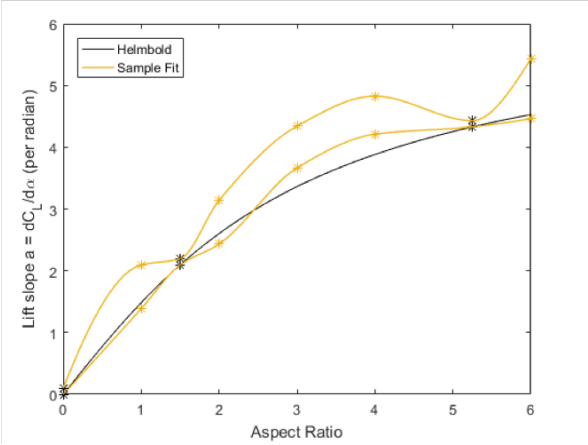

Figure 23: Another yellow line representing a spline fit of the second Monte Carlo sample of each distribution. Helmbold's correction for low-aspect ratio wings is shown in black for reference.

	X1	Y_B	Sample
L_1	1		S_3
L_2	2		S_3
L_3	3		S_3
L_4	4		S_3
L_5	6		S_3
H_1	1.5		S_3
H_2	5.25		S_3

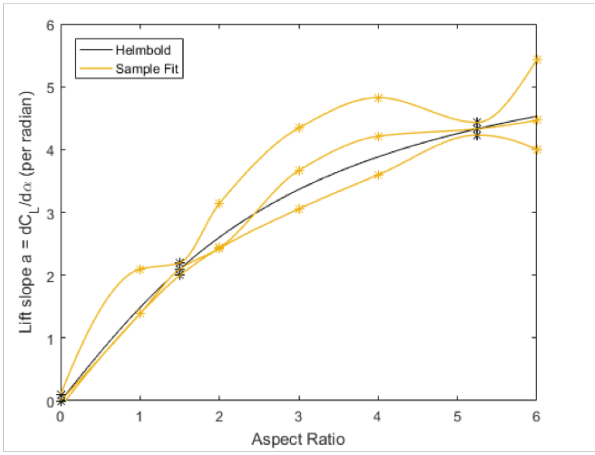

Figure 24: Another yellow line representing a spline fit of the third Monte Carlo sample of each distribution. Helmbold's correction for low-aspect ratio wings is shown in black for reference.

design space. The solid green line is the mean of the prediction and the green dashed lines are the uncertainty bounds. The black line is the truth model (Hemlbold) and the red line is the original low fidelity prediction (Prandtl) for reference. Notice how the uncertainty bounds decrease significantly near the high fidelity points and then increase as one moves farther away from the points. The average error of the biased prediction model is approximately 40% less than the error of the original low fidelity model.

	X1	Y_B	Sample
L_1	1		S_n
L_2	2		S_n
L_3	3		S_n
L_4	4		S_n
L_5	6		S_n
H_1	1.5		S_n
H_2	5.25		S_n

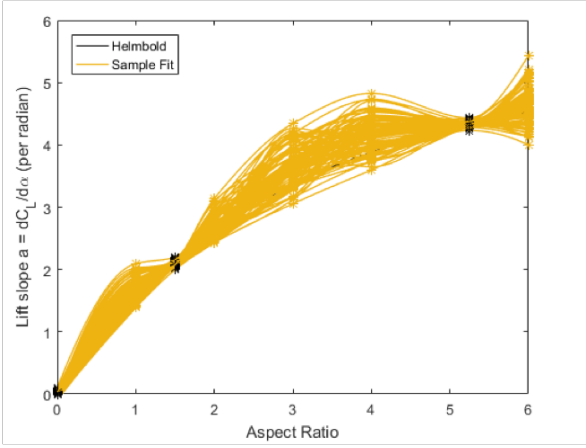

Figure 25: Yellow lines representing the fits of all the third Monte Carlo samples of each distribution.

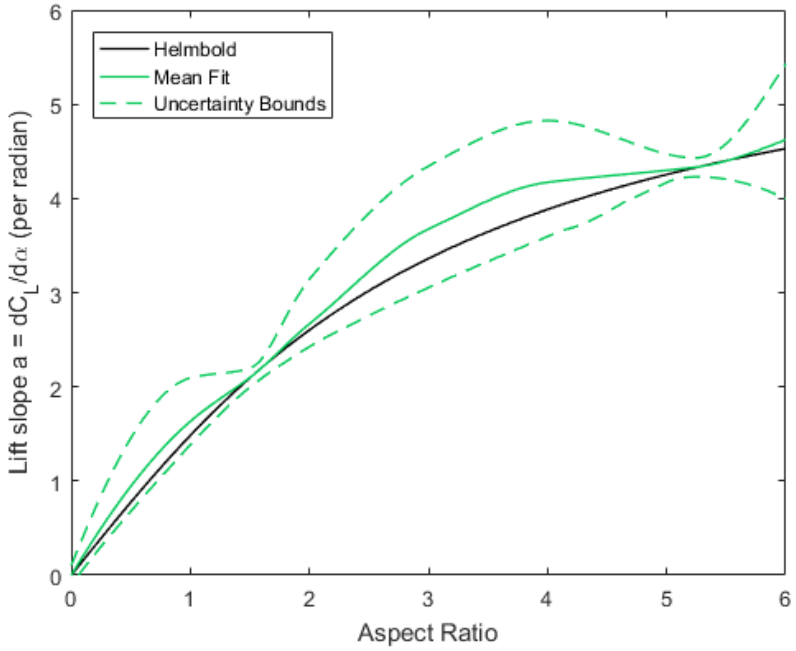

Figure 26: Final prediction of Helmbold's equation shown in green. The green dashed lines represent the uncertainty bounds.

Additionally, the amount of uncertainty can be used to determine where additional resources should be spent to improve the model. In this example, the largest amount of uncertainty occurs at the point $x = 3.25$. If an additional high fidelity simulation is conducted at that location, the results of the prediction improve significantly. This methodology is repeated again with the addition of a high fidelity point at $x = 3.25$.

The results are shown in Figure 27. The prediction is shown in green with the uncertainty bounds represented by the green dashed lines. Helmbold's equation for low aspect ratio wings is shown in black for reference. Notice how the prediction model improves significantly. The error of this new biased prediction is 28% less than the error of the first biased model. This process can be used over and over until the model achieves an accuracy that the decision maker deems appropriate.

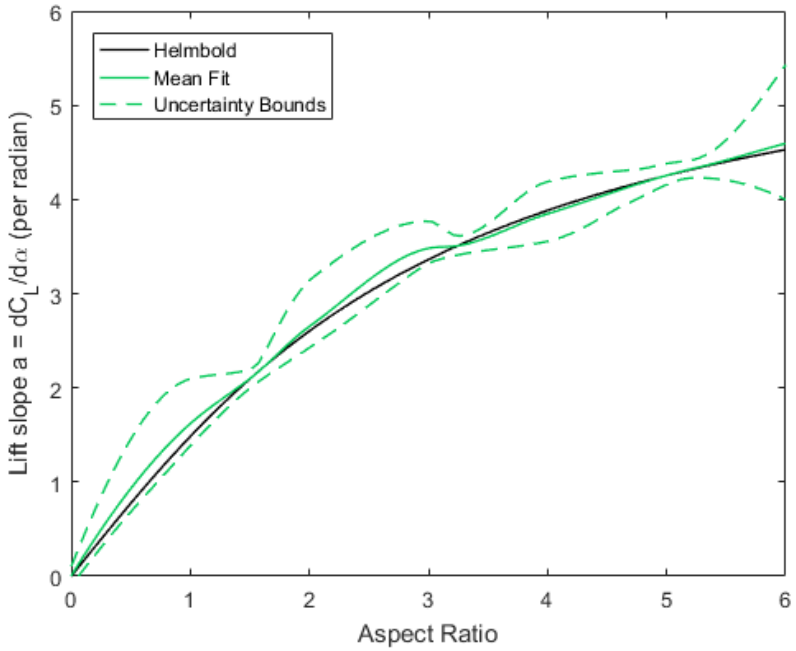

Figure 27: Final prediction of biasing method for the second iteration.

CHAPTER IV

EXPERIMENTAL PLAN

The information presented in Chapter 3 resulted in a set of formal research questions and hypotheses that, once tested, will result in the final formulation of a methodology that aims to achieve the overarching research objective. Overall, there are four research questions and hypotheses that must be tested through a set of formal experiments. This chapter will discuss the details about the experimental plan developed to test the hypotheses. Once the final methodology has been formulated, a final validation experiment will be conducted on a representative technology. The details of the experimental setup and results for the demonstration experiment are discussed in Chapter 6

The objective of each experiment is to enable each hypothesis to be either supported or refuted. Therefore, the experiments are designed to produce the necessary information to make these statements about the hypotheses. The analysis conducted for this thesis is divided into four different experiments. Figure 28 depicts how each experiment maps to the different research questions and hypotheses, as well as the different steps in the proposed methodology.

Each of the following sections provide a thorough description of the four experiments. The chapter that follows will provide the results of the experiments as well as discussions on what the results mean in terms of supporting or refuting the hypotheses. The first two questions can be answered by experimenting on known mathematical functions. Questions 3 and 4 will be more appropriately answered using real world data. At the conclusion of Experiments 1-3, the steps of the MUSIC methodology will be finalized. The final experiment, Experiment 4, will provide a full execution

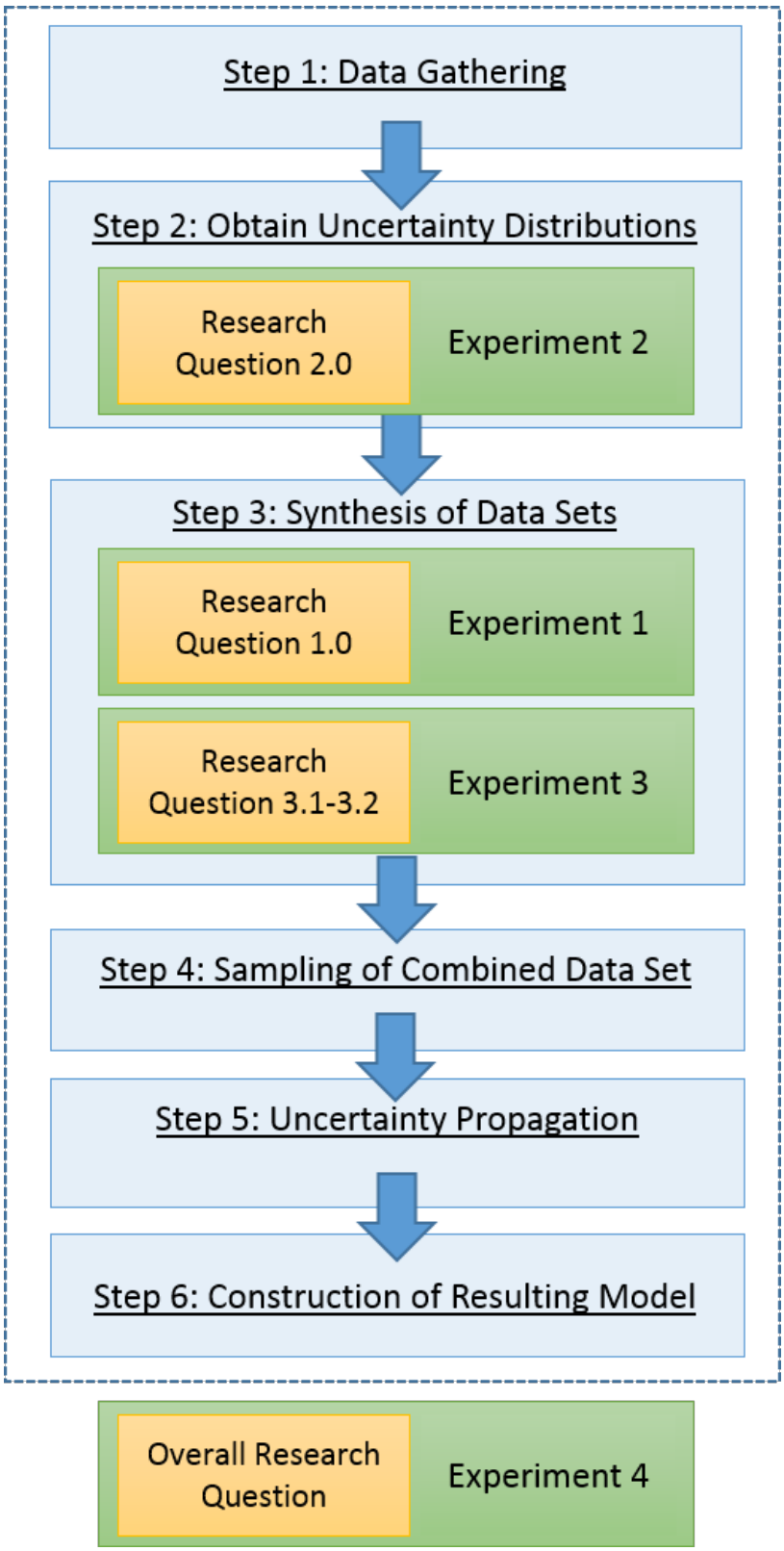

Figure 28: Experimental Plan for Testing Hypotheses

of the resulting methodology and the results will be compared to the performance of Bayesian Model Averaging from the literature. A final experiment will apply the methodology to the Hamilton Standard propeller data set to validate the methodology on a more representative technology. The results from this final experiment will provide the final validation of the methodology's performance.

There is a need to identify appropriate metrics that can be used for comparison purposes during the experiments. Various metrics are commonly used to compare the quality of a model. The most effective metric is the model representation error (MRE) which compares the error between the predicted model and validation points. For this research the MRE is normalized by the range of the validation data. A good model is considered to be where the mean of the percent MRE is close to zero and the standard deviation of the percent MRE is less than one. Another metric used is the change in the level of inferred uncertainty. This metric is important to include because reducing the level of uncertainty is a primary goal of the MUSIC methodology. The inferred uncertainty will be normalized by the maximum level of uncertainty of the initial low fidelity data set. The number of validation points outside of the final uncertainty bounds will be the final metric used.

4.1 Experiment 1

The first experiment addresses the following question:

Research Question 1: How will the low fidelity distributions be biased in the input space?

This question will be addressed first because the biasing step is vital to the entire method. Therefore, determining the most appropriate proximity function needs to be identified first. It has been discussed throughout this document that the Kriging

algorithm is used in the uncertainty community to represent the amount of uncertainty in throughout the design space. However, this representation of uncertainty is relative, and not a true representation of the uncertainty. A better way to describe the uncertainty representation from Kriging is as the change in uncertainty. Part of the motivation for this thesis came from using Kriging and wondering if the change in uncertainty calculated by Kriging could be used to propagate the true given uncertainty distributions at specific locations in the design space to obtain a better prediction of the uncertainty throughout the entire design space.

The specifics of the Kriging algorithm are discussed in Section 2.6. The algorithm uses the squared exponential function to model the change in uncertainty. A genetic algorithm uses the training data to determine the most appropriate values for the scale parameter in each dimension. Therefore, this first experiment will test the squared exponential function with the scaling parameter, θ, set by the Kriging algorithm as the proximity function. The following hypothesis has been developed from the literature review.

Hypothesis 1: A proximity function that uses the Kriging algorithm to determine a unique scaling parameter, θ, for each dimension will more effectively bias the low fidelity uncertainty distributions.

Comparisons are made against two other proximity functions: the squared exponential function with the scaling parameter fixed at 10, and a linear function that evenly spans the entire design space. The scaling parameter for the second proximity function will be set to 10 because this creates a bell shaped curve that traverses the entire design space. The linear proximity function is defined as $P(x) = -x + 1$ where x is the Euclidean distance between the points of interest in the design space. Figure 29 shows the different proximity based functions that will be compared in this experiment. The linear function is shown in red, the squared exponential function with $\theta = 10$ is shown

in blue, and examples of the squared exponential function with $\theta = 1$ and $\theta = 50$ are shown in black and green respectively.

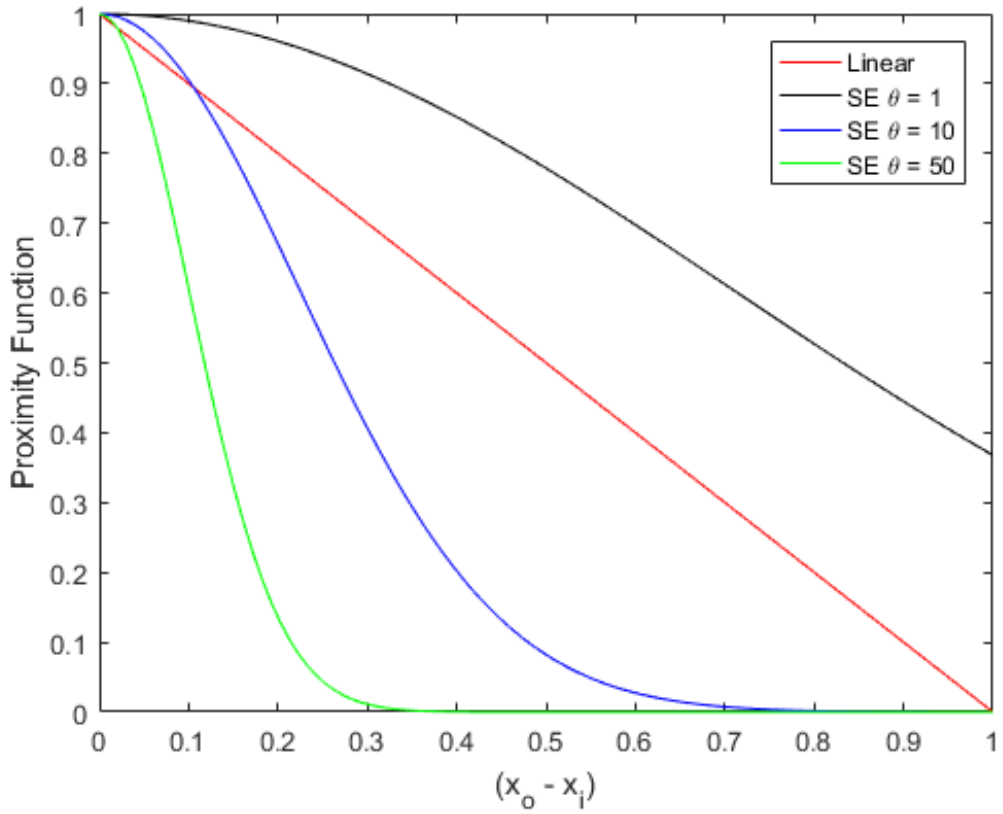

Figure 29: Different proximity function options.

Two mathematical functions, shown in Figure 30, were created to test the different proximity functions. The black function, which represents the truth model, is quadratic in the X_1 dimension and cubic in the X_2 dimension. The red function, which represents a lower fidelity simulation, is quadratic and slightly shifted in the first dimension when compared to the truth model, and linear in the second dimension. The red function was created this way to give the appearance that the low fidelity simulation has some error in the prediction of the magnitude and that it is missing some physics.

As previously mentioned, high fidelity data is expensive to generate. Additionally, multiple test configurations are likely to have similar geometries to save on cost.

Therefore, the high fidelity data set generated from the black truth model consists of six total data points that are clustered in two different areas of the design space. Recall the previous discussion about advanced concepts being evolutionary, not revolutionary. This means that the engineer or decision maker has some general insight into what the true design space should look like. Thus, the high fidelity data points are set so that there is more variation in the cubic dimension because it is known that the low fidelity model is missing some of the physics in this dimension. A normal distribution with a standard deviation of 1% of the overall range is used to represent a small amount of uncertainty surrounding the high fidelity data.

In contrast to high fidelity simulations, low fidelity simulations are much cheaper, so an 11 by 11 grid of points is used to cover the entire design space. The uncertainty for the low fidelity data set is represented by a triangular distribution where the largest amount of error between the two functions is used to define the bounds throughout the entire design space. The largest amount of error is 0.2362. Therefore, the upper and lower bounds represent $\pm$ 31.5% of the overall range. The locations of the high and low fidelity points throughout the design space for each data set are shown in Figure 31.

Now that the data sets have been defined, simulations will be run to determine the most appropriate method for biasing the low fidelity data. Again, the experiment will test the linear function, the squared exponential function with $\theta = 10$, and the squared exponential function with unique values of θ for each dimension that are found using the Kriging algorithm. The change in the model representation error (MRE) statistics normalized by range as well as the change in the inferred uncertainty will be used as the metrics for determining which method is best.

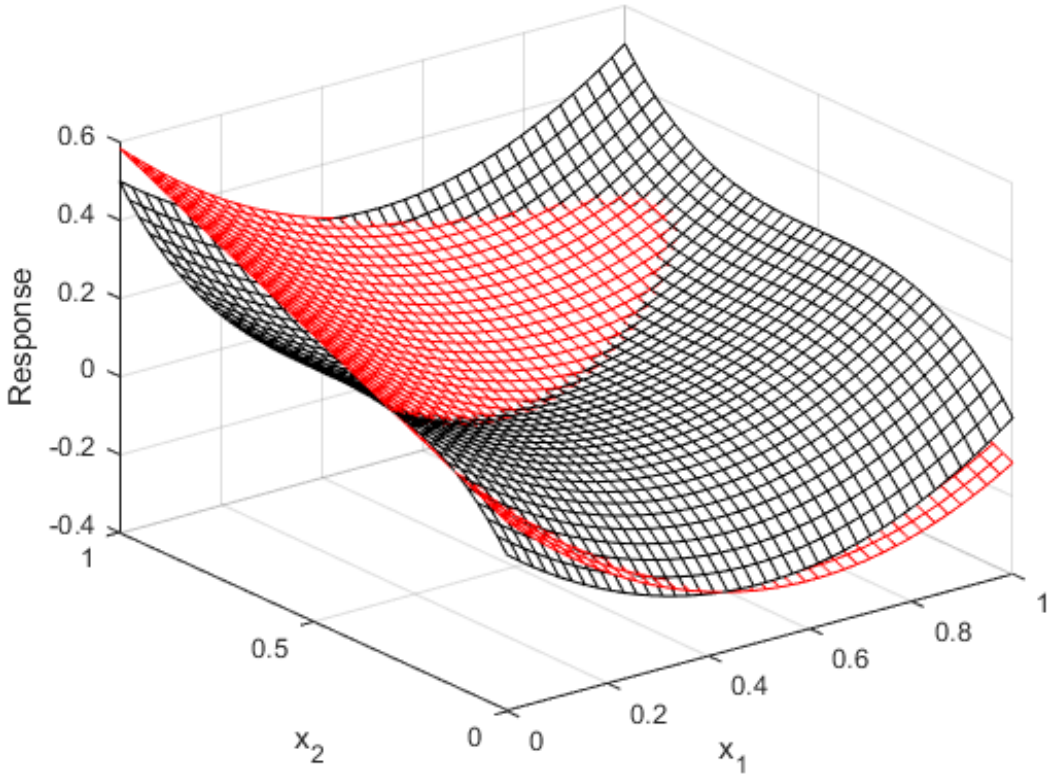

Figure 30: Mathematical functions that are used to generate the high and low fidelity data sets. Black is the truth model and red is the low fidelity function.

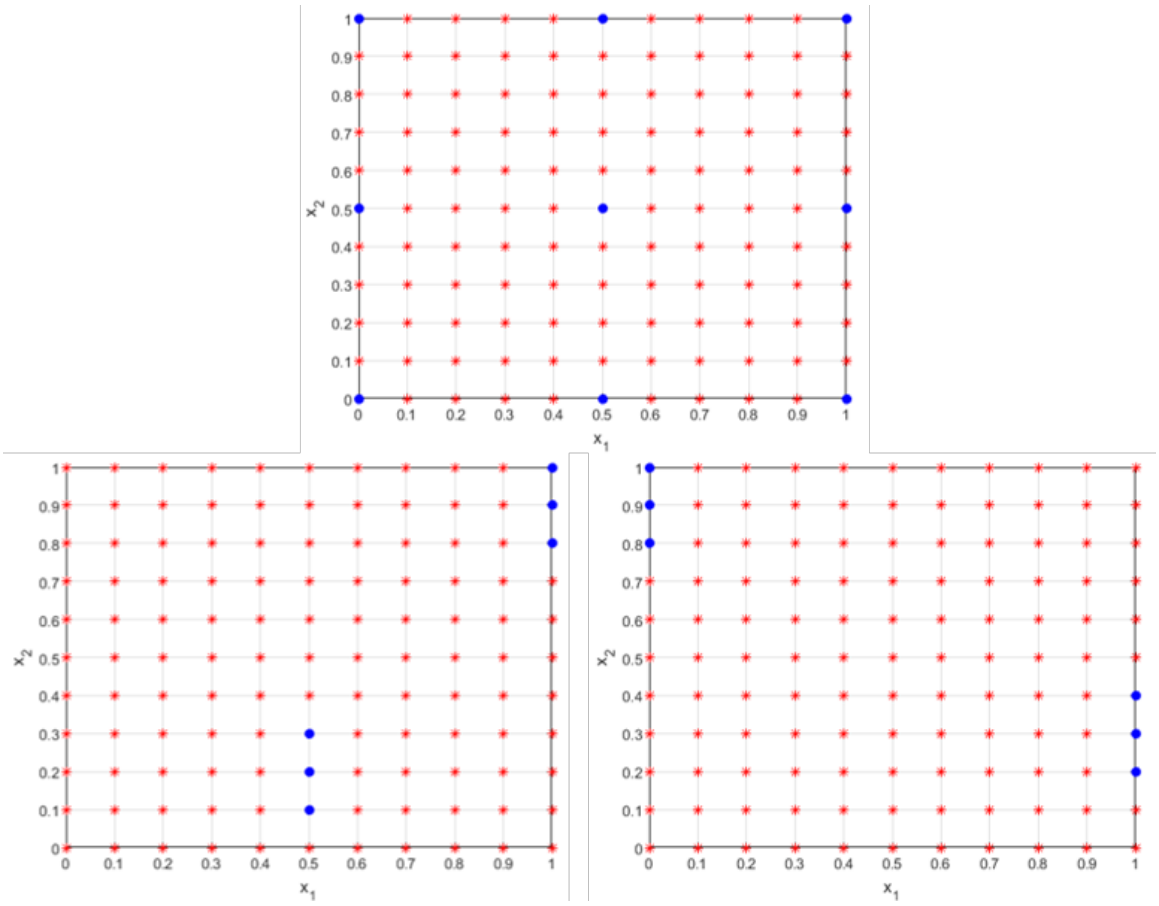

Figure 31: Distribution of high and low fidelity data points throughout the design space. The red asterisks represent the low fidelity points and the blue circles represent the high fidelity points.

4.2 Experiment 2

The second experiment addresses the following research question:

Research Question 2: Does the type of uncertainty distribution used for the low fidelity data sets affect the results given that it can be bounded and it has a unique mode?

This question will be investigated by comparing the results from the biasing method using different distributions to represent the uncertainty of the low fidelity data sets. The comparison will be done with triangular and a Weibull distributions. A triangular distribution was chosen because it is relatively simple to use and is commonly used to represent uncertainty distributions in industry. The Weibull distribution was chosen because it is a versatile distribution. Depending on the shape and scale parameters, the Weibull distribution can be an exponential, Rayleigh, or even similar to a Gaussian distribution. It is also commonly used for uncertainty representation because it has one bound that can be used to represent the theoretical upper limit of the benefit of a technology[59, 48]. For this application, think of the Weibull distribution as starting out like a Gaussian distribution that can then be skewed as needed.

The triangular distribution is defined by the mode and the upper and lower bounds. For this experiment this distribution will be implemented in the methodology the same way it was used in the problem formulation chapter. The three parameter Weibull distribution is defined by a location parameter, a shape parameter, and a scale parameter. The equation for the pdf is as follows

$$f(x,k,\lambda,\theta) = \frac{k}{\lambda}\left(\frac{x-\theta}{\lambda}\right)^{k-1} e^{-\left(\frac{x-\theta}{\lambda}\right)^{k}} \tag{35}$$

where k is the shape parameter, λ is the scale parameter, and θ is the location parameter. The values of these parameters allow for a wide range of distributions. To simplify the process of defining the Weibull distribution, the triangular distributions developed in the initial portion of the experiment are used to define the Weibull distributions. This is done by sampling the triangular distributions and then fitting a Weibull distribution to the samples. Defining the Weibull distribution from the triangular distribution will ensure that they both have the same mode as well as the same bounds. It is also important to note that the type of distribution does not impact the biasing process because the biasing process is only dependent on the mode and the bounds. This means that both the bounds and the amount of skew for the two distribution types will be nearly identical. Therefore, the following hypothesis has been developed.

Hypothesis 2: The type of distribution used to represent the uncertainty of the low fidelity data does not significantly impact the results of the methodology as long as it has a unique mode and is bounded.

The mathematical functions and data sets generated for Experiment 1 will also be used for this experiment. Each distribution will be applied to the data sets and then put through the biasing process that was determined in Experiment 1. Once again the model representation error statistics and the amount of inferred uncertainty will be used to determine if the type of distribution has an impact on the results.

4.3 Experiment 3

Recall the discussion in Section 3.3 about how an additional mid fidelity level data set will be handled by the methodology. If additional data sets that include additional knowledge are obtained, then the MUSIC methodology must be able to account for them. A notional illustration of the problem is shown in Figure 32 (repeated from

Section 3.3 for convenience). The mid fidelity level data point shown in blue will most likely improve the final uncertainty characterization because it adds knowledge, but it probably should not be included in the biasing process the same way the high fidelity points are included. This thought experiment lead to a two part question.

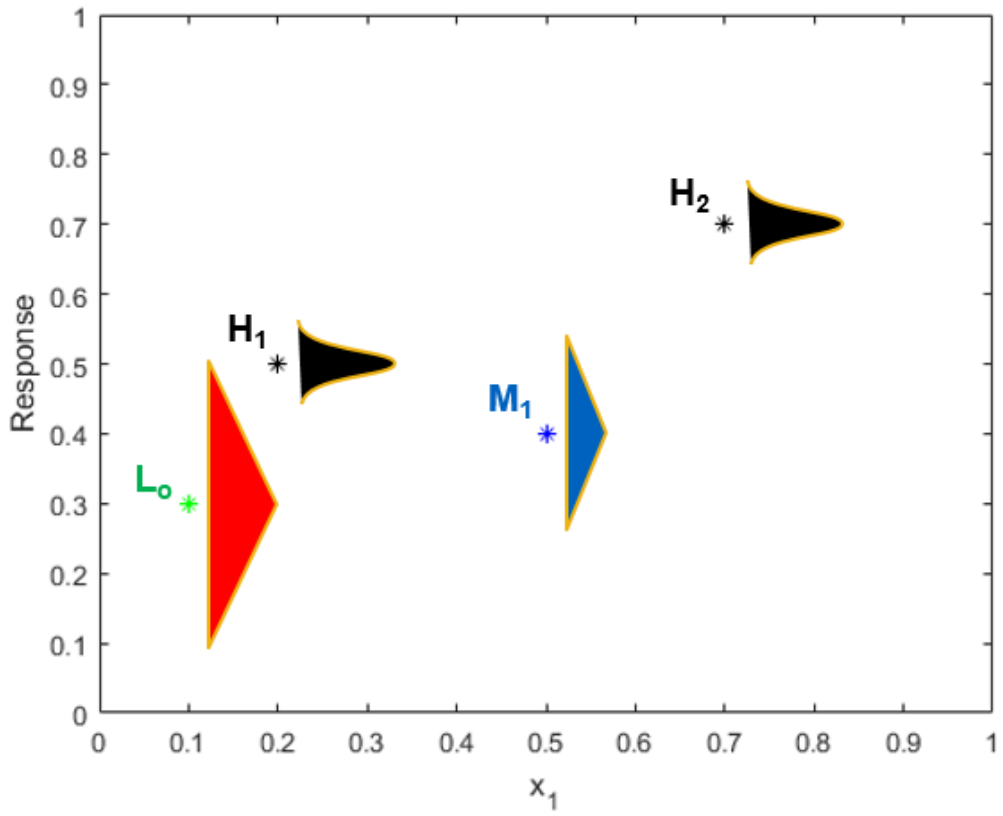

Figure 32: Notional example of a design space with a mid fidelity point.

Question 3.1 and Hypothesis 3.1 are shown below.

Research Question 3.1: Will the addition of a mid fidelity level data set further improve the final uncertainty characterization?

Hypothesis 3.1: Including a mid fidelity level data set will improve the final uncertainty characterization.

The biasing equation for two levels of fidelity discussed in Section 3.3.1 is repeated below

$$B_{L_o} = U_{L_o} \sum_{i=1}^{n} B_{H_i} \tag{36}$$

where B_{H_i} is the bias impact of the i^{th} high fidelity data point for n high fidelity data points. A modification is made to the equation to include a mid fidelity level data set as follows

$$B_{L_o} = U_{L_o} \left(\sum_{i=1}^{n} B_{H_i} + \sum_{j=1}^{k} B_{M_j} \right) \tag{37}$$

where B_{M_i} is the bias impact of the j^{th} mid fidelity data point for k mid fidelity data points. Note that in the equation's current form, the mid fidelity data set is treated exactly the same way as the high fidelity data set in equation 43.

To test hypothesis 3.1, the analysis of a two-dimensional wing section with an infinite aspect ratio made up of NACA 16-series airfoils will be used. The following paragraphs give a brief explanation of some lower fidelity lift slope prediction models. See McCormick for more details[78].

The analysis of a two-dimensional wing section with an infinite aspect ratio is equivalent to that of an airfoil. Thus from thin airfoil theory the lift slope is

$$a_o = \left(\frac{dC_l}{d\alpha} \right) = 2\pi \tag{38}$$

where α is the angle of attack in radians. As planes began to fly faster, it became necessary to include a compressibility correction. The Prandtl-Glauert rule is a simple compressibility correction that allows for the incompressible lift slope to be modified to account for compressibility effects. The rule is defined as

$$a_{o,comp} = \frac{a_o}{\sqrt{1 - M_\infty^2}} \tag{39}$$

where $a_{o,comp}$ is the compressible lift slope for an airfoil and M_∞ is the free-stream Mach number. This compressibility correction can be incorporated in to Equation 38

to estimate the compressible lift slope of an infinite wing section which results in the following equation.

$$a = \frac{2\pi}{\sqrt{1 - M_\infty^2}} \tag{40}$$

This equation works well for quick back of the envelope estimates of the lift slope for a high aspect ratio subsonic wings where three dimensional effects are negligible. Equation 40 be referred to as the Prandtl-Glauert equation for the remainder of this document.

However, as free stream Mach numbers crept toward transonic Mach numbers, engineers began to sweep the wings to decrease the impact of wave drag[6]. Kuchemann modified the traditional lift slope equations to account for sweep[60]. The final equation for an infinite aspect ratio compressible swept wing is shown below

$$a = \frac{a_o \cos\Lambda}{\sqrt{1 - M_\infty^2 \cos^2\Lambda}} \tag{41}$$

where Λ is the sweep angle. A specific name is not given to this equation in common aerodynamics literature, but it will be referred to as Kuchemann's equation for the remainder of this document. Equations 40 and 41 will be used to estimate a the lift coefficient for an airfoil section on a swept wing as follows

$$C_l = a(\alpha - \alpha_{C_{l_o}}) \tag{42}$$

where $\alpha_{C_{l_o}}$ is the zero lift angle of attack which is dependent on the camber of the airfoil. Note that for the NACA 16 series airfoils the camber is book kept in terms of the design lift coefficient.

From the equations outlined above, the free-stream Mach number, the angle of attack, and the design lift coefficient will be the three input variables for this experiment. The sweep angle and thickness to chord ratio will be held constant at 45^o and 15% respectively. The Prandtl-Glauert equation (Equation 40) will be used to generate the low fidelity data set because it does not account for sweep while the

Table 2: Input ranges for experiment 3

Design C_l	Mach number	Angle of Attack
0.1 - 0.7 step = 0.1	0.4 - 0.7 step = 0.1	-6^o - 12^o step = 2^o

Table 3: High fidelity data sets

Data Set	Design C_l	Mach number	Angle of Attack
Set 1	0.1	0.4, 0.6	-4^o - 12^o
	0.7	0.5, 0.7	-4^o - 12^o
Set 2	0.3	0.4, 0.6	-4^o - 12^o
	0.7	0.5, 0.7	-4^o - 12^o

Kuchemann equation (Equation 41) will be used to generate the mid fidelity data sets because it does account for sweep. The high fidelity data sets will be generated using Xfoil[31]. Xfoil is a potential flow panel code that includes an interactive boundary layer formulation to account for viscosity. It also uses the Karmen-Tsien compressibility correction which performs better than the Prandtl-Glauert compressibility correction at higher subsonic and transonic Mach numbers. To account for sweep, a local Mach number defined as $\text{Mach}_{\text{loc}} = \text{Mach}_{\infty} \cos \Lambda$ will be used to simulate a swept wing section.

Table 2 shows the ranges for the three different input variables. Even though a full factorial sweep of all the input variables can be conducted in a short period of time for all three simulation fidelity levels, only the low fidelity data set generated from the Prandtl-Glauert equation will cover the entire design space. Two separate high fidelity data sets will be created using Xfoil. They are shown in Table 3. The only difference in the data sets is that data set 1 has data at design lift coefficient equal to 0.1 while data set 2 has high fidelity data for a design lift coefficient equal to 0.3 instead. This means that for the second data set the MUSIC method will be forced to extrapolate beyond the bounds of the high fidelity data.

The experiment will be conducted as if it is a real world experiment where the low fidelity data blankets the entire design space and a limited number of high fidelity data

points are included using the MUSIC method. The resulting prediction is analyzed to determine where additional data points are needed. Additional data points from the Kuchemann equation will then be added. Observations regarding hypothesis 3.1 will then be made at this point in the experiment.

4.3.1 Part 2: Bias Weight Factor Study

Once the mid fidelity level data set is included in the combined data set, question 3.2 and hypothesis 3.2 can be addressed. They are as follows.

Research Question 3.2: By introducing the mid fidelity level data set, do changes need to be made to the existing biasing process?

Hypothesis 3.2: If the final results are sensitive to a weight factor, then a fidelity level weight function needs to be developed.

To change the influence of the mid fidelity data set, another term is added to Equation 43. The updated form of the equation is

$$B_{L_o} = U_{L_o}\left[\sum_{i=1}^{n} B_{H_i} + \left(\sum_{j=1}^{k} B_{M_j}\right) W_M\right], \tag{43}$$

where W_M is the mid fidelity weight factor. A sensitivity study will be conducted, where the weight factor will vary from 0 to 1 in increments of 0.25. A weight factor of 1 means that the mid fidelity data set is treated as if it is another high fidelity data set. When the weight factor is set to 0, the mid fidelity data set is treated as if it is another low fidelity data set. It is important to clarify that a weight factor of 0 does not mean the mid fidelity level data set is mathematically removed from the methodology. A weight factor of 0 means the mid fidelity level data set does not have any influence on the low fidelity data, but it is still included in the model as if it is another low fidelity data set. Observations regarding hypothesis 3.2 will then be

made at this point in the experiment. A summary of the entire experiment will also follow.

4.4 Experiment 4

Experiment 4 will address the overall impact of the resulting methodology from this research. Bayesian model averaging (BMA) is a current multifidelity method that is described in Section 2.5. The purpose of creating the MUSIC method is to address some of the shortcomings of the BMA method. Specifically that BMA does not work well with sparse data sets and that it does not take proximity into account when making inferences about the uncertainty. This experiment will address the following research question and hypothesis:

Research Question 4: Does the MUSIC method provide a better resulting prediction of performance compared to current methods like Bayesian model averaging?

Hypothesis 4: The MUSIC methodology described in this thesis will provide a better uncertainty characterization of the performance throughout the entire design space compared to Bayesian model averaging when applied to advanced concepts with sparse data.

The swept wing section data sets using the NACA 16-series airfoils from the previous experiment will be used again for this validation experiment. Recall that the Prandtl-Glauert equation is used to generate the low fidelity data set, the Kuchemann equation is used to generate the mid fidelity data sets, and Xfoil is used to create the high fidelity data sets where $\text{Mach}_{\text{loc}} = \text{Mach}_{\infty} \cos \Lambda$. The same wind tunnel data set from Lindsey et al. will be used for validation[67].

Recall from the discussion about Bayesian model averaging that a correction surrogate needs to be created so that the likelihood function used later on in the process

Table 4: High fidelity data for the correction surrogate

design C_l	$Mach_\infty$	angle of attack	C_l
0.1	0.4	-6^o	-0.383
		12^o	1.036
	0.7	-6^o	-0.354
		12^o	0.733
0.7	0.4	-6^o	-0.108
		12^o	1.250
	0.7	-6^o	-0.007
		12^o	1.293

does not unfairly bias one data set over the other. After the correction surrogate is generated, the likelihood surrogate needs to be generated from a separate high fidelity data set. In general, two data points per dimension are needed to create a surrogate at a minimum. i.e. the number of high fidelity points required $= 2^d$ where d is the number of dimensions. The number of high fidelity data points doubles for BMA because two separate surrogates are required. To support the hypothesis that the MUSIC method will provide better results compared to BMA for sparse data sets, the minimum number of data points required by BMA will be used. There are 3 dimension, thus 8 points are needed for each surrogate, resulting in a total of 16 data points. Table 4 shows the high fidelity data that will be used to create the correction surrogate. The correction surrogates are then used to correct both the mid and low fidelity data sets.

The full range of the data generated by the Prandtl-Glauert equation will again be used as the low fidelity data set. The mid fidelity data set will consist of 80 data points generated by the Kuchemann equation.

An additional set of high fidelity data is needed to create the likelihood surrogates. Once again, this is the major drawback associated with BMA since it requires twice the minimum amount of data compared to the MUSIC method. The second set of high fidelity data is shown in Table 5. The likelihood surrogates are then used to combine the data sets and create the final prediction model throughout the entire

Table 5: High fidelity data set for the likelihood surrogates

design C_l	$Mach_\infty$	angle of attack	C_l
0.1	0.4	-6^o	-0.383
		-4^o	-0.252
		8^o	0.7123
		12^o	1.036
	0.7	-6^o	-0.354
		-4^o	-0.170
		8^o	0.671
		12^o	0.733
0.7	0.4	-6^o	-0.108
		-4^o	-0.111
		8^o	1.036
		12^o	1.250
	0.7	-6^o	-0.007
		-4^o	0.165
		8^o	1.059
		12^o	1.293

design space. There are some repeated points from the first data set to ensure that the entire design space is covered by both surrogates. However, there will not be an issue with double dipping on the high fidelity data because all of the points used to generate the surrogates will be replaced by the high fidelity data in the model during last step in the process.

The same data points given in Tables 4 and 5 will be used to create a prediction using the MUSIC method. The two different methods will be compared using the MRE statistics, inferred uncertainty statistics, as well as the number of validation points that are not captured by the inferred uncertainty bounds. To further support the hypothesis, an additional test will be conducted where only the first high fidelity data set is applied to the MUSIC method. The purpose is to test how well the MUSIC method performs is circumstances when there is not enough data for BMA.

CHAPTER V

EXPERIMENTAL RESULTS

This chapter discusses the results for the first two experiments. Recall that the data used for these experiments is generated from two arbitrary mathematical functions to specifically test the biasing step of the methodology. The functions are designed to emulate a real world application where the high fidelity data gives a very good prediction of the true results throughout the design space, while the low fidelity data does not give good results in some portions of the design space due to missing physics. For more details on the derivation and reasoning behind the choice of these function, see Section 4.1.

5.1 Experiment 1 Results

The first experiment addresses the following research question.

Research Question 1: How will the low fidelity distributions be biased in the input space?

The purpose of this experiment is to determine if using the Kriging function to set the unique values for the scaling parameter in the squared exponential function results in an effective proximity function. The squared exponential function with unique scaling parameters, θ_s, set by the Kriging algorithm is compared against two other proximity functions: a linear function and the squared exponential function with the scaling parameter set to 10. The different proximity functions are shown in Figure 33 where the linear function is in red, the squared exponential function with $\theta = 10$ is shown in blue, and two other squared exponential functions with $\theta = 1$ and $\theta = 50$ are

shown in black and green as examples of squared exponential functions with different scaling parameter values. Recall from previous discussions that a literature review led to Kriging, which is a nonlinear surrogate modeling technique commonly used in machine learning to model uncertainty. A crucial part of the Kriging algorithm is the use of training data to determine the scaling parameters of the squared exponential functions that best fit the data. The squared exponential functions defined by the data are commonly used to represent the change in uncertainty. However, Kriging can only provide a prediction of the uncertainty in one area of the design space relative to another, not the true uncertainty. Applying the change in uncertainty from Kriging to the given uncertainty distributions may provide a better prediction of the uncertainty throughout the design space. Therefore, the following hypothesis was developed.

Hypothesis 1: A proximity function that uses the Kriging algorithm to determine a unique scaling parameter, θ, for each dimension will more effectively bias the low fidelity uncertainty distributions.

The mathematical functions used to generate the high and low fidelity data sets are shown in Figure 34. The initial inferred uncertainty bounds, which are the low fidelity uncertainty bounds defined as the largest amount of error between low and high fidelity functions, are shown in Figure 35 from two different perspectives. The low and high fidelity functions are shown in red and the black respectively for reference. These initial inferred uncertainty bounds will serve as the baseline for the level of uncertainty. The mode of each low fidelity data point is defined by the red function. Therefore the red and yellow functions shown in Figure 35 represent the prediction if just the low fidelity data were to be used without using the MUSIC method. The results for three separate data sets are individually discussed in the following sections.

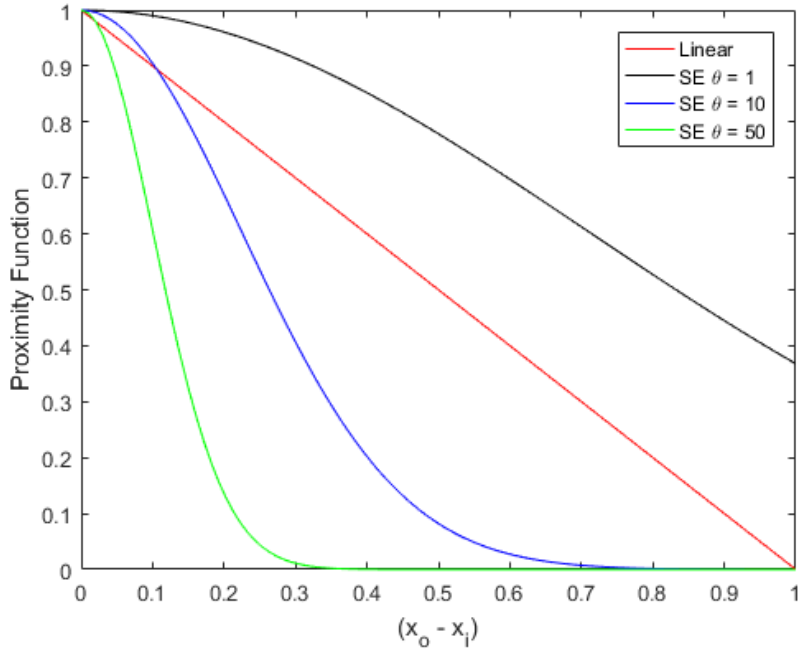

Figure 33: Proximity function options.

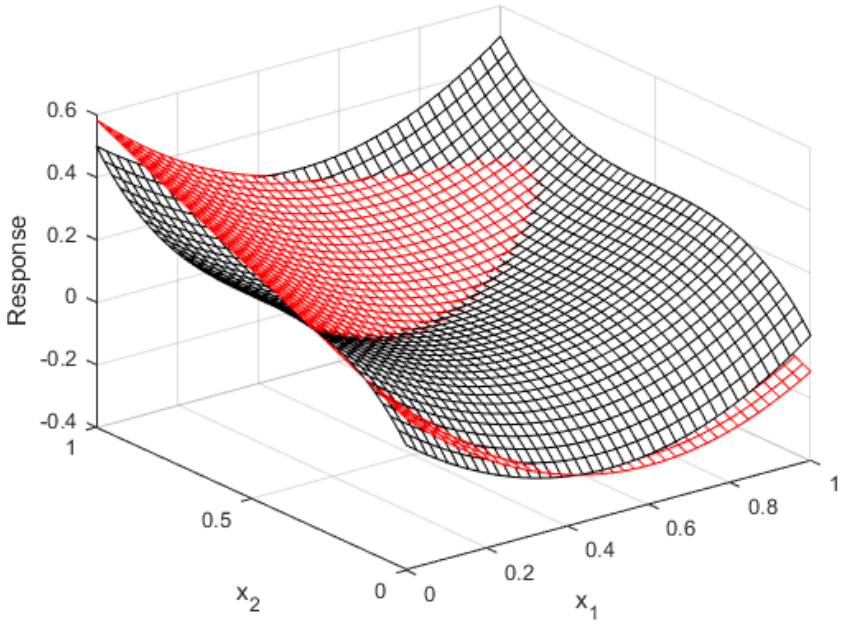

Figure 34: Mathematical functions used to generate the high and low fidelity data sets. Black is the truth model and red is the low fidelity function.

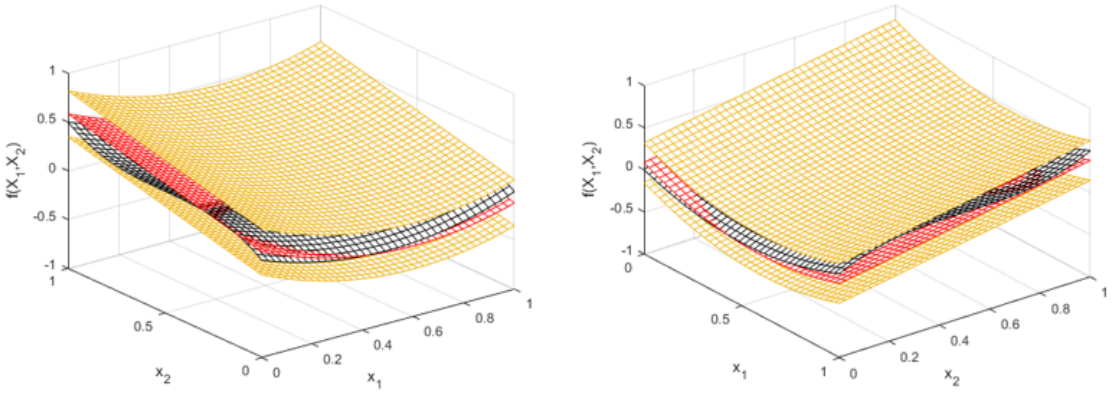

Figure 35: Initial inferred uncertainty bounds on the mathematical functions.

5.1.1 Data Set 1

In the first data set, the high fidelity points are evenly distributed throughout the design space in a nine point grid. The data set is shown in Figure 36 where the red asterisks are the low fidelity points and the blue circles are the high fidelity points.

Table 6 shows the results for the three different proximity functions compared against the low fidelity prediction by itself. All three functions reduce the standard deviation, but only the squared exponential function with unique θ parameters moves the mean closer to 0 compared to the other two functions. It should be noted that the shift in the mean is dependent on the location of the data points. Therefore, it is not appropriate to compare the shift in the mean between the proximity function results and the initial low fidelity prediction. However, contrasting the shift in the mean between the three proximity functions is a fair comparison.

Unlike the mean MRE metric, it is appropriate to compare the reduction in the

Table 6: Results for data set 1

Method	Mean MRE	STDevMRE	ΔU
No biasing	2.00%	12.04%	-
Linear	-5.20%	8.23%	-70.86%
SE $\theta = 10$	-3.96%	7.16%	-56.32%
SE unique θ	-1.18%	8.16%	-35.19%

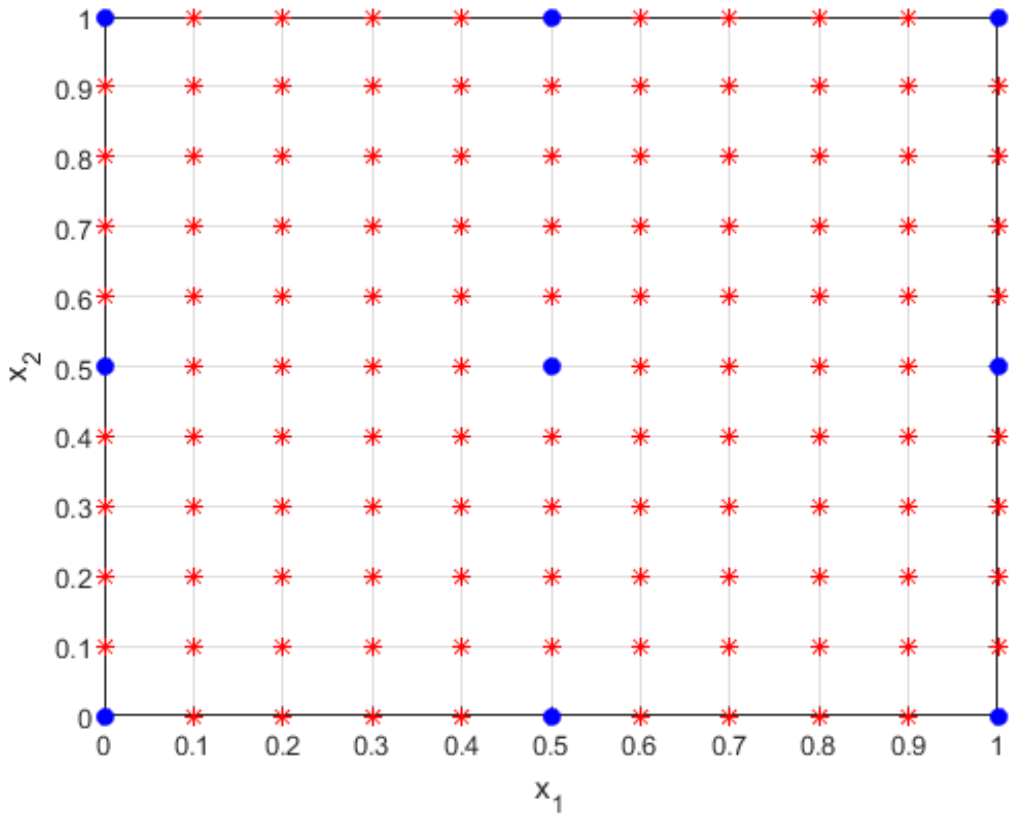

Figure 36: Data set 1. The blue circles are the high fidelity points.

standard deviation between the three proximity function results and the initial low fidelity prediction. The results show that the linear function and the squared exponential function with $\theta = 10$ decrease the inferred uncertainty significantly more compared to the squared exponential function with unique θ parameters. A closer look at the resulting figures shows that these drastic changes in the uncertainty bounds may not be a good thing.

The results for the linear proximity function are shown in Figure 37. The figure in the top left shows the final mean prediction colored by the level of uncertainty as a percentage of range of the initial uncertainty bounds. The color bar to the right of the figure maps the color of the plot to the percentage of the initial uncertainty bounds. Thus, bright yellow, or 100 on the color bar indicates no change compared to the initial uncertainty bounds. The final mean prediction changes significantly near

the high fidelity data as expected, and the overall inferred uncertainty is reduced by 70.86%. The figure in the top right shows the contours of the final prediction model in percent uncertainty reduction. Again this figure shows that the inferred uncertainty is drastically reduced. A closer look at the figures on the bottom show that the significant changes in the uncertainty bounds are detrimental to the final uncertainty prediction. These two figures show the final prediction given by the MUSIC method from two different perspectives where the black mesh is the truth model, the red mesh is the final mean prediction from MUSIC, and the uncertainty bounds from MUSIC are in represented by the yellow meshes. These figures show that even though the uncertainty bounds are significantly reduced, they are shifted beyond the true function in some places and thus no longer bound the true function. These regions have been circled by red dotted lines.

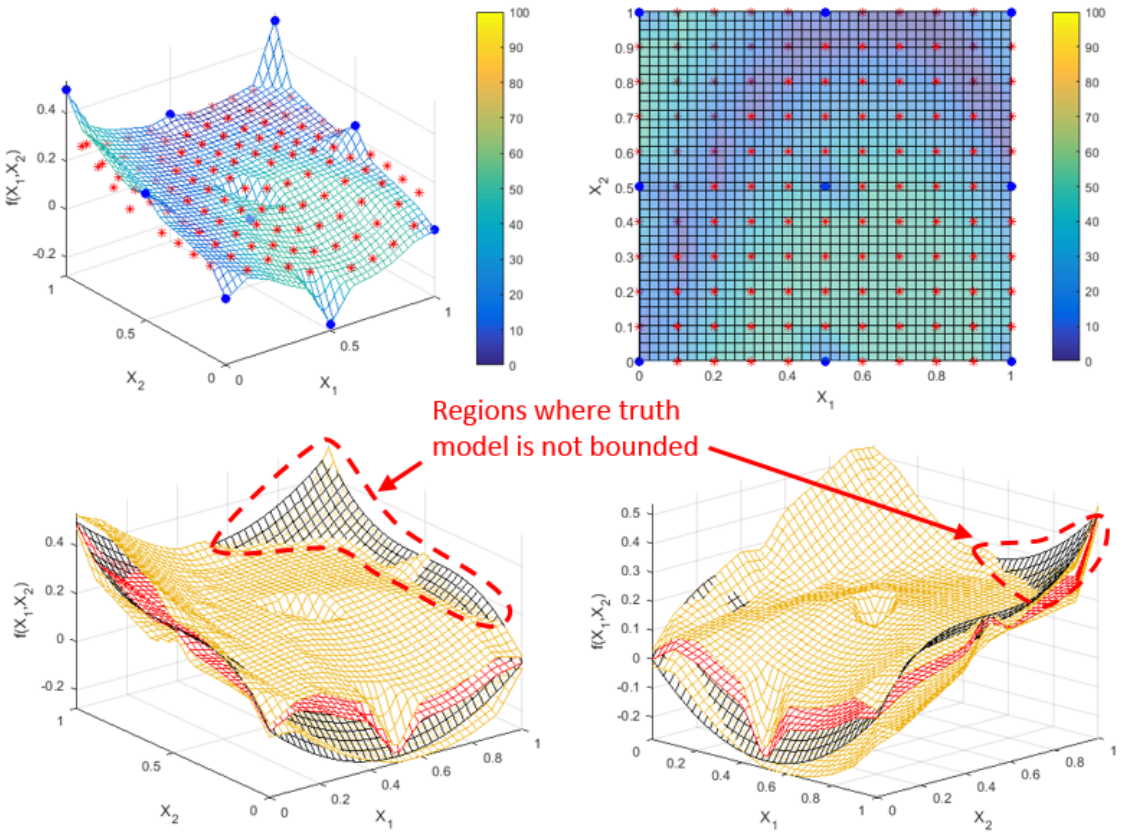

Figure 37: Prediction of the combined data using the linear proximity function.

The results for the squared exponential function with $\theta = 10$ are shown in Figure 38. The figure in the top left shows the final mean prediction colored by the level of uncertainty as a percentage of range of the truth model. Notice how the final mean prediction changes more uniformly compared to the linear proximity function. The uncertainty is reduced significantly, but not as much as the linear proximity function. Even though the uncertainty bounds are not shifted as much compared to the linear function, the figures on the bottom show that squared exponential function with $\theta = 10$ still shifts the bounds beyond the true function in some locations in the design space. These regions have been circled by red dotted lines.

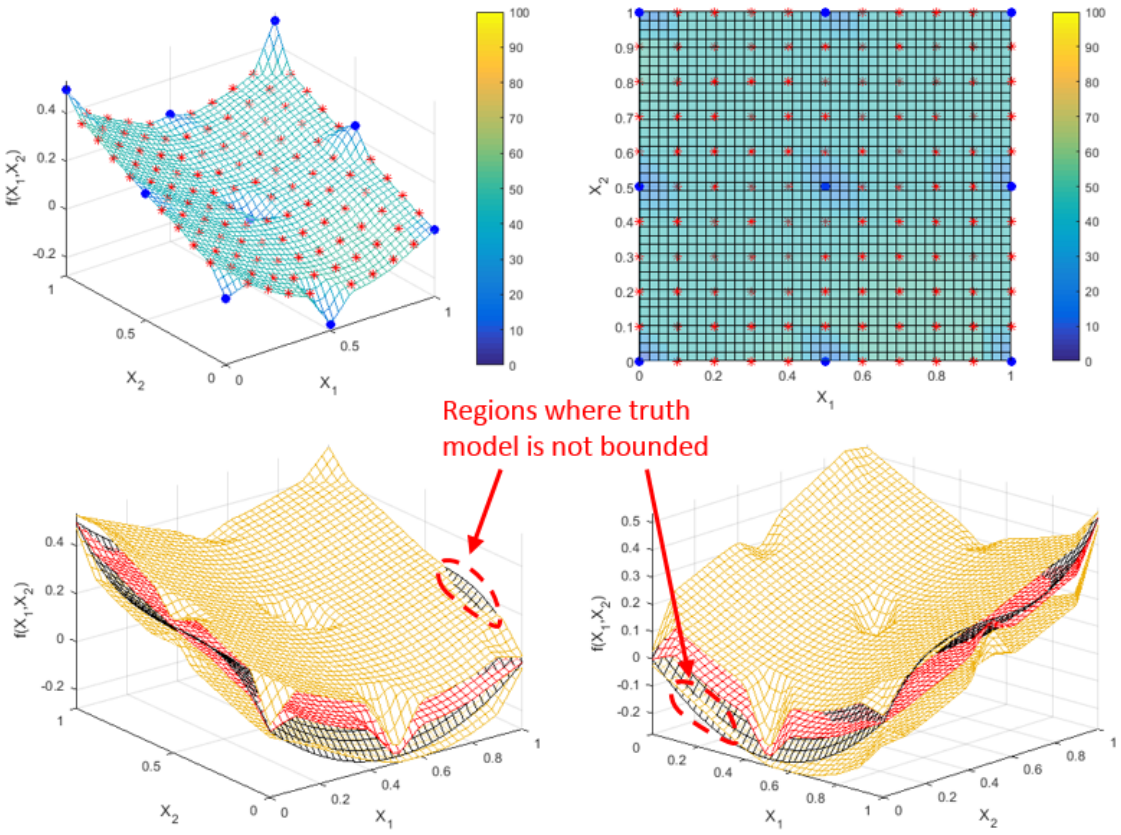

Figure 38: Prediction of the combined data using the square exponential proximity function with $\theta = 10$.

For the squared exponential function with unique θ parameters, the Kriging algorithm found a value for $\theta_1 = 22.94$ and $\theta_2 = 53.65$. The resulting proximity functions

for each dimension are shown in Figure 39. Notice how the proximity functions do not extend nearly as far in the design space compared to the other two proximity functions shown in Figure 33. Also notice that the value for θ_2 is larger than θ_1. This means that the Kriging algorithm is able to correctly determine that there is more nonlinearity in the X_2 dimension with only 6 points. Therefore, the influence of high fidelity data points will not extend as far in the X_2 dimension compared to the X_1 dimension.

The results for the squared exponential function with unique θ parameters are shown in Figure 40. The two figures on top illustrate that the proximity function does not decrease the level of inferred uncertainty as much as the other two proximity functions. However, the two plots on the bottom show that the bounds properly contain the true function throughout the design space. Using proximity functions defined by Kriging algorithm results in a smaller amount of bias because the influence of the high fidelity points does not extend as far in the design space.

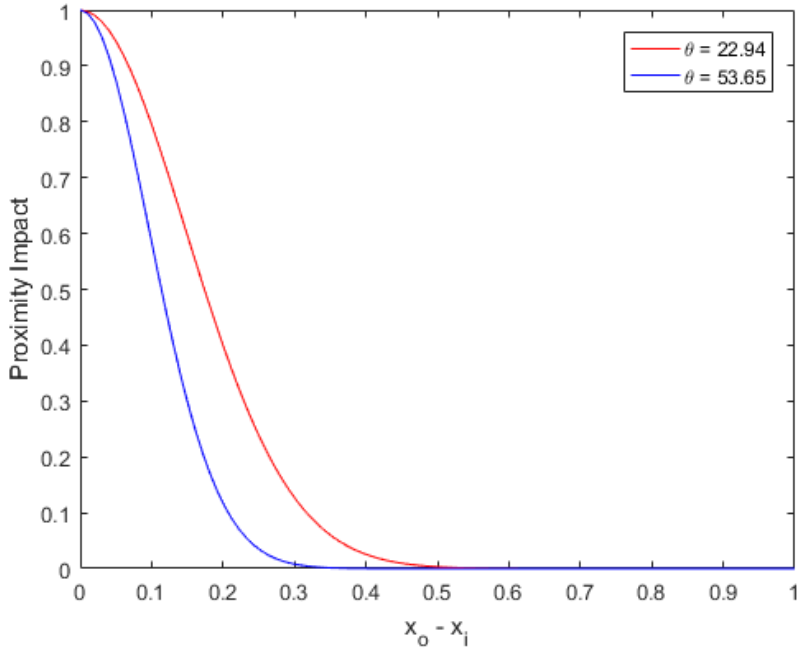

Figure 39: Squared exponential proximity functions with unique θ parameters found using the Kriging algorithm.

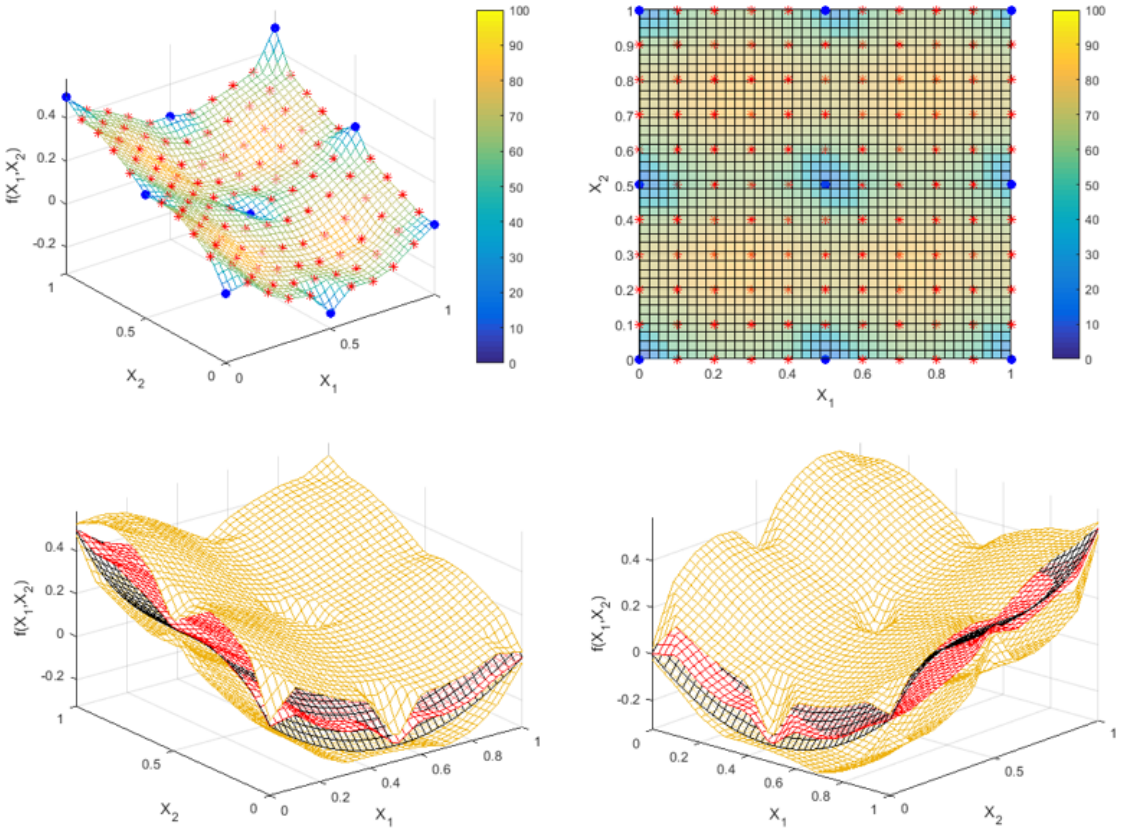

Figure 40: Prediction of the combined data using the square exponential proximity function with a unique θ parameter for each dimension.

5.1.2 Data Set 2

Recall from the experimental description in Section 4.1 that high fidelity experiments are likely to be clustered within the design space. This is due to the fact that high fidelity experiments are expensive, thus models are built so that small changes can be made to individual design variables to obtain some coverage of the design space without building additional models. For example, a wind tunnel model of a new airplane can cost millions of dollars to build. It may only be feasible to build one model, but the model may have interchangeable trailing edges or winglets. Therefore, in the second data set the high fidelity points are clustered in two locations to more realistically represent a high fidelity data set in the design space. The data set is shown in Figure 41 where the red asterisks represent the low fidelity data points and

Table 7: Results for data set 2

Method	Mean MRE	STDev MRE	ΔU
No biasing	2.00%	12.04%	-
Linear	-13.03%	9.51%	-59.01%
SE $\theta = 10$	-8.39%	8.81%	-43.47%
SE unique θ	-3.45%	9.41%	-26.20%

the blue circles represent the high fidelity data points.

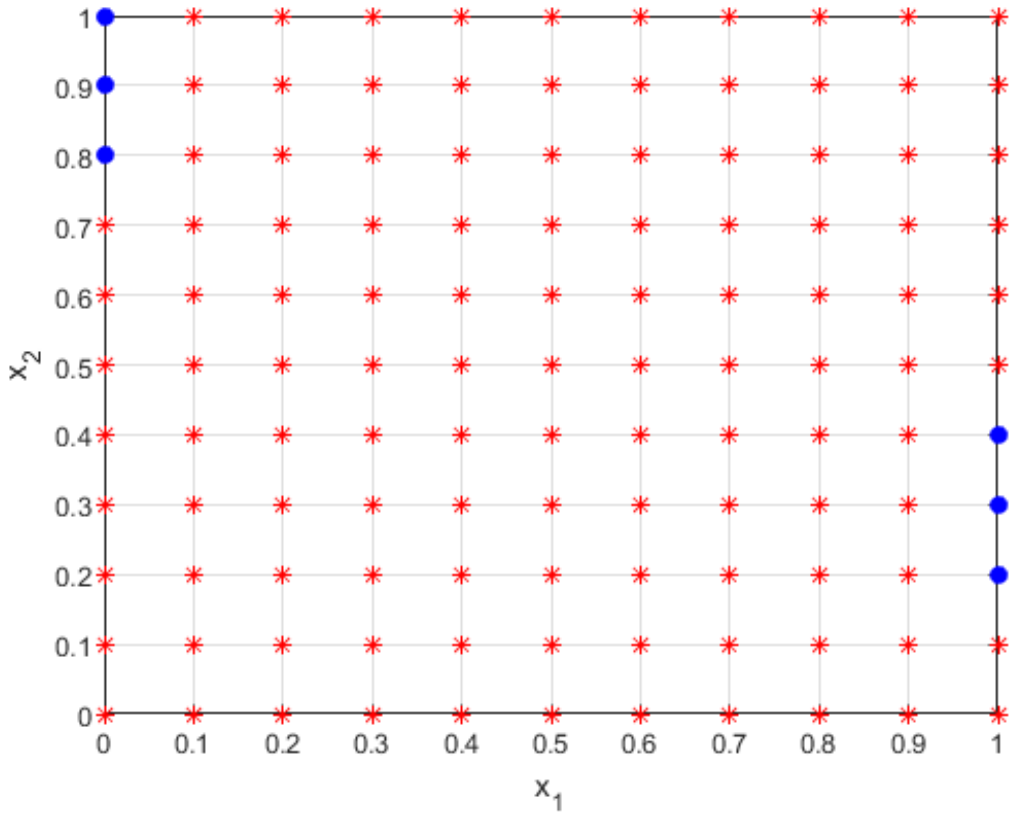

Figure 41: Data set 2.

Table 7 shows the results for the three different biasing methods compared against the low fidelity prediction for the second data set. All three functions reduce the standard deviation, but none of the functions shift the mean closer to 0. However, the shifting of the mean further away from 0 should not be overly scrutinized because it is heavily dependent on the location of the data points. The linear function and the squared exponential function with $\theta = 10$ reduce the uncertainty more compared

to the squared exponential function with unique θ parameters, but they once again shift the bounds such that they no longer contain the true function.

The results for the linear proximity function are shown in Figure 42. The top two plots show the final prediction colored by the level of uncertainty as a percentage of the initial level of uncertainty. The final prediction does a better job of capturing the curvature of the design space compared to the previous data set because the clustering of the high fidelity points gives a better representation of the design space. The linear function again reduced the uncertainty by a large margin, -59.01%. Compared to the previous data set, the linear function does a better job of keeping the true function inside the bounds, but it still fails to capture true function some areas. The red dotted lines in bottom two plots indicate the areas in the design space where the true function is outside of the bounds predicted by MUSIC.

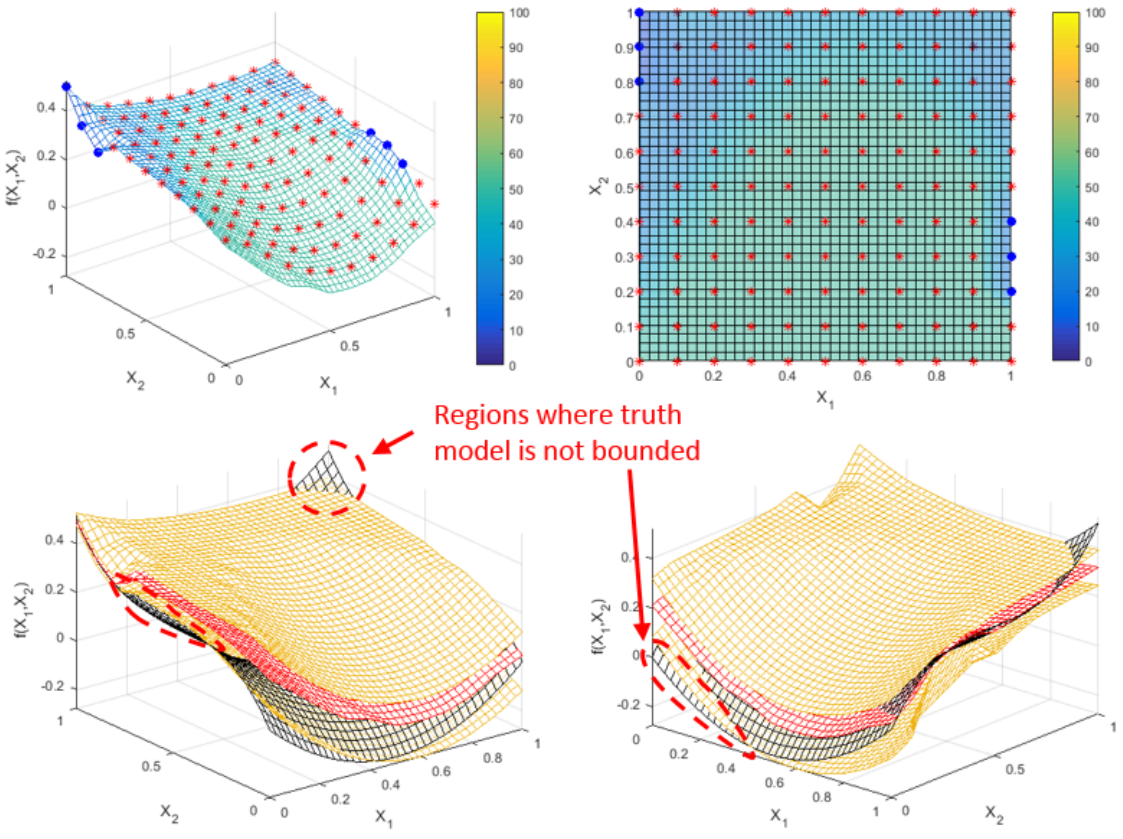

Figure 42: Prediction of the combined data using the linear proximity function.

The results for the squared exponential function with $\theta = 10$ are shown in Figure 43. Notice how once again the uncertainty is not reduced as much as in the linear model, but it does a better job containing the true function within the bounds compared to the linear model.

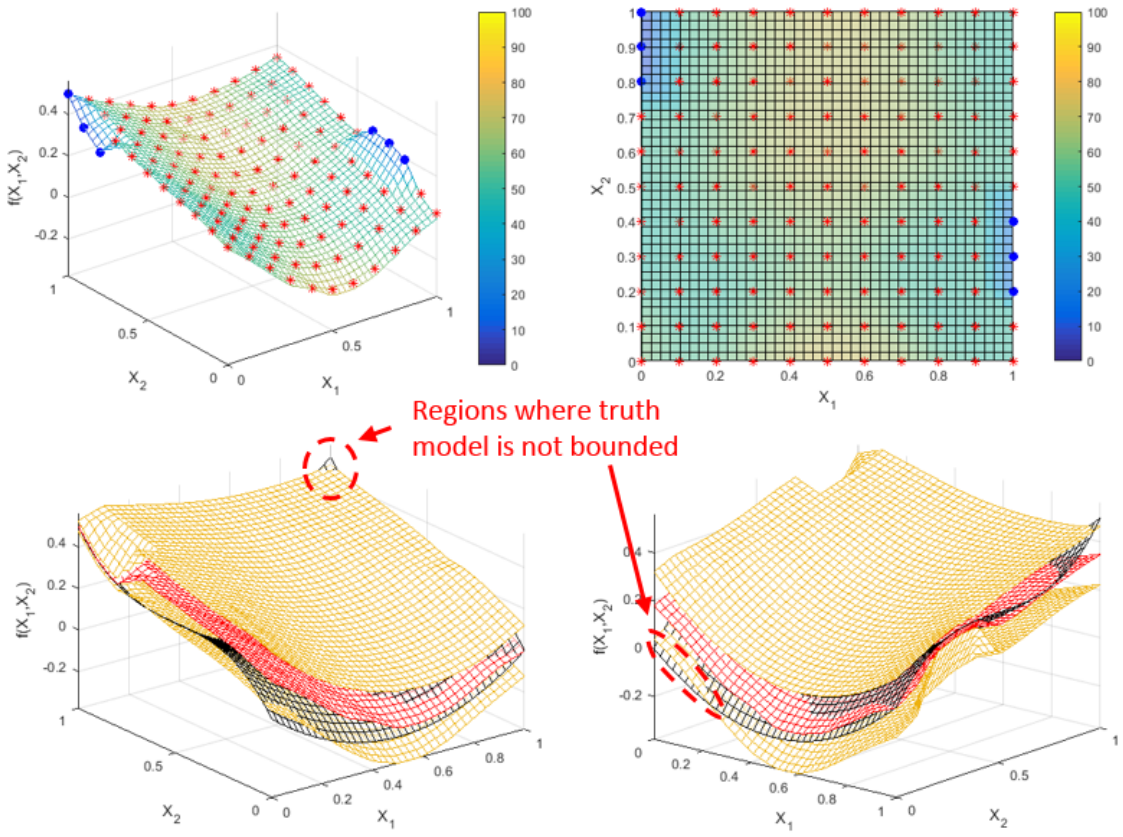

Figure 43: Prediction of the combined data using the square exponential proximity function with $\theta = 10$.

For the squared exponential function with unique θ parameters, the Kriging algorithm found a value for $\theta_1 = 21.37$ and $\theta_2 = 56.84$. The resulting squared exponential functions for each dimension are shown in Figure 44. Notice how much less these proximity function extend into the design space compared to the other proximity function shown in Figure 33. The results shown in Figure 45 show that the proximity function defined by the squared exponential function with unique θ parameter values does not reduce the uncertainty nearly as much as the other two proximity functions.

However, unlike the previous proximity functions, this proximity function is able to contain the true function within the bounds throughout the entire design space.

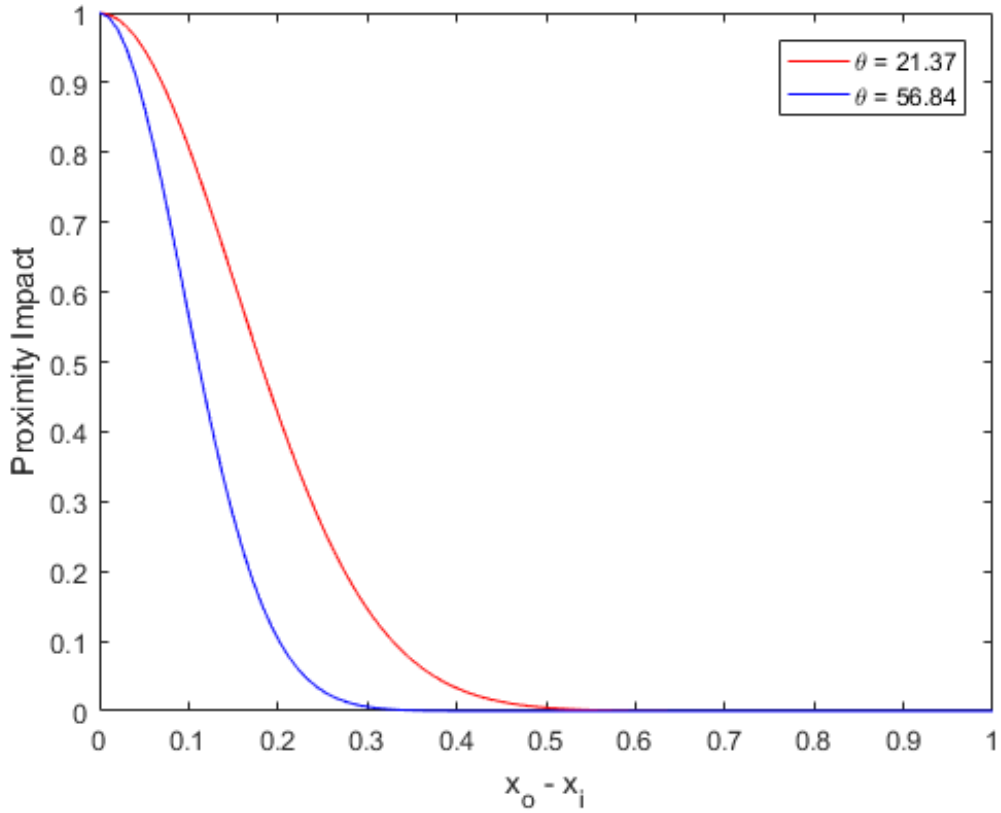

Figure 44: Squared exponential proximity functions with unique θ parameters found using the Kriging algorithm.

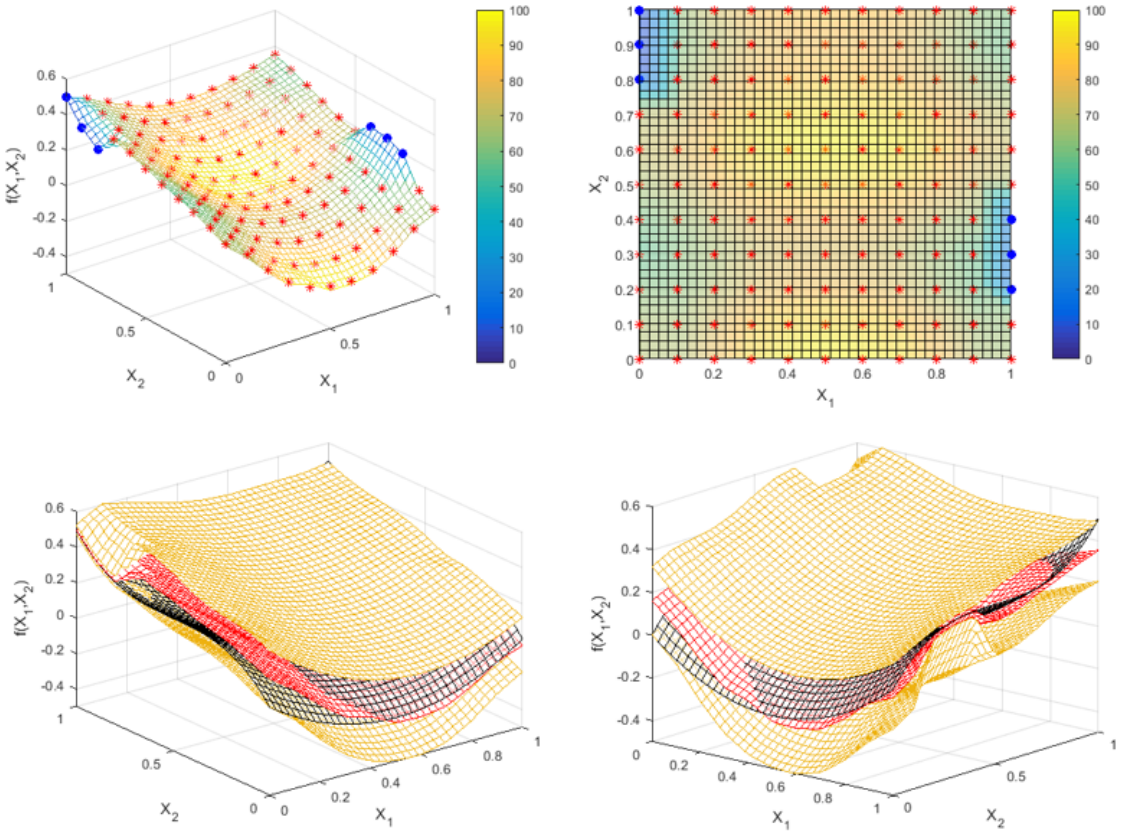

Figure 45: Prediction of the combined data using the square exponential proximity function with a unique θ parameters for each dimension.

5.1.3 Data Set 3

In the final data set the high fidelity points are again clustered in two locations to more realistically represent an expensive high fidelity data set in the design space. The data set is shown in Figure 46.

Table 8 shows the results for the three different biasing methods compared against the low fidelity prediction by for data set 3. Once again, all three functions reduce the

Table 8: Results for data set 3

Method	Mean MRE	STDev MRE	ΔU
No biasing	2.00%	12.04%	-
Linear	-3.81%	7.28%	-37.67%
SE $\theta = 10$	-2.57%	8.38%	-27.14%
SE unique θ	-0.66%	9.98%	-17.06%

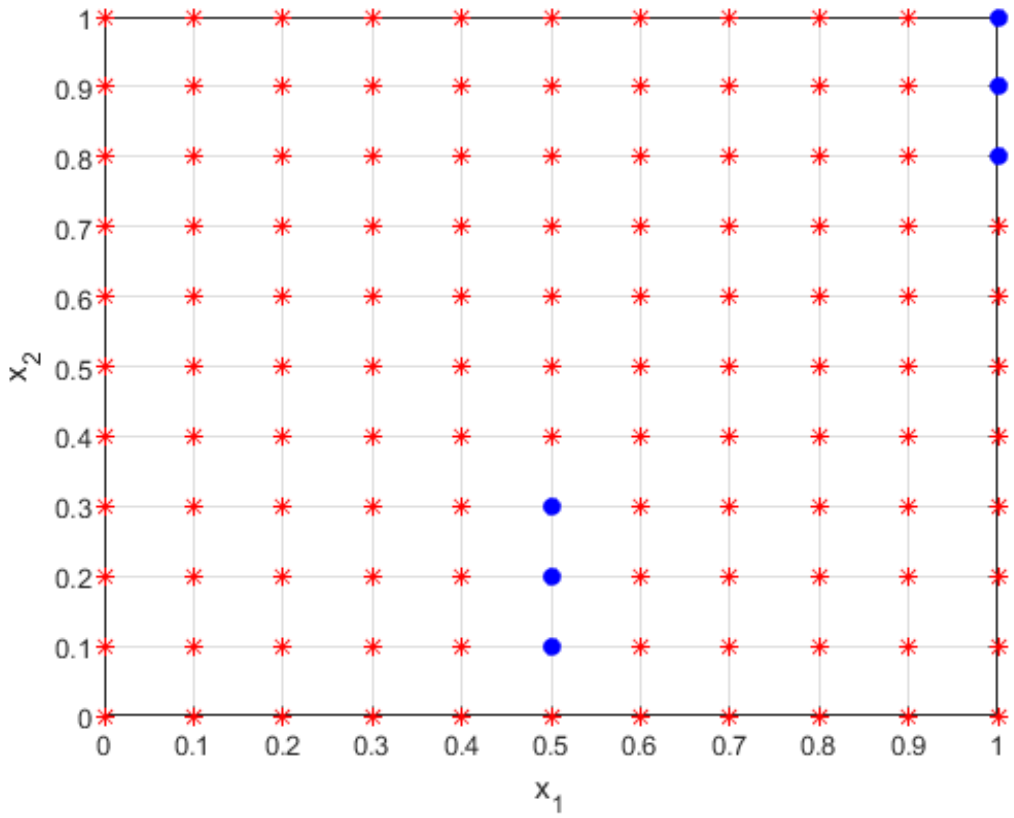

Figure 46: Data set 3. The blue circles are the high fidelity points.

standard deviation. Only the two squared exponential functions shift the mean closer to 0, but again the mean shift is affected more by the location of the points when the data is sparse. The linear function and the squared exponential function with $\theta = 10$ reduce the uncertainty more compared to the squared exponential function with unique θ parameters, but once again this drastic reduction in the level of uncertainty is not necessary a good result.

The results for the linear function are shown in Figure 47. Again the linear proximity function biases the uncertainty bounds to the extent that they no longer bound the true function throughout large portions of the design space. These areas of the design space are indicated by the red dotted lines in the bottom two plots in the figure.

The results for the squared exponential proximity function with $\theta = 10$ are shown

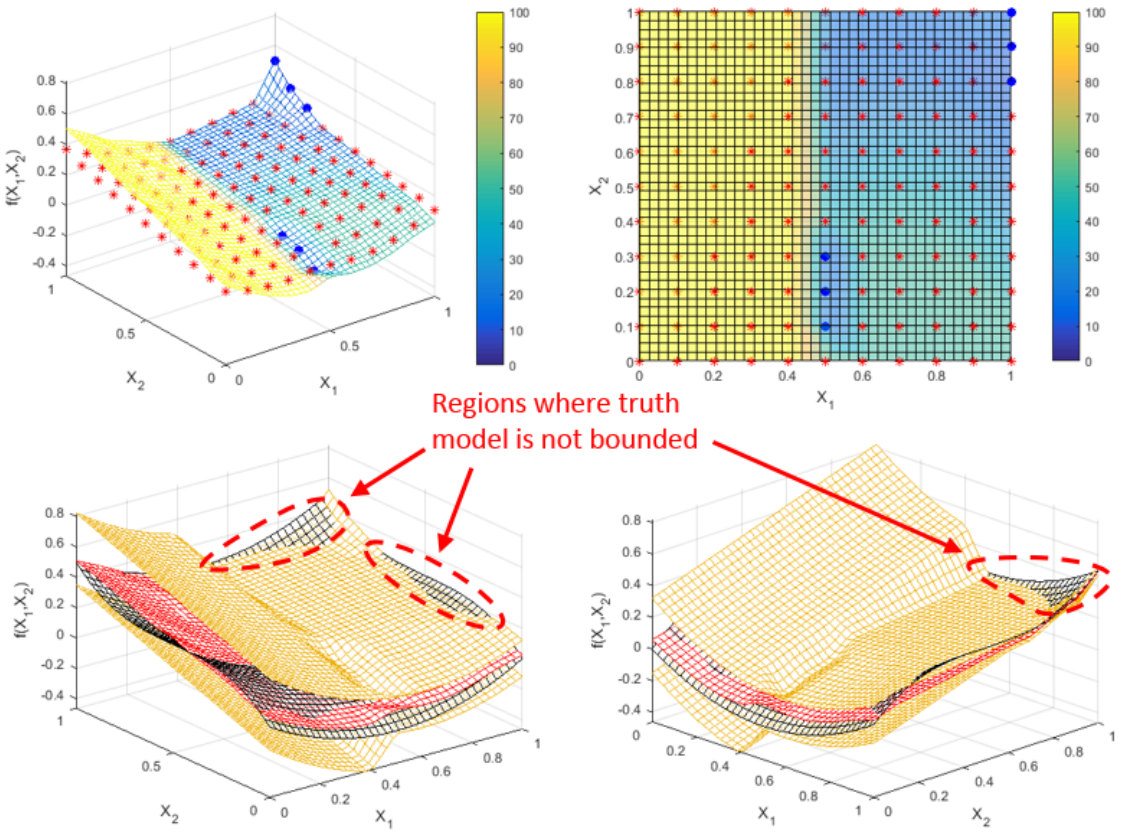

Figure 47: Prediction of the combined data using the linear proximity function.

in Figure 48. Notice how the function does a much better job keeping the true function within the bounds for this particular data set.

For the squared exponential function with unique θ parameters, the Kriging algorithm found a value for $\theta_1 = 51.57$ and $\theta_2 = 29.73$. The resulting square exponential functions for each dimension are shown in Figure 49. Once again the proximity function do not extend throughout the design space as much as the other two proximity functions in Figure 33. However, θ_1 is larger than θ_2 indicating that the Kriging algorithm was not able to correctly determine that the X_2 dimension is more nonlinear than the X_1 dimension. If the engineer does have some general knowledge about the design space, the θ values indicate that additional data is needed for the Kriging algorithm to properly characterize the design space. It is up to the engineer to determine if additional testing should be conducted, or to proceed as normal.

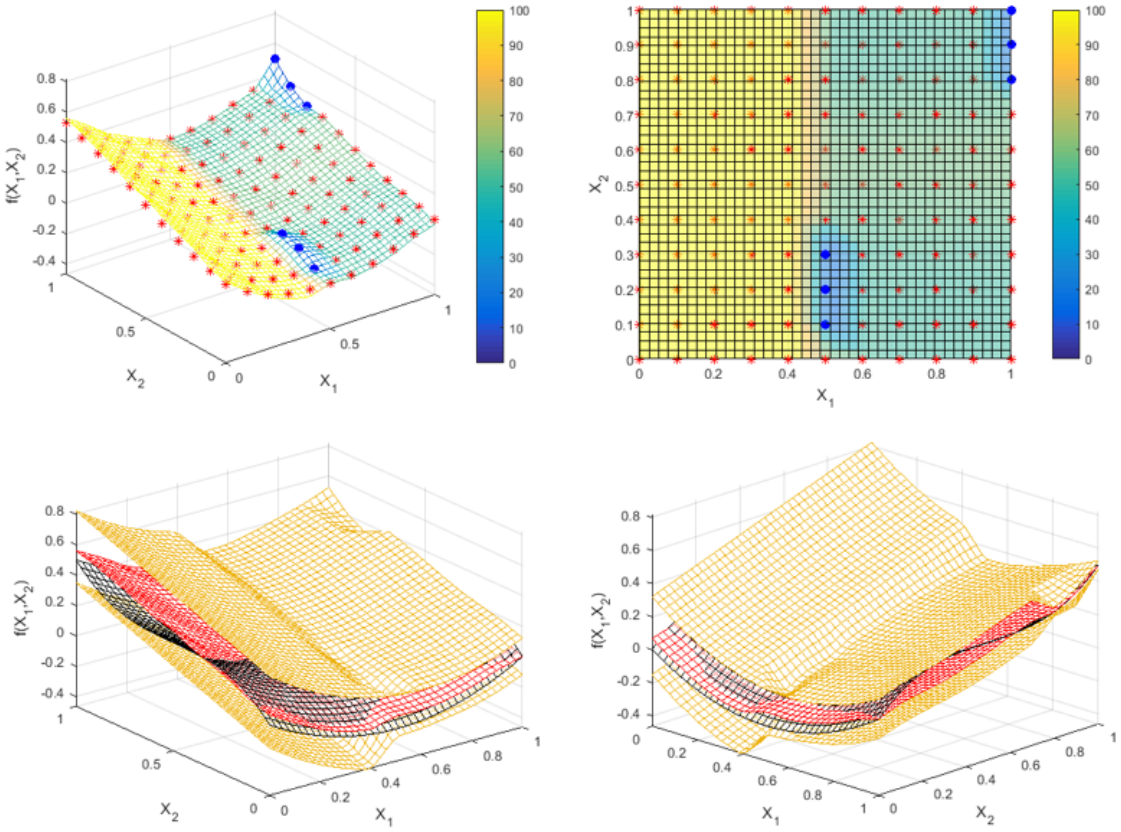

Figure 48: Prediction of the combined data using the square exponential proximity function with $\theta = 10$.

The results shown in Figure 50 once again show that even though this proximity function does not reduce the uncertainty as much as the other two functions, the true function is contained within the bounds.

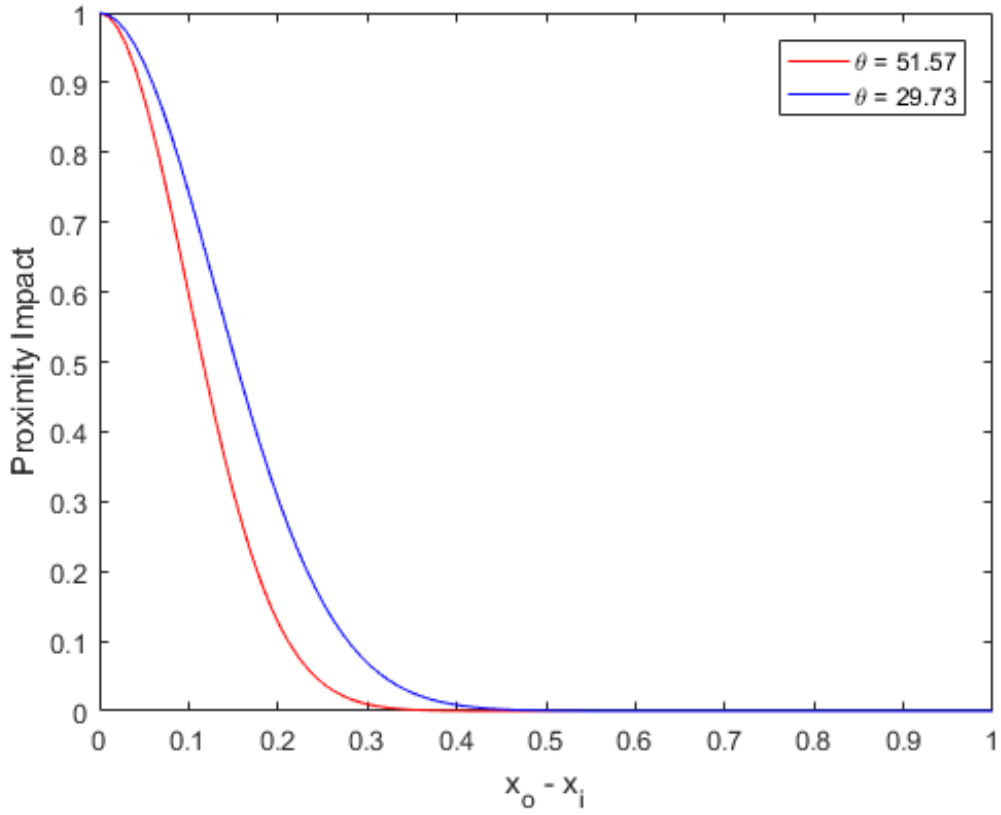

Figure 49: Squared exponential proximity functions with unique θ parameters found using the Kriging algorithm.

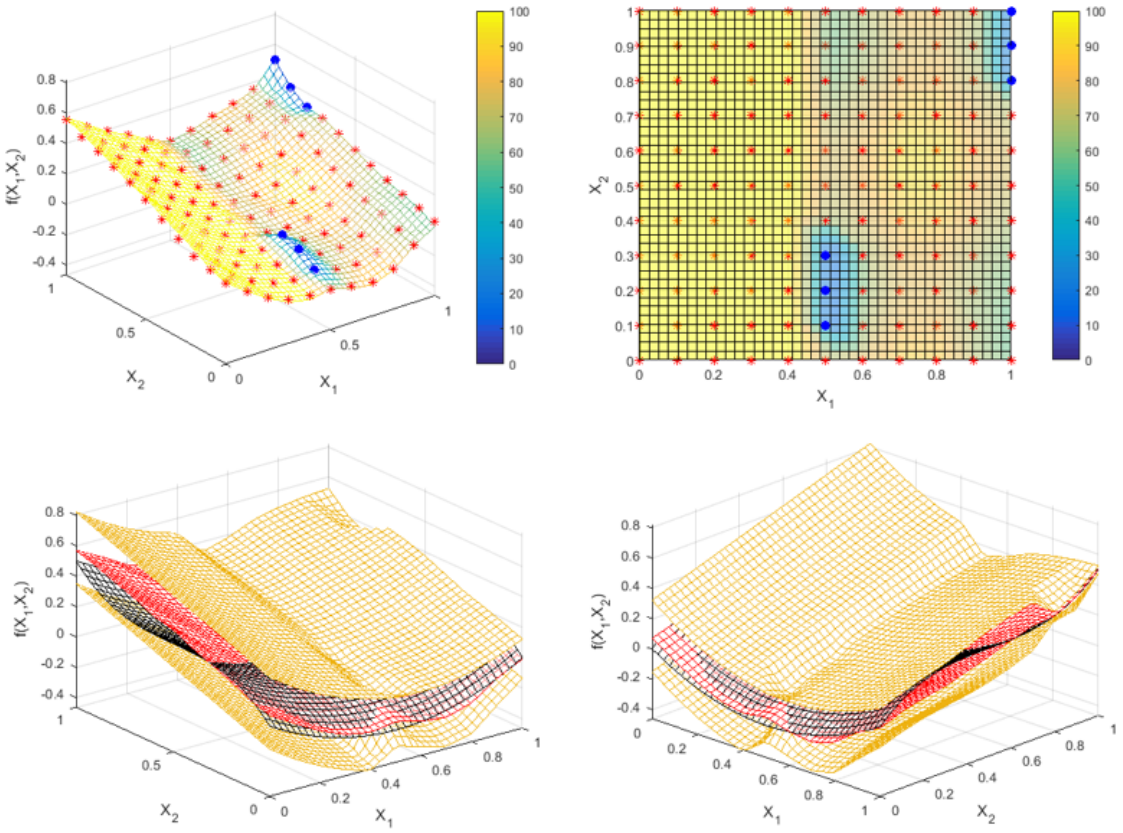

Figure 50: Prediction of the combined data using the square exponential proximity function with a unique θ parameters for each dimension.

5.1.4 Final Observations

The previous sections gave the results for the three different proximity functions tested on three separate data sets. All of the data sets had unique characteristics, but the results show that in all scenarios all three proximity functions successfully reduce the standard deviation of the error. The results also show that the mean of the MRE does not always shift closer toward 0. However, this is not a major concern because the shift in the mean MRE is heavily dependent on the location of the data. On the other hand, the shift in the mean MRE by each proximity function can be compared relative to the other proximity functions. Therefore, it is important to point out that the value for the mean of the MRE for the squared exponential function with unique θ values is closer to 0 compared to the other proximity functions for all three data sets.

Another important observation, and arguably the most important, is the strong tendency of the linear function and the squared exponential function with $\theta = 10$ to bias the distributions an excessive amount. When this occurs the true function no longer remains within the bounds of the prediction. The success of the squared exponential function with the unique θ parameters is due to the fact that the proximity function is scaled by the training data.

The unique θ values found for the first two data sets indicate that the Kriging algorithm was able to correctly determine that the X_2 dimension is more nonlinear than the X_1 dimension. Unfortunately the algorithm was not able to correction determine which dimension is more nonlinear for the third data set. The values for the θ parameters can be used in different ways. If the engineer has some prior knowledge of the design space, unexpected values for the θ parameters could be interpreted as needing more data. If the θ values is small compared to the θ values for the other dimensions (indicating very little change), then the engineer may choose to ignore the dimension with the small θ value. Thus reducing the order of model and simplifying

overall design process. These types of decisions are highly problem dependent and data dependent. The engineer may even choose not to act at all given the values for the θ parameters. It is important to point out that even though the Kriging algorithm is not able to correctly determine which dimension is more nonlinear for the third data set, the MUSIC method still performs well with regard to the important metrics.

The observations from this experiment support the hypothesis that using the Kriging algorithm to set unique scaling parameters for each dimension in the squared exponential function more effectively biases the low fidelity uncertainty distributions.

5.2 Experiment 2 Results

The second experiment in the experimental plan addresses the following research question:

Research Question 2: Does the type of uncertainty distribution used for the low fidelity data sets affect the results given that it can be bounded and it has a unique mode?

Recall, the purpose of the experiment is to compare the triangular and the Weibull distributions to determine if the type of distribution used to define the low fidelity uncertainty affects the results. The biasing process only impacts the mode and bounds; therefore, the following hypothesis was developed:

Hypothesis 2: The specific type of distribution does not have a significant impact on the results as long as it has a unique mode and is bounded.

The same mathematical test function described in Section 4.1 was used for this experiment as well. Figures 51 and 52 show the functions and the initial uncertainty bounds again for reference. The black function is the truth model, the red function is

used to create the low fidelity data sets, and the gold functions represent the initial inferred uncertainty bounds.

The triangular distribution is created the same way as before. The Weibull distribution is created from the triangular distribution for this experiment, by sampling the initial triangular distribution and then fitting a Weibull distribution to the samples to obtain the distribution parameters. This ensures that both distributions have the same mode and bounds. It is also likely that the Weibull distribution would be generated from resulting experimental samples.

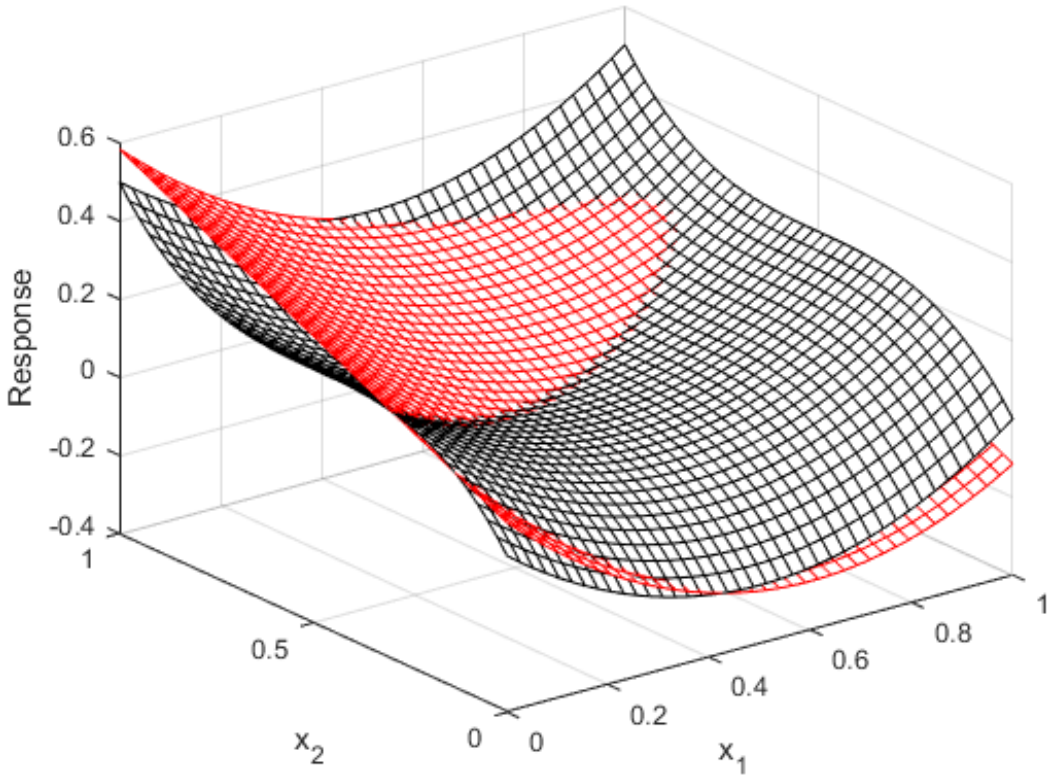

Figure 51: Mathematical functions that are used to generate the high and low fidelity data sets. Black is the truth model and red is the low fidelity function.

Due to the results from the first experiment, the proximity function is now fixed as the squared exponential function with unique θ parameters for each dimension. Additionally, the same three data sets are used to compare the effect of the different

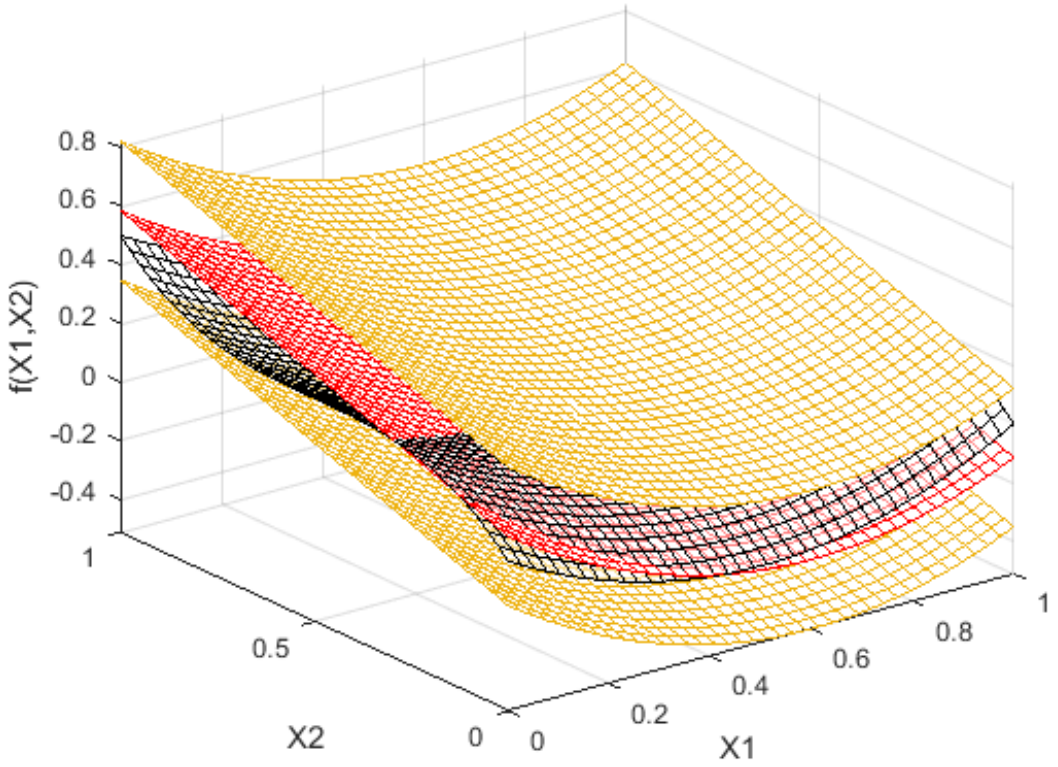

Figure 52: Initial inferred uncertainty bounds on the mathematical functions.

distribution type on the final prediction. The results of this assessment are shown in Table 9.

Table 9: Results for experiment 2: Impact of low fidelity distribution type.

Data Set	Triangular			Weibull		
	Mean MRE	StDev MRE	ΔU	Mean MRE	StDev MRE	ΔU
1	-1.18%	8.16%	-35.19%	-1.13%	8.34%	-34.27%
2	-3.46%	9.41%	-26.20%	-3.18%	9.40%	-25.07%
3	-0.48%	10.00%	-24.43%	-0.03%	9.89%	-23.38%

The results from this experiment show that the mean and standard deviation of the error change by less than 1/2% between the distribution type, and the difference between the change in inferred uncertainty is just over 1% between the distributions. The resulting figures are not shown because the change is negligible compared to those in the first experiment. The difference between the resulting predictions by

each distribution are not large enough to suggest that one type of distribution should be used instead of another. Therefore, the observations from this experiment support the hypothesis that the specific type of distribution used to represent the low fidelity uncertainty does not impact the results as long as it has a unique mode and is bounded.

5.3 Experiment 3 Results: Addition of a Mid Fidelity Level Data Set

Recall that the test case for experiments 3 and 4 is the prediction of the lift coefficient for a swept wing with an infinite span made up of NACA 16-Series airfoils. The three design variables used are the design C_l, Mach number, and angle of attack. The sweep and thickness to chord ratio are held constant at 45^o and 15% respectively. The low fidelity data set is generated using the Prandtl-Glauert equation (Equation 40) which used the Prandtl-Glauert compressibility correction.

The mid fidelity data set is generated using the Kuchemann equation (Equation 41) which adds a sweep correction to the Prandtl-Glauert equation. The computer software Xfoil is used to generate the high fidelity data set. Xfoil is a panel method code with the option to use viscous boundary layer methods to capture the viscosity. The software also uses the Karmen-Tsien compressibility correction which performs better compared to the Prandtl-Glauert correction at high subsonic Mach numbers[7]. Xfoil is two-dimensional; therefore, the Mach number given to the code is corrected for sweep i.e. $\text{Mach}_{\text{loc}} = \text{Mach}_{\infty} \cos \Lambda$. Wind Tunnel data for the NACA 16-series airfoils from Lindsey et al. is used for validation[67]. The error between the validation data and the individual data sets is used to define the upper and lower bounds of the uncertainty distributions for each data set. The uncertainty values defined from the error are shown in Table 10. Refer back to Section 4.3 for more details on the prediction of the lift coefficient of a infinite span swept wing section.

Table 10: Uncertainty bounds for each data set defined as the maximum amount of error between the data set and the validation data

Data Set	Uncertainty Bounds
Low Fidelity	+/- 1.23
Mid Fidelity	+/- 0.34
High Fidelity	+/- 0.15

Table 11: Low fidelity data set

Design C_l	Mach number	Angle of Attack
0.1 - 0.7	0.4 - 0.7	-6^o - 12^o
step = 0.1	step = 0.1	step = 2^o

5.3.1 Part 1: Including a Mid Fidelity Level Data Set

The purpose of part 1 of experiment 3 is to determine the impact of a mid fidelity level data set. This question came about because the author realized that there could be a potential problem with the method if there are more than two data sets. It is expected that including a mid fidelity level data set will improve the final prediction because knowledge is being added. Therefore, the following question and hypothesis will be tested in part 1 of this experiment.

Research Question 3.1: Will the addition of a mid fidelity level data set further improve the final uncertainty characterization?

Hypothesis 3.1: Including a mid fidelity level data set will improve the final uncertainty characterization.

The Prandtl-Glauert equation (Equation 40) is quick to run, and thus can blanket the entire design space. Table 11 shows the details of the input variable ranges and their corresponding step size which results in a total of 200 low fidelity level data points.

Next, two separate high fidelity data sets are created using Xfoil with 38 data points in each. The details of the high fidelity data sets are shown in Table 12.

Table 12: High fidelity data sets

Data Set	Design C_l	Mach number	Angle of Attack
Set 1	0.1	0.4, 0.6	-4^o - 12^o
	0.7	0.5, 0.7	-4^o - 12^o
Set 2	0.3	0.4, 0.6	-4^o - 12^o
	0.7	0.5, 0.7	-4^o - 12^o

The experiment is conducted in a manner that is meant to emulate the most likely way the MUSIC method would be used in the real world, where only a small number of high fidelity data points are available, yet low fidelity simulations can blanket the entire design space. After some initial predictions are made, additional data is gathered to gain knowledge in the weak areas of the design space. The same metrics used in the previous experiments will also be used to evaluate the current experiment. Recall that γ is the ratio of the number of validation points outside of the final predicted uncertainty bounds to the total number of validation points. The average amount of inferred uncertainty is normalized by the initial low fidelity uncertainty. This is why the average level of uncertainty for the low fidelity prediction is always 100%. Note that the population of the combined data set for both test cases will remain at 200 because the high fidelity data overlaps the low fidelity data, and as a result, those specific low fidelity data points are discarded.

5.3.1.1 Results Using High Fidelity Data Set 1

The results for the low fidelity data prediction by itself and the MUSIC method using the first high fidelity data set to bias the low fidelity data are shown in Table 13. The results show that the MUSIC method drastically improves upon the low fidelity

Table 13: Results for data set 1 without the addition of a mid fidelity level data set.

	LF Prediction	MUSIC
Mean MRE	27.33%	-12.20%
STDev MRE	26.56%	11.00%
AVG Inferred Uncertainty	100%	26.10%
γ	-	15/97

prediction. The MRE mean and standard deviation are improved by more than 50% and the average level of the inferred uncertainty is decreased by almost 75%. The MUSIC method captures a majority of the validation points, but it misses 15 out of the 97 validation points.

A post processing code for the MUSIC methodology searches through the final prediction and determines the areas in the design space with the largest amount of uncertainty. The code found that the uncertainty is highest when the design lift coefficient is equal to 0.5. Figure 53 shows two plots of final prediction from MUSIC of the lift coefficient as a function of Mach number and angle of attack at a design lift coefficient of 0.5. The plot on the left shows the mean of the prediction in gray and the overall uncertainty bounds in yellow. Notice how the uncertainty bounds spread away from each other as the Mach number and angle of attack increase. The figure on the right again shows the mean of the prediction, except that this time it is colored by the level of uncertainty. The color bar to the right indicates how the color of the plot changes in terms of percent uncertainty. Recall that 100% uncertainty means no change from the initial low fidelity uncertainty bounds.

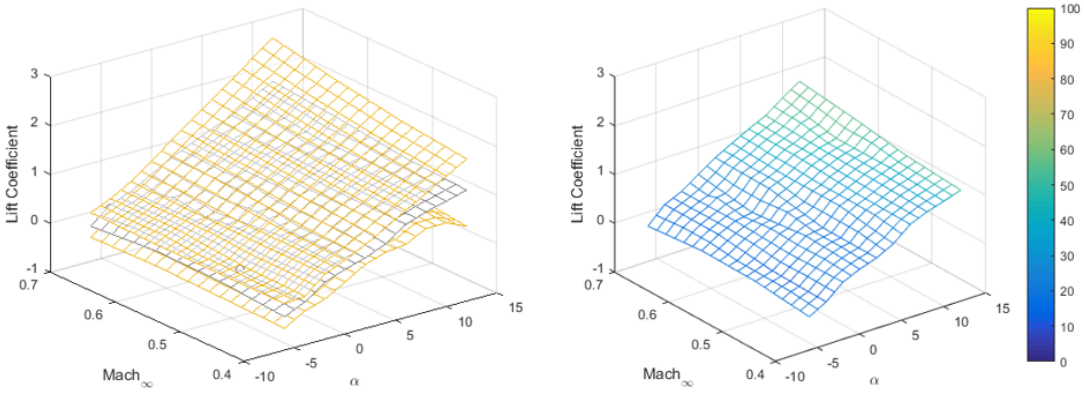

Figure 53: Prediction for the lift coefficient of a wing section as a function of Mach number and angle of attack at a constant design $C_l = 0.5$

A slice of the plots shown in Figure 53 at a Mach number of 0.7 is shown in Figure 54. The initial low fidelity prediction is shown in red with the initial low

fidelity bounds in green. The mean prediction from MUSIC is represented by the black line and the inferred uncertainty bounds from MUSIC are shown in yellow. The black circles are the validation data points. Notice how the mean prediction from MUSIC does a better job of capturing the validation data compared to the low fidelity prediction alone. Also notice how the inferred uncertainty bounds from MUSIC are much narrower compared to the initial low fidelity bounds. In addition, the level of inferred uncertainty increases with angle of attack. This is expected because the design space gets more complicated as the angle of attack increases.

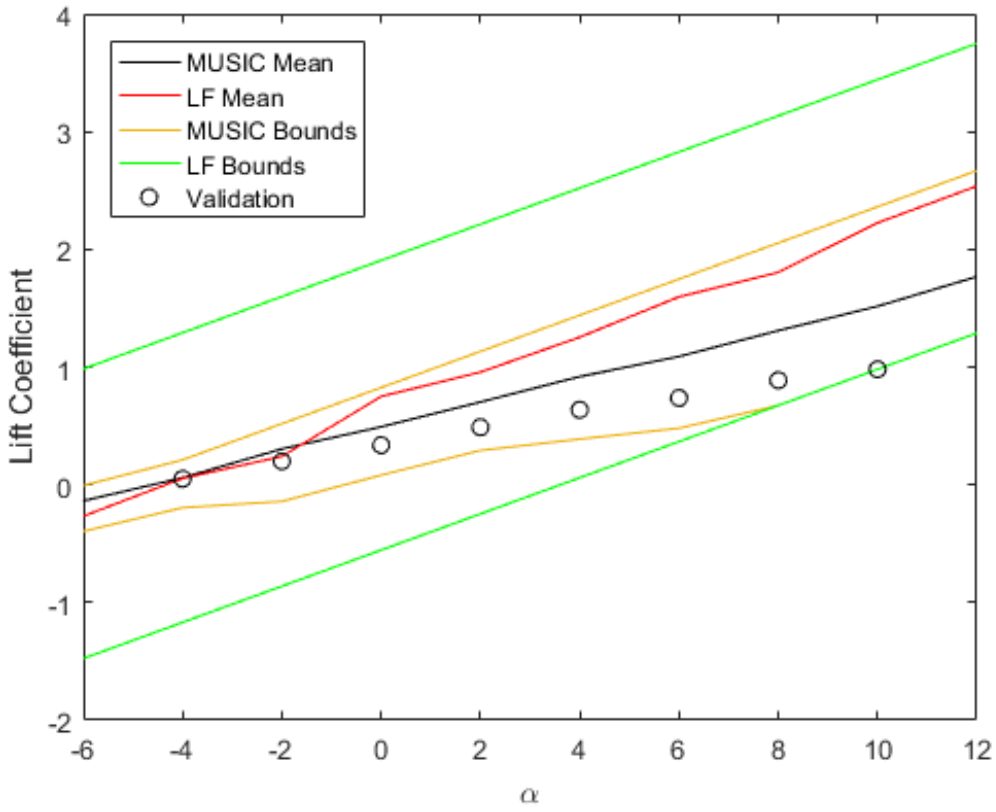

Figure 54: Prediction for the lift coefficient of a wing section as a function of angle of attack at design $C_l = 0.5$ and $M_\infty = 0.7$

The reason for showing this specific area of the design space is because the post processing code identified the area when the design lift coefficient is equal to 0.5 as a location where the model is weak. For this research weak means there is a high

level of inferred uncertainty. For the sake of this experiment imagine that a decision maker does not have enough resources to conduct high fidelity simulations in this area, but there are enough resources to conduct mid fidelity level experiments. Therefore, 40 mid fidelity simulations are run at the locations shown in Table 14. Once again the mid fidelity points overlap with the low fidelity points, so the population of the combined data set will remain at 200. The results for this test set with the addition of

Table 14: Mid fidelity level data set 1

Design C_l	Mach number	Angle of Attack
0.5	0.4 - 0.7	-6^o - 12^o
	step = 0.1	step = 2^o

the mid fidelity data are shown in Table 15. The results for the low fidelity prediction alone and the MUSIC method without the mid fidelity level data set are included in the table as well. The results show that the addition of the mid fidelity level data set improves the final prediction for every metric. Most importantly, the level of inferred uncertainty decreases to 21.71% and the number of validation points outside of the bounds decreases from 15 to 10 out of 97. Figure 55 shows a comparison of the

Table 15: Results for data set 1 including the mid fidelity level data set.

	LF Prediction	MUSIC	MUSIC with MF
Mean MRE	27.33%	-12.20%	-9.31%
STDev MRE	26.56%	11.00%	10.15%
AVG Inferred Uncertainty	100%	26.10%	21.71%
γ	-	15/97	10/97

MUSIC method results with and without the addition of the mid fidelity level data set. The two plots on top show the results for the MUSIC method without the mid fidelity level data set while the plots on the bottom show the results from the MUSIC method including the mid fidelity level data set. Referring to the three dimensional plots on the left, the level of inferred uncertainty increases with angle of attack and Mach number for the plot without the mid fidelity level data set. Notice how the

addition of the mid fidelity level data set decreases the level of inferred uncertainty at the higher angles of attack and Mach number.

The plots on the right side of the figure are slices from the plots on the left at Mach 0.7. A comparison of these two plots clearly shows that including the mid fidelity level data set improved the mean prediction as well as decreased the level of inferred uncertainty.

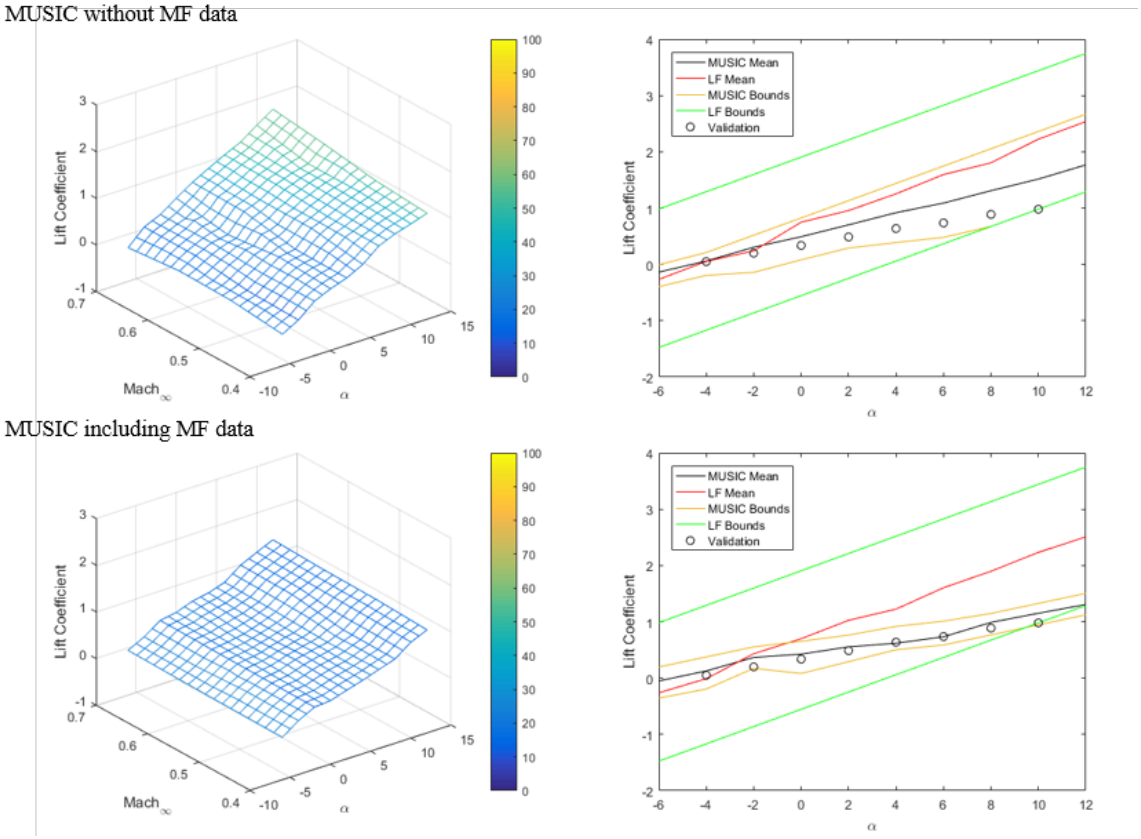

Figure 55: Plots of the prediction of lift coefficient of a wing section comparing the results from the MUSIC method with and without a mid fidelity level data set.

5.3.1.2 Results Using High Fidelity Data Set 2

Recall that the difference between the first and second high fidelity data sets is that the second high fidelity data set has data at design lift coefficient equal to 0.3 instead of 0.1. This means that MUSIC method is forced to extrapolate beyond the bounds of the high fidelity data. The results for the low fidelity data prediction by itself and

the MUSIC method using the second high fidelity data set to bias the low fidelity data are shown in Table 16. The results show that the MUSIC method again significantly

Table 16: Results for data set 2 without the addition of a mid fidelity level data set.

	LF Prediction	MUSIC
Mean MRE	27.33%	-13.57%
STDev MRE	26.56%	13.58%
AVG Inferred Uncertainty	100%	44.46%
γ	-	16/97

improves upon the low fidelity prediction. The MRE statistics and the level of inferred uncertainty are improved by more than 50%. The MUSIC method captures a majority of the validation points, but it misses 16 out of the 97 validation points. Looking back at the results for date set 1 in Table 13, notice that the results for data set 2 are not as good compared to data set 1. The reason for this is because of the constraint put on MUSIC that does not allow the uncertainty bounds to be biased in the extrapolated regions of the data set. Since the high fidelity data in set 2 does not include results below a design lift coefficient equal to 0.3, there is a large region of the design space where the MUSIC method is extrapolating. See Section 3.3 for a review of the constraints.

The post processing code found that the uncertainty is highest in the region of the design space where the design lift coefficient is equal to 0.1. However, this is not surprising because the constraint will not allow the bounds to be biased in that region. Figure 56 shows two plots of final prediction from MUSIC of the lift coefficient as a function of Mach number and angle of attack at a design lift coefficient of 0.1. The plot on the left shows the mean of the prediction in gray and the overall uncertainty bounds in yellow. The black circles are the validation data points. Notice how the distance between the uncertainty bounds is constant because of the constraint. The figure on the right again shows the mean of the prediction, except that this time it is colored by the level of uncertainty. The color bar to the right indicates how the color

of the plot changes in terms of percent uncertainty. Recall that 100% uncertainty means no change from the initial low fidelity uncertainty bounds. Once again, due to the constraint on the uncertainty bounds, the color of the mean prediction is bright yellow throughout the entire plot because there is no change in the bounds.

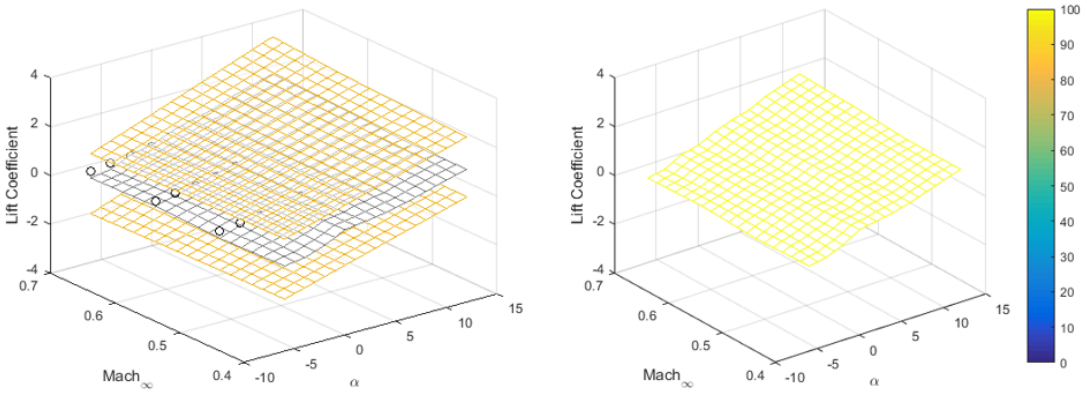

Figure 56: Prediction for the lift coefficient of a wing section as a function of Mach number and angle of attack at a constant design $C_l = 0.1$

A slice of the plots shown in Figure 56 at a Mach number of 0.7 is shown in Figure 57. The initial low fidelity prediction is shown in red with the initial low fidelity bounds in green. The mean prediction from MUSIC is represented by the black line and the black circles are the validation data points. The inferred uncertainty bounds from MUSIC are covered by the initial low fidelity bounds in green. Even though the uncertainty bounds are not allowed to be biased in the extrapolated regions of the space, the mode is allowed to be biased. Notice how the mean prediction from MUSIC does a better job of capturing the validation data compared to the low fidelity prediction alone.

The reason for showing these plots is because the area of the design space where the design lift coefficient is equal to 0.1 has been identified as a location where the model is weak, i.e. where there is a high level of inferred uncertainty. Once again imagine that a decision maker does not have enough resources to conduct high fidelity simulations in this area, but there are enough resources to conduct mid fidelity level

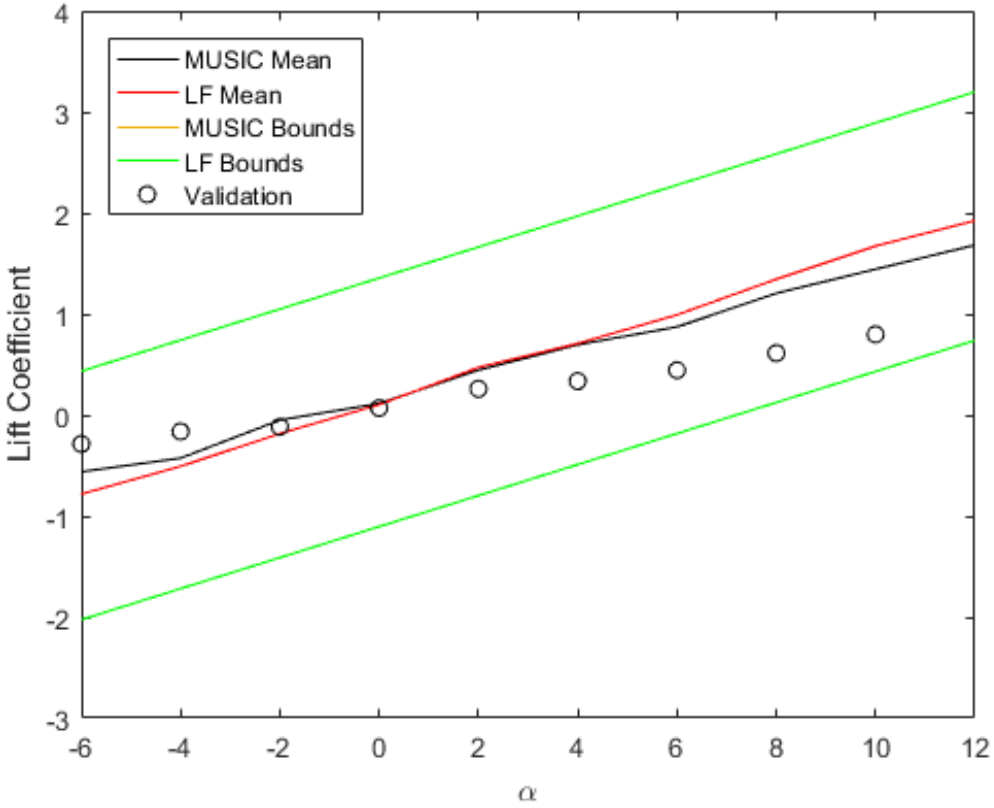

Figure 57: Prediction for the lift coefficient of a wing section as a function of angle of attack at design $C_l = 0.1$ and $M_\infty = 0.7$

experiments. Therefore, 40 mid fidelity simulations are run at the locations shown in Table 17. Once again the mid fidelity points overlap with the low fidelity points, so the population of the combined data set remains at 200. The results for this test

Table 17: Mid fidelity level data set 2

Design C_l	Mach number	Angle of Attack
0.1	0.4 - 0.7 step = 0.1	-6^o - 12^o step = 2^o

set with the addition of the mid fidelity data are shown in Table 18. The results for the low fidelity prediction alone and the MUSIC method without the mid fidelity level data set are included in the table as well. The results show that the addition of the mid fidelity level data set improves the final prediction for every metric. Most

importantly, the level of inferred uncertainty decreases to 25.25% and the number of validation points outside of the bounds decreases from 16 to 11 out of 97. The addition of the mid fidelity level data set on the second set of data had a more significant impact on the results because the mid fidelity level data was added into the extrapolated region.

Table 18: Results for data set 2 including the mid fidelity level data set.

	LF Prediction	MUSIC	MUSIC with MF
Mean MRE	27.33%	-13.57%	-10.44%
STDev MRE	26.56%	13.58%	9.93%
AVG Inferred Uncertainty	100%	44.46%	25.25%
γ	-	16/97	11/97

Figure 58 gives a comparison of the MUSIC method results with and without the addition of the mid fidelity level data set. The two plots on top show the results for the MUSIC method without the mid fidelity level data set while the plots on the bottom show the results from the MUSIC method including the mid fidelity level data set. Referring to the three dimensional plots on the left, the level of inferred uncertainty is drastically reduced by the addition of the mid fidelity level data set in the extrapolated region of the design space.

The plots on the right side of the figure are slices from the plots on the left at Mach 0.7. A comparison between these two plots clearly shows that including a mid fidelity level data set improved the mean prediction as well as decreased the level of inferred uncertainty.

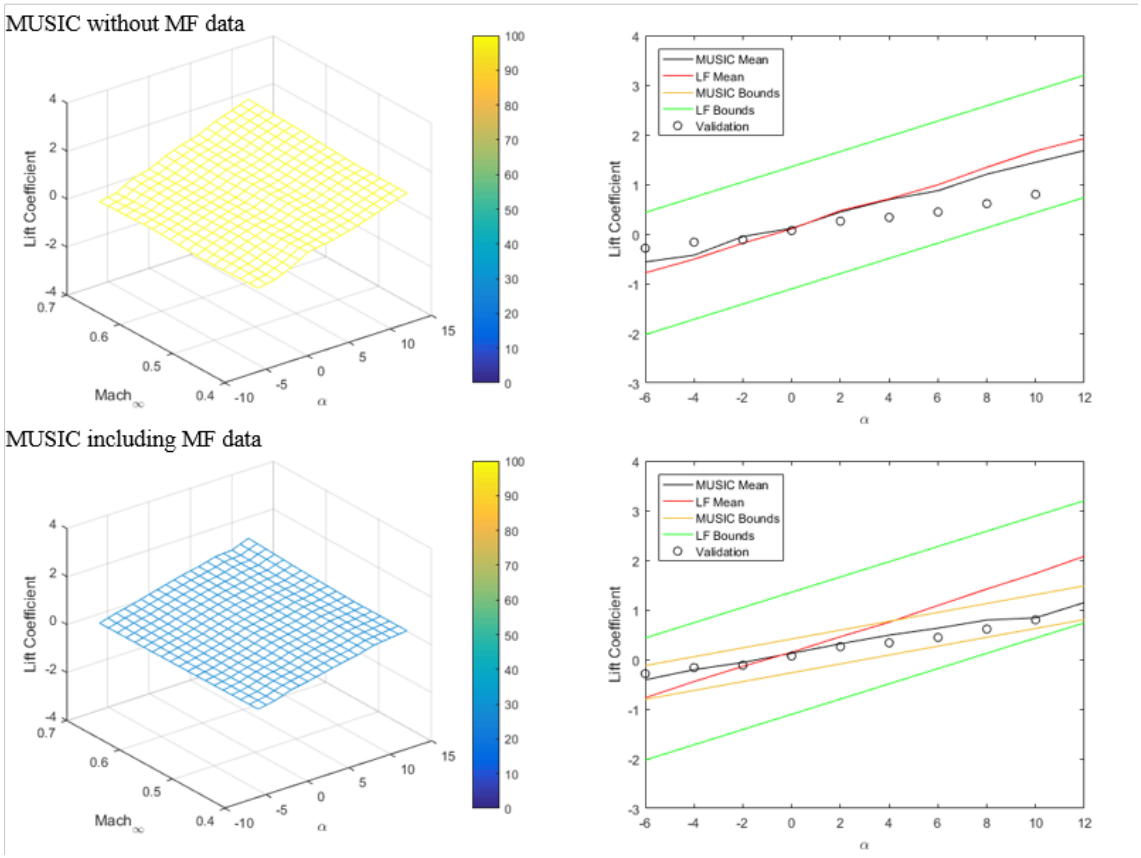

Figure 58: Plots of the prediction of lift coefficient of a wing section comparing the results from the MUSIC method with and without a mid fidelity level data set.

5.3.1.3 Final Observations From Part 1 of the Experiment

This first portion of the experiment tested two separate data sets to determine how the MUSIC methodology would handle the addition of a mid fidelity level data set within the bounds of the high fidelity data and in an extrapolated region beyond the bounds of the high fidelity data. The results from both data sets support the hypothesis that including a mid fidelity level data set will improve the final uncertainty characterization.

5.3.2 Part 2: Bias Weight Factor Study

The results from the previous section show that the addition of a mid fidelity level data set significantly improves the results. This next section of the experiment is

designed to determine if additional changes need to be made to the biasing process regarding how the mid fidelity level data set biases the low fidelity data. The following research question and hypothesis will be addressed.

Research Question 3.2: By introducing the mid fidelity level data set, do changes need to be made to the existing biasing process?

Hypothesis 3.2: If the final results are sensitive to a weight factor, then a fidelity level weight function needs to be developed.

Recall from Equation 43 from Section 4.3.1 that a weight factor is applied to the mid fidelity level data set to test the sensitivity of the results. The equation is repeated below.

$$B_{L_o} = U_{L_o}\left[\sum_{i=1}^{n} B_{H_i} + \left(\sum_{j=1}^{k} B_{M_j}\right) W_M\right]$$

where W_M is the mid fidelity level weight factor. To test the sensitivity, the weight factor is changed from 0 to 1 in increments of 0.25. Note that a weighting of 0 means that the data has no impact on the low fidelity data and is treated as if it is an additional low fidelity data set with different uncertainty bounds. A weight factor of 1 means that the data has the same impact on the low fidelity data as the high fidelity data set except that it has different uncertainty bounds. The results of the sensitivity test for the first data set are shown in Table 19. The results without the mid fidelity data set are repeated in column 1 for reference.

Table 19: Sensitivity results for data set 1 with the addition of 40 mid fidelity points at a design $C_l = 0.5$ at the full range of Mach numbers and angles of attack.

Scale factor	no MF data	0	0.25	0.50	0.75	1
Bias MRE	-12.20%	-9.26%	-9.28%	-9.28%	-9.29%	-9.31%
STDev MRE	11.00%	10.15%	10.15%	10.15%	10.15%	10.15%
AVG inferred U	26.10%	21.69%	21.71%	21.71%	21.72%	21.71%
γ	15/97	10/97	10/97	10/97	10/97	10/97

The results in Table 19 show that the addition of the mid fidelity data points improves the model with regard to the error statistics and the level of inferred uncertainty; however, these metrics show almost no sensitivity to the weight factor. In fact, the MRE standard deviation and the number of validation points outside of the bounds do not change at all.

The same sensitivity study is repeated for data set 2. The results are shown in Table 20. The initial results without the additional mid fidelity points are again shown in the first column for reference.

Table 20: Weight factor sensitivity results for data set 1 with the addition of 40 mid fidelity points at a design $C_l = 0.5$ at the full range of Mach numbers and angles of attack.

Scale factor	no MF data	0	0.25	0.50	0.75	1
Bias MRE	-13.57%	-10.92%	-10.73%	-10.60%	-10.50%	-10.44%
STDev MRE	13.58%	10.27%	10.15%	10.02%	9.96%	9.93%
AVG inferred U	44.46%	25.61%	24.77%	25.00%	25.16%	25.25%
γ	16/97	12/97	12/97	11/97	11/97	11/97

The results in Table 20 again show that the addition of the mid fidelity data points improves the model with regard to the error statistics and the level of inferred uncertainty. However, there is once again almost no sensitivity in the results to the weight factor. There is slightly more variation compared to the results from data set 1, but the difference negligible.

The results from the sensitivity studies suggest that the final prediction is not sensitive to a weight factor applied to the mid fidelity data set came as a surprise to the author. Further investigation into the results revealed some interesting observations. Recall the additional constraints applied at the end of the biasing process discussed in Section 3.3. The constraints were added to ensure that the results make physical sense. For instance, if the upper and lower uncertainty bounds were to cross over each other, it would not be possible to generate the biased distribution. The constraints are listed again below.

- The mode is not allowed to shift beyond the inferred uncertainty bounds
- The mode and the bounds are not allowed to shift beyond their nearest neighbor
- The bounds are not allowed to expand beyond their original definition
- The bounds are not allowed to shrink past the mode
- The bounds are not allowed to be biased in the extrapolated regions

To make sense of the surprising results, the bias calculation needs to be reviewed. The amount of bias applied to a given low fidelity point is dependent on all of the mid and high fidelity points. In addition, the amount of bias for each dimension is dependent on the scale factor θ in each proximity function. The scale factors for this application are large because the design space is mostly linear. This results in proximity functions that span extensive portions of the design space which ultimately results in a substantial amount of bias being applied to each low fidelity data point. Essentially, the high values for the scale factors θs cause the amount of bias to be well beyond the threshold of the constraints. Even though, the bias calculations are sensitive to the weight factor, the changes in the amount of bias are beyond the constraint thresholds, and thus are not propagated to the results. Further investigation into the data revealed that between 74% and 77% of the low fidelity data points were beyond the threshold of at least one of the constraints.

Figures 59 and 60 show the proximity functions for each data set. The proximity functions for the three input variables indicate that all of them have an impact on over 50% of the design space. This results is a large amount of bias. The unexpected results from the sensitivity study could be due to the fact that the design space is relatively linear, or that the biasing portion of the function overpowers the weight factor. Additional experiments need to be conducted to determine if the results from the weight factor study are problem dependent.

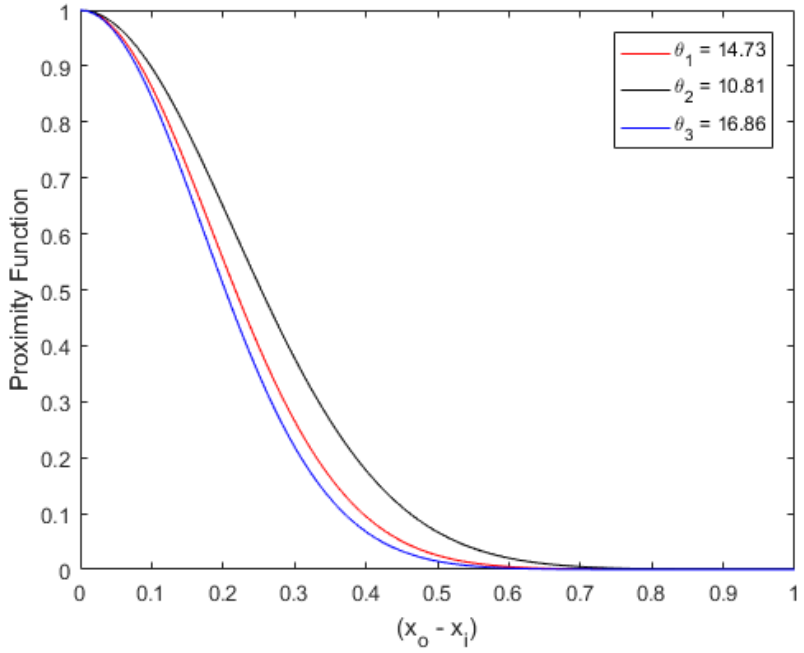

Figure 59: Proximity functions for data set 1. θ_1 is for the design lift coefficient dimension, θ_2 is for the free-stream Mach number, and θ_3 is for the angle of attack.

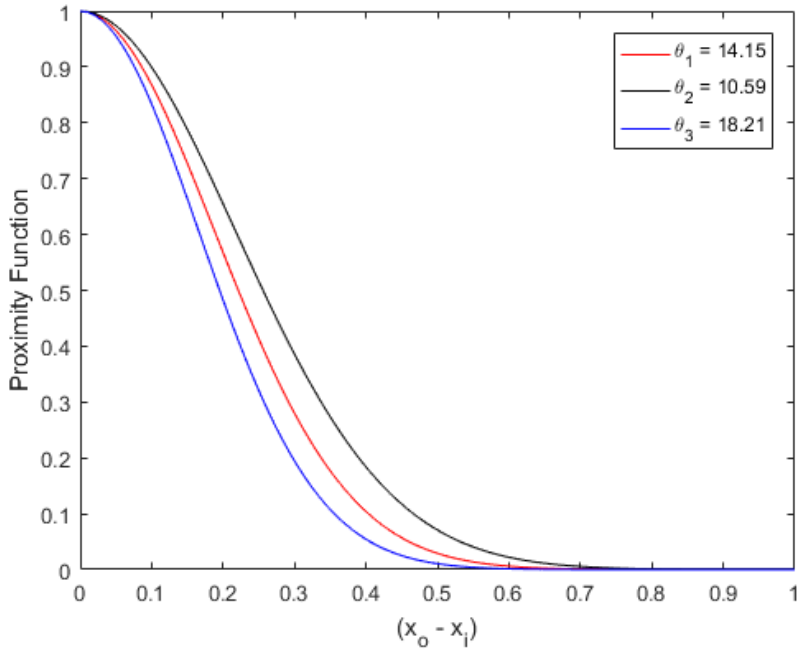

Figure 60: Proximity functions for data set 2. θ_1 is for the design lift coefficient dimension, θ_2 is for the free-stream Mach number, and θ_3 is for the angle of attack.

In the following section, a similar experimental set up is applied to the drag coefficient of the NACA 16 series airfoils. The drag coefficient has more nonlinearity compared to the lift coefficient, and as such should provide some insight into whether or not the weight factor sensitivity is problem dependent. For the drag experiment, the input variables are the design lift coefficient, the thickness to chord ratio, and the angle of attack. The free stream Mach number will be held constant at 0.45. Table 23 shows the high fidelity data set obtained from Wind tunnel tests described by Lindsey et al.[67]. Lindsey et al. state that the wind tunnel measurement error for the drag coefficient is +/- 0.0005; therefore the uncertainty surrounding the high fidelity design points are represented with Gaussian distributions where the mean is equal to the nominal point measured in the wind tunnel and the standard deviation is 0.00025 so that +/- 2 standard deviations represent the measurement error. The distribution is also truncated at +/- 2 standard deviations, because drag cannot physically go to infinity.

STAR CCM+, which is a commercially available CFD program, is used to generate the mid fidelity level data set[103]. Since the high fidelity level data set only covers the extremes of the design lift coefficient range, the CFD simulations are run at design lift coefficients of 0.4 and 0.5 to fill the void. The simulations are steady and use the Spalart-Allmaras turbulence model with a segregated solver[106]. Unstructured meshes were created for each airfoil type. They consist of approximately 75,000 nodes with polyhedral cells throughout except for prism layers near the airfoil wall. Table 22 shows the mid fidelity level data set resulting from the STAR CCM+ simulations. The largest amount of error between the STAR CCM+ data and the wind tunnel data was found to be 0.0046. Therefore, the mid fidelity level data set will be represented by a triangular distribution where the mode is equal to the output from the simulation and the bounds are +/- 0.0046 from the mode. Note that the lower bound is not allowed to go below 0 because drag cannot be less than 0.

Table 21: High fidelity level data set for the additional experiment on the drag coefficient

Design C_l	Thickness Ratio	Angle of Attack (deg)	C_d
0.2	0.09	-2	0.0079
0.2	0.09	0	0.0047
0.2	0.09	2	0.0070
0.2	0.09	4	0.0098
0.2	0.09	6	0.0206
0.2	0.12	-4	0.0105
0.2	0.12	-2	0.0073
0.2	0.12	0	0.0070
0.2	0.12	2	0.0082
0.2	0.12	4	0.0106
0.2	0.12	6	0.0146
0.2	0.12	8	0.0210
0.7	0.12	-4	0.0153
0.7	0.12	-2	0.0093
0.7	0.12	0	0.0091
0.7	0.12	2	0.0100
0.7	0.12	4	0.0107
0.7	0.12	6	0.0133
0.7	0.12	8	0.0231

Table 22: Mid fidelity level data set for the additional experiment on the drag coefficient

Design C_l	Thickness Ratio	Angle of Attack (deg)	C_d
0.4	0.12	-2	0.0119
0.4	0.12	0	0.0119
0.4	0.12	2	0.0125
0.4	0.12	4	0.0136
0.4	0.12	6	0.0155
0.5	0.09	-2	0.0110
0.5	0.09	0	0.0111
0.5	0.09	2	0.0117
0.5	0.09	4	0.0129
0.5	0.09	6	0.0152
0.5	0.15	-2	0.0135
0.5	0.15	0	0.0137
0.5	0.15	2	0.0145
0.5	0.15	4	0.0159
0.5	0.15	6	0.0180

Once again Xfoil is used to generate the low fidelity level data set. Table shows the input ranges for the design variables. A total of 91 low fidelity level data points were generated using Xfoil. The full set of results from the Xfoil simulations is shown in Appendix B. An additional 78 points from the wind tunnel tests conducted by Lindsey et al. will be used for validation. See Appendix B for the full set of drag data. The largest amount of error between the Xfoil data and the wind tunnel data was found to be 0.0083. Therefore, the mid fidelity level data set will be represented by a triangular distribution where the mode is the output from Xfoil and the bounds are +/- 0.0083 from the mode. Again, a constraint is applied to the lower bound so that the drag coefficient does not go below 0.

Table 23: Low fidelity level data set ranges for the additional experiment on the drag coefficient. See Appendix B for the full data set including the drag coefficient predictions

Design C_l	Thickness Ratio	Angle of Attack (deg)
0.2 - 0.7	0.09 - 0.15	-4 - 8
step = 0.1	step = 0.03	step = 2

Figure 61 shows the results for the prediction of the drag coefficient as a function of Mach number and angle of attack at a design lift coefficient equal to 0.5. The plot shown in the figure is the final prediction of the mean using the MUSIC method colored by the level of inferred uncertainty. Notice how there is much more variation in the level of uncertainty compared to the lift coefficient predictions from earlier in this chapter.

The results from the sensitivity study on the weight parameter reveal once again that changing the weight factor between 0 and 1 has a negligible effect on the results. Looking into the data again shows that between 69% and 83% of the data points are beyond the threshold for at least one of the constraints. Even if the proximity function scale factors are artificially increased to lower the impact of the high fidelity data points, the weight factor still has a negligible impact.

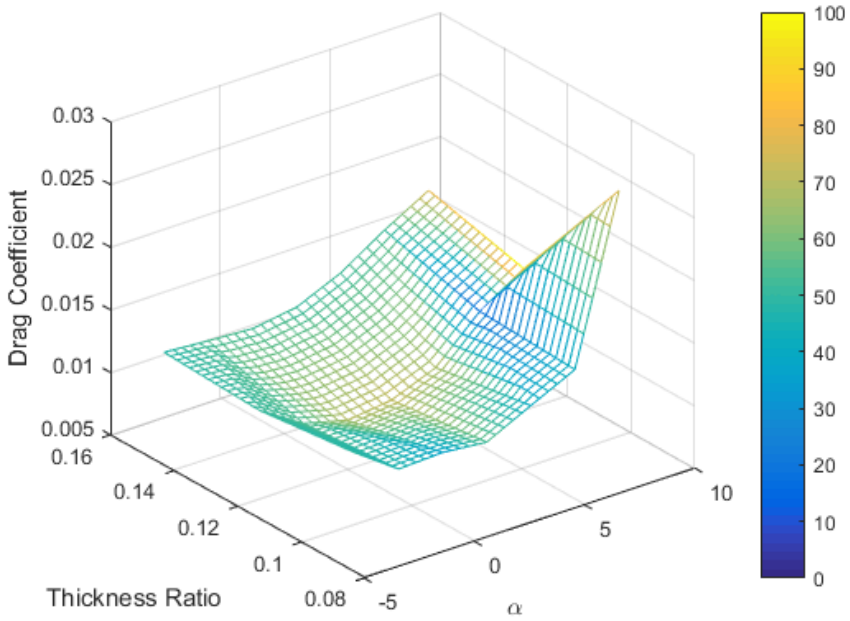

Figure 61: Drag coefficient prediction as a function of Mach number and angle of attack at Design $C_l = 0.5$

5.3.3 Final Observations

This first portion of the experiment tested two separate data sets to determine how the MUSIC methodology would handle the addition of a mid fidelity level data set within the bounds of the high fidelity data and in an extrapolated region beyond the bounds of the high fidelity data. The results from both data sets support the hypothesis that including a mid fidelity level data set will improve the final uncertainty characterization.

The results from part 2 of this experiment surprisingly show that the MUSIC methodology is not sensitive to a mid fidelity level weight factor, and thus the results do not support the hypothesis that a fidelity level weight function needs to be developed. Even the results using a more nonlinear design space do not support the hypothesis. The observations indicate that the biasing terms dominate over the weight factor in the overall biasing function (Equation 43). However, the author

suggests that additional experiments should be conducted on other nonlinear design spaces to determine if the results are truly insensitive to a weight factor or if they are problem dependent. Some additional discussion on these unexpected results is included in Chapter 7.

5.4 Experiment 4 Results: Comparison to Bayesian Model Averaging

The purpose of the final experiment is to validate the entire methodology by comparing it against Bayesian model averaging. A detailed description of Bayesian model averaging is given in Section 2.5. Bayesian model averaging is a current multifidelity method that is commonly used in industry. The purpose of the MUSIC method is to address some of the shortcomings of Bayesian model averaging to improve performance predictions for advanced technologies. Specifically that BMA does not work well with sparse data sets, and the uncertainty inferences do not take proximity into account. The following research question and hypothesis are addressed by this experiment.

Research Question 4: Does this method provide a better resulting prediction of performance compared to current methods like Bayesian model averaging?

Hypothesis 4: The methodology described in this thesis will provide a better uncertainty characterization of the performance throughout the entire design space compared to Bayesian model averaging when applied to advanced concepts with sparse data.

Recall that this experiment is applied to the prediction of the lift coefficient for a swept wing section similar to experiment 3. The low fidelity data set generated by the Prandtl-Glauert equation once again blankets the entire design space. A smaller

Table 24: High fidelity data for the correction surrogate

design C_l	$Mach_\infty$	angle of attack	C_l
0.1	0.4	-6^o	-0.383
		12^o	1.036
	0.7	-6^o	-0.354
		12^o	0.733
0.7	0.4	-6^o	-0.108
		12^o	1.250
	0.7	-6^o	-0.007
		12^o	1.293

amount of mid fidelity data is incorporated in to the model. The first step in the Bayesian model averaging process is the creation of a correction surrogate for each data set. Twelve high fidelity data points, shown in Table 24, are used to create the surrogates for 200 low fidelity data points and 85 mid fidelity data points.

The next step of the process is to apply the correction surrogates to all of the points in the mid and low fidelity data sets. This is important so that the likelihood function does not unfairly bias the mid fidelity data set. After the data sets are corrected, likelihood surrogates are created using a different high fidelity data set shown in Table 25. The likelihood surrogates are used to combine the data sets into the final prediction surrogate.

The final step in the process is to add the high fidelity data points into the final prediction. The MUSIC method is applied to the same data sets. Table 26 shows a comparison of the results for each method using the same set of metrics used in the previous experiments.

The results show that both methods improve upon just using the low fidelity data set by itself as expected. When comparing the two methods, the MUSIC method does not perform better than BMA with regard to the MRE statistics. However, recall that the MRE statistics are normalized by the range of the validation data which is 1.41 in this case. Additionally, the uncertainty range for the high fidelity data is +/- 0.15. Therefore, de-normalizing the error statistics shows that the mean prediction

Table 25: High fidelity data set for the likelihood surrogates

design C_l	$Mach_\infty$	angle of attack	C_l
0.1	0.4	-6^o	-0.383
		-4^o	-0.252
		8^o	0.7123
		12^o	1.036
	0.7	-6^o	-0.354
		-4^o	-0.170
		8^o	0.671
		12^o	0.733
0.7	0.4	-6^o	-0.108
		-4^o	-0.111
		8^o	1.036
		12^o	1.250
	0.7	-6^o	-0.007
		-4^o	0.165
		8^o	1.059
		12^o	1.293

Table 26: Comparison between the MUSIC method and Bayesian model averaging. The predicted results using only the low fidelity data are given for reference.

	LF Prediction	MUSIC	BMA
Mean MRE	-27.33%	-8.82%	-2.94%
STDev MRE	26.55%	10.15%	3.76%
AVG inferred U	100%	24.35%	42.07%
γ	-	14/97	0/97

from the MUSIC method is still within the bounds of the high fidelity uncertainty distributions. Furthermore, the primary goal of the MUSIC method is to reduce the level of inferred uncertainty which is does by approximately 20% more compared to BMA.

The final mean predictions of the lift coefficient from each method are shown in Figure 62 as a function of Mach number and angle of attack at a constant design $C_l = 0.3$. Both plots are colored by the level of inferred uncertainty where bright yellow, or 100, indicates no change from the initial low fidelity uncertainty. The final prediction from BMA is shown in the plot on the left, and the final prediction from MUSIC is shown in the plot on the right. Notice how the level of inferred uncertainty for the MUSIC method is much less compared to BMA throughout most of the plot.

To get a better interpretation of the results, slices of the predictions shown in Figure 62 at a free-stream Mach number of 0.5 are shown in Figure 63. The BMA prediction is shown in the plot on the left and the MUSIC prediction is shown in the plot on the right. The black line in each plot represents the mean prediction from the respective method, and the yellow lines represent the uncertainty. For reference, the red line is the initial low fidelity prediction and the green lines are the initial uncertainty bounds. The black circles are the validation points. BMA predicts the actual trend slightly better than MUSIC, but both methods do a good job of capturing the actual trend. Also notice that both methods reduce the inferred uncertainty bounds compared to the initial uncertainty bounds. However, the MUSIC method reduces the level of inferred uncertainty significantly more than BMA.

The final step in this experiment is to test the situation where there are not enough data points available to use the BMA method, but there are enough for the MUSIC method. Remember the MUSIC method only requires 8 data points for a 3 dimensional problem like this one. The results from final test are shown in Table 27. The predicted results using only the low fidelity data are given for reference in Column

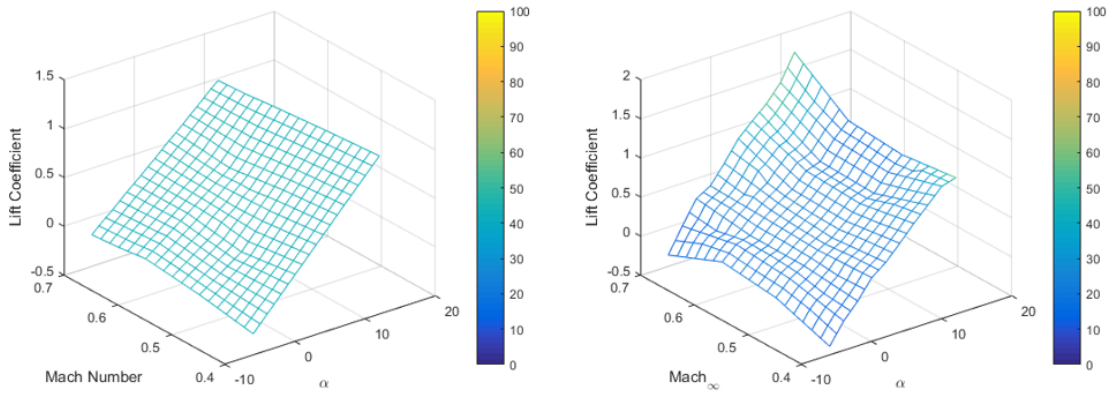

Figure 62: Prediction of C_l from BMA on the left and MUSIC on the right as a function of Mach number and angle of attack at a constant design $C_l = 0.3$.

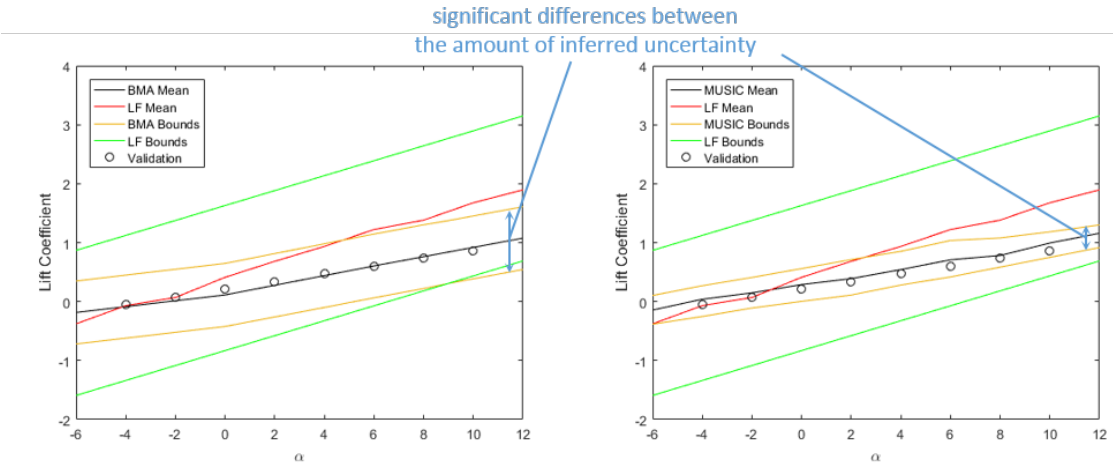

Figure 63: Slices of the predictions shown in Figure 62 at a free-stream Mach number of 0.5. BMA on the left and MUSIC on the right.

1. Column 2 shows the results for the MUSIC method using only 8 high fidelity data points. Columns 3 and 4 are repeated from Table 26 for reference as well. Notice how with only 8 points the MUSIC method still gives good results especially with regard to the level of inferred uncertainty.

In addition the metrics used to compare the two methods, Figure 64 illustrates another shortcoming of BMA. The plots show the same final predictions from MUSIC and BMA as in Figure 62, except that they also include the inferred uncertainty bounds. Once again BMA is on the left an MUSIC is on the right. It has already

Table 27: Comparisons between the Bayesian model averaging and MUSIC method. The second column shows the results for the MUSIC method with only 8 data points.

	LF Prediction	MUSIC (8 pts)	MUSIC (16 pts)	BMA (16 pts)
Mean MRE	-27.33%	-8.97%	-8.82%	-2.94%
STDev MRE	26.55%	10.30%	10.15%	3.76%
AVG inferred U	100%	26.55%	24.35%	42.07%
γ	-	13/97	14/97	0/97

been mentioned that MUSIC reduces the level of inferred uncertainty more than BMA, but this figure illustrates that the inferred uncertainty bounds for BMA are nearly uniform throughout the space. This is a problem with BMA because when it is used with sparse data sets, a decision maker cannot use the method to determine where the model is weakest, and thus where additional resources need to be applied to close the knowledge gap. Recall that the term weak in this research refers to an area where the level of inferred uncertainty is high. The reason for the uniformity is because the minimum amount of data was used to create the likelihood surrogate. As more data is added, the uniformity will decrease, but it may not be possible to generate more data during the conceptual design phase. In contrast, the same amount of data is used by the MUSIC method, and because of the biasing process developed by this research, the level of inferred uncertainty changes significantly compared to BMA.

One final observation that should be mentioned is that if a user wants to add an additional data set to BMA, the data points must be located at the same locations in the design space as the high fidelity data set so that the surrogate models can be generated. In contrast, the MUSIC method is capable of including any number of data points at any location in the design space.

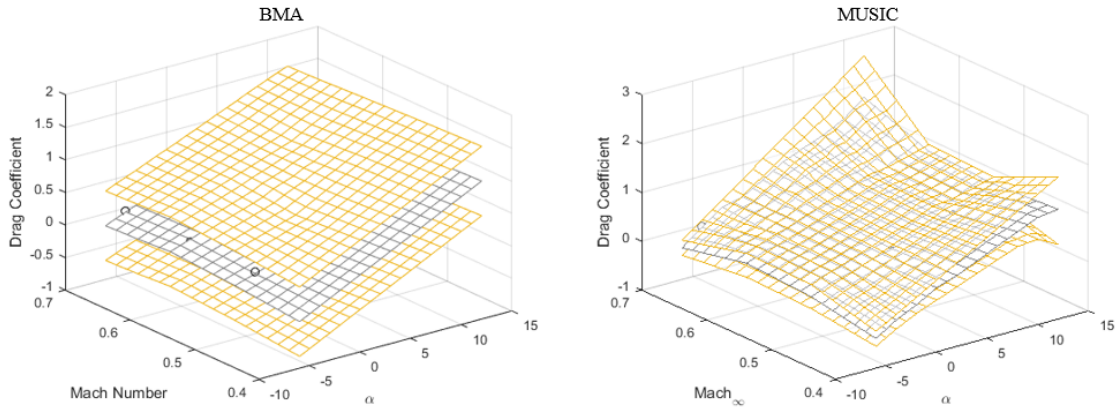

Figure 64: Comparison between BMA and MUSIC of the final prediction for design $C_l = 0.3$ included the inferred uncertainty bounds. BMA is on the left and MUSIC is on the right.

5.4.1 Final Observations

Even though the MUSIC method does not out perform BMA for all of the metrics, MUSIC is superior with regard to uncertainty characterization of sparse data set. Both methods improve upon the low fidelity prediction by improving the mean prediction and decreasing the amount of inferred uncertainty. A summary of the observations are listed below.

- For a hypercubic space, 2^d points are required in order to make a surrogate that covers the entire d dimensional design space. For the 3 dimensional test problem used in this experiment, 8 data points are required. The results show that MUSIC can successfully generate a prediction that is more accurate and has less inferred uncertainty than the low fidelity data prediction alone. However, BMA requires 16 points because two separate surrogates need to be generated. Thus BMA limited by the amount of available data.

- The results also show that MUSIC decreased the average amount of inferred uncertainty by approximately 20% more compared to BMA when 16 points are used for both methods.

- Adaptive sampling is commonly used to apply resources more efficiently. For example a decision maker may want to use the level of inferred uncertainty as an indicator for where the model is weak, and thus where additional tests need to be conducted. This process is repeated until the decision maker is pleased with the prediction throughout the design space. The inferred uncertainty prediction from MUSIC can be used by a decision maker to determine where a model weak. However, the inferred uncertainty in the BMA prediction is nearly uniform throughout the design space; therefore, it cannot be used to determine where the weak.

- To add an additional data set to the BMA prediction, the data points must be at the same input locations as the high fidelity data points in order to create both surrogates. The MUSIC method is capable of including any number of data points at any location in the design space.

The positive benefits listed above due to using the MUSIC method out-weigh the minor imperfections. One of the objectives of this research is to create a traceable and transparent methodology to reduce the level of inferred uncertainty so that it can be used for resource allocation. Therefore, the results from this experiment support the hypothesis that the MUSIC methodology described in this thesis provides a superior uncertainty characterization of the performance throughout the entire design space compared to Bayesian model averaging when applied to advanced technologies with sparse data.

CHAPTER VI

METHODOLOGY DEMONSTRATION ON HAMILTON STANDARD PROPELLERS

The results from Experiment 1-4 provided answers to the formal Research Questions by either supporting or refuting the corresponding hypotheses. These answers enabled the finalization of the methodology that achieves the overarching research objective. Figure 65 provides a final depiction of the methodology and demonstrates how all of the answered research questions have provided more details in the process.

It is observed that the research questions mainly impact Step 2 and Step 3 of the methodology (they are highlighted in green in Figure 65. The results from experiment 2 support the hypothesis that it does not matter what type of distribution is utilized for the non-experimental data. Therefore, Step 2 now states that any distribution type can be utilized for non-experimental data and normal distributions will be assumed for experimental data. For Step 3, the details were provided by the results from experiments 1 and 3. The results from experiment 1 show that a squared exponential function with unique values for θ perform best with regard to the metrics, and that the Kriging algorithm can be used to identify the unique θ values. Next, in experiment 3, the appropriate way to scale the fidelity levels was investigated. The results show that for the specific test case at hand, the fidelity level weighting does not matter; however, it should be investigated for each case at hand when there are more than two data sets. Once the weighting is implemented, if necessary, the data sets can be combined in Step 3.

The final step of this research is to demonstrate the finalized methodology from top to bottom. Within this chapter the entire methodology is demonstrated and the

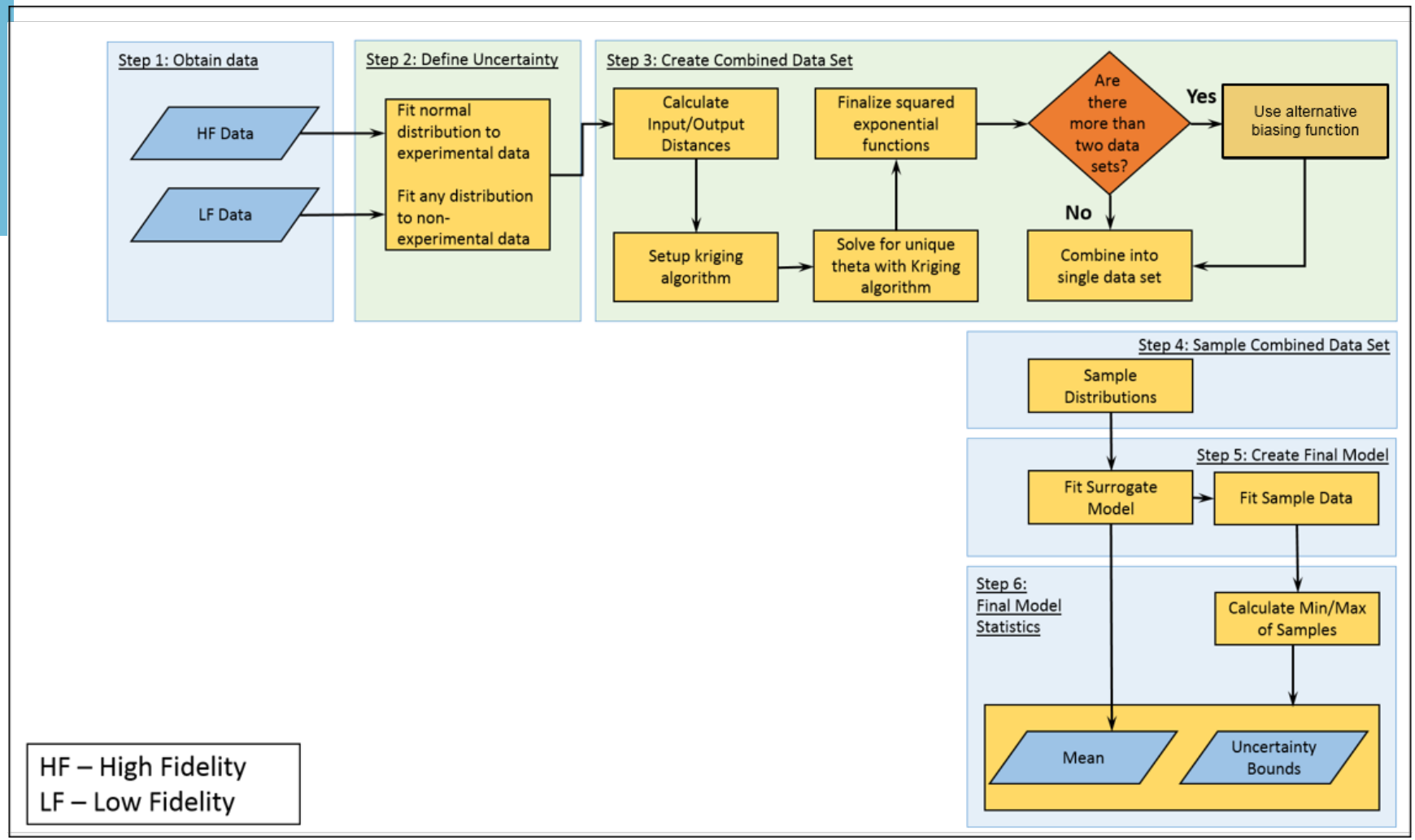

Figure 65: Finalized MUSIC Methodology.

results are provided.

The first step in the process is to obtain the necessary data. It has been mentioned numerous times in this document that there are not enough resources during the conceptual design phase to generate high fidelity data. However, it is common in the aerospace industry for projects to start and stop, so it is advantageous for researchers to investigate if there may be some data sets available from previous experiments. For example, extensive testing was conducted on the open rotor propulsion technology during the 1980's[42]. At the time this technology was referred to as a propfan or unducted fan. Despite the promising results from the tests, the technology was shelved for various economic reasons. However, research was recently conducted on the open rotor as part of NASA's environmentally responsible aviation project[112]. Tests were conducted on both single and counter rotating configurations.

Even though this research is intended to be used on advanced technologies, there is not enough data to validate the method. Therefore, the following research will utilize data from Hamilton Standard general aviation propellers to demonstrate the methodology. The Hamilton Standard data set was chosen because of the amount of data that is available to the public which is required to validate the methodology. The four bladed propeller maps in Hamilton Standard's "Generalized Method of Propeller Performance Estimation" are used to represent the high fidelity data set[1]. The propeller code OpenProp, discussed in Section 6.2, is used to generate the low fidelity data set. The maps within the Hamilton Standard document are said to accurately define the propeller performance for a specific geometry of interest over the range of potential operating conditions. The maps provide the coefficient of power and efficiency in terms of the following non-dimensional parameters.

- Blade activity factor (AF)
- Integrated design lift coefficient (C_{L_i})

- Advance ratio (J)
- Blade pitch angle β

Activity factor represents the integrated power absorption capability of the blade elements[69]. It can be thought of as a propellers ability to absorb power and is defined as

$$AF = \frac{100,000}{16} \int_{r_H}^{R} \left(\frac{b}{D}\right) x^3 dx \tag{44}$$

where r_H is the hub radius, R is the radius, $\frac{b}{D}$ is the chord to diameter ratio and $x = \frac{r}{R}$ (relative station). The integrated design lift coefficient is defined as

$$C_{L_i} = 4 \int_{r_H}^{R} C_{l_D} x^3 dx \tag{45}$$

where C_{l_D} is the blade section design lift coefficient. The advance ratio is a measure of how far forward the propeller moves per revolution, and is defined as

$$J = \frac{V}{ND} \tag{46}$$

where V is the velocity and N is the number of revolutions per unit time. Finally the blade pitch angle is the angle of the blade at the 3/4 radius.

The activity factor and integrated design lift coefficient are high level design variables that are not specific to one propeller geometry. This is commonly done so that the propeller maps can be applied to a wide range of geometries. However, an actual geometry is needed so that this methodology can be applied. Thus a representative family of general aviation propeller geometries will be used for this demonstration. The propeller geometries are from a Hamilton Standard study called the "Advanced General Aviation Propeller Study" by Worobel and Mayo[116]. The geometry is reproduced in Figures 69-68. The plots define the variation blade camber distributions for different integrated design lift coefficients, the thickness to chord ratio, the cord to diameter ratio, and the twist for different activity factors and integrated design lift coefficients. Surfaces were fit to the data from the figures so that different activity

factors and integrated design lift coefficient could be generated while maintaining the same general geometry.

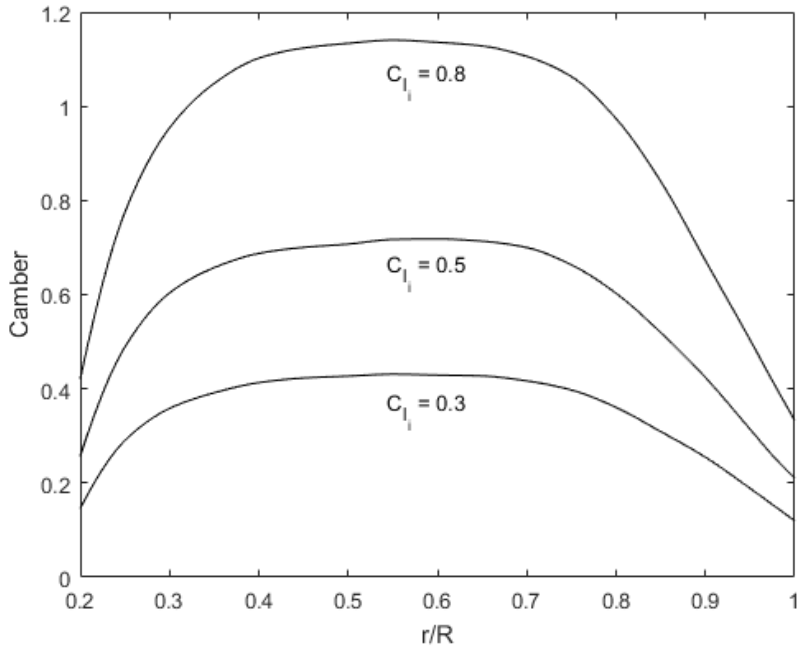

Figure 66: Blade camber distribution

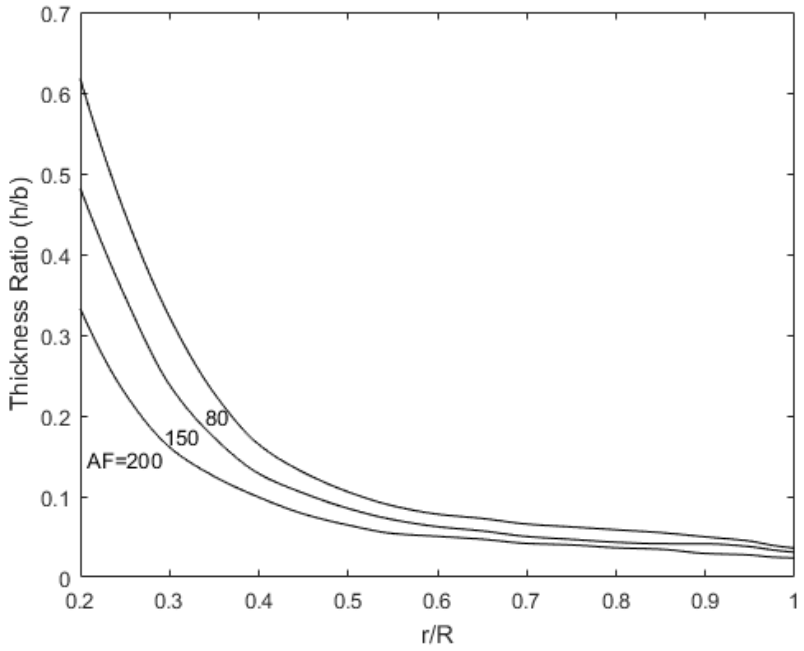

Figure 67: Blade thickness distribution

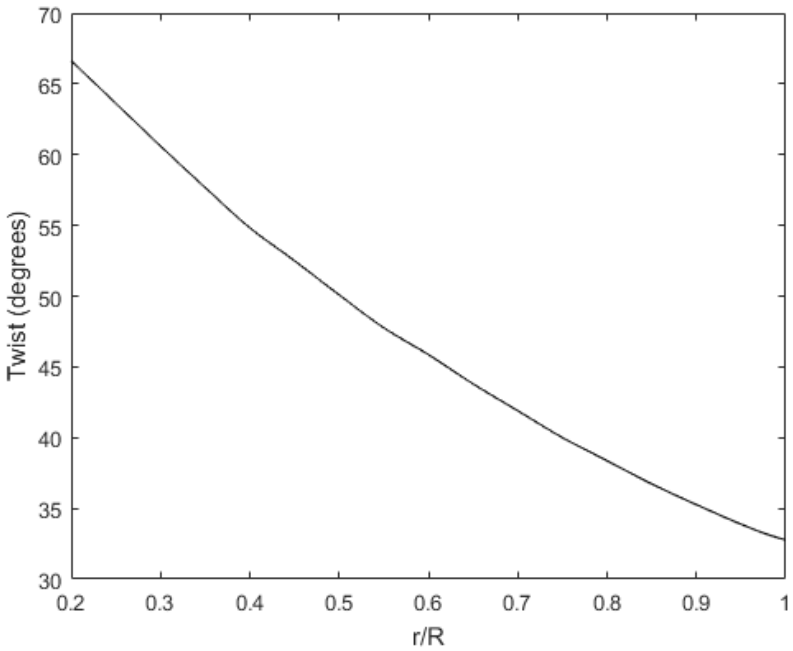

Figure 68: Blade pitch distribution

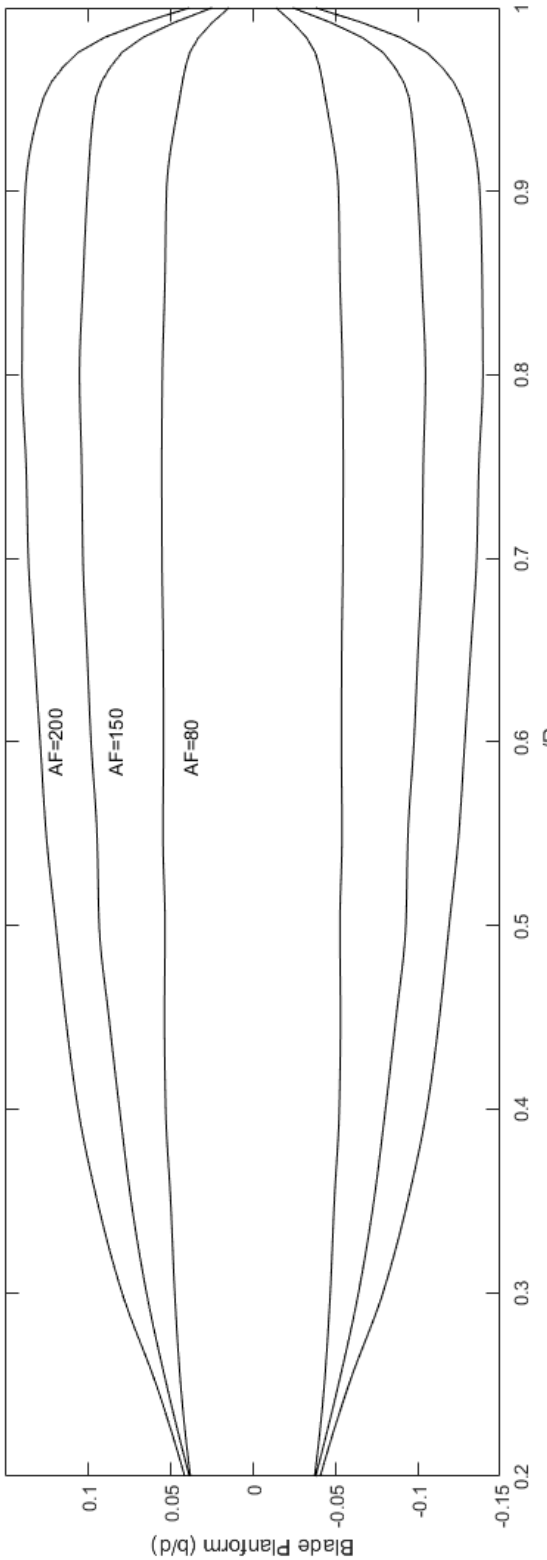

Figure 69: Blade planform distribution

The Hamilton Standard blades utilize NACA 64-Series and 16-series airfoil sections. The sections of the blade near the root operate at lower Mach numbers; thus, the NACA 64-series airfoils are used for these sections because they have a better range of peak lift to drag ratio[15]. The NACA 16-series airfoils are commonly used for the outer sections of propeller blades because they were designed to have high critical Mach numbers. The specific radial location where each type of airfoil is used is not given in the report by Worobel and Mayo. A NASA study by Black and Menthe on advanced eight blade propellers gives the specific locations of where the different airfoils are used along the blade[12]. Similar airfoils are used, so the author decided to use the information from the NASA report to define the locations of the airfoil sections on the Hamilton Standard blade. Therefore, the 64-series airfoil starts at $r/R = 0.239$ and stops at $r/R = 0.367$. Then there is a transition section to the beginning of the 16-series airfoil at $r/R = 0.449$. The 16-series airfoil is used for the remainder of the blade. To account for the transition section of the blade, a linear weighting is applied to the sectional data depending on where the section is located along the transition section e.g. if the section is toward the 16-series end of the transition zone, then the sectional coefficients are weighted more toward the 16-series coefficients.

The design variable ranges are defined in Table 28. The ranges for blade pitch angle and advance ratio were chosen to be near the peak efficiency for each propeller geometry. This is because OpenProp does not give good results, or even converge, for operating conditions where the propeller blades are stalled. This is largely due to the fact that the sectional airfoil data is only given for angles of attack that are pre-stall. OpenProp will also not perform well for stalled propeller blades because of some of the assumptions. Therefore, simulations will not be conducted for operating conditions that are expected to result in efficiencies below 70%. Note that the advance ratios ranges are specific to each geometry and blade pitch angle. In addition, there is

not enough 16-series wind tunnel data available to perform simulations at integrated design lift coefficients above 0.5. Additional parameters that need to be defined are the propeller diameter, tip speed, and free stream Mach number. Values for these additional dimensional inputs were chosen based on typical propeller operating conditions. These values are held constant for every geometry.

Table 28: OpenProp design variable ranges. The advance ratio ranges are specific to each geometry and blade pitch angel.

Activity Factor	80, 100, 140
C_{L_i}	0.15, 0.3, 0.5
β	35, 40, 45
Advance Ratio	various

6.1 Airfoil Definitions

The NACA 16-series airfoils are the result of a significant amount of research and testing during the 1930s. As planes began to fly faster there was a need for airfoil sections that were better suited for high speed applications. This meant developing airfoils with high critical Mach numbers.

Airfoils developed before the 1930s tend to have high negative pressures near the leading edge of the airfoil. High negative pressures correspond to high induced velocities which gradually taper off to the free-stream conditions toward the trailing edge of the airfoil. For example, Figure 70 shows the coefficient of pressure distribution for a NACA 2412 airfoil. Notice how the point of minimum pressure is located near the leading edge. The pressure then gradually returns to the free-stream conditions toward the aft end of the airfoil.

Fundamental tests of high-speed flow indicated that the for a given lift coefficient the critical Mach number could be increased if the induced velocity could be decreased near the leading edge and increased over the rear portion of the airfoil[108, 110]. The NACA 16-Series airfoils came out of this fundamental research. Figure 71 shows

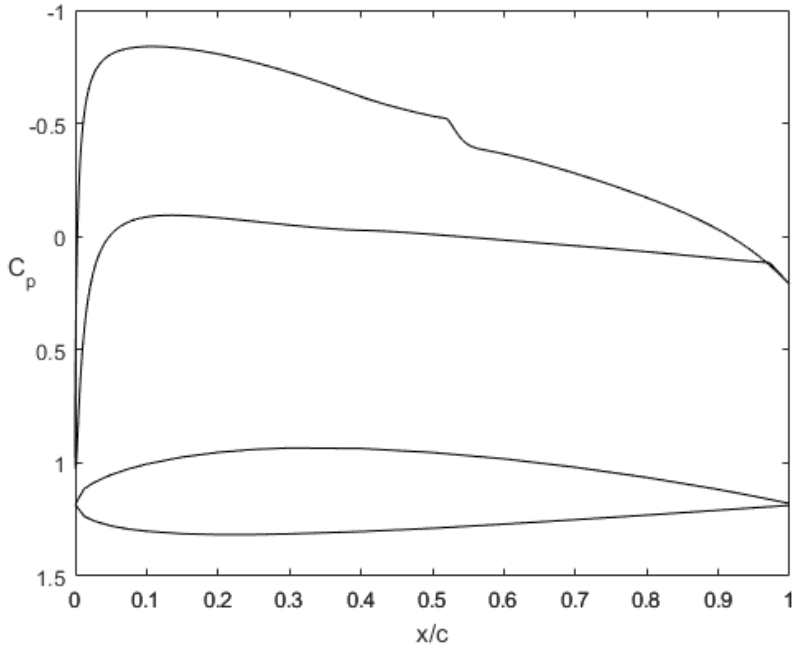

Figure 70: Coefficient of pressure distribution over a NACA 2412 airfoil. Re = 8.5e5, M = 0.3, Alpha = 2 deg, Cl = 0.4749, Cd = 0.0063, L/D = 75.34

the coefficient of pressure distribution for a NACA16-512 airfoil. Notice how the coefficient of pressure is more uniformly distributed compared to the NACA2412 airfoil shown in Figure 70.

The camber line for the NACA 16-Series airfoils was derived using Glauert's expressions for the local induced velocity at a point on an airfoil in terms of the circulation[40]. With the goal of having a nearly uniform pressure distribution, the following expression for the camber line was developed by assuming a constant vorticity.

$$\frac{y_c}{C_l} = \frac{1}{4\Pi}\left(ln\frac{1}{1-x} + xln\frac{1-x}{x}\right) \tag{47}$$

where y_c is the coordinate of the camber line and x is the location along the chord normalized by the chord. Unfortunately this equation has discontinuities at the leading and trailing edges. Stack derived a different equation using a Fourier series method

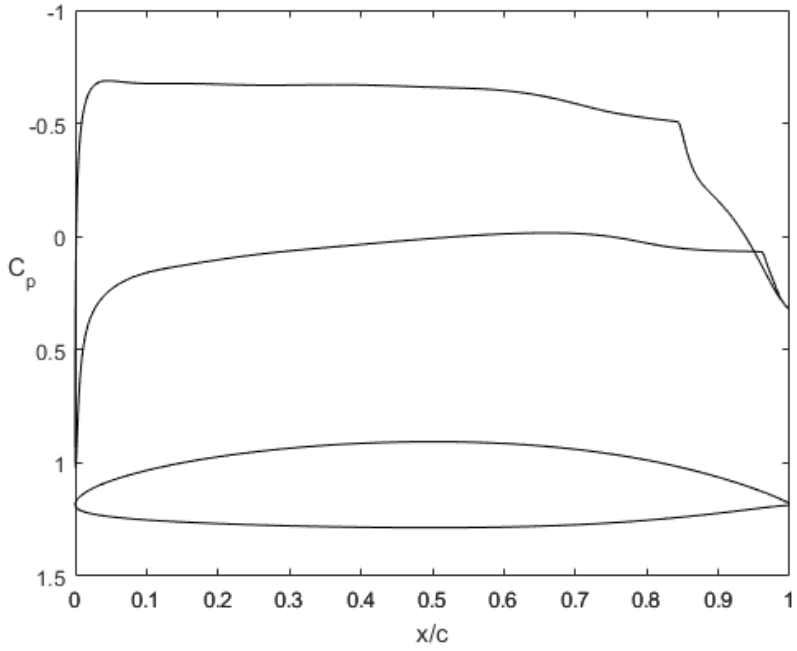

Figure 71: Coefficient of pressure distribution over a NACA16-512 airfoil. Re = 8.5e5, M = 0.3, Alpha = 2 deg, Cl = 0.6189, Cd = 0.00646, L/D = 95.79

that gives similar results[109]. The equation is as follows

$$\begin{aligned}\frac{y_c}{c} = \frac{C_l}{4\Pi}(&0.3833 - 0.333\cos 2\theta - 0.0333\cos 4\theta \\ &- 0.0095\cos 6\theta - 0.0040\cos 8\theta \\ &- 0.0020\cos 10\theta - 0.0012\cos 12\theta)\end{aligned} \tag{48}$$

where $\frac{x}{c} = \frac{1}{2}(1 - \cos\theta)$ and c is the airfoil chord.

The thickness distribution for the NACA 16-series airfoils was developed with the same thought process as the camber line i.e. high critical Mach numbers. Lindsey, Stevenson, and Daley give the following equation for the thickness distribution[67].

$$\begin{aligned}\pm y_1 &= 0.01\frac{t}{c}\left(0.989665x_1^{1/2} - 0.239250x_1 - 0.041000x_1^2 - 0.559400x_1^3\right) \\ \pm y_2 &= 0.01\frac{t}{c}\left[0.010000 + 2.325000(1 - x_2) - 3.420000(1 - x_2)^2 + 1.460000(1 - x_2)^3\right]\end{aligned} \tag{49}$$

where subscript 1 indicates the equation to be used from the leading edge to the point of maximum thickness ($\frac{x}{c} = 0.5$), and subscript 2 is to be used for the portion of the

airfoil from the point of maximum thickness to the trailing edge. The derivation of Equation 49 is not included in this document. The reader is encouraged to reference Stack and Von Doenhoff or Ladson et al. for a derivation of the thickness distribution of the modified NACA 4-series airfoil because the NACA 16-series can be thought of as a special case of the modified NACA 4-series airfoils[111, 61].

Lindsey, Stevenson, and Daley conducted a thorough investigation of the aerodynamic properties of the NACA 16-series airfoil[67]. All experimental data related to the NACA 16-series airfoils referenced in this thesis comes from their report.

6.2 Open Prop Validation

Low fidelity propeller simulations are performed using OpenProp[33, 32]. A majority of the theory comes from Coney, Kerwin, Kerwin and Hadler, and Carlton[22, 56, 57, 18]. OpenProp is based on moderately-loaded lifting line theory which means that the trailing vorticity is aligned to the local flow (i.e. the vector sum of the free-stream plus the induced velocity)[32]. The code assumes a constant pitch and constant radius in the wake. This is a source of error as these assumptions are only valid for moderately loaded blades. The blades are modeled as discrete two-dimensional sections with specific sectional properties at each section similar to blade element theory discussed in Section C.3.2. A vortex lattice method is used to compute the induced velocities from the helical trailing vortex filaments that are shed from the discrete blade sections.

Some minor changes were made to the OpenProp propeller code. First and foremost the code is a marine propeller code, so the properties of the medium were changed from water to air at standard sea level conditions. OpenProp is also written as a design code. Meaning that the user gives the code various performance parameters and then the code designs a propeller to meet the desired performance characteristics. There is an analysis portion of the code, but it must first be given

a valid design. The author modified the code so that it can accept a given propeller geometry to be used in the analysis portion of the code. This was achieved by writing a pre-analysis section based on Goldstein's propeller theory[41]. Appendix C.3.2 discusses Goldstein's propeller theory in detail. This pre-analysis code produces a valid propeller design that can be read by the OpenProp analysis code. OpenProp can then perform the off-design analysis as usual.

Lifting line codes rely heavily on the two dimensional airfoil data for each section of the blade. Therefore, a significant amount of time was spent on the sectional characteristics portion of the code because they are so vital to the performance of any lifting line method. The internal OpenProp sectional airfoil calculation method does not incorporate any sort of correction for compressibility. Thus, a modification was made to the code to allow for sectional airfoil data to be obtained in multiple different ways:

- Calculate the sectional airfoil properties internally using the method derived by Drela and Youngren for Xrotor[30]. This method uses a Prandtl-Glauert compressibility correction as well as corrections for post stall properties.
- Read the sectional airfoil properties from a table provided by the user.
- Obtain the sectional airfoil properties from a surrogate model provided by the user.

Patt and Youngren discuss the importance of using the most appropriate surrogate modeling method when fitting sectional data at multiple Mach numbers[92]. They suggest using an artificial neural network (ANN) with multiple hidden layers. However, ANNs do not perform as well with noisy data, so the data needed to be cleaned up first. The sectional data for the NACA 16-series was taken from a series of plots in Lindsey et al.[67]. The data came from wind tunnel experiments, and was then taken from the resulting plots as opposed to the tabular data. To clean up the

noise, the lift data was fit with a first order polynomial and the drag data was fit with a fourth order polynomial. The smooth data was then fit with an ANN with five hidden layers. Figure 72 shows the actual versus predicted and the residual versus predicted plots for the ANN fits for C_l and C_d. The plots in Figure 72 and the error statistics in Table 29 show that the ANNs fit the data well.

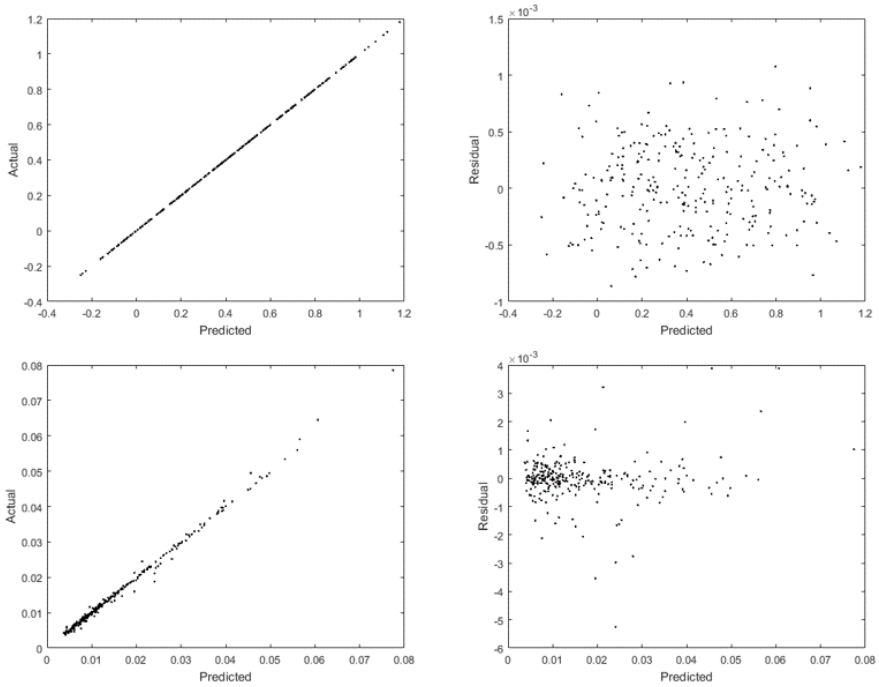

Figure 72: Actual vs. predicted and residual vs. predicted plots for the NACA 16-series ANN fits. The top two plots are for C_l and the bottom two plot are for C_d

The NACA 64-series airfoils are used for the root sections of the blades because they have a better range of peak lift to drag ratio at lower Mach numbers where the root sections operate[15]. The coordinates for these airfoils were obtained from "The Theory of Wing Sections" by Abbott and Von Doenhoff[3]. The commonly used airfoil analysis code called XFOIL was used to generate the performance characteristics for these airfoils (C_l and C_d) as a function of Mach and angle of attack).

XFOIL is a potential flow solver that can optionally include an interactive boundary layer formulation and stability mode[31]. To account for compressibility the code

uses the Karman-Tsien compressibility correction. Xfoil will give sufficient performance results for the root section airfoils because they operate in the lower subsonic Mach number range. A series of simulations were run on the airfoils with Mach numbers ranging from 0.3 to 0.6 and angles of attack from -5° to 10°. Unfortunately the author was only able to obtain coordinates for the 6-series airfoils up to 21% thickness to chord ratio. This was mentioned as a source of error in the previous section because some of the root sections for the low activity factor blade are thicker than 21%. The results from Xfoil do not have noise, so it was not necessary to smooth them out before fitting them with an ANN. Figure 73 shows the actual versus predicted and the residual versus predicted plots for the ANN fits for C_l and C_d. Once again, the plots in Figure 73 and the error statistics in Table 29 show that the ANNs fit the data well.

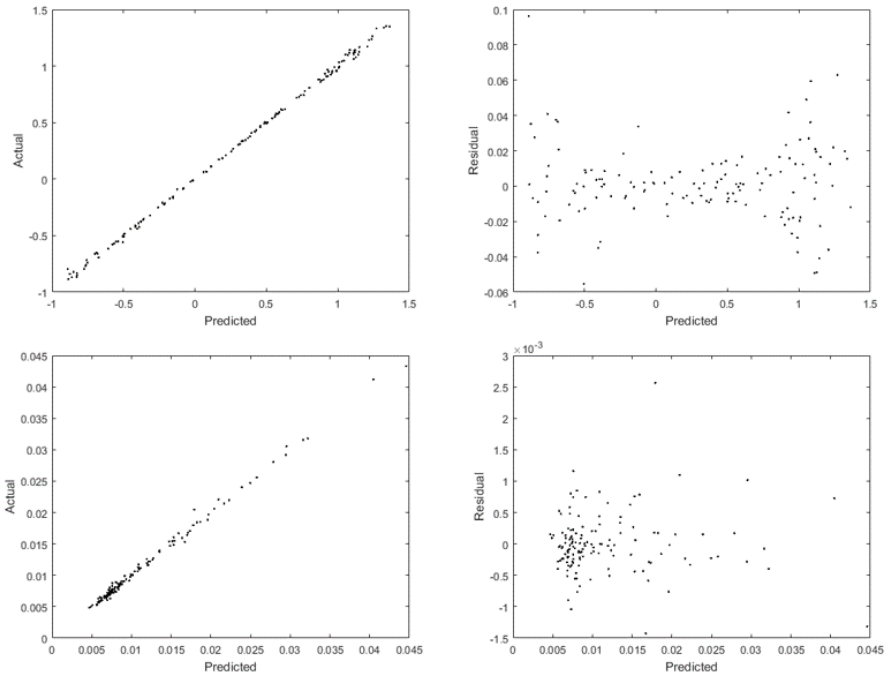

Figure 73: Actual vs. predicted and residual vs. predicted plots for the NACA 64-series ANN fits. The top two plots are for C_l and the bottom two plot are for C_d

Once the sectional data surrogates have been generated, they can be included in OpenProp. OpenProp was tested over the entire range of the design space.

Table 29: Error statistics for the ANN fits of the NACA 16-series and 64-series airfoils

	NACA 16-Series		NACA 64-Series	
	C_l	C_d	C_l	C_d
Mean MRE	3.09e-4%	0.16%	0.05%	-0.01%
STDev MRE	0.03%	1.01%	0.9%	0.72%

6.3 Obtain the Uncertainty Distributions

It is important that the uncertainty distribution associated with every data point in each data set is obtained or defined prior to the data synthesis process because the biasing function is dependent on the defined uncertainty distribution. Note that the uncertainty distribution does not need to be constant across an entire data set. The different ways of defining uncertainty are discussed in section 2.4. Finding the most appropriate definition of uncertainty is outside the scope of this research. Again, the intent of this research is to formulate a methodology for predicting the uncertainty of an advanced concept at unknown locations in the design space by synthesizing the given uncertainty distributions from multiple sources of data. The uncertainty surrounding the experimental data is defined by a Gaussian distribution where the mean is the nominal value given in the experimental documents and the standard deviation is determined by the measurement error. Lindsey et al. state that the measurement error for the wind tunnel tests is ± 0.005 for C_l and ± 0.0005 for C_d[67]. Hamilton Standard does not provide any error statistics related to their maps, so it will also be assumed that the measurement error for the Hamilton Standard maps is ± 0.005 for C_P and $\pm 0.5\%$ for efficiency.

For this research it is important that the uncertainty for each data point has a unique mode. This is because the data combination process will bias this point toward the higher fidelity data points based on a weighting system. It is common in industry to represent uncertainty distributions with triangular distributions. A triangular distribution is used because the results from experiment 2 (Section 5.2)

show that the different distributions have a negligible impact on the final outcome. The nominal value output from OpenProp is the peak and the bounds are defined by comparison the Hamilton Standard maps. The largest amount of error is used to conservatively define the low fidelity uncertainty distributions.

The design variables listed in Table 28 result in a total of 638 low fidelity points. When compared against Hamilton Standard data, OpenProp predicts efficiencies that ranged from 7% high to 20% low. These ranges are used to define the uncertainty distributions for the low fidelity data. Some sources of error are listed below. This is not an exhaustive list.

- Major OpenProp assumptions - Fixed pitch wake, no wake contraction, no tip loss factor
- The thickness ratio for the NACA 64-series airfoil data does not go beyond 21%
- The thickness ratio for the NACA 16-series airfoil data does not go below 6%
- Errors in the airfoil sectional caused by the use of a surrogates
- Inaccuracies in the Xfoil results for the 64-series airfoils

6.4 Data Biasing, Synthesis Process and Construction of the Final Performance Prediction Model

The process for biasing the low fidelity data and creating a combined data set is discussed in Section 3.3. Multiple research question came about when deciding the best way to bias the low fidelity data. Sections 4.1 and 4.3 discuss the experiments that were designed to address these questions. The results from experiment 1, discussed in Section 5.1 support the hypothesis that using the squared exponential function with unique scaling parameters for each dimension defined by Kriging result in the best proximity function. Only two levels of fidelity are used in for this demonstration, so the results from experiment 3 are not relevant.

Recall that a Monte Carlo sampling process is preferred when propagating uncertainty distributions. Therefore, the combined biased data set is sampled and fit with a linear interpolation method 1000 times to generate a good representation of the combined uncertainty throughout the design space.

The mean of all of the surrogates becomes the final performance prediction model and the overall bounds of the surrogates become the final inferred uncertainty bounds.

6.5 Results

The proximity functions for the prediction of efficiency for each dimension are shown in Figure 74. Notice how the activity factor and the integrated design lift coefficient have a much broader impact on the space.

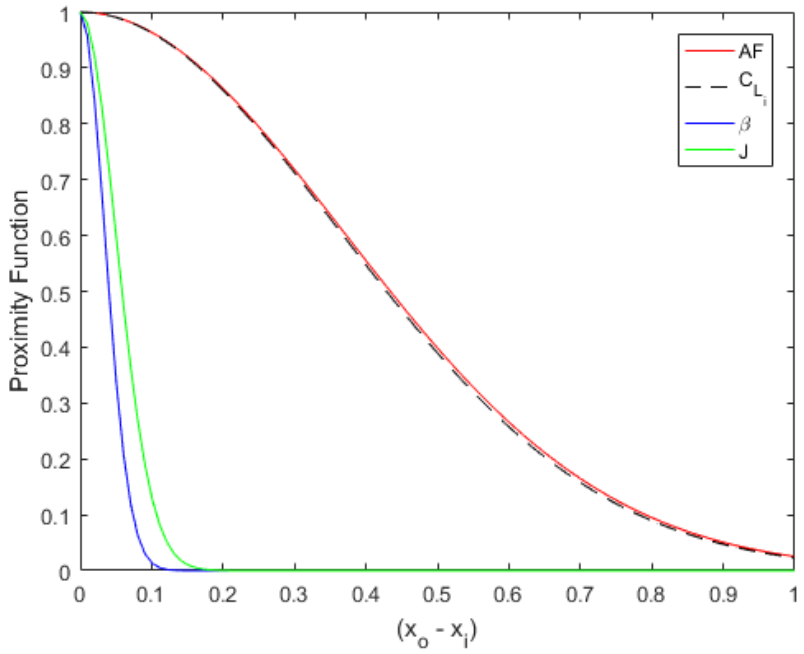

Figure 74: Proximity functions for the prediction of the efficiency.

The results for the prediction of efficiency are shown in Table 30. The change in the mean MRE is minor, but there is a significant decrease in the standard deviation of the MRE as well as the level of inferred uncertainty. Figure 75 shows the prediction of the efficiency for the Hamilton Standard propeller with an activity factor of 100

and an integrated design lift coefficient of 0.5 at blade pitch angles ranging from 35^o to 45^o. The mean prediction is represented by the black mesh and the inferred uncertainty bounds are represented by the yellow meshes. Figure 76 shows a slice of the results shown in Figure 75 at a blade pitch angle of 45^o. Again the mean prediction is shown in black and the inferred uncertainty bounds are shown in yellow. The original low fidelity prediction from OpenProp is shown in red with the original uncertainty bounds shown in green for reference. The black circles represent the validation data.

Table 30: Results for the prediction of efficiency.

	OpenProp Only	My Method
Mean MRE	2.25%	4.08%
STDev MRE	14.55%	9.03%
Uncertainty	-	15.62%

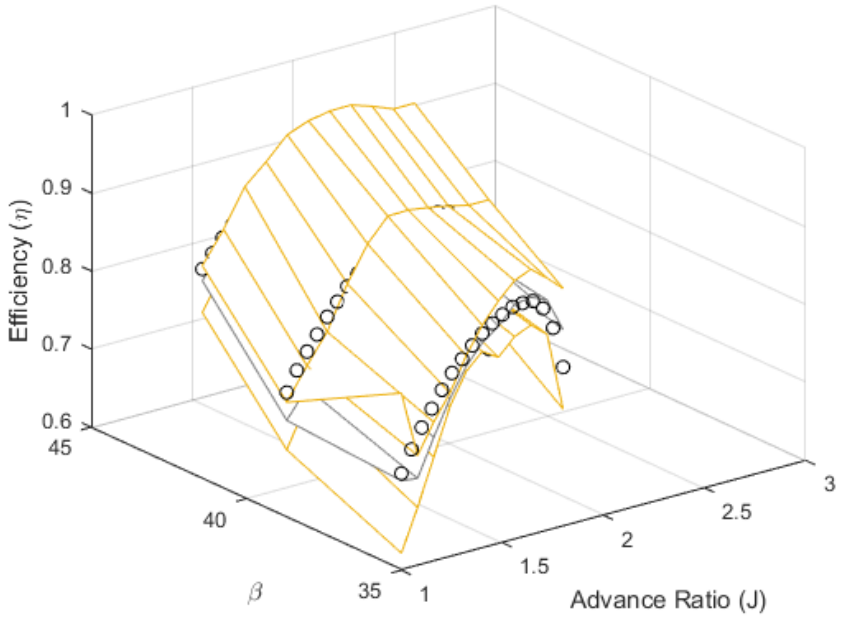

Figure 75: Prediction of the efficiency of the Hamilton Standard Propeller with AF = 100 and an integrated design lift coefficient of 0.5

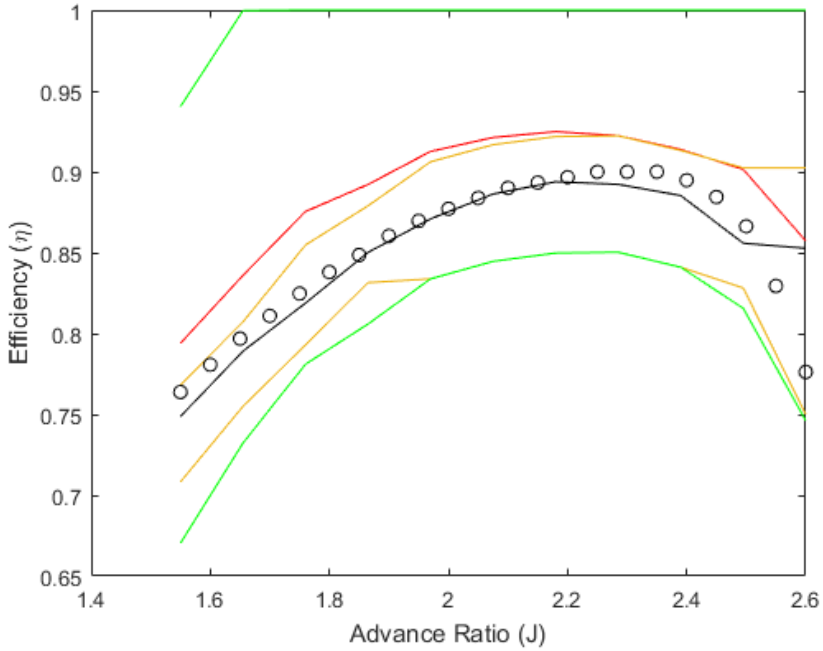

Figure 76: Slice from Figure 75 at a blade pitch angle of 45^o

The proximity functions for the prediction of the coefficient of power for each dimension are shown in Figure 77. Notice how the blade pitch angle has a broad impact on the space similar to the activity factor and the integrated design lift coefficient. This is different from the efficiency prediction.

The results for the prediction of coefficient of power are shown in Table 31. The change in both the MRE statistics is negligible, but the level of inferred uncertainty drops significantly to 39.99%. Figure 78 shows the prediction of the efficiency for the Hamilton Standard propeller with an activity factor of 100 and an integrated design lift coefficient of 0.5 at blade pitch angles ranging from 35^o to 45^o. The mean prediction is shown in black and the inferred uncertainty bounds are shown in yellow. Figure 79 shows a slice of the results shown in Figure 78 at a blade pitch angle of 35^o. Again the mean prediction is shown in black and the inferred uncertainty bounds are shown in yellow. The original low fidelity prediction from OpenProp is shown in red with the original uncertainty bounds shown in green for reference. The black circles

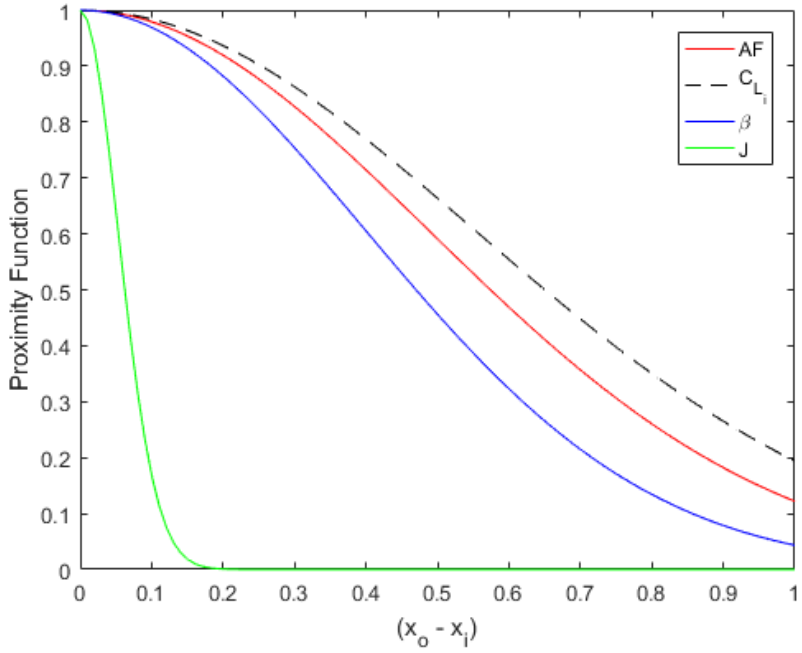

Figure 77: Proximity functions for the prediction of the coefficient of power.

represent the validation data.

Table 31: Results for the prediction of coefficient of power.

	OpenProp Only	My Method
Mean MRE	1.11%	0.73%
STDev MRE	5.40%	5.64%
Uncertainty	-	39.99%

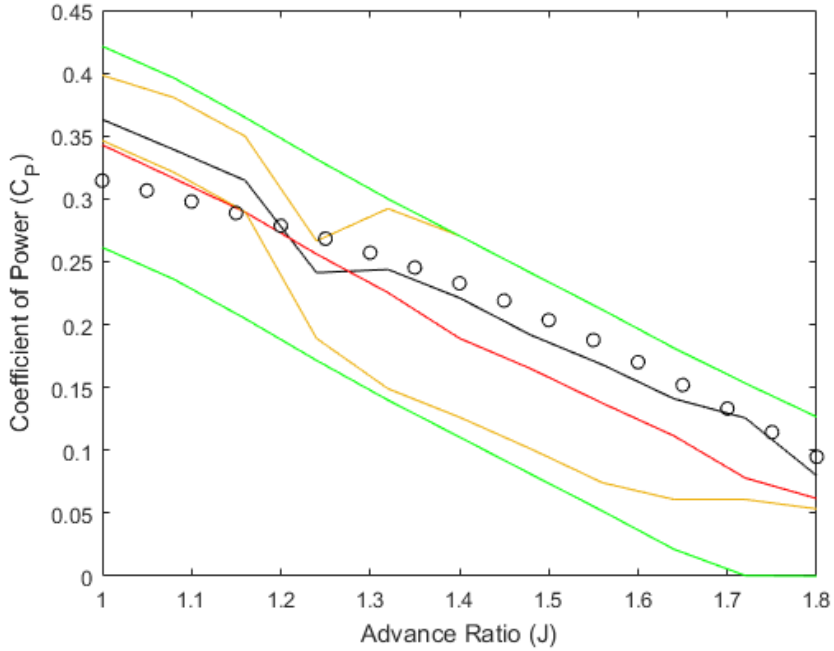

Figure 78: Prediction of the coefficient of power of the Hamilton Standard Propeller with AF = 100 and an integrated design lift coefficient of 0.5

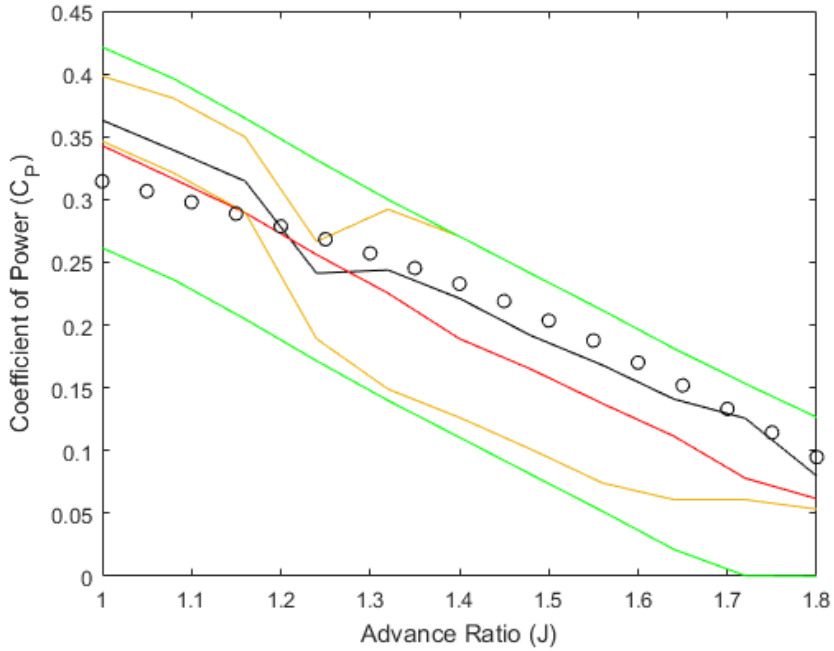

Figure 79: Slice from Figure 78 at a blade pitch angle of 35^o

6.5.1 Final Observations

The final prediction of the performance of the Hamilton Standard propellers shows strong agreement with the actual maps. The level of inferred uncertainty is reduced significantly for both the efficiency and coefficient of power predictions. The standard deviation of the MRE is reduced for the efficiency prediction. The MRE statistics for the coefficient of power do not show any significant change. The only problem with the predictions is that approximately 25% of the validation data is outside of the uncertainty bounds. A majority of the points are not far outside of the bounds, but nevertheless the prediction does not capture the 25% of the validation data.

CHAPTER VII

CONCLUSION

7.1 Summary of Findings

The objective of this research was to formulate a methodology to characterize the uncertainty throughout the design space based on the relative location of the desired design to the higher fidelity designs when given resulting uncertainty distributions of multiple sources of multifidelity data simulations for sparse data situations. The resulting methodology, Multifidelity Uncertainty using Statistical Inference Characterization (MUSIC), has been developed through a series of experiments. The observations from the validation experiments show that MUSIC is able to meet the stated research objective, specifically that it superior to Bayesian model averaging when applied to sparse data situations.

It is important to re-state that this research focused on the synthesis of the resulting uncertainty distributions from multiple probabilistic simulations at different fidelity levels of the same concept. This is in contrast to propagating the uncertainty distributions on the design variables through some sort of modeling and simulation environment to create the resulting uncertainty distribution. Additionally, is important for the reader to understand that no sources of uncertainty are identified or reduced by this method. The uncertainty characterization in this method is an inference based on knowledge from known points nearby.

Bayesian model averaging is a method that is commonly used to synthesize probabilistic distributions from multiple sources of data. The results from this research show that BMA does not provide sufficient results when the available high fidelity

data is sparse. Compared to the MUSIC methodology, BMA requires twice the minimum amount of data because two separate surrogates need to be generated. One of the ways that BMA does not provide sufficient results is that the inference process only happens at known points, and then a surrogate is generated to fill in the rest of the design space. This results in a relatively uniform level of inferred uncertainty if the data is sparse. Recall that one of the objectives is to provide the decision maker with an indication of where there are high levels of inferred uncertainty in the design space so that they can apply additional resources efficiently. The results illustrate that MUSIC is capable of providing the user with variations in the level of inferred uncertainty throughout the design space, while BMA does not provide a sufficient change in the level of inferred uncertainty for the decision maker to determine where to apply additional resources.

Another shortcoming of BMA is with regard to including additional data sets. The additional data set must have data points at the same locations as the high fidelity data points in order to create both surrogates. In contrast, the MUSIC methodology can incorporate any number of additional data points at any location in the design space.

Even if there is enough data to use BMA, the MUSIC method decreased the amount of inferred uncertainty approximately 20% more while maintaining an acceptable level of accuracy. Additionally, the MUSIC method is also able to provide sufficient results even when there was not enough high fidelity data to use BMA.

In the final chapter, the MUSIC method is applied to a representative advanced technology. There is not a sufficient amount of data available to validate the method on the open rotor technology, so the performance of Hamilton Standard general aviation propellers is used. The results from this final demonstration show that the MUSIC method is able to provide sufficient results when applied to a representative technology.

Overall, the results from this research support the hypothesis that the MUSIC methodology provides a more useful representation of the inferred uncertainty of the performance of an advanced technology throughout the entire design space compared to Bayesian model averaging with sparse data.

7.2 Summary of Research Questions and Experiments

A set of formal research questions and hypotheses were defined to architect the methodology. From these research questions and hypotheses, a set of experiments were designed to test the hypotheses. The first research question, stated below, is to help define the best way to bias the low fidelity data.

Research Question 1: How will the low fidelity uncertainty distributions be biased in the input space?

Hypothesis 1: A proximity function that uses the Kriging algorithm to determine a unique scaling parameter, θ, for each dimension will more effectively bias the low fidelity uncertainty distributions.

An experiment was conducted to compare three different proximity functions: linear function, squared exponential functions with a constant value for the scale parameter, and the squared exponential function with unique values for the scale parameter for each dimension. The results support the hypothesis that creating a proximity function that uses the Kriging algorithm to define a unique set of scaling parameters for each dimension more effectively biases the low fidelity data. The MRE statistics as well as the level of inferred uncertainty are used to determine the best proximity function.

The second question is asked to understand whether or not the type of distribution used to define the low fidelity uncertainty. The question and hypotheses are as follows.

Research Question 2: Does the type of distribution used to define the uncertainty of the low fidelity data sets affect the results given that it is bounded and it has a unique mode?

Hypothesis 2: The type of distribution used to represent the uncertainty of the low fidelity data does not significantly impact the results of the methodology as long as it has a unique mode and is bounded.

An experiment was conducted to compare the triangular and the Weibull distributions. Both of these distributions are commonly used to define uncertainty in the industry. The results show a negligible difference between the final predictions, and thus support the hypothesis that the type of distribution used to define the uncertainty does not significantly impact the results as long as it has a unique mode and can be bounded.

The third research question is a two part question about how an additional mid fidelity level data set will be handled by the methodology. If additional data sets that include additional knowledge are obtained, then the MUSIC methodology must be able to account for them. It is expected that by including a mid fidelity level data set will improve the final prediction because knowledge is being added. The following question and hypothesis were tested in part 1 of this experiment.

Research Question 3.1: Including a mid fidelity level data set will improve the final inferred uncertainty prediction.

Hypothesis 3.1: Including a mid fidelity level data set will improve the final inferred uncertainty prediction.

An experiment was conducted using the prediction of the lift coefficient for a section of an infinite aspect ratio swept wing. An initial iteration of the method is done with just the high and low fidelity level data sets. The level of inferred uncertainty is then used to determine where additional mid fidelity data should be placed. A second iteration of the method is done with the addition of the mid fidelity level data set. Two separate test were conducted to determine how the MUSIC method would perform. As expected, the results show that the addition of a mid fidelity level data set improves the final prediction. A second test was conducted to determine how the MUSIC method would perform in a situation where the high fidelity data does not span the entire design space. The results are similar for this test.

Part 2 of this experiment tested whether or not changes need to be made to the biasing calculation process. The following question and hypothesis were be tested in part 2 of the experiment.

Research Question 3.2: By introducing the mid fidelity level data set, do changes need to be made to the existing biasing process?

Hypothesis 3.2: If the final results are sensitive to a weight factor, then a fidelity level weight function needs to be developed.

For this part of the experiment, a weight factor is added to the biasing equation to see the effect of representing the mid fidelity data set as if it is a low fidelity data set or a high fidelity data set. The weight factor was varied between 0 and 1 to determine the level of sensitivity.

The experiment was again repeated twice, and unfortunately the results are almost completely insensitive to the weight factor and thus do not support the hypothesis. It was initially thought that reason for the lack of sensitivity was because of the specific

application. The airfoil design space is mostly linear resulting in small scale factors for the proximity function (small scale factors equate to broad proximity functions). This means that regardless of the impact of the mid fidelity data set, the amount of bias placed on each low fidelity point is already well past the pre-defined constraints.

Another test was conducted using drag because the design space is not as linear. Once again, there is no change in the sensitivity results. The observations regarding the constraints indicate that the biasing terms dominate over the weight factor in the overall biasing function. However, due to the surprising nature of the results, the author recommends conducting additional experiments on other nonlinear design spaces to determine if the results are truly insensitive to a weight factor or if they are problem dependent.

The final question addressed the overall capabilities of the entire methodology compared to an existing method from the literature, Bayesian model averaging. The question is stated below.

Overarching Research Objective: Does the MUSIC method provide a more accurate representation of the inferred uncertainty compared to current methods like Bayesian model averaging?

Overarching Hypothesis: The MUSIC methodology will provide a more accurate uncertainty characterization of the performance throughout the entire design space compared to Bayesian model averaging when applied to advanced technologies with sparse data.

Experiment 4 was designed to predict the lift coefficient for a wing section using both BMA and the MUSIC method. The results of the experiment show that the MUSIC method out performed BMA in a majority of the metrics. The most significant difference is the level of inferred uncertainty. The MUSIC method decreased

the level of inferred uncertainty by approximately 20% more compared to BMA. Another shortcoming of BMA is that is requires more high fidelity data because two separate surrogates must be generated. Additionally, the data must be at the same locations for all of the data sets so that the surrogates can be generated. BMA also has a mostly uniform level of uncertainty making it difficult for a decision maker to determine where the model is weakest.

After the completion of Experiments 1-4, a final demonstration of the resulting methodology was performed. The purpose of this demonstration was to apply the methodology to a system that is representative of an advanced technologies. Since there is not enough data available for any of the advanced propeller technologies, the method was applied to Hamilton Standard general aviation propellers. The results show that the method continues to work well.

7.3 Summary of Contributions

This thesis provides several contributions to the fields of advanced system design and development and probabilistic analysis. The primary contribution from this thesis is the MUSIC methodology, which provides a traceable and transparent formulation for inferring a level of uncertainty based on the proximity to a known point in a design space for sparse data situations. This method provides an effective way for a decision maker to decide where to conduct additional experiment to further improve the prediction. The method is an alternative to other existing methods, such as Bayesian model averaging, which do not work well with sparse data, or even at all if there is not enough data to create the surrogates.

The second contribution is the development of a biasing method for synthesizing sparse data sets from multifidelity data sources. The biasing process developed for this method could be applied to a variety of other applications within the machine learning and uncertainty analysis communities. The data can come from multiple

sources of multifidelity data, or from a different design within the same design space.

Lastly, is the contribution this research has to the overall design of advanced concepts, systems, and technologies. The ability to create these models with less required data allows important design space explorations and trade studies to be performed in a quicker, cheaper manner. This is important to engineers because of the need to maximize the amount of knowledge that can be gained from a finite amount of resources, or trying to minimize the amount of required resources altogether during a technology development program. The MUSIC methodology formulated throughout this research helps accomplish these objectives.

7.4 Future Work

A few areas have been identified for potential extensions of this research. First, it is recommended that future research focus on further exploring the sensitivity of an experimental fidelity level weight factor on the data synthesis results when more than two data sets are being utilized. Further experimentation could be planned and conducted to determine if a sensitivity exists when the underlying physics is more complex than the scenarios tested within this research. Determining an effective fidelity level hierarchy would be a significant contribution to the uncertainty community.

Another area of future work is further investigation into the biasing process and determining how it can be extended to known locations instead of known points. The biasing process could potentially be improved by biasing the low fidelity data by proximity to a known location instead of known data points. This is because if a lot of high fidelity data points are tightly clustered in a specific location, they can magnify the amount of influence one specific location in the design space has on the lower fidelity data set. Coming up with a way to bias that data based on known locations instead of points could alleviate this problem.

Lastly, more research could be done on different surrogate modeling techniques

used within the MUSIC methodology. The method currently uses a linear interpolation technique to fit the various sample sets. However, this type of surrogate model does not result in a smooth surface for the final prediction. More research on other surrogate modeling methods may result in smoother predictions and even accelerate the process.

APPENDIX A

HAMILTON STANDARD MAPS

Three Hamilton Standard propeller maps are included for reference. All three maps come from the Generalized Method of Propeller Performance Estimation document[1]. Note that the efficiency is included as contours on the coefficient of power maps instead of having a dedicated efficiency map.

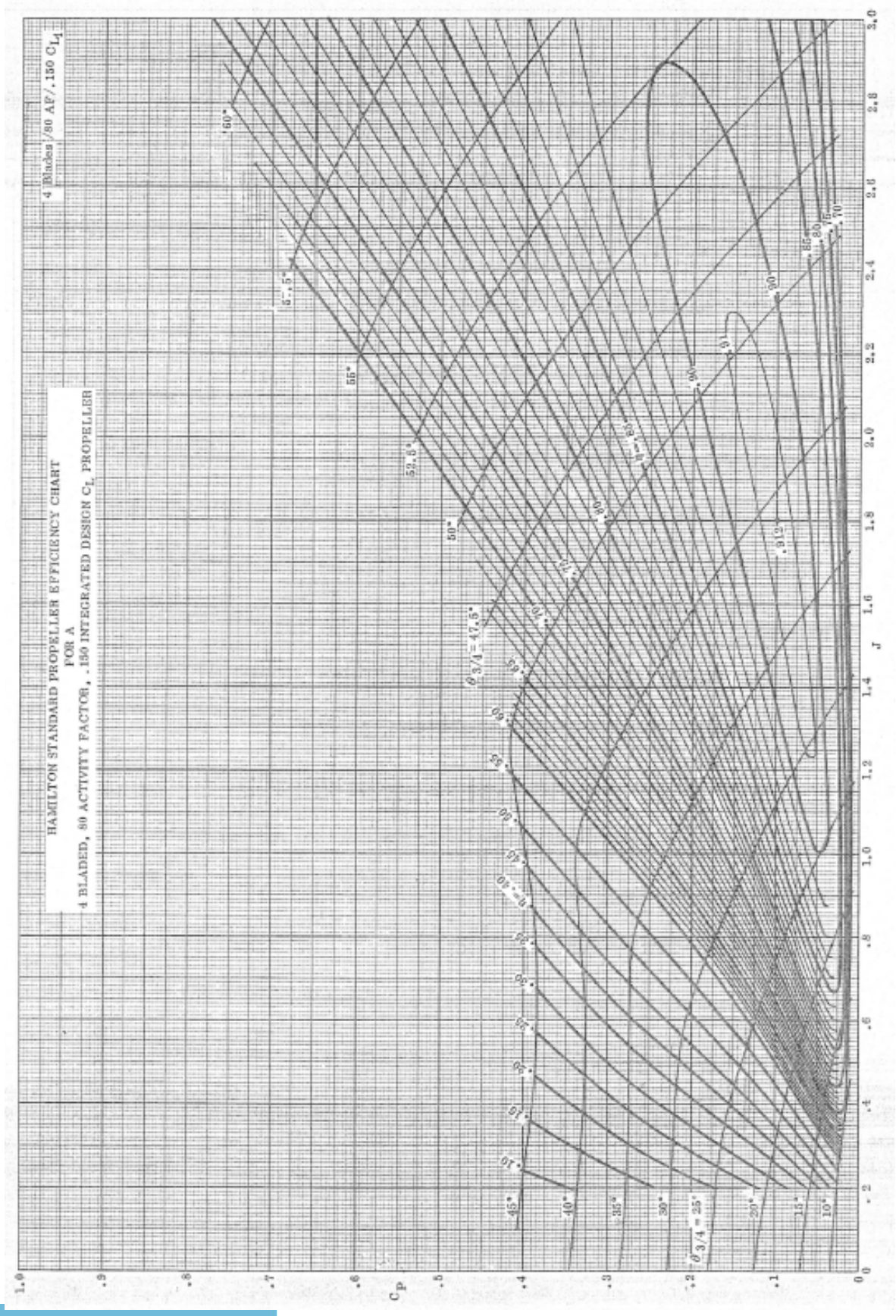

Figure 80: Hamilton Standard propeller map: activity factor = 80, integrated design lift coefficient = 0.15

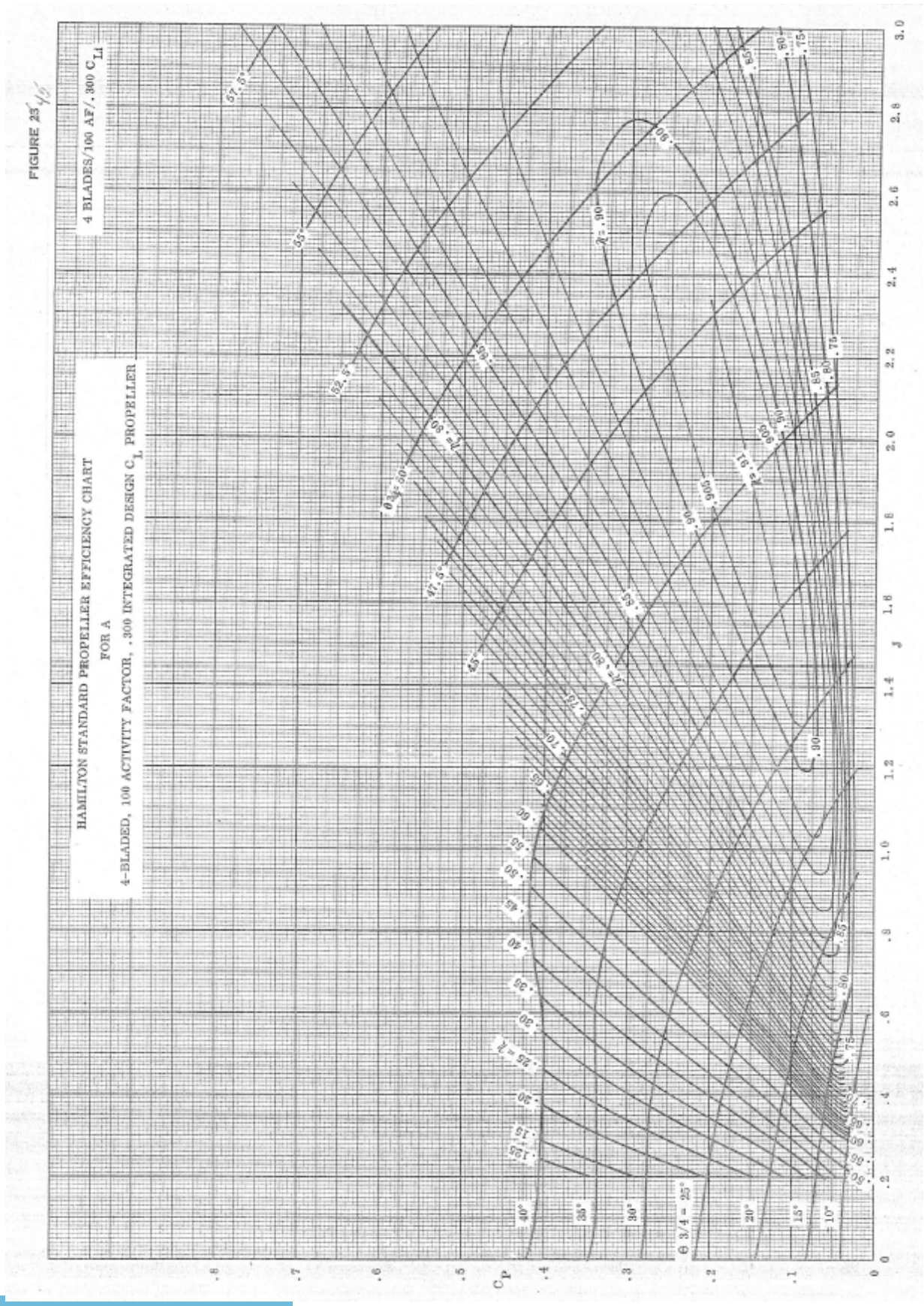

Figure 81: Hamilton Standard propeller map: activity factor = 100, integrated design lift coefficient = 0.30

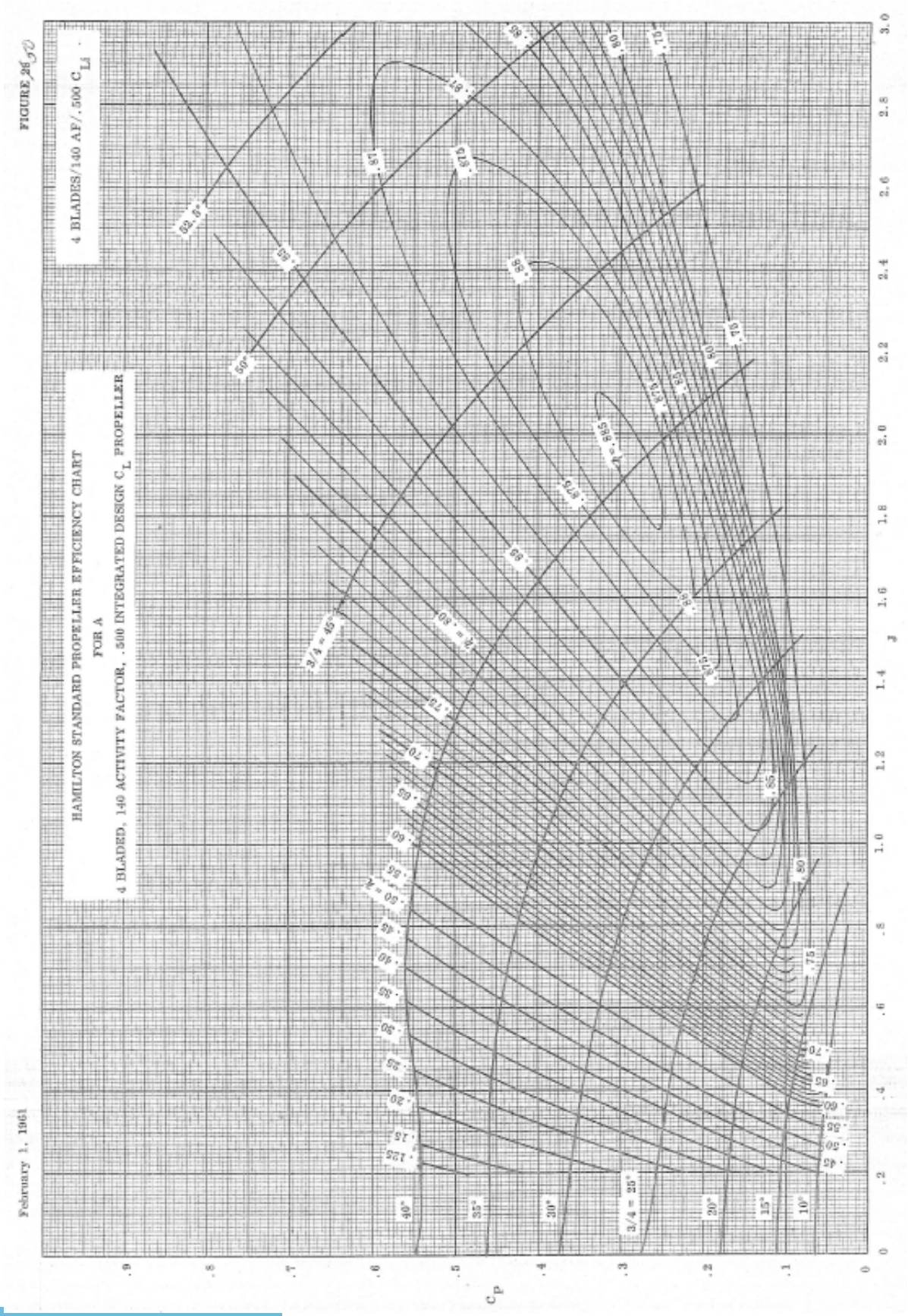

Figure 82: Hamilton Standard propeller map: activity factor = 140, integrated design lift coefficient = 0.50

APPENDIX B

DATA FOR DRAG COEFFICIENT STUDY IN EXPERIMENT 3

Table 32: Low fidelity level data set for the additional experiment on the drag coefficient

Design C_l	Thickness Ratio	Angle of Attack (deg)	C_d
0.2	0.09	-4	0.0110
0.2	0.09	-2	0.0069
0.2	0.09	0	0.0046
0.2	0.09	2	0.0048
0.2	0.09	4	0.0102
0.2	0.09	6	0.0242
0.2	0.09	8	0.0486
0.2	0.12	-4	0.0095
0.2	0.12	-2	0.0054
0.2	0.12	0	0.0052
0.2	0.12	2	0.0052
0.2	0.12	4	0.0090
0.2	0.12	6	0.0133
0.2	0.12	8	0.0233
0.2	0.15	-4	0.0090
0.2	0.15	-2	0.0057
0.2	0.15	0	0.0059
0.2	0.15	2	0.0058
0.2	0.15	4	0.0075
0.2	0.15	6	0.0135
0.2	0.15	8	0.0182
0.3	0.09	-4	0.0119
0.3	0.09	-2	0.0073
0.3	0.09	0	0.0046
0.3	0.09	2	0.0047
0.3	0.09	4	0.0104
0.3	0.09	6	0.0115
0.3	0.09	8	0.0439

Continuation of low fidelity level data set for the additional experiment on the drag coefficient

Design C_l	Thickness Ratio	Angle of Attack (deg)	C_d
0.3	0.12	-4	0.0096
0.3	0.12	-2	0.0062
0.3	0.12	0	0.0051
0.3	0.12	2	0.0053
0.3	0.12	4	0.0084
0.3	0.12	6	0.0138
0.3	0.12	8	0.0221
0.3	0.15	-4	0.0095
0.3	0.15	-2	0.0058
0.3	0.15	0	0.0059
0.3	0.15	2	0.0060
0.3	0.15	4	0.0073
0.3	0.15	6	0.0131
0.3	0.15	8	0.0193
0.4	0.09	-4	0.0133
0.4	0.09	-2	0.0074
0.4	0.09	0	0.0047
0.4	0.09	2	0.0047
0.4	0.09	4	0.0104
0.4	0.09	6	0.0156
0.4	0.09	8	0.0422
0.5	0.09	-4	0.0160
0.5	0.09	-2	0.0075
0.5	0.09	0	0.0047
0.5	0.09	2	0.0048
0.5	0.09	4	0.0096
0.5	0.09	6	0.0151
0.5	0.09	8	0.0323
0.5	0.12	-4	0.0100
0.5	0.12	-2	0.0076
0.5	0.12	0	0.0053
0.5	0.12	2	0.0055
0.5	0.12	4	0.0075
0.5	0.12	6	0.0145
0.5	0.12	8	0.0201
0.5	0.15	-4	0.0097
0.5	0.15	-2	0.0070
0.5	0.15	0	0.0060
0.5	0.15	2	0.0064
0.5	0.15	4	0.0076
0.5	0.15	6	0.0143
0.5	0.15	8	0.0222

Continuation of low fidelity level data set for the additional experiment on the drag coefficient

Design C_l	Thickness Ratio	Angle of Attack (deg)	C_d
0.7	0.09	-4	0.0218
0.7	0.09	-2	0.0078
0.7	0.09	0	0.0049
0.7	0.09	2	0.0050
0.7	0.09	4	0.0086
0.7	0.09	6	0.0161
0.7	0.09	8	0.0269
0.7	0.12	-4	0.0111
0.7	0.12	-2	0.0080
0.7	0.12	0	0.0055
0.7	0.12	2	0.0059
0.7	0.12	4	0.0073
0.7	0.12	6	0.0154
0.7	0.12	8	0.0229
0.7	0.15	-4	0.0103
0.7	0.15	-2	0.0086
0.7	0.15	0	0.0063
0.7	0.15	2	0.0067
0.7	0.15	4	0.0083
0.7	0.15	6	0.0146
0.7	0.15	8	0.0240

Table 35: Validation data set for the additional experiment on the drag coefficient

Design C_l	Thickness Ratio	Angle of Attack (deg)	C_d
0.2	0.09	-2	0.0079
0.2	0.09	0	0.0047
0.2	0.09	2	0.0071
0.2	0.09	4	0.0099
0.2	0.09	6	0.0206
0.2	0.12	-4	0.0105
0.2	0.12	-2	0.0074
0.2	0.12	0	0.0070
0.2	0.12	2	0.0082
0.2	0.12	4	0.0107
0.2	0.12	6	0.0147
0.2	0.12	8	0.0211
0.3	0.09	-4	0.0108
0.3	0.09	-2	0.0073
0.3	0.09	0	0.0064
0.3	0.09	2	0.0065
0.3	0.09	4	0.0092
0.3	0.09	6	0.0199
0.3	0.12	-4	0.0116
0.3	0.12	-2	0.0070
0.3	0.12	0	0.0069
0.3	0.12	2	0.0081
0.3	0.12	4	0.0101
0.3	0.12	6	0.0151
0.3	0.12	8	0.0283
0.3	0.15	-4	0.0118
0.3	0.15	-2	0.0084
0.3	0.15	0	0.0077
0.3	0.15	2	0.0084
0.3	0.15	4	0.0104
0.3	0.15	6	0.0143
0.3	0.15	8	0.0220
0.4	0.09	-4	0.0122
0.4	0.09	-2	0.0078
0.4	0.09	0	0.0072
0.4	0.09	2	0.0069
0.4	0.09	4	0.0082
0.4	0.09	6	0.0169
0.4	0.09	8	0.0430

Continuation of validation data set for the additional experiment on the drag coefficient

Design C_l	Thickness Ratio	Angle of Attack (deg)	C_d
0.5	0.09	-4	0.0153
0.5	0.09	-2	0.0074
0.5	0.09	0	0.0061
0.5	0.09	2	0.0070
0.5	0.09	4	0.0101
0.5	0.09	6	0.0198
0.5	0.12	-4	0.0111
0.5	0.12	-2	0.0089
0.5	0.12	0	0.0070
0.5	0.12	2	0.0069
0.5	0.12	4	0.0097
0.5	0.12	6	0.0155
0.5	0.15	-4	0.0123
0.5	0.15	-2	0.0097
0.5	0.15	0	0.0085
0.5	0.15	2	0.0090
0.5	0.15	4	0.0115
0.5	0.15	6	0.0164
0.5	0.15	8	0.0245
0.7	0.09	-4	0.0237
0.7	0.09	-2	0.0112
0.7	0.09	0	0.0076
0.7	0.09	2	0.0079
0.7	0.09	4	0.0102
0.7	0.09	6	0.0151
0.7	0.09	8	0.0261
0.7	0.12	-4	0.0153
0.7	0.12	-2	0.0093
0.7	0.12	0	0.0091
0.7	0.12	2	0.0100
0.7	0.12	4	0.0108
0.7	0.12	6	0.0134
0.7	0.12	8	0.0232
0.7	0.15	-4	0.0144
0.7	0.15	-2	0.0127
0.7	0.15	0	0.0115
0.7	0.15	2	0.0111
0.7	0.15	4	0.0124
0.7	0.15	6	0.0163

APPENDIX C

FLOW ANALYSIS METHODS

The fluid flow around objects can be analyzed using three main approaches: experimental, theoretical, and numerical. All three methods have unique advantages and some unfortunate disadvantages. Experimental methods are those where a physical model is built and tested in an environment appropriate for the problem at hand, such as a wind tunnel test. The advantages of experimental methods are that the results are realistic and useful for learning about important trends that may not be well understood, or even for discovering new trends. However, experimental methods require costly equipment and models. There are also concerns related to scaling, tunnel corrections, and measurement difficulty.

Numerical (or computational) methods are based on the Navier-Stokes equations. Even though these equations were developed over 150 years ago, no closed form solutions to the full set of equations exists. However, the equations can be solved through numerical integration using a computer. These types of programs or codes are referred to as computational fluid dynamics (CFD) programs. Numerical methods are advantageous because they can solve problems with complicated geometries and flow physics, or simulate flow conditions that are challenging to test experimentally. They can also obtain information about regions of the flow that are difficult to test with experimental equipment. Relative to experimental methods, numerical methods are more cost effective because they don't require expensive test equipment and changes to the tests can be made more easily. The disadvantages are that the simulations still use simplified physics, and require extensive computational power. Numerical errors may exist and can propagate throughout a solution. However, these methods

are being used more and more as computers become faster.

Theoretical methods are physics based like the Navier-Stokes equations, but a number of simplifying assumptions are made to make the equations easier to solve. The simplified equations can be solved nearly instantaneously, but the solutions are limited to idealized geometries and simple flow physics.

All three of these approaches are used to support each other in the real world. Theoretical methods are typically used during the early conceptual design stages of a project. CFD programs are validated using experimental data. Experimental tests are used to validate nearly finalized designs. The three categories of flow analysis methods applied to propeller systems are discussed in the following sections.

C.1 Experimental Methods

Experimental testing on advanced propeller systems began in the mid 1970s due to the high oil prices. The testing program was a collaboration between Hamilton Standard, General Electric, and NASA. In order for these new engines to become a viable alternative to the traditional turbofan, engineers knew they needed to match the speeds of current commercial aircraft. Propellers have always been more efficient than turbofan engines; however, their efficiency dramatically decreases at high speeds due to compressibility losses. Thus, engineers attempted to incorporate every possible way of mitigating compressibility losses into their designs. Some of the major design themes were, small thickness to chord ratio, high power loading to reduce diameter, higher number of blades to reduce individual blade loading, high tip sweep angle. The nacelle and spinner geometry was even incorporated into the design to reduce choking of the flow near the root of the blade. Seven different single rotating geometries were tested with efficiencies approaching 80%. Blade sweep increased the efficiency by 3%. However, engineers found that there was significant losses due to inherent helical trajectory (swirl) of the air leaving the highly loaded blades, and they came to the

conclusion that most of these losses could be recovered by including a second counter rotating blade row. Due to the success of the single rotating tests, NASA and GE decided to fund research for counter rotating systems.

Engineers at GE decided the pusher type of counter rotating system, called the unducted fan (UDF), would perform best compared to the conventional turbofan. The overall objective was to investigate, both theoretical and experimental counter rotating blade designs. Hoff wrote a detailed report of this testing program [47]. Full development of the UDF began in 1983. Scaled tests rigs (see Figure 83) were built with 24.5 inch diameter blades to match those tested by Hamilton Standard. Tests were conducted in GE's anechoic testing chamber as well at the 8x6 supersonic tunnel and 9x16 low speed tunnel at NASA Lewis (now called NASA Glenn Research Center). Furthermore, recent tests were also conducted as part of NASA's Environmentally Responsible Aviation (ERA) project.

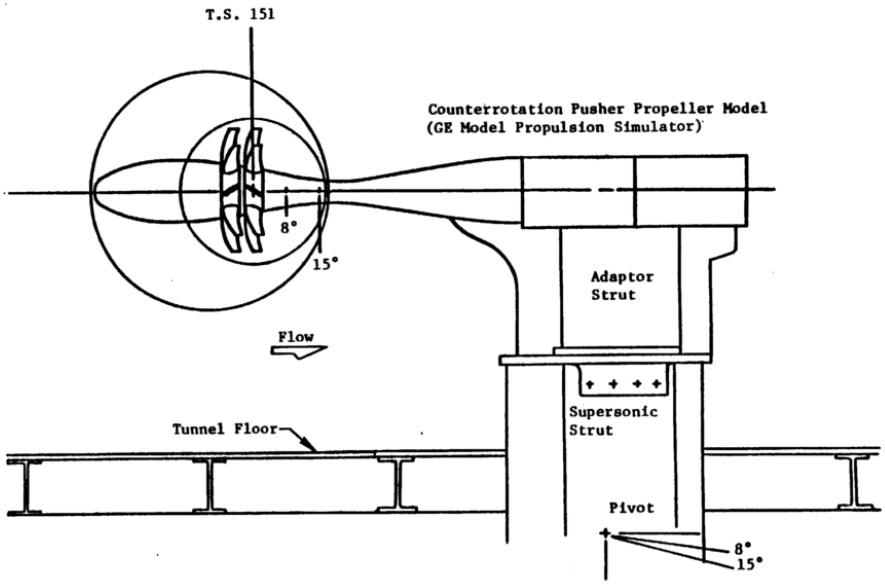

Figure 83: Pusher configuration rig schematic for NASA 8x6 supersonic wind tunnel[47]

C.2 Numerical Methods

Numerical methods are considered to be higher fidelity then theoretical methods because less assumptions are made i.e. they are a higher order simulation. However, not making as many assumptions results a complex set of partial differential equations that can only be solved through time consuming computer algorithms. Some past results for numerical simulations of open rotors are discussed in Hoff, Khalid et al., and Srivastava [47, 58, 107]. Go through the details of these reports.

C.3 Theoretical Methods

The primary focus of propeller modeling will be to understand how changes to the blade geometry impacts the performance. The specific performance metrics that are needed are the thrust coefficient C_T, power coefficient C_P, and efficiency η. A majority of the following discussion on theoretical methods is based on *Aerodynamics of V/STOL Flight* by McCormick and *Mechanics of Flight* by Phillips[77, 94].

C.3.1 Momentum Theory

Classical momentum theory is based on the principles of momentum and energy, and is one of the most basic methods for predicting propeller performance. Momentum theory is based on the idea that the flow through a propeller is exactly captured within a streamtube. The streamtube extends to infinity upstream and downstream from the propeller. Figure 84 shows a streamtube with a thin disc representing the propeller blades. Since the individual propeller blades are replaced with a uniform disk, the following assumptions are made.

- The flow is inviscid and incompressible.
- The velocity and pressure are constant across each cross section of the streamtube.

- There is no rotational component of flow (better approximation for a pair of counter rotating propellers.)
- The static pressure inside and outside the propeller slipstream are equal to the undisturbed free stream static pressure.

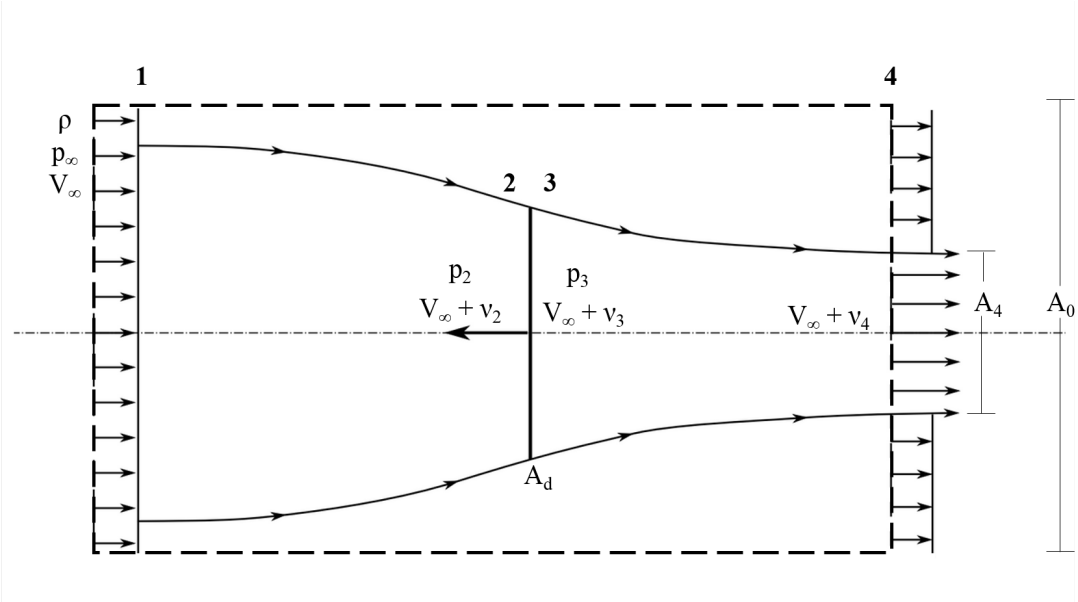

Figure 84: Momentum theory diagram.

The notation in Figure 84 will remain constant throughout the chapter. Where... Explain notation in the figure.

The derivation of momentum theory begins with the conservation of mass. The mass flow rate at station 1 is

$$\dot{m}_1 = \rho V_\infty A_o \tag{50}$$

and the mass flow rate out at station 4 is

$$\dot{m}_4 = \rho V_\infty (A_o - A_4) + \rho (V_\infty + \nu_4) A_4, \tag{51}$$

where ν_4 should be thought of as some additional velocity or excess velocity due to the rotor at the far wake. There also must be some inflow through the top and bottom

of the control volume, $\dot{m}_{tb}$. Conservation of mass states that the mass flow into the control volume must equal the mass flow out of the control volume. Therefore,

$$\rho V_\infty A_o + \dot{m}_{tb} = \rho V_\infty (A_o - A_4) + \rho (V_\infty + \nu_4) A_4. \tag{52}$$

Thus,

$$\dot{m}_{tb} = \rho \nu_4 A_4 \tag{53}$$

The next step is to perform conservation of mass through the rotor disk.

$$\dot{m}_{disk} = \rho A_d (V_\infty + \nu_2) = \rho A_d (V_\infty + \nu_3) \tag{54}$$

Where ν_2 and ν_3 are the excess velocities immediately upstream and downstream from the rotor disk. Recall that the areas just before and after the disk are equal ($A_2 = A_3 = A_d$). From the continuity equation applied immediately upstream and downstream from the rotor disk, it is known that there is not velocity jump across the disk. Therefore, $\nu_2 = \nu_3 = V_i$, where V_i will be referred to as induced velocity throughout this entire section. Also,

$$\dot{m}_{disk} = \rho A_4 (V_\infty + \nu_4) \tag{55}$$

from conservation of mass.

From conservation of momentum, the thrust is equal to the momentum flux out of the control volume minus the momentum flux into the control volume. Note: momentum flux is $\dot{m}V$.

$$T = \left[\rho V_\infty^2 (A_o - A_4) + \rho (V_\infty + \nu_4)^2\right] - \left[\rho V_\infty^2 A_o + \rho \nu_4 A_4 V_\infty\right] \tag{56}$$

This simplifies to

$$T = \rho A_4 (V_\infty + \nu_4) \nu_4, \tag{57}$$

which says that the thrust is equal to the mass flow rate through the rotor disk times the excess velocity between stations 1 through 4.

Axial force, or thrust T, on the disk can also be expressed in terms of a pressure difference.

$$T = A_d(p_3 - p_2) \tag{58}$$

where A_d is the area of the disk, p_2 is the upstream pressure, and p_3 is the downstream pressure.

The continuity equation is used to show that there is no change in velocity across the disk; however, velocity does change as the fluid approaches the propeller disk and as it leaves the propeller disk. Apply Bernoulli's equation above and below the disk.

$$p_\infty + \frac{1}{2}\rho V_\infty^2 = p_2 + \frac{1}{2}\rho(V_\infty + V_i)^2 \tag{59}$$

$$p_3 + \frac{1}{2}\rho(V_\infty + V_i)^2 = p_\infty + \frac{1}{2}\rho(V_\infty + \nu_4)^2 \tag{60}$$

Subtract Equation 59 from Equation 60

$$p_3 - p_2 = \rho\left(V_\infty + \frac{\nu_4}{2}\right)\nu_4 \tag{61}$$

Now that we have obtained a relationship for the pressure difference across the disk, this can be plugged back into Equation 58 to get an equation for thrust in terms of velocity.

$$T = A_d(p_3 - p_2) = A_d\rho\left(V_\infty + \frac{\nu_4}{2}\right)\nu_4 \tag{62}$$

In order to get the thrust in terms of the free stream conditions and the induced velocity of the rotor disk, the excess velocity in the far wake needs to be determined. There are still too many unknowns (A_4 and ν_4) to set Equations 57 and 62 equal to each other. However, recall Equation 57 states that the thrust is equal to the mass flow rate through the rotor times the excess velocity between stations 1 and 4, and that $\dot{m}_{disk} = \rho A_d(V_\infty + \nu)$. Therefore Equation 57 can be written as

$$T = \rho A_d(V_\infty + V_i)\nu_4. \tag{63}$$

Setting Equation 63 equal to 62 and simplifying results in

$$\nu_4 = 2V_i \tag{64}$$

which sates that the excess velocity in the far wake is twice the induced velocity. Therefore, the streamtube must contract. The final equation for thrust is

$$T = \rho A_d (V_\infty + V_i) 2V_i \tag{65}$$

which can be put into quadratic form and solved to find the induced velocity.

$$0 = 2\rho A_d V \nu^2 + 2\rho A_d V_\infty V_i - T \tag{66}$$

$$V_i = -\frac{V_\infty}{2} \pm \sqrt{\frac{V_\infty^2}{4} + \frac{T}{2\rho A_d}} \tag{67}$$

The positive solution corresponds to a propeller and the negative corresponds to a wind turbine where energy is removed from the flow. At sea level static conditions where $V_\infty = 0$

$$V_i = \sqrt{\frac{T}{2\rho A_d}}. \tag{68}$$

We now have an equation for the induced velocity in terms of thrust and free stream velocity. This same expression for induced velocity can be put into the equation for power as well.

To find the ideal efficiency, the ideal power the propeller supplies to the air is needed which is the difference in the flux of kinetic energy passing through the propeller disk. The enthalpy can be ignored because the fluid is assumed to be incompressible and the ultimate static pressures far upstream and downstream are equal to the ambient static pressure.

$$P_i = \frac{1}{2}\dot{m}((V_\infty + 2V_i)^2 - V_\infty^2)) \tag{69}$$

which simplifies to

$$P_i = 2\dot{m} V_i (V_i + V_\infty). \tag{70}$$

Recall that $T = \dot{m} 2V_i$. Therefore the final equation for ideal power is

$$P_i = T(V_i + V_\infty). \tag{71}$$

Equation 67 for induced velocity can be plugged in to get the ideal power in terms of the thrust and free stream velocity. The ideal efficiency is defined as the ratio of the useful power over the ideal power,

$$\eta_i = \frac{P_{use}}{P_i}, \tag{72}$$

where $P_{use} = TV_\infty$. The ideal efficiency simplifies as follows

$$\eta_i = \frac{TV_\infty}{T(V_\infty + V_i)} = \frac{V_\infty}{V_\infty + V_i} = \frac{1}{1 + \frac{V_i}{V_\infty}} \tag{73}$$

Momentum theory provides an idealized one-dimensional solution that is frequently regarded as an upper limit for propeller performance, yet the assumptions significantly limit its application. The method does not provide any information with regard to the details of the geometry, and it does not apply well to highly loaded blades. A more sophisticated approach must be taken.

C.3.2 Blade Element Theory

Blade element theory takes into account each rotor blade and discretizes the blades radially into small segments of chord, c_r and width, dr. A differential blade element located at radius r is shown in Figure 85. Combined blade element-momentum theory uses principles from momentum theory to obtain an approximation for the induced velocity V_i at each radial section.

As the propeller spins, the differential blade element makes a ring which from basic geometry has and area of

$$A_r = \pi(r + dr)^2 - \pi r^2 = 2\pi r dr. \tag{74}$$

Using Equation 65 from momentum theory and putting it into differential form results the following expression for thrust

$$dT = \rho(2\pi r dr)(V_\infty + V_i \cos\epsilon_b)2V_i \cos\epsilon_b \tag{75}$$

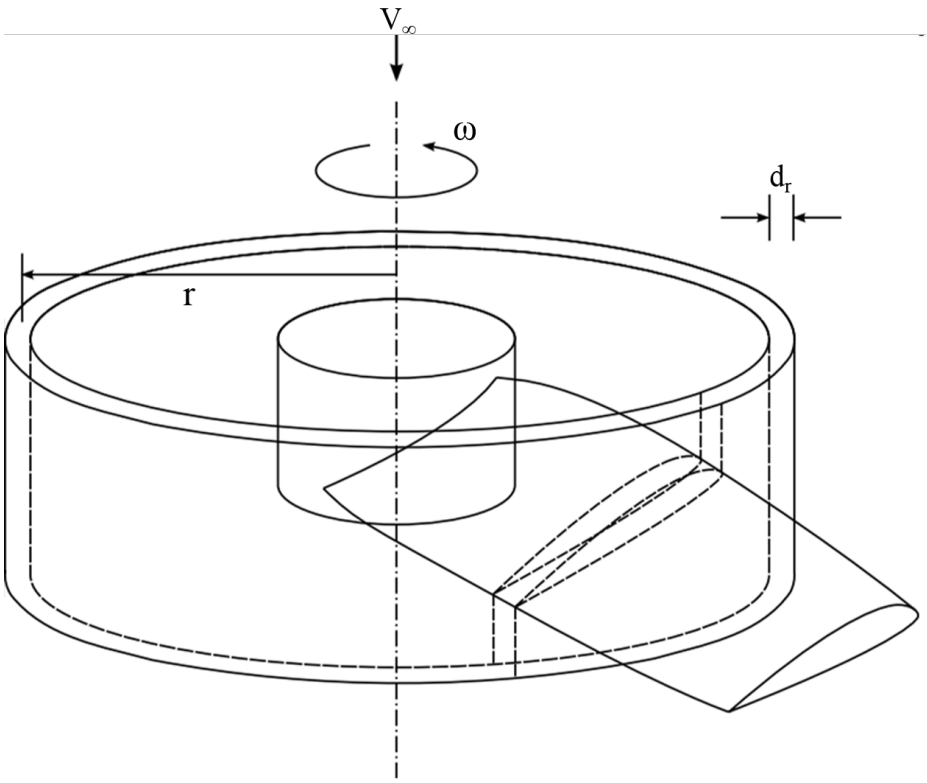

Figure 85: Blade element theory diagram

Some basic equations for lift and drag can be formed by looking more closely at the blade section velocity diagram shown in Figure 86. The blade element in the figure is on the down stroke flying from left to right. From fundamental aerodynamics, the equation for lift on an airfoil is

$$L = \frac{1}{2} C_l \rho A V_e^2, \tag{76}$$

or in differential form

$$dL = \frac{1}{2} C_l \rho (c_r \cdot dr) V_e^2. \tag{77}$$

A second equation for thrust can be obtained from geometry.

$$dT = dL \cos \epsilon_b - dD \sin \epsilon_b = \frac{1}{2} B C_l \rho (c_r \cdot dr) V_e (\cos \epsilon_b - \mu \sin \epsilon_b) \tag{78}$$

where B is the number of blades and μ is the drag-to-lift ratio.

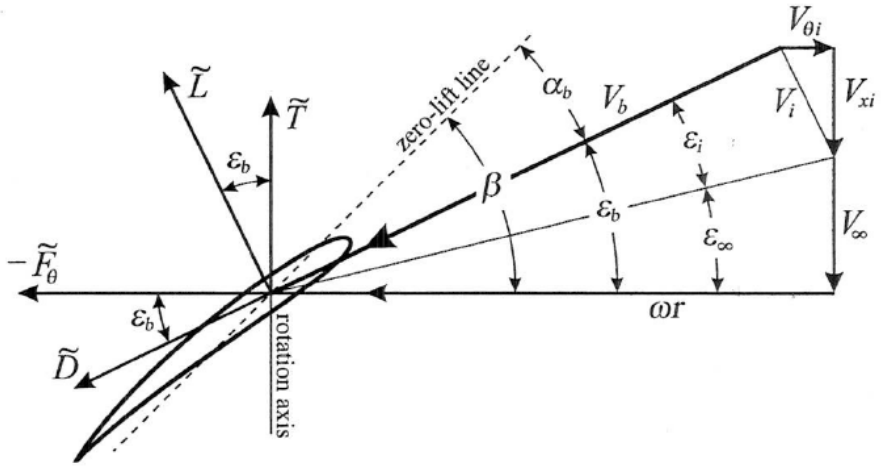

Figure 86: Velocity diagram for a blade section[94]

Next, set Equations 78 and 75 equal to each other and divide both sides by $2\rho dr \cos\epsilon_b$.

$$dT = 2\pi r(V + V_i \cos\epsilon_b)V_i = \frac{1}{4}BC_l cV_e^2(1 - \mu\tan\epsilon_b) \tag{79}$$

Solve for induced velocity

$$V_i = \frac{BC_l cV_e^2(1 - \mu\tan\epsilon_b)}{4(2\pi r)(V_\infty + V_i\cos\epsilon_b)} \tag{80}$$

Some additional simplifications can be made if we assume that ϵ_i and μ are small. $\mu\tan\epsilon_i \approx 0$ and

$$V_i = \frac{BC_l cV_e^2}{4(2\Pi r)(V_\infty + V_i\cos\epsilon_b)}. \tag{81}$$

From geometry

$$\sin\epsilon_b = \frac{V_\infty + V_i\cos\epsilon_b}{V_e}.$$

However,

$$\sin\epsilon_b = \sin(\epsilon_\infty + \epsilon_i) = \sin\epsilon_\infty\cos\epsilon_i + \cos\epsilon_\infty\sin\epsilon_i,$$

and if ϵ_i is small,

$$\sin(\epsilon_\infty + \epsilon_i) = \sin\epsilon_\infty + \epsilon_i\cos\epsilon_\infty.$$

Therefore,

$$V_\infty + V_i\cos\epsilon_i = (\sin\epsilon_\infty + \epsilon_i\cos\epsilon_\infty)V_e.$$

Sub this expression back into equation 81 to get a simplified expression for the induced velocity.

$$V_i = \frac{BC_l c_r V_e}{4(2\pi r)(\sin\epsilon_\infty + \epsilon_i \cos\epsilon_\infty)}. \tag{82}$$

Looking back at Figure 86

$$\tan\epsilon_i \approx \frac{V_i}{V_e} \approx \epsilon_i.$$

Divide equation 82 by V_e

$$\epsilon_i \approx \frac{BC_l c}{4(2\Pi r)(\sin\epsilon_\infty + \epsilon_i \cos\epsilon_\infty)} \tag{83}$$

The solidity ratio, σ, is defined as the ratio of the area of the blades to the area of the propeller disk.

$$\sigma = \frac{BcR}{\Pi R^2} = \frac{Bc}{\Pi R}$$

Also

$$x = \frac{r}{R}$$

Thus, an expression for the induced angle of attack can be obtained

$$\epsilon_i \approx \frac{\sigma}{8x} \frac{a_o(\beta - \epsilon_\infty - \epsilon_i)}{\sin\epsilon_\infty + \epsilon_i \cos\epsilon\infty}, \tag{84}$$

where a_o is the slope to the lift curve ($C_l = a_o\alpha$). Equation 84 can be rearranged into quadratic form shown below.

$$\epsilon_i^2 \cos\epsilon_\infty + \epsilon_i \sin\epsilon_\infty = \frac{\sigma}{8x} a_o(\beta - \epsilon_\infty - \epsilon_i) \tag{85}$$

Since ϵ_i is assumed to be small, the equation for the induced angle of attack can be simplified even further.

$$\epsilon_i \approx \frac{\beta - \epsilon_\infty}{1 + \frac{8x \sin\epsilon_\infty}{\sigma a_o}} \tag{86}$$

We now have an equation for the induced angle of attack given the propeller geometry, β, V_∞, ω, and c_r. The induced angle of attack can be used to find effective

angle of attack, α_e, which is used to obtain C_l and C_d. The thrust and power can now be predicted:

$$T = \frac{B}{2}\rho \int_0^R V_e^2 c_r C_l \cos\epsilon_b (1 - \mu \tan\epsilon_b) dr \tag{87}$$

$$P = \frac{B}{2}\rho \int_0^R \omega R V_e^2 c_r C_l \cos\epsilon_b (\mu + \tan\epsilon_b) dr \tag{88}$$

which can be used to obtain the nondimensional form.

The combined blade element momentum theory is an improvement over momentum theory, yet it does not account for the losses at the tips. Blade element theory by itself, or vortex theory, adds additional improvements to our propeller model. Once again from Figure 86 the elemental thrust and circumferential component of force are

$$dT = l\cos\epsilon_b - d\sin\epsilon_b \tag{89a}$$

$$dF_\theta = -d\cos\epsilon_b - l\sin\epsilon_b. \tag{89b}$$

At radius r

$$\epsilon_b = \tan^{-1}\left(\frac{V_\infty + v_{xi}}{\omega r - V_{\theta i}}\right) \qquad \epsilon_\infty = \tan^{-1}\left(\frac{V_\infty}{\omega r}\right) \qquad \epsilon_i = \epsilon_b - \epsilon_\infty$$

$$\epsilon_i = \tan^{-1}\left(\frac{V_\infty + V_{xi}}{\omega r - V_{\theta i}}\right) - \tan^{-1}\left(\frac{V_\infty}{\omega r}\right)$$

$$\alpha_e = \beta - \epsilon_b = \beta - \epsilon_\infty - \epsilon_i$$

$$V_e^2 = (\omega r - V_{\theta i})^2 + (V_\infty + V_{xi}) = \omega^2 r^2 \left[\left(1 - \frac{V_{\theta i}}{\omega r}\right)^2 + \left(\frac{V_\infty}{\omega r} + \frac{V_{xi}}{\omega r}\right)^2\right] \tag{90}$$

The local section lift and drag at radius r can be expressed as

$$l = \frac{1}{2}\rho\omega^2 r^2 c_r C_l \left[\left(1 - \frac{V_{\theta i}}{\omega r}\right)^2 + \left(\frac{V_\infty}{\omega r} + \frac{V_{xi}}{\omega r}\right)^2\right] \tag{91a}$$

$$d = \frac{1}{2}\rho\omega^2 r^2 c_r C_d \left[\left(1 - \frac{V_{\theta i}}{\omega r}\right)^2 + \left(\frac{V_\infty}{\omega r} + \frac{V_{xi}}{\omega r}\right)^2\right] \tag{91b}$$

which can be subbed into Equations 89a and 89b.

$$dT = \frac{1}{2}\rho\omega^2 r^2 c_r \left[\left(1 - \frac{V_{\theta i}}{\omega r}\right)^2 + \left(\frac{V_\infty}{\omega r} + \frac{V_{xi}}{\omega r}\right)^2\right](C_l\cos\epsilon_b - C_d\sin\epsilon_b) \tag{92a}$$

$$dF_\theta = -\frac{1}{2}\rho\omega^2 r^2 c_r \left[\left(1 - \frac{V_{\theta i}}{\omega r}\right)^2 + \left(\frac{V_\infty}{\omega r} + \frac{v_{xi}}{\omega r}\right)^2\right](C_d\cos\epsilon_b - C_l\sin\epsilon_b) \tag{92b}$$

The elemental thrust for the full prop is

$$\frac{dT}{dr} = \frac{B}{2}\rho\omega^2 r^2 c_r \left[\left(1 - \frac{v_{\theta i}}{\omega r}\right)^2 + \left(\frac{V_\infty}{\omega r} + \frac{V_{xi}}{\omega r}\right)^2\right](C_l \cos\epsilon_b - C_d \sin\epsilon_b) \tag{93}$$

and the torque, Q, required to turn the propeller is the moment that is produced about the axis of propeller rotation.

$$\begin{aligned}\frac{dQ}{dr} &= -BrdF_\theta \\ &= \frac{B}{2}\rho\omega^2 r^3 c_r \left[\left(1 - \frac{V_{\theta i}}{\omega r}\right)^2 + \left(\frac{V_\infty}{\omega r} + \frac{V_{xi}}{\omega r}\right)^2\right](C_d \cos\epsilon_b - C_l \sin\epsilon_b)\end{aligned} \tag{94}$$

Given that the propeller geometry is known along with the forward speed and rotational speed, the section lift and drag coefficients are a function of the radial coordinate, r, and the local effective angle of attack, α_i. However, Equations 93 and 94 still contain four unknowns: elemental thrust dT, elemental torque dQ, and the two components of induced velocity, $V_{\theta i}$ and V_{xi}. More information is needed.

C.3.3 Vortex Theory of Propellers

A propeller is nothing more than a rotating wing. As such, lift cannot be generated on a propeller without the generation of vorticity. Similar to a wing, vortex lifting law applied to a finite propeller blade can be used to relate the bound vorticity to the lift. The lift is related to the fluid density, ρ, effective velocity, V_e, and section circulation, Γ through the Kutta-Joukowski theorem.

$$l = \rho V_e \Gamma \tag{95}$$

Goldstein developed a theory for predicting the induced velocity in 1929[41]. He makes two key assumptions: the vortex sheet shed from a rotating propeller is assumed to lie on a helical surface of constant pitch, and the induced velocity is normal to the resultant velocity. Some additional velocity relationships can be made using

the normality assumption.

$$V_e = \sqrt{\omega^2 r^2 + V_\infty^2}\cos\epsilon_i = \frac{\omega r}{\cos\epsilon_\infty}\cos\epsilon_i \tag{96a}$$

$$V_i = \sqrt{\omega^2 r^2 + V_\infty^2}\sin\epsilon_i = \frac{\omega r}{\cos\epsilon_\infty}\sin\epsilon_i \tag{96b}$$

$$V_{xi} = V_i\cos\epsilon_b = \frac{\omega r}{\cos\epsilon_\infty}\sin\epsilon_i\cos(\epsilon_i + \epsilon_\infty) \tag{96c}$$

$$V_{\theta i} = V_i\sin\epsilon_b = \frac{\omega r}{\cos\epsilon_\infty}\sin\epsilon_i\sin(\epsilon_i + \epsilon_\infty) \tag{96d}$$

Applying Equations 90 and 91a to 95 relates the local section circulation to the local velocities.

$$\Gamma = \frac{1}{2}\omega r c_r C_l\sqrt{\left(1 - \frac{V_{\theta i}}{\omega r}\right)^2 + \left(\frac{V_\infty}{\omega r} + \frac{V_{xi}}{\omega r}\right)^2} \tag{97}$$

or by applying the relationships in Equations 96

$$\Gamma = \frac{1}{2}\omega r c_r C_l\frac{\cos\epsilon_i}{\cos\epsilon_\infty} \tag{98}$$

From Goldstein's vortex theory

$$B\Gamma = 4\pi\kappa r V_{\theta i} \tag{99}$$

where the proportionality constant, κ, known as Goldstein's kappa factor, can be found graphically[41]. An approximation to Goldstein's kappa factor can be found from the following

$$B\Gamma \approx 4\pi f r V_{\theta i}. \tag{100}$$

where f is known as Prandtl's tip loss factor cite(Prandtl and Betz1927) which is expressed as

$$f = \frac{2}{\pi}\cos^{-1}\left\{\exp\left[-\frac{B(1 - 2r/d_p)}{2\sin\beta_R}\right]\right\}, \tag{101}$$

where β_R is the pitch angle at the tip of the blade. Applying equations 96d and 98 to 100 gives us

$$\frac{Bc_r}{16r}C_l - \cos^{-1}\left\{\exp\left[-\frac{B(1 - 2r/d_p)}{2\sin\beta_t}\right]\right\}\tan\epsilon_i\sin(\epsilon_\infty + \epsilon_i) = 0 \tag{102}$$

If we know the propeller geometry, the forward velocity, and the rotational speed, the only unknown is the induced angle, ϵ_i, which can be solved for numerically.

Now that he induced angle of attack is known, the total thrust and torque can be found by integrating equations 93 and 94 from the hub, r_h, to the tip, R.

$$\begin{aligned} T &= \int_{r_h}^{R} \frac{dT}{dr} dr \\ &= \frac{B\rho\omega^2}{2} \int_{r_h}^{R} r^2 c_r \frac{\cos^2 \epsilon_i}{\cos^2 \epsilon_\infty} \left[C_l \cos(\epsilon_\infty + \epsilon_i) - C_d \sin(\epsilon_\infty + \epsilon_i) \right] dr \end{aligned} \tag{103}$$

$$\begin{aligned} Q &= \int_{r_h}^{R} \frac{dQ}{dr} dr \\ &= \frac{B\rho\omega^2}{2} \int_{r_h}^{R} r^3 c_r \frac{\cos^2 \epsilon_i}{\cos^2 \epsilon_\infty} \left[C_d \cos(\epsilon_\infty + \epsilon_i) + C_l \sin(\epsilon_\infty + \epsilon_i) \right] dr \end{aligned} \tag{104}$$

This all sounds great except that these propellers will be operating in the transonic region. Therefore, some of the assumptions made in Goldstein's vortex method may not be valid.

Chang and Miller extended the capabilities of vortex theory to include compressibility and sweep[20, 81]. Their predictions for advanced single rotating propellers are quite accurate. Figure 87 shows a comparison of the results from Chang's method with SR-3 experimental results. However, the accuracy decreases when applied to counter rotating systems as shown by Lesieutre[66].

C.4 Empirical Methods

Empirical methods rely on knowledge from past experiments. This past experimental data is typically fit with some sort of regression model to create a surrogate. These types of models work great for understanding conventional designs, yet they are usually not appropriate for advanced concepts. Extrapolating beyond the bounds of your data does not work well with regressions.

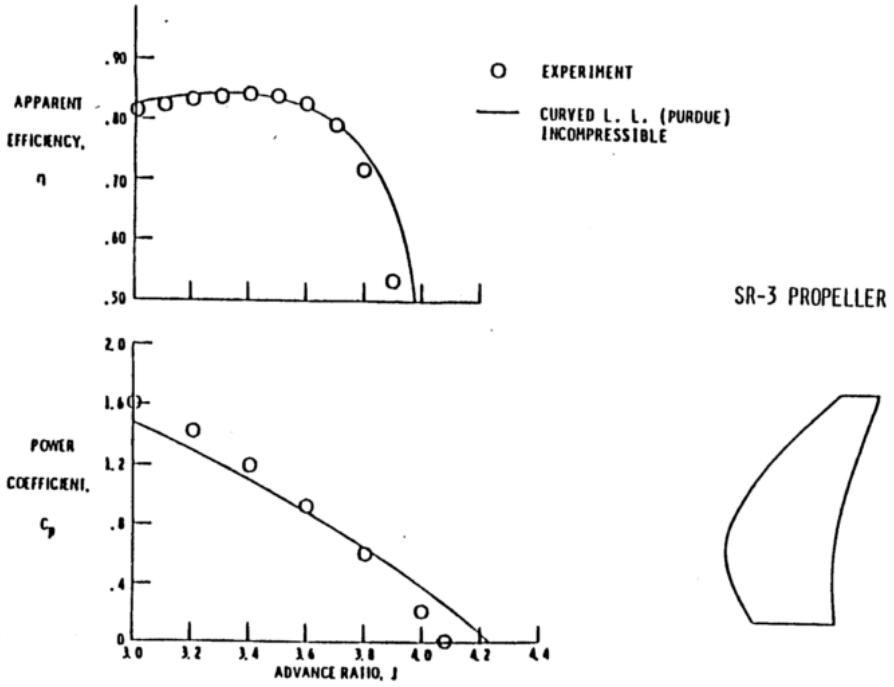

Figure 87: Comparison of results from Chang's prediction with SR-3 experimental data[20]

C.5 Current Methods

There are two current approaches for predicting the performance of counter rotating advanced propellers. The first is to use a system identification method. Unfortunately, there are only two counter rotating geometries available to the public. There is no way to validate a surrogate model made from only two data points. A decision maker would not trust the predictions coming from this model.

Scaling the performance map from a known system to match the design point of a new system is another method commonly used for turbomachinery components. The problem with scaling is knowing how much scaling is satisfactory. Scaling to a design with different geometries also introduces more error.

REFERENCES

[1] *Generalized Method of Propeller Performance Estimation*. Hamilton Standard, pdb 6101 r ed., 1963.

[2] *Annual Energy Outlook 2013*. U.S. Energy Information Administration, 2013.

[3] Abbott, I. H. and Von Doenhoff, A. E., *Theory Of Wing Sections*. New York: Dover Publications, 1959.

[4] Aeschliman, D. P. and Oberkampf, W. L., "Experimental Methodology for Computational Fluid Dynamics Code Validation," *AIAA Journal*, vol. 36, no. 5, 1998.

[5] Airbus, "Mapping Demand: Global Market Forecast 2016-2035," tech. rep., Airbus, 2016.

[6] Anderson Jr, J. D., *Aircraft Performance and Design*. McGraw-Hill, 1999.

[7] Anderson Jr, J. D., *Fundatmentals of Aerodynamics*. McGraw-Hill, fourth edi ed., 2007.

[8] Apley, D. W., Liu, J., and Chen, W., "Understanding the Effects of Model Uncertainty in Robust Design With Computer Experiments," *Journal of Mechanical Design*, vol. 128, no. 4, p. 945, 2006.

[9] Balci, O., "Credibility Assessment of Simulation Results: The State Of The Art," in *Proceedings of the Conference on Simulation Methodology and Validation*, (Orlando), The Society for Computer Simulation, 1987.

[10] Billings, S., *Nonlinear System Identification: NARMAX Methods in the Time, Frequency, and Spatio-Temporal Domains*. West Sussex: John Wiley and Sons, 2013.

[11] Bishop, C. M., *Pattern Recognition and Machine Learning*. New York: Springer Science, 2006.

[12] Black, D. M. and Menthe, R. W., "Aerodynamic Design and Performance Testing of an Advanced 30 Degree Swept Eight Bladed Propeller at Mach Numbers From 0.20 to 0.85," *NASA CR-3047*, 1978.

[13] Boehm, B. W., *Software Engineering Economics*. Prentice-Hall, 1981.

[14] Boeing, "Current Market Outlook 2015-2034," tech. rep., Boeing Commercial Airplanes, 2015.

[15] Borst, H. V., "Summary of Propeller Design Procedures and Data. Volume I. Aerodynamic Design and Installation," *USAAMRDL Technical Report 73-34A*, 1973.

[16] Bowles, M. D., *The Apollo of Aeronautics*. Washington, D. C.: U.S. Government Printing Office, 2010.

[17] Bradley, R. G., "CFD Validation Philosophy," in *AGARD Symposium on Validation of Computational Fluid Dynamics*, (Lisbon), pp. 1–1 – 1–6, General Dynamics Corporation, 1988.

[18] Carlton, J., *Marine Propellers and Propulsion*. Elsevier Ltd, first ed., 1994.

[19] Carson, J. S., "Convincing Users Of Model's Validity Is Challenging Aspect Of Modeler's Job," *Industrial Engineering*, vol. 18, no. June, pp. 74–85, 1986.

[20] Chang, L. K., *The Theoretical Performance of High Efficiency Propellers*. Ph.d. thesis, Purdue University, 1980.

[21] Cheng, C.-t., Niu, W.-j., Feng, Z.-k., Shen, J.-j., and Chau, K.-w., "Daily Reservoir Runoff Forecasting Method Using Artificial Neural Network Based on Quantum-behaved Particle Swarm Optimization," *Water*, vol. 7, no. 8, pp. 4232–4246, 2015.

[22] Coney, W. B., *A Method For The Design Of A Class Of Optimum Marine Propulsors*. Ph.d thesis, Massachusetts Institute of Technology, 1989.

[23] Cressie, N., "The Origins of Kriging," *Mathematical Geology*, vol. 22, no. 3, pp. 239–252, 1990.

[24] Cumpsty, N., *Jet Propulsion: A Simple Guide to the Aerodynamic and Thermodynamic Design and Performance of Jet Engines*. Cambridge University Press, 2nd ed., 2003.

[25] Currin, C., Mitchell, T., Morris, M., and Ylvisaker, D., "Bayesian Prediction of Deterministic Functions, With Applications to the Design and Analysis of Computer Experiments," *Journal of the American Statistical Association*, vol. 86, no. 416, pp. 953–963, 1991.

[26] Delaurentis, D. A. and Mavris, D. N., "Uncertainty Modeling and Management in Multidisciplinary Analysis and Synthesis," in *38th Aerospace Sciences Meeting & Exhibit*, no. January, (Reno), American Institute of Aeronautics and Astronautics, 2000.

[27] Domke, B. *http://www.b-domke.de/AviationImages/Propfan/0809.html*, Aviation Images.

[28] Draper, D., Hodges, J., Leamer, E., Morris, C., and Rubin, D., "A Research Agenda for Assessment and Propagation of Model Uncertainty," *N-2683-RC, RAND Corporation*, 1987.

[29] Draper, D., "Assessment and Propagation of Model Uncertainty," *Journal of the Royal Statistical Society. Series B*, vol. 57, no. 1, pp. 45–97, 1995.

[30] Drela, M. and Youngren, H., "Xrotor Propeller Design Code."

[31] Drela, M. and Youngren, H., "Xfoil 6.9 User Primer," 2001.

[32] Epps, B. P., "OpenProp v2.4 Theory Document," tech. rep., 2010.

[33] Epps, B. P., Stanway, M. J., and Kimball, R. W., "OpenProp: An Open-source Design Tool for Propellers and Turbines," tech. rep., Massachusetts Institute of Technology, Cambridge, 2009.

[34] Federal Aviation Administration, "FAA Aerospace Forecast: Fiscal Years 2016-2036," tech. rep., 2016.

[35] Ferson, S. and Oberkampf, W. L., "Validation of Imprecise Probability Models," *International Journal of Reliability and Safety*, vol. 3, pp. 3–22, 2009.

[36] Ferson, S., Oberkampf, W. L., and Ginzburg, L., "Model Validation and Predictive Capability for the Thermal Challenge Problem," *Computer Methods in Applied Mechanics and Engineering*, vol. 197, pp. 2408–2430, 2008.

[37] Fishman, G. S. and Kiviat, P. J., "The Statistics of Discrete-Event Simulation," *Simulation*, vol. 10, pp. 185–195, 1968.

[38] Forrester, A. I. J., Sóbester, A., and Keane, A. J., *Engineering Design via Surrogate Modelling: A Practical Guide*. John-Wiley and Sons, 2008.

[39] Ghoreyshi, M., Badcock, K. J., and Wookgate, M. A., "Accelerating the Numerical Generation of Aerodynamic Models for Flight Simulation," *Journal of Aircraft*, vol. 46, no. 3, pp. 972–980, 2009.

[40] Glauert, H., *The Elements of Aerofoil and Airscrew Theory*. Cambridge University Press, 1926.

[41] Goldstein, S. and A, P. R. S. L., "On the Vortex Theory of the Screw Propeller," *Journal of the Aeronautical Sciences (Institute of the Aeronautical Sciences)*, vol. 4, pp. 1–7, 1929.

[42] Hager, R. D. and Vrabel, D., "Advance Turboprop Project," *NASA SP-495*, 1988.

[43] Helton, J. C., Johnson, J. D., and Oberkampf, W. L., "An Exploration of Alternative Approaches to the Representation of Uncertainty in Model Predictions," *Reliability Engineering and System Safety*, vol. 85, pp. 39–71, jul 2004.

[44] Helton, J. C. and Oberkampf, W. L., "Alternative Representations of Epistemic Uncertainty," *Reliability Engineering and System Safety*, vol. 85, pp. 1–10, jul 2004.

[45] Hodges, J. S., "Uncertainty, policy analysis and statistics," *Statistical Science*, vol. 2, no. 3, pp. 259–291, 1987.

[46] Hoeting, J. A., Madigan, D., Raftery, A. E., and Volinsky, C. T., "Bayesian Model Averaging : A Tutorial," *Statistical Science*, vol. 14, no. 4, pp. 382–417, 1999.

[47] Hoff, G. E., "Experimental Performance and Acoustic Investigation of Modern, Counterrotating Blade Concepts," *NASA CR-185158*, 1990.

[48] Jimenez, H., *A Strategic Planning Approach For Operational-Environmental Tradeoff Assessments in Terminal Areas*. PhD thesis, Georgia Institute of Technology, 2009.

[49] Jones, D. R., "A Taxonomy of Global Optimization Methods Based on Response Surfaces," *Journal of global optimization*, vol. 21, pp. 345–383, 2001.

[50] Kaplan, S. and Garrick, B. J., "On The Quantitative Definition of Risk," *Risk Analysis*, vol. 1, pp. 11–27, mar 1981.

[51] Kass, R. E. and Raftery, A. E., "Bayes Factors," *Journal of American Statistical Association*, vol. 90, no. 430, pp. 773–795, 1995.

[52] Keane, A. J., "Cokriging for Robust Design Optimization," *AIAA Journal*, vol. 50, pp. 2351–2364, nov 2012.

[53] Keane, A. J. and Nair, P. B., *Computational Approaches for Aerospace Design: The Pursuit of Excellence*. West Sussex: John-Wiley and Sons, 2005.

[54] Kennedy, M. C. and O'Hagan, A., "Predicting the Output From a Complex Computer Code When Fast Approximations are Available," *Biometrika*, vol. 87, pp. 1–13, 2000.

[55] Kennedy, M. C. and O'Hagan, A., "Bayesian Calibration of Computer Models," *Journal of the Royal Statistical Society: Series B (Statistical Methodology)*, vol. 63, no. 3, pp. 425–464, 2001.

[56] Kerwin, J. E., "Hydrofoil and Propellers," *MIT 13.04 Lecture Notes*, 2001.

[57] Kerwin, J. E. and Hadler, J. B., *Priniciples of Naval Architecture: Propulsion*. The Society of Naval Architects and Marine Engineers (SNAME), 2010.

[58] Khalid, S. A., Wojno, J. P., Breeze-Stringfellow, A., Lurie, D. P., Wood, T. H., Ramakrishnan, K., and Paliath, U., "Open Rotor Designs for Low Noise and High Efficiency," in *ASME Turbo Expo 2013*, (San Antonio), pp. 1–14, 2013.

[59] Kirby, M. R. and Mavris, D. N., "Forecasting Technology Uncertainty in Preliminary Aircraft Design," in *World Aviation Conference*, (San Francisco), American Institute of Aeronautics and Astronautics, 1999.

[60] Kuchemann, D., *The Aerodynamic Design of Aircraft*. Oxford: Pergamon Press, 1978.

[61] Ladson, C. L., Brooks, C. W., Hill, A. S., and Sproles, D. W., "Computer Program To Obtain Ordinates for NACA Airfoils," *NACA TM 4741*, 1996.

[62] Laurenceau, J. and Sagaut, P., "Building Efficient Response Surfaces of Aerodynamic Functions with Kriging and Cokriging," *AIAA Journal*, vol. 46, pp. 498–507, feb 2008.

[63] Law, A. M. and Kelton, W. D., *Simulation Modeling and Analysis*. McGraw-Hill, 2nd ed., 1991.

[64] Leamer, E. E., *Specification Searches*. New York: John Wiley and Sons, 1978.

[65] Lee, C. and Mavris, D., "Bayesian collaborative sampling for aero-propulsion design of an engine and nacelle," *48th AIAA/ASME/SAE/ASEE Joint Propulsion Conference and Exhibit 2012*, no. August, pp. 1–21, 2012.

[66] Lesieutre, D. J., *The Theoretical Performance of Counter-rotating Propeller Systems*. Master's thesis, Perdue University, 1985.

[67] Lindsey, W. F., Stevenson, B., and Daley, B. N., "Aerodynamic Characteristics of 24 NACA 16-Series Airfoils at Mach Numbers Between 0.3 and 0.8," *NACA TN 1546*, no. September, 1948.

[68] Liu, Y., Chen, W., Arendt, P., and Huang, H.-Z., "Toward a Better Understanding of Model Validation Metrics," *Journal of Mechanical Design*, vol. 133, no. 7, 2011.

[69] Lowry, J. T., *Performance of Light Aircraft*. American Institute of Aeronautics and Astronautics, 1999.

[70] Mackman, T. J., Allen, C. B., Ghoreyshi, M., and Badcock, K. J., "Comparison of Adaptive Sampling Methods for Generation of Surrogate Aerodynamic Models," *AIAA Journal*, vol. 51, pp. 797–808, apr 2013.

[71] Madigan, D., York, J., and Allard, D., "Bayesian Graphical Models for Discrete Data," *International Statistical Review*, vol. 63, no. 2, pp. 215–232, 1995.

[72] Madigan, D., Raftery, A. E., Volinsky, C. T., and Hoeting, J. A., "Bayesian Model Averaging," in *Proceedings of the AAAI Workshop on Integrating Multiple Learned Models*, (Portland), pp. 77–83, 1996.

[73] Mankins, J. C., "Technology readiness and risk assessments: A new approach," *Acta Astronautica*, vol. 65, pp. 1208–1215, nov 2009.

[74] Mankins, J. C., "Technology readiness assessments: A retrospective," *Acta Astronautica*, vol. 65, pp. 1216–1223, nov 2009.

[75] March, A. and Willcox, K., "Multifidelity Approaches for Parallel Multidisciplinary Optimization," in *12th AIAA Aviation Technology, Integration, and Operations (ATIO) Conference*, no. September, (Indianapolis), pp. 1–23, 2012.

[76] Mattingly, J. D., *Elements of Propulsion: Gas Turbines and Rockets*. Reston, VA: American Institute of Aeronautics and Astronautics, 7th ed., 2006.

[77] McCormick, B. W., *Aerodynamics of V/STOL Flight*. Orlando: Academic Press, 1967.

[78] McCormick, B. W., *Aerodynamics, Aeronautics, and Flight Mechanics*. New York: John Wiley and Sons, 2nd ed., 1995.

[79] Mehta, U. B., "Some Aspects of Uncertainty in Computational Fluid Dynamics Results," *Journal of Fluids Engineering*, vol. 113, no. 4, pp. 538–543, 1991.

[80] Meyers, R. H., Montgomery, D. C., and Anderson-Cook, C. M., *Response Surface Methodology*. Hoboken: John Wiley and Sons, third edit ed., 2009.

[81] Miller, C. J., *Optimally Designed Propellers Constrained By Noise*. PhD thesis, Purdue University, 1984.

[82] Minka, T. P., "Bayesian model averaging is not model combination," tech. rep., 2002.

[83] Monteith, K., Carroll, J. L., Seppi, K., and Martinez, T., "Turning Bayesian Model Averaging into Bayesian Model Combination," in *The 2011 International Joint Conference on Neural Networks*, pp. 2657–2663, Ieee, jul 2011.

[84] Naylor, T. H. and Finger, J. M., "Verification of Computer Simulation Models," *Management Science*, vol. 14, no. 2, pp. B92–B106, 1967.

[85] Neelamkavil, F., *Computer Simulation and Modelling*. New York: John Wiley and Sons, 1987.

[86] Oberkampf, W. L. and Barone, M. F., "Measures of Agreement Between Computation and Experiment: Validation Metrics," *Journal of Computational Physics*, vol. 217, pp. 5–36, sep 2006.

[87] Oberkampf, W. L., DeLand, S. M., Rutherford, B. M., Diegert, K. V., and Alvin, K. F., "Error and Uncertainty In Modeling and Simulation," *Reliability Engineering and System Safety*, vol. 75, pp. 333–357, mar 2002.

[88] Oberkampf, W. L. and Roy, C. J., *Verification and Validation in Scientific Computing*. New York: Cambridge University Press, 2010.

[89] Oberkampf, W. L., Trucano, T. G., and Hirsch, C., "Verification, Validation, and Predictive Capability In Computational Engineering and Physics," *Applied Mechanics Reviews*, vol. 57, no. 5, p. 345, 2004.

[90] OPEC, *World Oil Outlook*. 2012.

[91] Pate-Cornell, M. E., "Uncertainties In Risk Analysis : Six Levels of Treatment," *Reliability Engineering and System Safety*, vol. 54, 1996.

[92] Patt, D. and Youngren, H., "Improving Blade-Element Design Methods for High Speed Proprotors," in *AHS Specialists' Conference on Aerodynamics*, (San Francisco), American Helicopter Society International, 2010.

[93] Peherstorfer, B., Willcox, K., and Gunzburger, M., "Survey of Multifidelity Methods in Uncertainty Propagation, Inference, and Optimization," tech. rep., 2016.

[94] Phillips, W. F., *Mechanics of Flight*. John Wiley and Sons, 2004.

[95] Raftery, A. E., Madigan, D., and Volinsky, C. T., "Accounting for Model Uncertainty in Survival Analysis Improves Predictive Performance," *Bayesian Statistics*, vol. 5, pp. 323–349, 1996.

[96] Regal, R. R. and Hook, E. B., "The Effects Of Model Selection On Confidence Intervals For The Size Of A Closed Population," *Statistics in Medicine*, vol. 10, no. 5, pp. 717–721, 1991.

[97] Roache, P. J., *Verification and Validation in Computational Science and Engineering*. Albuquerque: Hermosa, 1998.

[98] Rohrbach, C. and Metzger, F. B., "The Prop-Fan - A New Look In Propulsors," in *AIAA/SAE 11th Propulsion Conference*, (Anaheim), American Institute of Aeronautics and Astronautics, 1975.

[99] Rohrbach, C., Metzger, F. B., Black, D. M., and Ladden, R. M., "Evaluation of Wind Tunnel Performance Testings of an Advanced 45 Degree Swept Eight-Bladed Propeller at Mach Numbers From 0.45 to 0.85," *NASA CR-3505*, 1982.

[100] Roy, C. J. and Oberkampf, W. L., "A Comprehensive Framework for Verification, Validation, and Uncertainty Quantification in Scientific Computing," *Computer Methods in Applied Mechanics and Engineering*, vol. 200, pp. 2131–2144, jun 2011.

[101] Sacks, J., Welch, W. J., Mitchell, T. J., and Wynn, H. P., "Design and Analysis of Computer Experiments," *Statistical Science*, vol. 4, no. 4, pp. 409–435, 1989.

[102] Schwartz, H. D., Lee, C. H., and Mavris, D. N., "Multifidelity Aerodynamics with Second Order Augmented Kriging Adaptive Sampling," in *31st AIAA Applied Aerodynamics Conference*, (San Diego), pp. 1–10, 2013.

[103] Siemens PLM Software, "Star-CCM+," 2016.

[104] Simpson, T. W., Mauery, T. M., Korte, J., and Mistree, F., "Kriging Models for Global Approximation in Simulation-Based Multidisciplinary Design Optimization," *AIAA Journal*, vol. 39, no. 12, pp. 2233–2241, 2001.

[105] Simpson, T. W., Toropov, V., Balabanov, V., and Viana, F. A. C., "Design and Analysis of Computer Experiments in Multidisciplinary Design Optimization: A Review of How Far We Have Come or Not," *12th AIAA/ISSMO Multidisciplinary Analysis and Optimization Conference*, no. September, pp. 1–21, 2008.

[106] Spalart, P. R. and Allmaras, S. R., "A One-Equation Turbulence Model for Aerodynamic Flows," in *30th Aerospace Sciences Meeting & Exhibit*, (Reno), American Institute of Aeronautics and Astronautics, 1992.

[107] Srivastava, R., *An Efficient Hybrid Scheme for the Solution of Rotational Flow Around Advanced Propellers*. Ph.d thesis, Georgia Institute of Technology, 1990.

[108] Stack, J., "Tests Of Airfoils Designed To Delay The Compressibility Burble," *NACA Report No. 118*, 1939.

[109] Stack, J., "Tests of Airfoils Designed to Delay the Compressibility Burble," *NACA Report No. 763*, 1943.

[110] Stack, J., Lindsey, W. F., and Littell, R. E., "The Compressibility Burlble and The Effect of Compressibility On Pressures and Forces Acting On An Airfoil," *NACA Report No. 646*, 1938.

[111] Stack, J. and Von Doenhoff, A. E., "Tests of 16 Related Airfoils at High Speeds," *NACA Report No. 492*, 1934.

[112] Stephens, D. B., "Data Summary Report for the Open Rotor Propulsion Rig Equipped With F31/A31 Rotor Blades," *NASA TM-2014-216676*, 2014.

[113] Thunnissen, D. P., *Propagating and Mitigating Uncertainty in the Design of Complex Multidisciplinary Systems*. Ph.d. thesis, California Institute of Technology, 2005.

[114] Van Horn, R. L., "Validation of Simulation Results," *Management Science*, vol. 17, no. 5, pp. 247–258, 1971.

[115] Wasserman, L., "Bayesian Model Selection and Model Averaging.," *Journal of Mathematical Psychology*, vol. 44, pp. 92–107, mar 2000.

[116] Worobel, R. and Mayo, M. G., "Advanced General Aviation Propeller Study," *NASA CR-114289*, 1971.

[117] Ziemianski, J. A. and Whitlow Jr., J. B., "NASA/Industry Advanced Tuboprop Technology Program," in *16th Congress of the International Council of the Aeronautical Sciences*, (Jerusalem), 1988.

VITA

Henry D. Schwartz is from Salt Lake City, Utah. He attended Washington University in St. Louis where he received his B.S. in Aerospace Engineering in May 2009. While attending WashU, he participated in the university nano-satellite competition. As a member of the team he was in charge of the construction of the solar panels for the Akoya/Bandit nano-satellite. He also collaborated on the assembly and testing of the Bandit propulsion system. In additional to his academic research, Henry co-founded the Engineers Without Boarders chapter at WashU where he traveled to El Salvador to assisted local engineers with the design of clean water infrastructure in a small mountain village. After his undergraduate education, Henry worked for L3 Communications: Communications Systems West as a transition engineer. While at L3 his primary responsibility was to support systems engineering in the process of design-to-production ready assemblies. He also assisted with metal fabrication and tooling design. Henry decided to leave L3 after one year to attend graduate school at the Georgia Institute of Technology where he obtained his M.S. in Aerospace Engineering in May 2012 and Ph.D. in Aerospace Engineering in May 2017. While at Georgia Tech, he worked as a graduate researcher in the Aerospace Systems Design Laboratory and conducted research for both NASA and GE.